Spectral-element simulations of turbulent wall-bounded flows including transition and separation

by

Johan Malm

December 2011
Technical Reports
Royal Institute of Technology
Department of Mechanics
SE-100 44 Stockholm, Sweden

Akademisk avhandling som med tillstånd av Kungliga Tekniska Högskolan i Stockholm framlägges till offentlig granskning för avläggande av teknologie doktorsexamen fredagen den 16 december 2011 kl 10.15 i sal F3, Kungliga Tekniska Högskolan, Lindstedtsvägen 26, Stockholm.

Universitetsservice US–AB, Stockholm 2011

To Margit and Susanna, my dear little family

Spectral-element simulations of turbulent wall-bounded flows including transition and separation

Johan Malm
Linné FLOW Centre, Swedish e-Science Research Centre (SeRC)
KTH Mechanics
SE-100 44 Stockholm, Sweden

Abstract

The spectral-element method (SEM) is used to study wall-bounded turbulent flows in moderately complex geometries. The first part of the thesis is devoted to simulations of canonical flow cases, such as temporal K-type transition and turbulent channel flow, to investigate general resolution requirements and computational efficiency of the numerical code `nek5000`. Large-eddy simulation (LES) is further performed of a plane asymmetric diffuser flow with an opening angle of 8.5°, featuring turbulent flow separation. Good agreement with numerical studies of Herbst *et al.* (2007) is obtained, and it is concluded that the use of a high-order method is advantageous for flows featuring pressure-induced separation. Moreover, it is shown, both *a priori* on simpler model problems and *a posteriori* using the full Navier–Stokes equations, that the numerical instability associated with SEM at high Reynolds numbers is cured either by employing over-integration (dealiasing) or a filter-based stabilisation, thus rendering simulations of moderate to high Reynolds number flows possible.

The second part of the thesis is devoted to the first direct numerical simulation (DNS) of a truly three-dimensional, turbulent and separated diffuser flow at $Re = 10\ 000$ (based on bulk velocity and inflow-duct height), experimentally investigated by Cherry *et al.* (2008). The massively parallel capabilities of the spectral-element method are exploited by running the simulations on up to 32 768 processors. Very good agreement with experimental mean flow data is obtained and it is thus shown that well-resolved simulations of complex turbulent flows with high accuracy are possible at realistic Reynolds numbers even in complicated geometries. An explanation for the discovered asymmetry of the mean separated flow is provided and it is demonstrated that a large-scale quasi-periodic motion is present in the diffuser.

In addition, a new diagnostic measure, based on the maximum vorticity stretching component in every spatial point, is designed and tested in a number of turbulent and transitional flows. Finally, Koopman mode decomposition is performed of a minimal channel flow and compared to classical proper orthogonal decomposition (POD).

Descriptors: spectral-element method, direct numerical simulation (DNS), large-eddy simulation (LES), turbulence, transition, over-integration, three-dimensional separation, massively parallel simulations, proper orthogonal decomposition (POD), Koopman modes, vorticity stretching, coherence.

Preface

This doctoral thesis is concerned with the topic of fluid mechanics, which has been studied through numerical simulations. It is divided into two parts, where the first one is an introduction to the field and a summary of the present work. This summary makes no pretension to be complete, but is instead intended to make the material in the papers accessible to a wider audience by putting the work into a historic perspective. The second part is a collection of the papers listed below. Please note that 'Ohlsson' was my previous name before year 2010, and therefore refers to me. A summary of the papers together with a list of the conferences where the work was presented is given at the end of Part I, where also the division of work among the authors is stated. Note that the published papers have been adjusted to comply with the present thesis format for consistency, but their content is unchanged except for minor corrections.

The research project was initiated by Dr. Philipp Schlatter who has acted as co-advisor and Prof. Dan S. Henningson who has been the main supervisor. The following collaborators have moreover contributed to the work: Prof. Paul F. Fischer, Prof. Catherine Mavriplis, Prof. Neil D. Sandham and Dr. Shervin Bagheri.

Stockholm, November 2011
Johan Malm

Paper 1. Ohlsson, J., Schlatter, P., Mavriplis, C., & Henningson, D. S. 2011 The spectral-element and pseudo-spectral methods: A comparative study. *Spectral and High Order Methods for Partial Differential Equations, LNCSE* **76**, 459–468.

Paper 2. Ohlsson, J., Schlatter, P., Fischer, P. F. & Henningson, D. S. 2011 Stabilization of the spectral-element method in turbulent flow simulations. *Spectral and High Order Methods for Partial Differential Equations, LNCSE* **76**, 449–458.

Paper 3. Ohlsson, J., Schlatter, P., Fischer, P. F. & Henningson, D. S. 2010 Large-eddy simulation of turbulent flow in a plane asymmetric diffuser by the spectral-element method. *Direct and Large-Eddy Simulation VII*, 197–204.

Paper 4. Malm, J., Bagheri, S., Schlatter, P. & Henningson, D. S. 2010 Koopman mode decomposition of a minimal channel flow. *Internal report.*

Paper 5. Malm, J., Schlatter, P. & Sandham, N. D. 2011 A vorticity stretching diagnostic for turbulent and transitional flows. *Theor. Comput. Fluid Dyn.* Accepted.

Paper 6. Ohlsson, J., Schlatter, P., Fischer, P. F. & Henningson, D. S. 2010 Direct numerical simulation of separated flow in a three-dimensional diffuser. *J. Fluid Mech.* **650**, 307–318.

Paper 7. Malm, J., Schlatter, P., Fischer, P. F. & Henningson, D. S. 2011 Coherent structures and dominant frequencies in a turbulent three-dimensional diffuser. *J. Fluid Mech.* Under revision.

"The whole of science is nothing more than a refinement of everyday thinking."

Albert Einstein (1879–1955)

Contents

Part II - Papers

Part I

Summary

CHAPTER 1

Introduction

1.1. The unsolved problem of classical physics

The intricate nature of turbulent fluid[1] flows has for centuries puzzled researchers. In times when modern physics successfully discovered new areas such as relativity theory and quantum mechanics, the influential fluid mechanics researcher Sir Horace Lamb (1849–1934) stated that,

> *"I am an old man now, and when I die and go to heaven there are two matters on which I hope for enlightenment. One is quantum electrodynamics, and the other is the turbulent motion of fluids. And about the former I am rather optimistic."*

Almost a century later, a complete theory to predict the motion of a turbulent flow is still lacking. It is considered to be one of the unsolved problems of physics[2] of the same dignity as the existence of dark matter and the unknown future of our universe. For a novice in the field, it may indeed seem a bit odd that it is possible to develop a theory for the motion on scales of 10^{-35} m and determine the compound of stars in distant galaxies, whereas it is impossible to determine the exact path of a bark boat on a river or a hurricane over the Atlantic ocean. It appears even more surprising given that the equations governing the fluid motion have been known for more than two centuries. These are based on classical, elementary mechanics and are obtained by applying Newton's second law of motion to a fluid element, thereby arriving at the *Navier–Stokes equations*, independently derived by G. G. Stokes and M. Navier in the early 1800's (see Chapter 2.1). The Navier–Stokes equations constitute a set of non-linear, time dependent, partial differential equations (PDEs), to which analytical solutions exist in rare special cases but most commonly are out of reach. Not only solutions are difficult to *find*. The Clay Mathematics Institute offers $1,000,000 to the mathematician who can prove the *existence*

[1] A *fluid* is a substance which will deform under infinitely small shear stresses. Typical fluids include gases, liquids and plasmas.

[2] Richard Feynman, the winner of the Nobel Prize in physics 1965 (quantum electrodynamics), once said that turbulence is "the most important unsolved problem of classical physics", which indeed gives some justice to the statement by Sir Horace Lamb.

of a smooth and unique solution to the Navier–Stokes equations in three dimensions[3]. One of the main source of difficulties is the *non-linearity* of the equations, which makes them chaotic under certain conditions. While still deterministic, this means that the solution is highly sensitive to initial conditions. In other words, a disturbed initial condition (no matter how little) will after a sufficiently long time change the solution completely. Therefore, trying to predict the weather next year is (and will most likely continue to be) an impossible task. Another problem is the *non-locality* of the equations, which is due to the fact that the pressure in one point in space depends on the velocity field in all other points. The implication is that all scales in a turbulent flow depends on each other — from the largest (which can be of, say, the size of an entire airplane) down to the smallest (on the order of millimetres). This poses difficulties, not only for the analytical, but also for the numerical treatment of the equations (these issues are further discussed in Chapter 2.2). Many peculiarities are hidden in the equations, of which one is the occurrence of turbulence itself. Although described by the same set of equations, a fluid flow in general can be classified either as *laminar* (ordered and regular) or *turbulent* (random, chaotic and highly time dependent). The transition between these two states depends principally on the dimensionless *Reynolds number* (Re) relating the amount of inertia to the viscous forces in the flow, but also on the amplitude of disturbances active in the flow and the flow geometry. For every flow, there exist a critical Reynolds number, Re_c, above which the flow is likely to be turbulent.

Although being an unresolved problem, turbulence is of major importance for engineering and geophysical applications. *Eliminating* turbulence on airplane wings could save up to 15 % fuel consumption (Schrauf 2005), since turbulence leads to a larger friction drag. *Increasing* turbulence in engines would enhance the mixing of fuel and oxygen and therefore lead to a more efficient combustion process. The reason for both phenomena above is simply that turbulence is a consequence of the fundamental principle, in which nature wants to reduce gradients (*i.e.* even out and mix). It follows that the transport heat, contaminants and momentum in a turbulent flow occurs at a much higher rate than for the laminar counterpart where transport relies on diffusion, which is a slow process on the molecular level. Typically, this difference is 10^{10} times in the oceans (see *e.g.* Pond & Pickard 1983). Finally, understanding turbulence *per se* could for instance help to predict severe weather events more accurately (at least in the short term) and thus save lives and property to a larger extent.

1.2. Numerics as a promising tool to study turbulence

So what can we do to in order to gain further knowledge of the dynamics of turbulent flows? As we have seen, we are still far from a theoretical solution to the turbulence problem. Asymptotic analysis, in which one studies the limiting behaviour of a flow when a parameter (*e.g.* the Reynolds number)

[3]See rules and problem description at http://www.claymath.org/millennium/

becomes very large (or small), can in some cases provide useful information (see *e.g.* Cousteix & Mauss 2007). Experiments in a controlled environment such as a wind tunnel was for a long time the only option, and continues to be of major importance. Its advantages consist in the obvious fact that a 'real' flow is observed. Moreover, relatively high Reynolds numbers can be reached. However, precautions must be taken. For instance, since the viscosity of a fluid is temperature dependent[4], the temperature of the working fluid must be accurately controlled, such that the Reynolds number is not modified. In addition, the disturbances within and around the wind tunnel (*e.g.* noise from the engine driving the flow or traffic outside the laboratory) or unexpected roughness at the walls need to be controlled. Beside that, there are problems related to the measurements. In particular, there are difficulties involved in measuring the flow velocity sufficiently close (typically a few micrometers) to a solid wall. It is even hard to know where the wall *is* (see Örlü *et al.* 2010, for an excellent review). In addition, the measurement devices need to be small enough to be able to measure the velocity field without disturbing the flow and to truly respond to scales smaller than its own dimensions (see *e.g.* Örlü & Alfredsson 2010). Measuring pressure fluctuations is another problem (see Tsuji *et al.* 2007). A more general review regarding issues in experimental fluid mechanics can be found in Tropea *et al.* (2007).

With the advent of faster computers it has become feasible to solve the Navier–Stokes equations numerically in a discretized form, thereby finding solutions to the equations in cases where analytical solutions do not exist. The study of fluid mechanics by numerical means is usually referred to as *computational fluid dynamics* (CFD), and is considered to be a science in its own right. Assuming that (i) the Navier–Stokes equations constitute a good model for fluid flows (which they generally do given that the fluid is considered to be a continuum and not a rarefied gas[5], and that relativistic velocities are not reached); (ii) proper boundary conditions are imposed (this is usually the most difficult part), and (iii) high enough spatial and temporal resolutions are used, this approach compares very well to experimental data. A fourth point to consider is the numerical discretization errors, to be discussed further in Chapter 2.3. One of the key attractions of a numerical simulation is that it produces well-resolved data in time and space. The data do not only need to be velocity or pressure fields, since all kinds of exotic quantities can be computed on the fly or in successive post-processing steps. Especially quantities based on pressure are notoriously difficult to obtain via experiments. Moreover, when dealing with high temperatures and pressures (such as the environment in a combustion chamber) experiments can be cumbersome, while simulations have no difficulties. Finally, the ability to simulate 'wrong' physics should not be underestimated as a great tool to understand flow physics. For instance, this

[4]For ideal gases, $\mu \sim \sqrt{T}$, where μ is the dynamic viscosity and T is the temperature (Kundu & Cohen 2008).

[5]Formally, this is true if the *Knudsen number,* $Kn \ll 1$ (see *e.g.* Gombosi 1994).

can be accomplished by studying the effects of imposing artificial boundary and initial conditions on the flow. An example is the concept of 'minimal flow unit' introduced by Jiménez & Moin (1991). The basic idea is to simulate a turbulent flow in a channel (or any other canonical flow) and successively decrease the domain size until the point just before the flow relaminarises, but turbulence still can be sustained. The observed turbulence in such a small domain contains less degrees of freedom and thus facilitates understanding of the basic dynamics. The same idea is used in Paper 5 to investigate the basic properties of vorticity stretching in near-wall turbulence, and in Paper 4 to investigate the Koopman mode decomposition (see Chapter 4). Another example by Jiménez & Pinelli (1999) is to explicitly filter the turbulent scales above a certain distance from the wall in order to examine the dependence of the near-wall turbulence on the outer flow structures.

Solving the Navier–Stokes equations numerically without averaging and modelling is referred to as *direct numerical simulation* (DNS) (used in Papers $1, 2, 4, 5, 6$ and 7.). As point (iii) above suggests (and which holds true for all numerical techniques solving PDEs in general) enough resolution in time as well as space has to be used. The implication for a turbulent flow simulation, where the spatial resolution scales as $Re^{3/4}$ in each direction and the temporal resolution scales as $Re^{1/2}$ (*e.g.* Pope 2000; Moin & Kim 1997), is that this leads to a computational impossibility for high Reynolds numbers. As a consequence, DNS has traditionally been obliged to reside in the low Reynolds number regime, far from the ones at which experiments are performed. The early numerical flow simulations focused on weather prediction, where simpler forms of the Navier–Stokes equations where solved. In a first attempt by L. F. Richardson around 1922, the result of a 6 hours weather forecast took 6 weeks to compute by hand and did not give very realistic results (see the historical review by Lynch 2008). Around 25 years later Charney *et al.* (1950) performed the first correct weather forecast on ENIAC (Electronic Numerical Integrator And Computer), one of the very first electronic computers. The early simulations of the full Navier–Stokes equations were mainly focused on the laminar flow regime (Fromm & Harlow 1963). The first direct computation of turbulence was performed by Orszag & Patterson (1972), who studied homogeneous isotropic turbulence. A milestone in the simulation of wall-bounded turbulence and the most cited paper[6] in the *Journal of Fluid Mechanics* was performed by Kim *et al.* (1987), involving a computer engineer to change broken processors during the simulation! The achieved Reynolds number of that simulation is today considered to be relatively low, but nevertheless it greatly contributed to understanding some properties of wall-bounded turbulence. More importantly, it made numerical simulations qualify as an equally valid option to study fluid mechanics besides experiments and theory. An example showing the possibility

[6]Most-cited ranking at *Cambridge Journals Online - Journal of Fluid Mechanics*, as given in November 2011.

FIGURE 1.1. Two equally valid ways to study flow dynamics: (*a*) through experiments (cigarette smoke) and (*b*) by solving the Navier–Stokes equations numerically (reaction flame, courtesy of Stefan Kerkemeier).

of simulations to mimic real flows can be seen in figure 1.1, where two transitional flows are depicted. In (*a*) an instantaneous picture of cigarette smoke (*i.e.* the 'experiment') is shown, whereas (*b*) shows a reaction flame obtained by solving the Navier–Stokes equations numerically.

From the 1970's until the present, computing hardware has followed the so-called *Moore's law* (Moore 1965), which states that the number of transistors that can be placed on a chip doubles every two years, *i.e.* featuring exponential growth. For many years, this could be directly related to an increase in processor clock-frequency and thus the number of floating point operations (FLOPS) that could be completed in every second. In recent years, the clock frequency for a given processor has almost reached its limit, and due to cooling issues vendors instead favour multi-core chip design in order to keep up with Moore's law. Nevertheless, these rapid developments in computer hardware (and software) have made simulations of turbulence, by means of DNS, approach experiments in terms of Reynolds number. In this context, the term 'numerical experiment' has recently been adopted, see *e.g.* Schlatter *et al.* (2011*b*); Kasagi (1998). One such example is the turbulent diffuser flow, which constitutes the main topic of the present thesis (Chapter 5 and Papers 6, 7), where the Reynolds number of $Re = 10\ 000$ exactly matched the experiment conducted by Cherry *et al.* (2008). For this, a spatial resolution of approximately 220 million grid points was employed.

For yet higher Reynolds number flows, *large-eddy simulation* (LES) (used in Paper 3) has in recent years evolved into a promising tool for flow predictions. Here, the evolution of the large scale structures of the flow (*i.e.* the *large*

eddies) are solved for, whereas the smaller structures, not resolved by the numerical grid, are modelled. Consequently, compared to DNS, LES reduces the computational burden significantly. The drawback, however, is that the models involved in LES are at the present not universal, and special care has to be taken as new flow cases are being studied (see *e.g.* Sagaut 2006). Finally, the numerical technique which can seriously deal with really high Reynolds numbers are the so-called Reynolds-averaged Navier–Stokes equations (RANS), where an ensemble average of the Navier–Stokes equations is solved for. The averaging process gives rise to unclosed terms which have to be modelled. Although RANS may be a rather crude way to describe a highly time-dependent flow, it may in many situations be sufficient to compute the mean flow characteristics, *e.g.* to get approximations of mean lift and drag forces on an airplane wing. The drawback is that the validity of the results strongly depends on the given closure term and that the fluctuating flow is small compared to the mean flow. In particular, flows experiencing adverse pressure gradients and separation are very hard to predict due to rapid changes in mean flow properties (Jakirlić *et al.* 2010*b*). Still, it is the most widely used approach for complex engineering flows, where typical Reynolds numbers can be on the order of millions. Due to its dependence on the modelling, this technique is of limited value for fundamental studies in fluid mechanics and not considered within this thesis. The interested reader is referred to *e.g.* Wilcox (1998).

1.3. Aim and outline of the present thesis

This thesis deals with the numerical solution of turbulent *wall-bounded* flows including *transition* and *separation*. 'Wall-bounded' means that the flow is close to a solid surface, at which the fluid velocity is zero (a so-called 'no-slip'[7] boundary condition). In fact, all flows considered are internal, meaning that the flow is either surrounded by walls or an infinite direction is assumed to exist by introducing periodic boundary conditions. These two types of boundary conditions are generally better defined than the ones used for open or external flows, such as the flow around a golf ball or an airplane wing, where the computational domain has to be artificially truncated. The 'transitional' flows, *i.e.* flows that during the course of the simulation go through laminar-turbulent transition, have mainly served as validation cases and no new physics has been investigated (see Chapter 3.2). 'Separation' relates to the phenomenon when a flow departures from the surface, leading to reversed flow, which is commonly occurring behind blunt bodies (as opposed to streamlined bodies), such as a football. A brief background concerning this topic and some results are contained in Chapter 3.3 and 5. The tool used to solve the flow equations numerically in a discretized form is the *spectral-element method* (SEM). It is a high-order and accurate numerical method suited to solve non-linear, time-dependent PDEs such as the Navier–Stokes equations. Its ability to build more

[7] Mathematically speaking, this means $u = w = 0$, where u, w denote the streamwise and spanwise velocities, respectively. In addition, $v = 0$, where v is the wall-normal velocity, if the walls are impermeable.

complex geometries than traditional spectral methods and still maintain high accuracy makes the spectral-element method attractive to research purposes and, perhaps later on, industry.

The main goal throughout the work has been to accurately simulate 'real' turbulent flows on massively parallel computers, thereby matching the Reynolds numbers employed in experiments. For this, work regarding numerical stability and computational efficiency as well as detailed validations has been an important part.

The thesis is organised as follows. The rest of Part I continues to introduce concepts used in the present research project, with the help of some illustrative results. Thus, Chapter 2 introduces the governing equations and how to solve them using the spectral-element method. In Chapter 3 simulations of turbulence, transition and separation using the spectral-element method are briefly discussed. Chapter 4 deals with a few techniques used for the flow analysis, whereas Chapter 5 is devoted to the physics of a complex three-dimensional separated flow. Chapter 6 contains the conclusions and outlook. Finally, in Chapter 7, one finds summaries of the papers together with author contributions and a list of conferences where the work was presented. Part II contains seven papers on numerical stability, turbulent separation, vortex stretching and Koopman mode decomposition.

CHAPTER 2

Flow simulations using high-order methods

Continuing the route embarked in the last chapter, where we introduced the concept of numerically solving the equations of motion governing a fluid flow, we will here on a more technical level outline how to proceed. We will start by introducing the equations which are solved when we deal with direct numerical simulations (DNS) and how to arrive at a slightly different set of equations when using large-eddy simulation (LES). Then, in section 2.2, some of the difficulties in solving these equations will be recapitulated and the concept of high-order numerical methods (section 2.3) is introduced. In particular, we will advocate for the use of these in flow simulations. The *pseudo-spectral* and the *spectral-element* methods, which are the high-order methods used in this thesis, are mentioned. The rest of the chapter (sections 2.4–2.6) is devoted to the spectral-element method, which is the method responsible for the bulk of the results in this thesis. In particular, the discretization and implementation are outlined as well as some central issues regarding the stability of the method.

2.1. Governing equations

The governing equations for an incompressible and Newtonian[1] fluid flow are given by the Navier–Stokes equations, here written in non-dimensional form,

$$\frac{\partial \boldsymbol{u}}{\partial t} + \boldsymbol{u}\cdot\nabla\boldsymbol{u} = -\nabla p + \frac{1}{Re}\nabla^2\boldsymbol{u} \tag{2.1a}$$

$$\nabla\cdot\boldsymbol{u} = 0, \tag{2.1b}$$

where $\boldsymbol{u}(\boldsymbol{x},t) = (u_1,u_2,u_3)^{\mathrm{T}} = (u,v,w)^{\mathrm{T}}$ is the velocity field and $p(\boldsymbol{x},t)$ is the pressure field in space, $\boldsymbol{x} = (x_1,x_2,x_3)^{\mathrm{T}} = (x,y,z)^{\mathrm{T}}$, and time, t. Throughout the thesis the convention will be used that x denotes the streamwise, y the wall-normal and z the spanwise directions, respectively. The incompressibility of the considered flow reduces the continuity equation (conservation of mass), equation (2.1*b*), to the constraint that the velocity field is solenoidal. The Reynolds number, $Re = UL/\nu$, governing the state of the flow (laminar, transitional or turbulent) is based on characteristic velocity and length scales, U and L respectively, together with the kinematic viscosity ν. These characteristic scales are used to non-dimensionalise the variables appearing in equation

[1] In a *Newtonian* fluid (such as most gases and liquids), the shear stress, τ, is proportional to the strain rate, $\partial u/\partial y$, with the proportionality constant being the fluid's dynamic viscosity, μ, *i.e.* for a simple shear flow $\tau = \mu\frac{\partial u}{\partial y}$.

(2.1). In this process, the time is normalised by L/U, whereas the pressure is normalised by $\rho U^2/2$, where ρ is the constant density. The evolution of the large-scale structures, denoted by $\bar{\boldsymbol{u}}(\boldsymbol{x},t)$ and $\bar{p}(\boldsymbol{x},t)$, are obtained by spatially filtering the Navier–Stokes equations, thereby giving the governing equations for LES,

$$\frac{\partial \bar{\boldsymbol{u}}}{\partial t} + \bar{\boldsymbol{u}} \cdot \nabla \bar{\boldsymbol{u}} = -\nabla \bar{p} + \frac{1}{Re}\nabla^2 \bar{\boldsymbol{u}} - \nabla \boldsymbol{\tau} \tag{2.2a}$$

$$\nabla \cdot \bar{\boldsymbol{u}} = 0. \tag{2.2b}$$

The filtering procedure gives rise to the so-called subgrid stresses (SGS) $\boldsymbol{\tau} = \overline{\boldsymbol{u}\boldsymbol{u}} - \bar{\boldsymbol{u}}\bar{\boldsymbol{u}}$, which have to be modelled, since they cannot be expressed solely in the known field, $\bar{\boldsymbol{u}}$. However, there exist several procedures where the subgrid stresses are *estimated* from the resolved field, thus closing equation (2.2). The simplest but also one of the most successful and widely used closure is the Smagorinsky eddy-viscosity model, where the subgrid stress depends on the resolved strain rate as

$$\boldsymbol{\tau} = -2\nu_t \bar{\boldsymbol{S}}. \tag{2.3}$$

$\bar{\boldsymbol{S}} = \frac{1}{2}(\nabla \bar{\boldsymbol{u}} + \nabla \bar{\boldsymbol{u}}^{\mathrm{T}})$ is here the strain rate tensor and the eddy viscosity is computed by

$$\nu_t = C\Delta^2 |\bar{\boldsymbol{S}}|, \tag{2.4}$$

(Smagorinsky 1963) where $|\bar{\boldsymbol{S}}|$ is defined as $|\bar{\boldsymbol{S}}| = \sqrt{2\bar{\boldsymbol{S}}\bar{\boldsymbol{S}}}$ and Δ is the filter width, usually computed from the local grid spacing. In the case of the *dynamic* Smagorinsky model, the model coefficient, C, is computed according to the dynamic procedure proposed by Germano *et al.* (1991) and Lilly (1992), where a test filter is used to model the behaviour of the largest unresolved scales. In the framework of SEM, the test filter is implemented in Legendre space (see also Blackburn & Schmidt 2003). To limit the fluctuation of the model coefficient, spatial averaging is used along the homogeneous spanwise direction (see Lilly 1992) together with clipping of the model coefficient (negative values are discarded).

2.2. Numerical and computational challenges

When we discuss numerical solutions to PDEs, such as the Navier–Stokes equations in the previous section, we are concerned with finding an appropriate discretization in time and space. In one space dimension this amounts to partition the continuous domain $x \in [x_0, x_{\mathrm{end}}]$ and $t \in [t_0, T]$ to a set of points $\{x_j\}$, $\{t_i\}$ and solve the governing discretized equations on these points. This leads to a discretization error (which is usually much larger than the round-off error due to finite precision). Depending on the method of choice (the numerical analysis part) and the given resolution (the computing part), the difference between the numerical solution and the true solution will vary[2].

[2]However, due to *Lax equivalence theorem*, for a well-posed problem and a consistent and stable numerical method, the numerical solution is guaranteed to converge to the true solution — at least for linear problems (see *e.g.* Leveque 2002).

Over the last decades, much research has been devoted to the numerical solution of the Navier–Stokes equations. There are three main difficulties which contribute to make the problem one of the most challenging in numerical analysis. First, the importance of accurate discretizations is particularly evident due to the *non-linearity*. Discretization errors are easily amplified and will lead to inaccurate results or even numerical instabilities. From a given initial condition of some typical spatial scale, a non-linear term has the ability to produce smaller and smaller scales (depending on the given forcing and boundary conditions), which easily can lead to regions in the flow with insufficient spatial resolution.

Secondly, the nature of the equations are *singularly-perturbed*, which means that they are governed by a small parameter which cannot be set to zero. This parameter is nothing but the inverse of the Reynolds number multiplying the second derivative term. Thus, setting it to zero would change the number of boundary conditions and therefore drastically the dynamics of the system. In that case, we would arrive at the Euler equations, which is a purely hyperbolic system. The implication of this parameter being nonzero is the presence of *boundary layers*, which get thinner with increasing Re. The solution will therefore contain dynamics simultaneously present at several different scales, which calls for demanding resolution requirements.

Thirdly, the incompressible Navier–Stokes equations are of a *mixed parabolic-hyperbolic* type, which implies that efficient numerical methods for purely parabolic problems (*e.g.* explicit marching methods) or hyperbolic problems (*e.g.* based on characteristics) are excluded. Conversely, in the case of a pure parabolic or hyperbolic problem, the algorithms employed can be more specialised and thus more efficient.

The two first points above lead to the presence of small scales in time and space. The *major challenge for simulations of flows* by means of DNS is therefore that the total resolution requirements scale as $n \sim Re^{11/4}$ (*e.g.* Pope 2000; Moin & Kim 1997). The use of parallel computers is thus unavoidable. One of the advantages of the incompressible formulation of the Navier–Stokes equations in equation (2.1) is that the equation governing the internal energy, e, of the fluid is decoupled from the system of equations. This approach enables the internal energy to be converted into temperature[3], which can then be treated as a passive scalar. In that case, one solves the heat equation as a complementary equation, which is not needed to advance the flow. While this approach reduces the number of independent variables from 6 $(\boldsymbol{u}, p, e, \rho)$ to 4 $(\boldsymbol{u}, p)$, it also leads to the *second challenge* in flow simulations, namely the necessity to solve an elliptic problem for the pressure (see section 2.5 for further details). Since elliptic problems involve a global coupling, *i.e.* a dependence of one variable (in this case the pressure) on another variable (velocity) and vice versa in the entire domain, this will complicate the parallelisation of the numerical method.

[3]This is accomplished through the relation $T = e/C_v$, where C_v is the specific heat at constant volume and T is the temperature.

From a physical point of view this means that pressure waves, *i.e.* the speed of sound, travel with infinite speed throughout the domain and are therefore 'sensed' in all other points. This is in contrast to compressible flows, where the speed of sound has a finite value. Practically, the processors involved in the computation need to communicate with each other in every time step.

Facing the above challenges seems indeed as a difficult task. A promising approach, which has gained interest in the past few years, are the lattice Boltzmann methods (LBM), which instead of solving the discrete Navier–Stokes equations solve a discrete variant of the more general Boltzmann equation. Their main strengths are computational speed, due to good parallel efficiency, together with their ability to handle complex geometries. There are however open issues regarding the accuracy at high Reynolds and Mach numbers. Further, most of the LBMs require the lattice structure to be uniform throughout the domain and therefore unnecessary resolution in certain regions is a consequence (Succi 2001). Holding on to the discrete Navier–Stokes equations, the best we can do is to choose a high-order numerical method — to be investigated in the next section.

2.3. High-order numerical methods

When solving a PDE, the solution is typically approximated by continuous functions, often polynomials, whose derivatives need to satisfy the governing equations at discrete (grid) points. The notion of 'order' for a numerical method refers to the order of these polynomials. This applies both to time and space discretizations, but in the following we shall focus on the space discretization. Let us for the sake of illustration consider an arbitrary (smooth) function $f(x)$ in one space dimension, approximated by $\tilde{f}(x)$. Based on the approximated solution, we can define the derivative, $f'(x) \approx \tilde{f}'(x)$. *Local* methods, such as most finite difference- (FD), finite volume- (FV), and finite element (FE) methods used in commercial CFD packages are of low order and approximate the derivatives based on the local solution, *i.e.* data values in the immediate neighbourhood. To be more specific, for a finite difference approximation, where the derivative and corresponding discretization error are derived from a Taylor expansion around point x_i, this implies

$$\tilde{f}'(x_i) = \frac{\tilde{f}(x_i + h) - \tilde{f}(x_i)}{h} + \mathcal{O}(h), \tag{2.5}$$

where h defines the distance between two adjacent grid points. Equation (2.5) thus states that the discretization error is proportional to the grid size, and by doubling the number of points, the error is reduced by a factor two. If the polynomial is of higher order, we can use not only neighbouring points to define the derivative at point x_i, but also points further away, which will enhance the accuracy and decrease the error of the approximation. Indeed, if we instead of the above one-sided finite difference employ a central finite difference, we get

$$\tilde{f}'(x_i) = \frac{\tilde{f}(x_i + h) - \tilde{f}(x_i - h)}{2h} + \mathcal{O}(h^2), \tag{2.6}$$

which means that the error decreases quadratically with the grid size and we would arrive at the same error as before by using $\sqrt{2}$ (instead of 2) times more grid points. Thus, the order of the approximated solution will be directly related to the number of grid points needed for a certain numerical error.

If we take this idea one step further, we can define derivatives based on polynomials that live on the entire interval. Consequently, they are not anymore local but instead we denote them as *global*. Such polynomials can be interpolants based on equidistant points, as in the finite difference example above, or more exotic polynomials such as Chebyshev or Legendre polynomials with a non-equidistant point distribution. The latter category is the preferred choice in problems with inhomogeneous boundary conditions, where the former has problems[4]. In fact, the global functions do not need to be polynomials at all. Perhaps the most obvious option one may think of are the trigonometric functions. By using these, we will arrive at Fourier spectral methods, further discussed below.

For sufficiently smooth problems, numerical methods based on global functions display a so-called *spectral convergence* or *spectral accuracy*, which is no longer an algebraic error decay as $\mathcal{O}(h^m)$, where $m = 1, 2, ...$ depending on the order of the method, but rather an exponential one, $\mathcal{O}(c^N)$, where N is the total number of points and $0 < c < 1$. Having such a rapid convergence of the solution implies that the discretization (or truncation) error in principle goes to zero and one is left with the round-off error, which is on the order of 10^{-16}. Other desirable properties, which are connected to the high level of accuracy, are the low amounts of numerical (*i.e.* artificial) viscosity and dispersion errors which yield particularly satisfactory results at high Re, where flow structures are not easily dissipated but rather convected for long distances and times. Coincidentally, the lack of numerical viscosity could also be a source of troubles. Especially at high Re, when the actual viscosity contributes with little damping in the system, high-order methods might suffer from stability issues. This is further discussed in section 2.6.

As the previous examples have shown, the resolution requirements for a given discretization error relaxes when employing higher-order methods. Clearly, this is computationally beneficial. However, the solution strategies used do also play a crucial role (see *e.g.* Vos *et al.* 2010, for an in-depth analysis of the issue). This will be further touched upon in section 2.5. A final reason to choose a high-order method, which may seem trivial but is becoming increasingly important, is the saving, transferring and post-processing of simulation data. As a high-order method can suffice to use much less resolution for a given accuracy compared to a low-order method, the data files will consequently be much smaller.

While the key to success for high-order methods is the global representation of the approximated functions, it is also their limitation. Troubles appear

[4]The *Runge phenomenon* (Runge 1901) will cause large oscillations of the approximated solution near the edge of the interval when an equidistant point distribution is employed.

whenever the geometrical complexity increases. Local methods, on the other hand, can be made geometrically very flexible, which is of particular importance when considering engineering applications. As we will soon see, the spectral-element method can handle moderately complex geometries, while maintaining high order.

Finally, a remark regarding the time discretization. The so-called CFL condition, which defines the maximum allowed time step given a particular grid size ($\mathrm{C} \equiv u_{\max}\Delta t/\Delta x$, $C \lesssim 1$) usually gives a time step so small that a relatively low order (typically $2-3$) is sufficient for the solution to be well converged in time. Note, however, that care must be taken in order to perform the time discretization accurately. For the Navier–Stokes equations, usually a semi-implicit time advancement is employed, with explicit treatment of the non-linear terms and implicit treatment of the viscous and pressure/incompressibility terms, see *e.g.* the review by Moin & Mahesh (1998).

In the following, we will review the two high-order methods used in the present thesis.

2.3.1. *The pseudo-spectral method*

As mentioned above, a (Fourier) *spectral method* is obtained when we wish to approximate the solution to the governing equations by a sum of trigonometric functions, *i.e.*

$$\boldsymbol{u}(\boldsymbol{x},t) = \sum_{\boldsymbol{\kappa}} e^{i\boldsymbol{\kappa}\cdot\boldsymbol{x}}\hat{\boldsymbol{u}}(\boldsymbol{\kappa},t), \tag{2.7}$$

where $\boldsymbol{\kappa}$ are the wavenumbers and $\hat{\boldsymbol{u}}$ are the Fourier modes. The lowest wavenumber (in the x-direction) is $|\boldsymbol{\kappa}_0| = 2\pi/L_x$, assuming L_x is the size of the domain in the x-direction; whereas the highest is given by $|\boldsymbol{\kappa}_{\max}| = 2\pi/\Delta x$, where x is the grid spacing. Upon substituting equation (2.7) into the governing equations, this amounts to a transformation of the Navier–Stokes equations into Fourier spectral space. Hence, the unknowns are the Fourier modes. The non-linear terms in the Navier–Stokes equations turns into a convolution sum when transformed into spectral space. To avoid the large number of operations involved in evaluating this sum, Orszag (1972) introduced the *pseudo-spectral methods*, where the solution is transformed into physical space prior to evaluating the non-linear terms, which then consists in performing simple multiplications. This reduces the cost from $\sim N^6$ operations in each time step, where N is the total resolution, to $\sim N^3 \log N$, given that the fast Fourier transform (FFT) is used. Virtually no method can compete with a pseudo-spectral method regarding accuracy and speed in canonical flow cases, such as channel flows (shown in Paper 1) or boundary layers. Thus, the largest direct numerical simulations so far have made use of pseudo-spectral methods; for instance the simulation of homogeneous isotropic turbulence in a triple-periodic box using ~ 69 billion points by Kaneda *et al.* (2003), or the boundary-layer simulation using ~ 7.5 billion points by Schlatter & Örlü (2010). However, their superiority also leads to the restriction that they only work efficiently for

these very simple geometries (Canuto *et al.* 1988). For instance, the expansion in Fourier series requires the solution to be periodic. For a growing boundary layer this can be circumvented by the use of a 'fringe' (Nordström *et al.* 1999) in the streamwise direction and expansion in Chebyshev polynomials in the wall-normal direction. This is however, at the limit of its complexity. Further details about the particular spectral code `simson` used in this thesis can be found in Chevalier *et al.* (2007).

2.3.2. *The spectral-element method*

A method that is capable of combining the accuracy of the Fourier spectral methods and the flexibility of methods based on low-order local approaches is the spectral-element method (SEM), introduced by Patera (1984). It is a high-order weighted residual technique similar to FEM, but based on orthogonal polynomials and highly accurate numerical quadrature. The original implementation by Patera (1984) was based on Chebyshev polynomials, but later implementations have rather been utilising Legendre polynomials. The method exhibits several favourable computational properties, such as the use of tensor products and naturally diagonal mass matrices, which makes it suitable for parallel implementations and large calculations.

In the following section, we will discuss how the discretization by the spectral-element method can be accomplished. Whereas the main steps are outlined here, the reader is referred to Fischer (1997); Tufo & Fischer (2001); Deville *et al.* (2002) for a more detailed description of the spatial discretization and time integration. Key concepts are the 'weak form' and 'Galerkin projection' together with 'high-order basis functions'. Then, in section (2.5), the practical implementation is sketched and the importance of efficient solution techniques by means of scalable coarse-grid solvers is highlighted.

2.4. Discretization by the spectral-element method

Assuming we are solving equation (2.1) in a domain Ω, the starting point for a SEM discretization, as in the case for FEM, is to cast the problem in the weak formulation, in which equation (2.1) is multiplied by a test function $(\boldsymbol{v}, q) \in H_0^1(\Omega)$ and integrated over Ω. Here, $H_0^1(\Omega)$ denotes the space of functions in $L^2(\Omega)$ (the space of square integrable functions defined on Ω) vanishing on the boundaries and whose first derivative is also in $L^2(\Omega)$. The viscous term is integrated by parts, such that the highest existent derivative is of first order. The problem (2.1) then becomes: *Find* $(u, p) \in H_0^1$, *such that*

$$\frac{\mathrm{d}}{\mathrm{d}t}(\boldsymbol{v}, \boldsymbol{u}) + (\boldsymbol{v}, \boldsymbol{u} \cdot \nabla \boldsymbol{u}) = (p, \nabla \cdot \boldsymbol{v}) - \frac{1}{Re}(\nabla \boldsymbol{v}, \nabla \boldsymbol{u}), \quad (\nabla \cdot \boldsymbol{u}, q) = 0, \quad \forall (\boldsymbol{v}, q) \in H_0^1 \tag{2.8}$$

where the inner products $(\cdot, \cdot)$ are defined as

$$(v, u) := \int_\Omega vu \, \mathrm{d}\boldsymbol{x}. \tag{2.9}$$

The discretization proceeds by the Galerkin approximation, where the test and trial spaces are restricted to the velocity and pressure spaces $X^N \subset H_0^1$ and $Y^N \subset L^2$ respectively following the $\mathbb{P}_N - \mathbb{P}_{N-2}$ SEM discretization by Maday & Patera (1989), where the pressure is associated with polynomials of two degrees lower than the velocities. This staggered approach was originally reasoned to avoid spurious pressure modes. However, more recent discretizations of SEM utilising $\mathbb{P}_N - \mathbb{P}_N$ shows that this does not have to be the case (Tomboulides *et al.* 1997). The FEM and SEM differ by the choice of X^N. While linear functions are commonly employed in FEM, for SEM this is typically a space of Nth-order Lagrange polynomial interpolants, $h_i^N(x)$, based on tensor-product arrays of Gauss-Lobatto-Legendre (GLL) quadrature points in a local element, Ω^e, $e = 1, ..., E$, satisfying $h_i^N(\xi_j^N) = \delta_{ij}$. Here, $\xi_j^N \in [-1, 1]$ denotes one of the $N + 1$ GLL quadrature points and δ_{ij} is the Kronecker delta. For a single element in $\mathbb{R}^3$ the representation of $\boldsymbol{u} \in X^N$ is

$$\boldsymbol{u}(\boldsymbol{x}^e(r, s, t))|_{\Omega^e} = \sum_{i=0}^{N} \sum_{j=0}^{N} \sum_{k=0}^{N} \boldsymbol{u}_{ijk}^e h_i^N(r) h_j^N(s) h_k^N(t), \tag{2.10}$$

where $\boldsymbol{x}^e$ is the coordinate mapping from the reference element $\hat{\Omega}$ to the local element Ω^e and $\boldsymbol{u}_{ijk}^e$ is the nodal basis coefficient. Inserting the SEM approximation equation (2.10) into equation (2.8) and employing Gaussian quadrature for the integrals, yields the semi-discretized equation

$$B\frac{\mathrm{d}\underline{\boldsymbol{u}}}{\mathrm{d}t} = D^{\mathrm{T}}\underline{p} - C(\underline{\boldsymbol{u}})\underline{\boldsymbol{u}} - \frac{1}{Re}K\underline{\boldsymbol{u}}, \;\; D\underline{\boldsymbol{u}} = 0, \tag{2.11}$$

where B and K are the spectral-element mass and stiffness matrices respectively, $C(\underline{\boldsymbol{u}})$ denotes the non-linear operator and D, D^{T} are the discrete divergence and gradient operators, respectively. Temporal discretization of equation (2.11) is based on high-order splitting techniques, described in Maday *et al.* (1990). In this way, the non-linear convective terms are allowed to be treated explicitly by second or third-order extrapolation (EXT2/3), in order to reduce computational cost, whereas the viscous terms are treated implicitly by a second or third-order backward differentiation scheme (BDF2/3) to ensure stability. This eventually leads to a linear symmetric Stokes system for the basis coefficient vectors $\underline{\boldsymbol{u}}^n$ and $\underline{p}^n$ to be solved at every time step, n,

$$H\underline{\boldsymbol{u}}^n - D^{\mathrm{T}}\underline{p}^n = B\underline{\boldsymbol{f}}^n, \;\; D\underline{\boldsymbol{u}}^n = 0. \tag{2.12}$$

Here, $H = (1/Re)K + (3/2\Delta t)B$ is the discrete equivalent of the Helmholtz operator $-(1/Re)\nabla^2 + 3/2\Delta t$ (in the case EXT2/BDF2 is used). In the RHS, $\underline{\boldsymbol{f}}^n$ accounts for the non-linear terms and for the cases we have external forcing in the Navier–Stokes equations.

2.5. Implementation

To be able to solve large flow problems involving millions of unknowns on thousands of processors, the final problem, equation (2.12), has to be treated with

special care. A detailed description of the linear solvers used in the spectral-element code `nek5000`, developed and maintained by Fischer *et al.* (2008*b*) and employed for the Navier–Stokes simulations in this thesis, can be found in Lottes & Fischer (2005) and Tufo & Fischer (2001). Here, the main steps are sketched.

The general idea is to decouple velocity and pressure by the operator splitting technique described in Maday *et al.* (1990) and Perot (1993), where first a Helmholtz equation is solved based on the pressure field from the previous time step, thereby giving an approximate, non-divergence free velocity field, $\underline{\hat{\boldsymbol{u}}}^n$,

$$H\underline{\hat{\boldsymbol{u}}}^n = B\underline{\boldsymbol{f}}^n + D^{\mathrm{T}}\underline{p}^{n-1}, \tag{2.13}$$

followed by a pressure correction step

$$E\delta\underline{p}^n = -D\underline{\hat{\boldsymbol{u}}}^n, \tag{2.14}$$

where $E := (2\Delta t/3)DB^{-1}D^{\mathrm{T}}$ (assuming BDF2) is the Stokes Schur complement and consistent Poisson operator for the pressure (Couzy 1995; Fischer 1997), introduced to avoid the slow convergence associated with the Uzawa algorithm (Arrow *et al.* 1958). The splitting error is of $\mathcal{O}(\Delta t^2)$ (Deville *et al.* 2002), *i.e.* not larger than the temporal discretization errors. Finally, the velocities and the pressure are updated

$$\underline{\boldsymbol{u}}^n = \underline{\hat{\boldsymbol{u}}}^n + \frac{2\Delta t}{3}B^{-1}D^{\mathrm{T}}\delta p^n, \tag{2.15}$$

$$\underline{p}^n = \underline{p}^{n-1} + \delta\underline{p}^n. \tag{2.16}$$

For large Re and small Δt, the Helmholtz operator is symmetric and strongly diagonally dominant, thus the d Helmholtz problems (equation 2.13), where d denotes the space dimension, are well conditioned and solved iteratively using conjugate gradients with a Jacobi preconditioner. In contrary, the Poisson problem, equation (2.14), is stiff, and the operator E is ill-conditioned. The reason for the stiffness is the infinite wave speed of the pressure caused by incompressibility, as discussed in Chapter (2.2). Thus, the bulk of the computational effort is spent here. Equation (2.14) is solved via spectral-element multigrid (SEMG) methods, where GMRES is accelerated by a preconditioner based on two overlapping Schwarz solves, typically on levels N and $N/2$ (Lottes & Fischer 2005) and a coarse grid solution. The global coarse-grid problem is based on linear finite elements on the element vertices and solved either using the direct and highly parallel so-called XX^{T}-solver or by using the iterative AMG (algebraic multigrid) approach, which is more communication intensive but gets relatively more efficient for larger problems (see Tufo & Fischer 2001; Lottes & Fischer 2005, respectively). The scalability of these solvers is a key issue in an efficient and massively parallel implementation, as this step introduces the global communication. The local problems (on element level) are solved using the fast diagnonalisation method (Lynch *et al.* 1964), which is based on decomposing the local operator as

$$E_e = \hat{E}_y \otimes I + I \otimes \hat{E}_x = \hat{D}_y B^{-1}\hat{D}_y^{\mathrm{T}} \otimes I + I \otimes \hat{D}_x B^{-1}\hat{D}_x^{\mathrm{T}}, \tag{2.17}$$

where I is the identity matrix and using the definition of E above (except for $2\Delta t/3$). The $\hat{}$ denotes the one-dimensional matrix operators defined on a reference element, in particular $\hat{D}_y$ and $\hat{D}_x$ denote the derivative matrices, respectively; and $\otimes$ is the Kronecker product. For simplicity we ignore boundary conditions and different meshes associated with the Schwarz procedure. If $\hat{E}_x$ and $\hat{E}_y$ are diagonalisable with

$$\hat{E}_x = S_x \Lambda_x S_x^{\mathrm{T}}, \qquad \hat{E}_y = S_y \Lambda_y S_y^{\mathrm{T}}, \tag{2.18}$$

where S_x and S_y consists (columnwise) of the eigenvectors of $\hat{E}_x$ and $\hat{E}_y$ respectively, and Λ_x and Λ_y are diagonal matrices with the respective eigenvalues, then E^e may be diagonalised as

$$E_e = (S_y \otimes S_x)(\Lambda_y \otimes I + I \otimes \Lambda_x)(S_y^{\mathrm{T}} \otimes S_x^{\mathrm{T}}), \tag{2.19}$$

giving the inverse as

$$E_e^{-1} = (S_y \otimes S_x)(\Lambda_y \otimes I + I \otimes \Lambda_x)^{-1}(S_y^{\mathrm{T}} \otimes S_x^{\mathrm{T}}), \tag{2.20}$$

which can be easily computed since $(\Lambda_y \otimes I + I \otimes \Lambda_x)$ is diagonal.

It is the tensor-product structure of the approximation (2.10), which gives rise to the expressions above, *e.g.* equation (2.19), for the local operators. To actually evaluate these operators, the naive approach for a matrix of size n, would mean a total of $\mathcal{O}(n^4)$ operations in 2D and large amount of memory storage. However, by employing *matrix-matrix products* the evaluation can be done in an order of magnitude fewer operations and in a much more cache efficient way. In essence, it exploits the following relationships (see *e.g.* Deville *et al.* 2002, for more details): Assuming we want to apply the combined operator $C = AB$ to a two-dimensional field, $\underline{u}$ of size $N \times M$, where $\underline{u} = (u_{00}, u_{10}, ..., u_{N0}, ..., u_{NM})^{\mathrm{T}}$. Then, the usual matrix-vector product would be

$$\underline{v} = C\underline{u}, \tag{2.21}$$

where $C = AB = (A \otimes I)(I \otimes B) = (AI \otimes IB) = (A \otimes B)$. By instead putting the entries of u_{ij} and v_{ij} into a rectangular matrix U_{ij} and V_{ij} of size $N \times M$ it can easily be verified that the following form is equivalent to equation (2.21),

$$V = BUA^{\mathrm{T}}, \tag{2.22}$$

which consists of two matrix multiplications with complexity $\mathcal{O}(n^3)$, assuming $M \sim N = n$. Thus, factorisations of tensor products of this kind reduces the total number of operations from $\mathcal{O}(n^{2d})$ to $\mathcal{O}(n^{d+1})$ in d dimensions and also reduces memory usage since no large matrices are explicitly formed. Last but not least, it enables the use of highly optimised matrix-matrix routines (`mxm`) to solve the final system of equations (see *e.g.* Fischer 1997).

In order to further speed up the convergence of the Poisson problem (2.14), the fact that the pressure field is unlikely to change abruptly over a series of successive time steps is utilised. The current solution is projected onto a space of previous solutions (over the last $\sim$ 20 time steps), and used as an initial guess for the iterative solution of the equation (2.14), further outlined in Fischer

(1998). Utilising all these methodologies altogether have resulted in very good scaling properties on several different architectures, of which some are briefly discussed below.

2.5.1. *Scaling of the numerical code* `nek5000`

This section provides some information about the efficiency and scaling properties of the spectral-element code `nek5000`. The specific hardwares utilised for the various computations in this thesis were the Cray XE6, the AMD Opteron cluster 'Ekman' at PDC (Stockholm) and the Blue Gene/P at ALCF (Argonne National Laboratory, ANL). As outlined below, the machines have rather different architectures. The Cray XE6 computer has dual 12-core nodes connected by a 3D-torus Gemini network. The actual CPUs are 2.1 GHz AMD Opteron 6100 series. Theoretical peak performance (TPP) on the maximum number of cores (32 768) used is 275.2 TFlop/s and the total amount of memory is 42.6 TByte. 'Ekman' is a distributed memory cluster, where each node consists of two AMD Opteron 2.2 GHz quad-cores, such that each node has effectively 8 cores. The interconnect is a full bisection bandwidth (FBB) InfiniBand fabric with a multiple root tree structure. All links are 4xDDR making the per-link bandwidth 2 GB/s. The Blue Gene/P has quad-core 450 PowerPC nodes at a clock frequency of 850 MHz. The network consists of both a torus network (6 GB/s) and a global collective network (2 GB/s). Here, the TPP is 222.8 TFlop/s and the memory is 65.5 TByte on the maximum number of cores used (65 536). The curves in figure 2.1 show strong scaling on the Cray XE6 ($\times$), 'Ekman' ($\circ$) and the Blue Gene/P ($+$) for exactly the flow case used for the production runs presented in Papers 6 and 7, where a total resolution of approximately 220 million grid points was utilised by employing 127 750 spectral elements with a polynomial order of 11, respectively. Ideal (linear) scaling is included for reference (*thin solid*). In particular, we show the mean wall time per time step, t_w, in seconds averaged over 200 time steps for increasing number of cores. On all machines, we can observe a very good usage of the hardware provided. More specifically, the scaling is essentially linear up to 16 384 cores on the Cray XE6 and up to 32 768 cores on the Blue Gene/P, with a speedup of 91 % and 84 %, respectively. It should be pointed out that for this large number of cores (32 768) there are less than 4 elements ($\sim$ 6700 grid points) present on each core, which puts high requirements on the efficiency of the global communication. After this point, the curves departure from the linear scaling, and we measure a speedup of 70 % on the Cray on 32 768 cores and 77 % on 65 536 cores. We note that the simulation on Blue Gene/P is in general approximately a factor 2 times slower for the same number of cores, which is mainly due to its $\sim$ 2 times slower processors. On the other hand, the linear scaling for Blue Gene/P is levelling off at a later point compared to Cray XE6.

2.6. Stabilisation at high Re

Due to the non-linearity of the advective term in the Navier–Stokes equations, the numerical quadrature employed for the integrals in equation (2.8) cannot

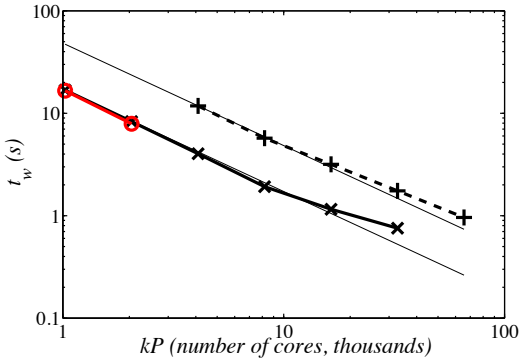

FIGURE 2.1. Wall time per time step for a fixed problem size (*i.e.* strong scaling) involving $\sim$ 220 million grid points, as a function of numbers of cores on Cray XE6, PDC ($\times$), Blue Gene/P, ANL ($+$) and the AMD Opteron cluster 'Ekman', PDC ($\circ$). Ideal scaling is included for reference (——).

be integrated exactly. These numerical errors – similar to aliasing errors in pseudo-spectral methods – are enhanced in turbulent flow simulations where sharper gradients are present leading to more excited modes in the polynomial expansion. At high Re, when little dissipation is provided, these errors are known to affect the stability of the method (see *e.g.* Fischer & Mullen 2001; Xu 2006; Wasberg *et al.* 2009) and some kind of stabilisation technique has to be used, where *e.g.* over-integration (see *e.g.* Kirby & Karniadakis 2003; Maday & Rønquist 1990; Canuto *et al.* 1988), filter-based stabilisation (Fischer & Mullen 2001) or the spectral vanishing viscosity (SVV) technique (Tadmor 1989; Pasquetti 2006; Karamanos & Karniadakis 2000) have been proposed. Among these, the two former techniques are further investigated in Paper 2. Over-integration is a way of performing dealiasing, where over-sampling is made by a factor 3/2 in order to exactly evaluate the quadrature of the inner products for the advective term. The other two techniques rather aim at reducing aliasing errors by filtering and dissipation. The inaccuracy of the integration arising from the weak form is realised by noting that Gaussian quadrature on the GLL points, defined by

$$\int_{-1}^{1} u(x)\mathrm{d}x = \sum_{k=0}^{N} \rho_k u(\xi_k), \tag{2.23}$$

holds as long as the integrand $u(x)$ is a polynomial of order $2N-1$. In SEM, where the Galerkin projection is employed, the integration of a polynomial $u \in \mathbb{P}_N$ is accompanied with the multiplication of a test function $v \in \mathbb{P}_N$ as given by equation (2.9). This amounts to integrate $q = uv \in \mathbb{P}_{2N}$, which can be done almost exactly with the resulting error being exponentially small. This is *e.g.* the case for the $\partial u_i/\partial t$ terms in the Navier–Stokes equations. The viscous term in the Navier–Stokes equations is always treated correctly since

here, $q = u'v' \in \mathbb{P}_{2N-2}$, where prime denotes the differentiation. On the other hand, the quadratic term in the Navier–Stokes equations gives rise to a polynomial $q = vuu' \in \mathbb{P}_{3N-1}$, which exceeds the critical order and will fail to be integrated correctly. However, if the original grid is extended with a factor of $3/2$ times more points in each direction, such that the quadrature order is $M = 3(N+1)/2-1$, all polynomials up to order $2M-1 = 2(3(N+1)/2-1)-1 = 3N$ — and hence q — can be integrated exactly, and no errors are created.

The idea behind over-integration is to recover a *true* Galerkin method, which amounts to do the following (here shown by a 1D example):

$$(v, u\frac{\partial u}{\partial x})_N \rightarrow (v, u\frac{\partial u}{\partial x})_M, \tag{2.24}$$

where $(\cdot,\cdot)_M$ denotes the inner product on the fine grid, which in practice is accomplished by interpolating the functions involved to the fine grid by the Lagrangian interpolation operator J defined as $J_{ij} = h_i^M(\xi_j^N)$, which, by use of equation (2.23) gives

$$\begin{aligned}(v, u\frac{\partial u}{\partial x})_M &= \sum_{k=0}^{M} \underline{v}(\xi_k)\rho_k \underline{u}(\xi_k) D_M \underline{u}(\xi_k) = \sum_{k=0}^{M} (Jv)_k \rho_k (Ju)_k D_M (Ju)_k = \\ &= (J\underline{v})^{\mathrm{T}} B_M \mathrm{diag}(J\underline{u}) D_M J\underline{u} = \underline{v}^{\mathrm{T}} J^{\mathrm{T}} B_M \mathrm{diag}(J\underline{u}) D_M J\underline{u} = \\ &= \underline{v}^{\mathrm{T}} C_M \underline{u}, \end{aligned} \tag{2.25}$$

where $B_M = \mathrm{diag}(\rho_k)$ is the diagonal mass matrix with integration weights on the *fine* grid, D_M denotes the derivative matrix on the fine grid, and $C_M = J^{\mathrm{T}} B_M \mathrm{diag}(J\underline{u}) D_M J$ finally denotes the $N \times N$ convective operator. This way of removing aliasing errors was employed in the scalar transport equation in Paper 2 as well as in the turbulent and transitional flow simulations throughout this thesis.

Alternatively, the removal of aliasing errors could be done in the following way, where the non-linear product is interpolated and collocated on the fine grid and then projected back with a spectral cut-off operator to the coarse grid prior to doing the integration. This method was considered for the Burgers' equation in Paper 2, where it indeed proved to remove aliasing errors. Symbolically, this would read

$$\begin{aligned}(v, u\frac{\partial u}{\partial x})_N &= \sum_{k=0}^{N} v_k \rho_k P_N \mathrm{diag}(Ju)_k D_M (Ju)_k = \\ &= \underline{v}^{\mathrm{T}} B_N P_N \mathrm{diag}(J\underline{u}) D_M J\underline{u} = \underline{v}^{\mathrm{T}} \tilde{C}_N \underline{u}, \end{aligned} \tag{2.26}$$

where P_N is the $N \times M$ projection operator transforming a function into Legendre spectral space, setting the $M - N$ last modes to zero and then transforming back to physical space. $B_N = \mathrm{diag}(\rho_k)$ is the diagonal mass matrix with integration weights on the *coarse* grid, D_M is again the derivative matrix on the fine grid, and $\tilde{C}_N = B_N P_N \mathrm{diag}(J\underline{u}) D_M J$ finally denotes the $N \times N$ convective operator. For either method, setting equation (2.25) or equation

(2.26) equal to some RHS (v, f) and testing with $v_i = h_i^N(\xi_j^N)$ gives finally a linear system of equations to solve.

The filter-based stabilisation for SEM was first proposed by Fischer & Mullen (2001), where also the efficiency and its good stabilisation properties were shown. The filter works in the following way: By defining an explicit filter operator, $F_\alpha = \alpha\Pi_{N-1} + (1-\alpha)I$, and $\Pi_{N-1} : \mathbb{P}_N(\Omega) \to \mathbb{P}_{N-1}(\Omega) \to \mathbb{P}_N(\Omega)$, where $\mathbb{P}_N(\Omega)$ is the space of polynomials of maximum degree N defined on Ω, α is a relaxation parameter such that $0 < \alpha < 1$ and I is the identity matrix, one acts on the velocity vector at each time step, such that

$$\underline{u}^{n+1} = F_\alpha \underline{\tilde{u}}^{n+1}, \tag{2.27}$$

where $\underline{\tilde{u}}^{n+1}$ is the unfiltered field at the current time step. This allows for a smooth damping of the highest mode with effectively no changes to the existing solver. The result is that spurious oscillations are removed and hence the stability of the method is enhanced. In Paper 2, we show that turbulent flow simulations, which are otherwise unstable, can be efficiently stabilised by employing one of the tools described above.

CHAPTER 3

Spectral-element simulations of turbulence, transition and separation

Having introduced the high-order spectral-element method in the previous chapter, we now turn to some of the flows studied in this work. This chapter aims at placing the spectral-element method in relation to other methods, which is put into practice by applying it to some well-known turbulent, transitional and separated flow cases. In addition, we will investigate how to generate realistic turbulent inflow conditions. As soon as this is done, we will explore a more recent flow in Chapter 5. Again, it should be stressed that it is not a complete overview. Rather, it is intended to be an essay introducing some important concepts together with some interesting results encountered during the course of this work.

3.1. Turbulence

3.1.1. *Fundamentals*

Over the past years, the spectral-element method has mainly been applied to laminar and transitional flows (*e.g.* Tufo & Fischer 2001; Sherwin & Karniadakis 1995; Tomboulides & Orszag 2000), but has in recent years gained attention also for turbulent flow simulations (Wasberg *et al.* 2009; Blackburn & Schmidt 2003; Iliescu & Fischer 2003; Bouffanais *et al.* 2006; Fischer *et al.* 2008*a*; Kirby & Karniadakis 2003), thanks to the stabilisation tools described in section 2.6. Advantages, among others, are the method's low numerical dissipation and dispersion errors, which benefit investigation of individual flow structures, and its parallel efficiency, as turbulent flow simulations tend to be computationally challenging. Finally, the geometrical flexibility enables studies of flow cases, which traditionally have been out of reach for high-order methods, *e.g.* the turbulent diffuser flow at $Re = 10\,000$ (based on bulk velocity and inflow-duct height) shown in figure 3.1(*b*).

In turbulent flows, one usually applies the Reynolds decomposition over homogeneous directions, denoted by

$$u_j = \langle u_j \rangle_{\mathrm{hom}} + u'_j = U_j + u'_j \tag{3.1}$$

such that $\langle u'_j \rangle = 0$, with u_j being the velocity in direction j for $j = 1, 2, 3$ and $u_1 = u$, $u_2 = v$, $u_3 = w$ and $\langle \cdot \rangle$ denoting an ensemble average. One of the very first simulations of wall-bounded turbulence by Kim *et al.* (1987) was

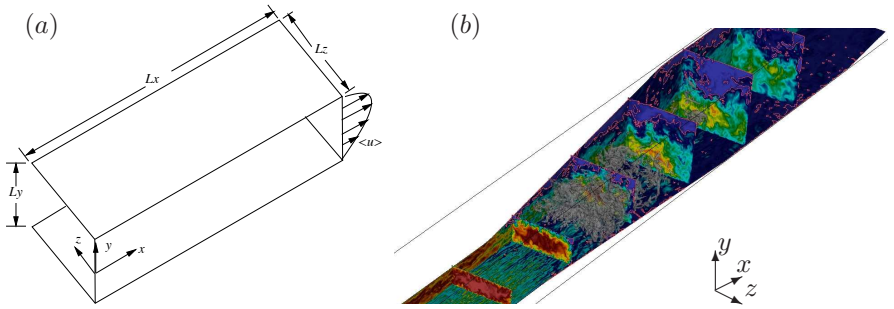

FIGURE 3.1. (*a*) Sketch of the plane channel flow configuration used as a reference case in this thesis. The coordinates $x_1 = x$ denote the streamwise, $x_2 = y$ the wall-normal and $x_3 = z$ the spanwise directions, respectively. (*b*) High-order numerical simulation of a turbulent diffuser flow at $Re = 10\,000$ studied in the present work.

performed in a channel geometry, *i.e.* a flow between two walls and with periodic boundary conditions in the spanwise and streamwise directions, here sketched in figure 3.1(*a*). This case will frequently appear throughout this thesis (Papers 1, 2, 4, 5), both when considering turbulent and transitional flows. When we are interested in turbulent statistics, the channel has dimensions $L_x \times L_y \times L_z = 4\pi h \times 2h \times 2\pi h$ and $L_x \times L_y \times L_z = 2\pi h \times 2h \times \pi h$ for the different Reynolds numbers considered, inspired by Moser *et al.* (1999). Here, h is the channel half width. When we investigate the properties of a 'minimal flow unit' (Chapter 4), a considerably smaller domain is chosen: $L_x \times L_y \times L_z = \pi h \times 2h \times 0.3\pi h$, similar to Webber *et al.* (1997). The channel flow's main attraction is that it is the most fundamental of all wall-bounded flows. It exhibits two statistically homogeneous directions in space given by x, z along with time, t, which enables good averaging of turbulent statistics. As time is a homogeneous direction, the simulation is said to be *temporal* as opposed to *spatial*, *i.e.* the flow evolves in time rather than in space. The fact that the flow is symmetric around the channel centre is additionally exploited to increase the convergence rate of the statistics. The rich homogeneity results in a sole dependence of all turbulent quantities on the wall-normal direction in one channel half. During the simulations, the mass flux is held constant by introducing a constant non-dimensional bulk velocity in the streamwise direction as

$$u_b = \frac{1}{L_y} \int_{-L_y/2}^{L_y/2} U(y) \mathrm{d}y = 1. \tag{3.2}$$

The corresponding fixed Reynolds number is defined as

$$Re_b = \frac{u_b h}{\nu} = \frac{2}{3} Re_{CL|\mathrm{lam}}, \tag{3.3}$$

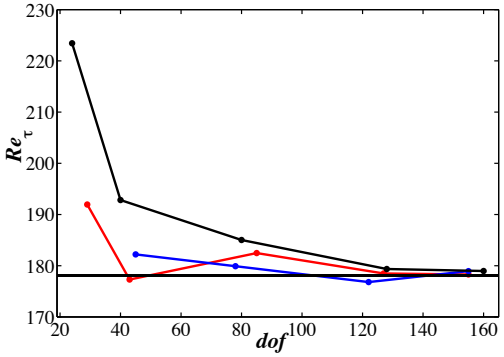

FIGURE 3.2. Computed Re_τ as a function of number of degrees of freedom in each spatial direction for the pseudo-spectral code (*black*) and different polynomial orders for the spectral-element code (*blue:* 11th order, *red:* 7th order). (——) DNS of Moser *et al.* (1999).

where $u_{CL|\mathrm{lam}} = u(y = 0) = 3/2$ for the laminar flow, h again being the channel half width and ν the viscosity. For simulations based on a fixed mass flux, the skin-friction Reynolds number, defined as (written in non-dimensional variables)

$$Re_\tau = \frac{u_\tau h}{\nu} = \sqrt{Re_b \left| \frac{\partial U(y)}{\partial y} \right|_{\mathrm{wall}}}, \tag{3.4}$$

where the 'friction velocity' in an incompressible flow is given by

$$u_\tau = \sqrt{\tau_w}, \tag{3.5}$$

and the wall shear stress,

$$\tau_w = \frac{1}{Re_b} \left| \frac{\partial U(y)}{\partial y} \right|_{\mathrm{wall}}, \tag{3.6}$$

is not given *a priori* as would be the case in a simulation driven by a fixed pressure gradient. Instead, it is computed and used to control the validity of a turbulent channel flow simulation or to track when or where transition occurs in a transitional flow simulation. An example of the former is shown in figure 3.2, where we compare the performance of the spectral-element method for two different polynomial orders (*blue:* 11th order, *red:* 7th order) to the pseudo-spectral method described in the previous section (*black*). The bulk Reynolds number is prescribed to be $Re_b = 2800$, which should give a $Re_\tau \approx 180$ for an accurate numerical simulation. The black horizontal line shows published spectral DNS data by Moser *et al.* (1999). We note that the actual skin-friction Reynolds number converges to the target Reynolds number with increased resolution. Here, dof = 'degrees of freedom' is defined as the resolution in one spatial direction. Clearly, the underresolved simulations overpredict the skin-friction. This well-known fact simply stems from a too steep velocity profile

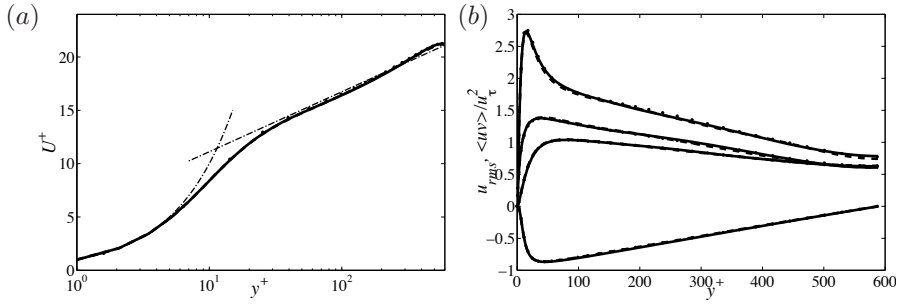

FIGURE 3.3. Turbulent channel flow simulations at $Re_\tau = 590$ with polynomial order 15 (a resolution of 288 in the homogeneous directions and 192 in the wall-normal direction) showing (a) mean velocity profile, (b) Reynolds stresses. (·····) Fourier pseudo-spectral DNS data by Moser *et al.* (1999), (–·–) log law, (———) SEM with filtering (5 %), (– – – –) SEM with over-integration + filtering (5 %).

close to the wall. We further observe that the convergence rate is similar for all cases, which indicate that 7th order basis functions are sufficient to capture one of the essential features in a turbulent flow.

Two other typical examples of flow quantities that need to be accurately captured in a turbulent flow simulation are shown in figure 3.3 for a channel flow conducted at the considerably higher Reynolds number $Re_\tau = 590$. In figure 3.3(a) the turbulent mean velocity profile is shown, whereas the mean fluctuations (around this mean flow) are reported in figure 3.3(b). We observe very good agreement between the results computed with the spectral-element code to results pertaining to the Fourier pseudo-spectral DNS by Moser *et al.* (1999) and the so-called 'log law' (see *e.g.* Pope 2000), given by

$$u^+ = y^+ \tag{3.7}$$

$$u^+ = \frac{1}{\kappa}\log(y^+) + B, \tag{3.8}$$

where $\kappa = 0.41$ and $B = 5.2$. The two spectral-element simulations differ in the way they are stabilised. One of them makes use of the spectral filter described in Chapter 2.6, whereas the other uses over-integration together with the filtering. The difference can be seen to be minute. Note that quantities in wall-bounded turbulent flows are conveniently expressed in 'plus-units', which denotes a scaling in viscous units (see the axes in figure 3.3). Thus, based on the friction velocity given by equation (3.5) one can define a length scale as $l^\star = \nu/u_\tau$. By applying this scaling, the wall-normal coordinate and the velocity become $y^+ = y/l^\star$ and $u^+ = U/u_\tau$, respectively.

In practice, the time average is computed during the simulation, whereas the spatial average is performed in a post-processing step. By saving not only

$\langle u_j \rangle$ but also $\langle u_j^2 \rangle$, the root-mean-square (r.m.s) can easily be computed as (here shown for the streamwise component),

$$u_{rms} = \sqrt{\langle u'^2 \rangle} = \sqrt{\langle u^2 \rangle - \langle u \rangle^2} = \sqrt{\langle u^2 \rangle - U^2}. \tag{3.9}$$

In a similar fashion, the rest of the terms in the Reynolds stress budget are computed.

3.1.2. *Turbulent inflow conditions*

This section is closed with a remark on boundary conditions for turbulent flow simulations. In most practical applications, turbulent flows evolve spatially rather than temporally, *i.e.* the statistics of the flow exhibit streamwise dependence. This poses a greater challenge due to the requirement of specifying proper turbulent inflow conditions, which strongly determine the downstream evolution of the flow. Much work has been devoted to finding inflow conditions that minimise the computational cost but still ensure a physically correct, fully developed turbulent flow.

A popular class of methods for the generation of turbulent inflow data consists of the so-called recycling techniques. One example are methods making use of an auxiliary, statistically homogeneous temporal simulation from which crossflow planes are extracted and transferred to the inlet boundary of the main simulation. This technique was employed *e.g.* by Kaltenbach (1993); Kaltenbach *et al.* (1999). In order to account for spatial growth of a boundary layer, Spalart & Leonard (1985) proposed a method based on re-scaling of the turbulent field at a certain downstream position and re-introducing the result at the inflow plane. Lund *et al.* (1998) proposes a modification of this method, which does not require periodic streamwise boundary conditions. Recently, this technique was used for large boundary-layer simulations by Simens *et al.* (2009). The advantage of the recycling methods is that they provide an accurate turbulent field at the inlet at a relatively low cost. A severe disadvantage is, however, the introduction of low temporal frequencies correlated to the frequency whereby the inflow planes are fed at the inlet, as pointed out by *e.g.* Spille-Kohoff & Kaltenbach (2001) and Lygren & Andersson (1999). This may not be noticeable in flows with favourable or zero pressure gradient. However, in flows subject to an adverse pressure gradient exhibiting pressure-induced separation, a certain periodicity of the inflow signal can trigger unsteady behaviour of the detachment point of a separation bubble, noted by *e.g.* Herbst *et al.* (2007) and Adams (2000).

The second class of methods aims at producing 'synthetic turbulence'. Here, the low-frequency correlations appearing for the recycling methods are avoided by introducing some kind of randomness to the inflow signal. The simplest approach is the superposition of random (white) noise on a desired mean velocity profile. Apart from its randomness, white noise has little in

common with natural turbulence regarding the Reynolds stresses and the energy spectrum. Moreover, the lack of mass conservation in the random fluctuations will increase the computational burden for numerical codes based on iterative techniques for continuity. The Reynolds stresses can be satisfied by locally modifying the amplitudes of the fluctuations, as described in Lund *et al.* (1998). Still, the fluctuations lack energy in the low wave number range, and it is well-known and noted by several authors, *e.g.* Kempf *et al.* (2005) and Lund *et al.* (1998), that these fluctuations will eventually be damped out by viscosity. Lee *et al.* (1992) solve this problem by applying an inverse Fourier transform to a natural turbulent energy spectrum with random phase angles between the different modes. The method has been tested by Le & Moin (1994) in a direct numerical simulation (DNS) of turbulent flow over a backward-facing step and by Stanley *et al.* (2002) in a DNS of a planar turbulent jet. A drawback of this technique is *e.g.* the need of knowing *a priori* the three-dimensional energy spectra of the turbulent flow under consideration. Kempf *et al.* (2005) propose the use of so-called digital filters for the generation of synthetic turbulence. These authors claim that their approach is more applicable than the inverse Fourier-transform method by Lee *et al.* (1992), as it allows for the local specification of a separate turbulent length scale for each coordinate direction. They have later proposed a method being similar to the digital-filter technique, but filtering of the random fluctuations is instead performed through diffusion of the small scales, resulting in increasing applicability and simplicity. Even though many of the methods based on random fluctuations have been claimed to mimic true and physically correct turbulence, experience tells another story. Rather long development sections are often needed for the flow to converge to a correct state. It is reported by Le & Moin (1994) that a development section corresponding to 20 boundary-layer thicknesses is required to recover the correct skin friction of the turbulent flow. Moreover, since non-physical transient behaviour may take place in the development section, the parameters specifying the synthetic turbulence at the inflow plane must be tuned to provide correct values for skin friction, momentum thickness and other quantities of interest in the downstream region of the development section. Keating *et al.* (2004) compared the previous reviewed methods using LES in a spatially developing channel at $Re_\tau = 400$ and concluded, similar to Kempf *et al.* (2005) and Lund *et al.* (1998), that synthetic turbulence generation methods that introduce realistic length scales are more suitable than uncorrelated random noise but even so, a fairly long development section is needed, compared to recycling methods based on auxiliary simulations.

A third class of methods circumventing the shortcomings of the previously listed methods builds on the introduction of an upstream extension of the inlet section, which allows for a natural transition process. This approach is seemingly the simplest and cleanest of all methods, but it is surprisingly discarded by most researchers due to the common opinion that it is computationally too expensive. It is often claimed that extending the inlet section in the upstream direction would not generally be feasible for turbulent simulations, since the

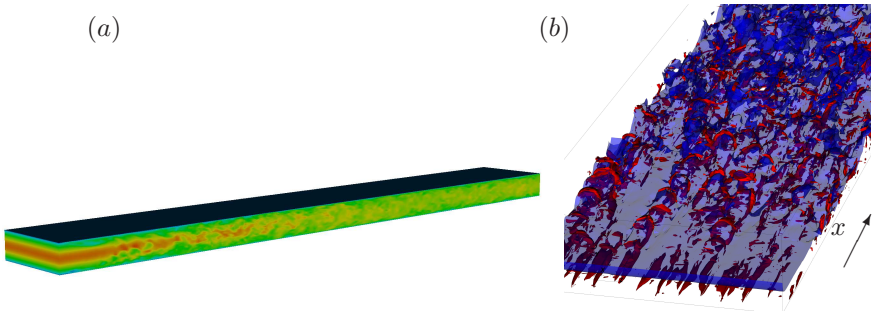

FIGURE 3.4. (*a*) Snapshot showing the evolution of a laminar plane Poiseuille inflow profile, leading to turbulent breakdown. The flow is from left to right, with the maximum amplitude of the force being located one channel-height downstream of the computational inlet. (*b*) The same snapshot as in (*a*) highlighting the formation of hairpin vortices in the forcing region. Isosurfaces of λ_2 (Jeong & Hussain 1995) (*red*) and streamwise velocity $u/u_b = 1$ (*blue*) are shown in the lower half of the domain.

natural transition process is slow, which would make the full simulation including the downstream flow of interest prohibitively expensive. This may be true for small set-ups where the inlet section constitutes a significant fraction of the total computational domain. However, for large simulations where the length of the inlet section is small in comparison with the total size of the set-up, triggering natural transition can very well be considered as an alternative. For the spatially evolving flow simulations in this thesis — except for Paper 3 where synthetic turbulence is used — a trip-forcing technique is employed. The technique is documented in Chevalier *et al.* (2007) and has been used with success in *e.g.* Ohlsson *et al.* (2010); Schlatter *et al.* (2009); Schlatter & Örlü (2010). The idea behind this forcing is the same as that behind experimental devices such as vibrating ribbons, unsteady blowing/suction slits or trip wires. It is based on randomness in time and space with prescribed length and time scales, thus avoiding spurious frequencies and artificial turbulence. The force, applied as a Gaussian in both the streamwise and wall-normal directions, points normal to the wall to promote the lift-up effect and thereby create streaks, depicted for a spatial channel flow simulation in figure 3.4. Note the formation of 'hairpin vortices' (see next section), which indicates a natural transition scenario. In figure 3.5 we display the skin-friction Reynolds number as a function of the downstream coordinate x. The development of a turbulent (*thin solid*) and a laminar Poiseuille (*thick solid, thick dashed, thin dashed*) velocity profile are investigated. In the laminar case we are varying the temporal and spatial frequency of the force, respectively. It can be concluded that irrespectively of the

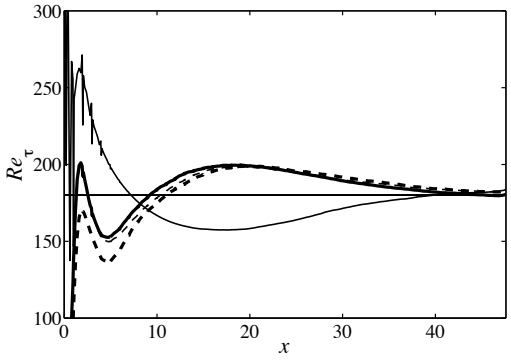

FIGURE 3.5. Streamwise evolution of Re_τ. (——) development of the turbulent mean velocity profile, (——), (- - - -), (- - - -) development of the laminar velocity profile for different length and time scales of the trip force. Horizontal line indicates the target value, $Re_\tau = 180$.

velocity profile chosen, fully developed turbulence is obtained around 40 channel half-heights downstream of the inflow plane. Furthermore, the trip force seems relatively robust with respect to the prescribed time and length scales.

3.2. Laminar-turbulent transition

The numerical simulation of transition to turbulence in moderately complex geometries (Tufo & Fischer 2001; Tomboulides & Orszag 2000; Lee *et al.* 2008) is particularly well-suited for the spectral-element method, where accuracy may be the most important feature. Initial disturbances are very sensitive and need correct treatment in order to break down to turbulence at the correct physical time or location. The diffuser geometry shown in figure 3.6 gives an example of a transitional flow in 2D at a low Reynolds number ($Re_b = 1000$ based on bulk velocity and channel half height). The laminar inflow profile becomes unstable and a shear layer instability occurs around $x = 15$. The shear layer then rolls up into vortices which are convected downstream. Since this simulation is strictly two-dimensional, no real turbulence will appear since turbulence is inherently three-dimensional. This particular geometry, where the opening angle is given by 8.5°, is further discussed in a three-dimensional setting in the next section. In order to facilitate comparison to other numerical schemes, however, a more generic flow configuration is chosen for the study of transitional flow. Here, we study so-called K-type transition at $Re_b = 3333$ in a plane channel geometry as the one in figure 3.1(a). This is a well-known transition scenario (see *e.g.* Kachanov 1994), first studied numerically by Gilbert & Kleiser (1990). It has turned into a canonical test case for transitional flow simulations (see *e.g.* Schlatter *et al.* 2004). The initial disturbances consist of a two-dimensional Tollmien-Schlichting (TS) wave with a streamwise wave number of $\alpha = 1.12$

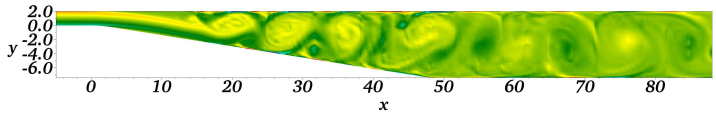

FIGURE 3.6. Shear layer instability occurring at $x = 15$ in a 2D diffuser flow at $Re_b = 1000$ based on bulk velocity, u_b, and channel half-height, h. Pseudocolour of spanwise vorticity $\omega_z = (\nabla \times \boldsymbol{u}) \cdot \boldsymbol{e_z}$ is shown.

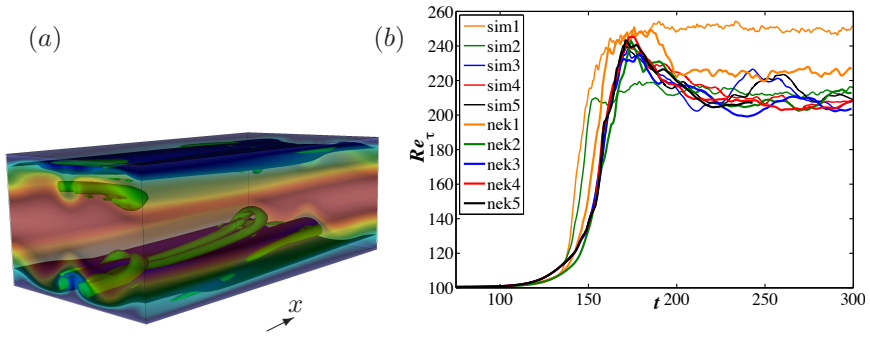

FIGURE 3.7. (a) Snapshot showing the hairpin vortex emerge at $t = 135$, shortly before the turbulent breakdown. Isosurfaces show λ_2 (*green*) (Jeong & Hussain 1995) and $u = 0.3$ (*blue*). Pseudocolours indicate streamwise velocity, ranging from blue (*low*) to red (*high*). (b) Evolution of the skin-friction Reynolds number, Re_τ, computed for a range of different resolutions by the spectral-element code (nek1-nek5) and pseudo-spectral code (sim1-sim5).

and an amplitude of 3 % of the laminar centre-line velocity; together with two three-dimensional oblique waves with wave numbers $\alpha = 1.12$ and $\beta = 2.1$ and amplitudes of 0.05 % each. This wave, superimposed on a laminar Poiseuille channel flow, experiences an exponential growth eventually leading to turbulent breakdown. Around $t = 120$ a so-called Λ-vortex appears, which develops into a hairpin vortex at $t \approx 135$ (Sandham & Kleiser 1992), depicted by green isosurfaces (λ_2) in figure 3.7(a). The particular flow shown here was computed by the pseudo-spectral code discussed earlier. Shortly thereafter ($t \approx 160$), the highly fluctuating transitional phase sets in; and finally, at $t \approx 220$, the flow has reached a fully developed turbulent state. As mentioned above, of primary importance for a numerical method when it comes to transitional flow simulations is to predict the point (in time or space) where laminar-turbulent transition occurs. Since the friction drag increases in turbulent flows, a suitable quantity to demonstrate transition is the skin-friction Reynolds number, Re_τ,

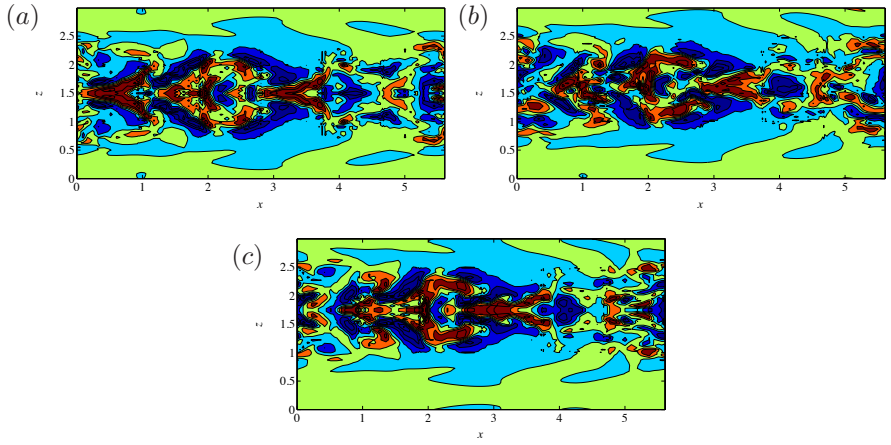

FIGURE 3.8. K-type transition at $Re_b = 3333$ showing wall-normal velocity in a wall-parallel plane at $y = 0.4$ at $t = 155$ close to the skin-friction peak and a partial breakdown is observed. The initial disturbance is shifted (b) one fourth and (c) one half element width compared to the unshifted case in (a).

shown in figure 3.7(b) as a function of time. The different curves correspond to various spatial resolutions for the spectral-element code (nek1-nek5) and the pseudo-spectral code (sim1-sim5), ranging from the lowest (1) to the highest (5) resolution. We note that the most underresolved cases lead to a premature transition, also noted by other authors. This is followed by an overprediction of the skin-friction in the fully turbulent phase. In line with the turbulent channel flow results, the two methods converge to a correct skin-friction peak (and corresponding time) for a similar degree of freedom ($\sim 128^3$ points).

Since the grid-point distribution is non-equidistant in the spectral-element method, simulations of localised flow structures may evolve differently depending on where they happen to be located in the computational domain. Here, we investigate this in the K-type transition described above. Figure 3.8 shows three cases where the same initial disturbance is shifted one fourth (figure 3.8b) and one half (figure 3.8c) element width in the spanwise direction, and compared to the unshifted case (figure 3.8a). What we see is a snapshot at $t = 155$ close to the skin-friction peak (see figure 3.7b), showing the wall-normal velocity component in a wall-parallel plane at $y = 0.4$. Since the initial TS wave is symmetric, symmetry should be preserved up until the turbulent breakdown. This is observed to be the case in (a) and (c), whereas the structure is slightly perturbed in (b). Indeed, the grid-point distributions for (a) and (c) are symmetric around the centre of the structure, save that the resolution where the structure is present is slightly higher in (a) compared to (c). This, however,

does not seem to have an impact on the solution, since the flow structures are more or less identically up to the turbulent phase. In contrast, we see that the symmetry is slightly broken in figure 3.8(b). Here, the surrounding grid is no longer symmetric with respect to the disturbance, and the resolution on one side is higher than on the other. However, with an increased resolution this slight asymmetry will disappear. Statistical quantities, such as the skin-friction Reynolds number in figure 3.7 are unaffected by this minor asymmetry seen in figure 3.8(b). At last, note in figure 3.8, that the spectral-element method, due to its non-dissipative nature, is capable of keeping the turbulent core clearly distinguished from the laminar co-flow on both sides.

The two last sections are closed with a final remark on p and h-refinement, referring to an increase of polynomial order or number of elements, respectively. As we have seen so far, a polynomial order of 7 for the basis functions is enough to capture integral quantities as well as instantaneous structures correctly. Two reasons contribute to make a lower order (but not too low) advantageous over a higher order. First, the CFL condition is less restrictive, which may be an important factor in convection dominated flows. Secondly, the work for the matrix-matrix products scale as $\mathcal{O}(KN^{d+1})$ (see previous section or Tufo & Fischer 1999), advocating a lower order. On the other hand, since the numerical error decreases as $\mathcal{O}(h^p)$, choosing p too low would destroy the exponential convergence rate, thereby increasing the iteration count for the linear solvers and thus the total work. In addition, the fact that p-refinement is controlled by a single parameter makes it easy to change the resolution without re-building the mesh (as would be the case for h-refinement). This can be exploited in turbulent flow simulations, where the first few flow-throughs typically are performed at a lower resolution and then used as an initial condition when continuing the simulation at the p-refined target resolution.

3.3. Separation

Flow separation may be one of the most important problems in fluid mechanics, due to its large impact on the performance of engineering applications, but also since satisfactory understanding is still lacking. In three-dimensional, unsteady flows even the definition of separation is disputed.

3.3.1. *Geometry- and pressure-induced separation*

According to Prandtl (1924) two necessary conditions have to be met in order to encounter flow separation: A positive (adverse) pressure gradient in the direction of the flow, *e.g.* due to a sudden expansion of a channel or deceleration of the flow over the trailing edge of an airplane wing; together with viscosity effects due to the presence of a boundary layer. If either of these two conditions are eliminated (*e.g.* by accelerating the flow or removing the boundary layer by suction at the wall, respectively), no separation will occur. The adverse pressure gradient can be achieved in two different ways, thereby marking the border between two important classes of separated flows. If the flow separates from

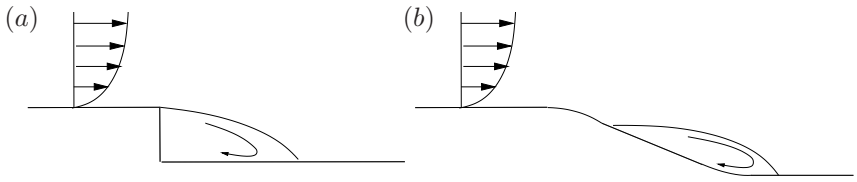

FIGURE 3.9. Sketch of (*a*) geometry-induced and (*b*) pressure-induced separation in typical two-dimensional configurations.

a sharp geometrical obstacle present in the flow, one generally speaks about 'geometry-induced' separation, schematically sketched in figure 3.9(*a*). Here, the separation is fixed to the point of highest curvature. The discontinuous derivative of the surface forces the flow to an infinite acceleration, which cannot be met and hence a low pressure is created at the sharp corner, thereby inducing backflow. An example of this flow is the backward facing step, where numerous studies have been conducted *e.g.* experimentally by Etheridge & Kemp (1978) and numerically by Le *et al.* (1997). When the adverse pressure gradient increases slowly, *e.g.* due to a mildly diverging channel, such as in a diffuser, the separation may take place (depending on the pressure gradient) over a smooth surface, often called 'pressure-induced' separation. This scenario is shown in figure 3.9(*b*). For an unsteady and turbulent flow, the latter case is the most challenging, both numerically and experimentally, since the point of separation can vary in both time and space, which puts high requirements on the experimental set-up and measurement technique as well as accurate numerical discretizations. Correspondingly, this type of separation has been less studied in the past but has recently gained some attention, *e.g.* experimentally by Obi *et al.* (1993); Buice & Eaton (2000); Törnblom *et al.* (2009) and numerically by Herbst *et al.* (2007); Kaltenbach *et al.* (1999); Na & Moin (1998); Skote & Henningson (2002). In the former case, the point of separation is always fixed, thus facilitating the treatment of the point of separation. However, the main task in these studies is to predict the point of attachment correctly, which for a turbulent flow may vary in time and space.

3.3.2. *Two-dimensional separation*

In a two-dimensional, laminar and steady flow, the point of separation may be defined as the point at the wall where the shear stress vanishes, such that

$$\tau_w = \mu \left. \frac{\partial u}{\partial y} \right|_{y=0} = 0, \tag{3.10}$$

assuming u being in the streamwise direction and y in the wall-normal direction (*i.e.* non-curved geometry). This leads to flow reversal near the wall and breaking away of the boundary layer from the surface. Purely two-dimensional and steady separation is of limited practical interest, since separation is strongly

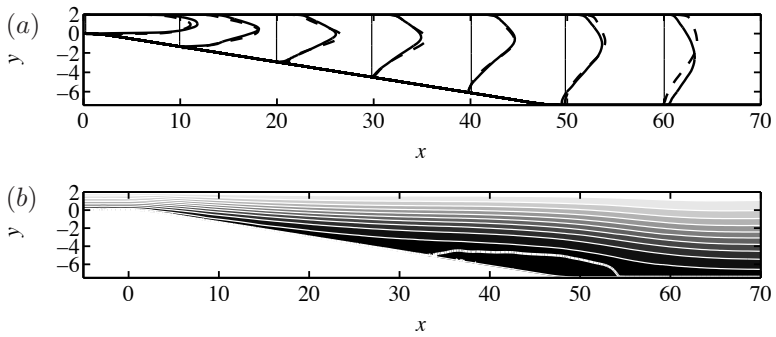

FIGURE 3.10. LES of a turbulent diffuser flow at $Re_b = 9000$ based on inflow channel half-height, h, and bulk velocity, u_b, (see Paper 3). (a) Mean velocity profiles $10 \cdot \langle \overline{u} \rangle + x$ where (———) indicates the present spectral-element code and (- - - -) are results from Herbst *et al.* (2007). (b) Contours of the stream function. Thick white contour levels indicate the value 10^{-5} of the stream function, thin white contours range from -0.1 to 2.0 with spacing 0.2.

connected to unsteadiness which is likely to be of three-dimensional character. However, for a steady two-dimensional freestream but an unsteady and turbulent boundary layer, some definitions based on the flow reversal at some fraction of the total time, γ_{pu}, have been proposed (Simpson 1981). Here, *incipient detachment* is defined as the point where $\gamma_{pu} = 0.99$ and the flow moves upstream 1 % of the time. Further, $\gamma_{pu} = 0.50$ means that instantaneous backflow occurs 50 % of the time, which in most investigations coincides with the time averaged wall shear stress, $\langle \tau_w \rangle$, being zero. In a turbulent but statistically two-dimensional internal flow, such as in a plane asymmetric diffuser in figure 3.10 and further discussed in Paper 3, there is a possibility to compute the stream function, $\Psi(x, y)$[1], (figure 3.10b) from the mean velocity field (averaged over time and in one statistically homogeneous direction). The geometry and a few selected velocity profiles are shown in figure 3.10(a), where a comparison to Herbst *et al.* (2007) is included. They used a 2nd order finite difference code for the same computation. The inflow channel (not shown) consists of fully developed turbulence at $Re_b = 9000$ based on bulk velocity and inflow channel half-height. Given the stream function, one may then define the mean separated region, often called the 'separation-bubble', as the region bounded by the mean dividing streamline. This is found by searching for the regions where the stream function is zero, indicated by the thick white line in figure 3.10(b). As mentioned previously, the instantaneous field within the separated region is highly three-dimensional and characterised by large energetic

[1]Defined such that $u \equiv \partial\Psi/\partial y$, $v \equiv -\partial\Psi/\partial x$.

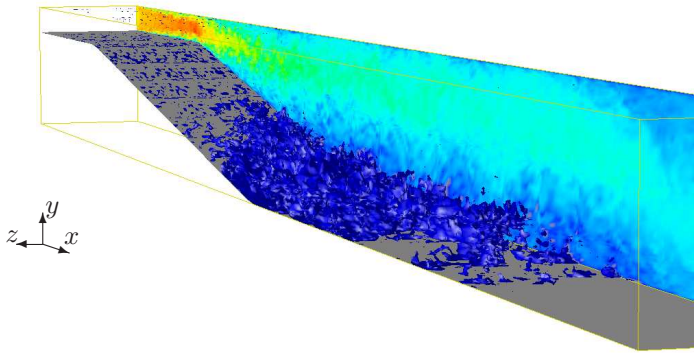

FIGURE 3.11. Snapshot showing isosurfaces of streamwise velocity with magnitude $u/u_b = -0.01$ and a plane with pseudo-colours of streamwise velocity.

structures (much larger than the turbulent eddies upstream of the separation point), exemplified by a snapshot in figure 3.11 of the same plane asymmetric diffuser at $Re_b = 9000$. Isosurfaces of streamwise velocity with magnitude $u/u_b = -0.01$ are shown.

The topic of three-dimensional separation, *i.e.* when the time-averaged mean flow possesses no spatial homogeneous directions, will be dealt with in Chapter 5. First, in Chapter 4, we will introduce analysis tools that can cope with such complex flows.

CHAPTER 4

Flow analysis

When observing a turbulent and complex flow, one is faced with an immense amount of information in time and space. To be able to grasp this information and understand the fundamental dynamics, some kind of data reduction procedure is needed. In some communities, the prevailing view point is that no coherence or order is associated to turbulence. Hence, turbulence is to such extent random that tools from statistical physics can be used. Probability distribution functions are commonly studied and enlightenment is sought via the study of mean quantities. This field has contributed with important concepts, such as the 'eddy viscosity', nowadays used in turbulence modelling. In other, more dynamical systems-oriented communities, the belief is that there are 'attractors' in a turbulent flow, to which the flow tends to return. More specifically, the flow is thought to be composed of typical or 'coherent' structures, which can be observed instantaneously. Experimental evidence of such structures, among which the turbulent near-wall streaks and the quasi-streamwise vortices are the most prominent ones in wall-bounded turbulence, have been reported in numerous studies (*e.g.* Kline *et al.* 1967; Blackwelder & Eckelmann 1979, respectively). The idea of coherence has proven to be applicable when constructing reduced-order systems. Compared to the full Navier–Stokes system, which typically contains millions or even billions of degrees of freedom, these systems consist of relatively few degrees of freedom, while retaining similar dynamics. Here, we shall adopt the latter of these two view points. First, in Chapter 4.1, the concept of modal decompositions — one of the corner stones in studies of coherence — is introduced. In particular, the proper orthogonal decomposition (POD) and the Koopman mode decomposition are considered. Then, in Chapter 4.2, we will define coherence simply by means of a scalar measure, which locates high concentrations of vorticity stretching.

4.1. Modal decompositions

Generally speaking, considering the flow field $\boldsymbol{u}(\boldsymbol{x}, t)$ with velocity vector $\boldsymbol{u} = (u, v, w)$, defined in physical space $\boldsymbol{x} = (x, y, z)$ and time t, a *modal decomposition* attempts to split the space and time dependence, such that

$$\boldsymbol{u}(\boldsymbol{x}, t) = \sum_{j=0}^{\infty} a_j(t)\boldsymbol{\phi}_j(\boldsymbol{x}). \tag{4.1}$$

Since we are dealing with numerical simulations of flows, our velocity fields are naturally truncated by the numerical simulation and the sum can without loss of generality be taken up to some $m \ll \infty$. The spatial modes $\boldsymbol{\phi}_j(\boldsymbol{x})$ and the temporal coefficients $a_j(t)$ remain to be determined. The decomposition (4.1) is however not at all unique and depending on the flow and aim of the analysis, different choices regarding $\boldsymbol{\phi}_j(\boldsymbol{x})$ and $a_j(t)$ may be appropriate. For linear problems, where $\dot{\boldsymbol{u}} = \mathbf{A}\boldsymbol{u}$, a natural choice for the modes are the eigenfunctions of the linear operator $\mathbf{A}$, referred to as *linear global eigenmodes*. These modes have traditionally been used in linear stability analysis (see *e.g.* Huerre & Monkewitz 1990; Theofilis 2011; Henningson & Åkervik 2008, for a review). Here, the growth of small perturbations around a laminar base flow solution are studied, and the modes are exponentially growing or decaying depending on the sign of the imaginary part of the corresponding eigenvalue. For laminar and transitional flows, which are dominated by self-sustained oscillations, *e.g.* the shedding of a two-dimensional cylinder wake or a laminar separation bubble, the linear unstable global eigenmode can in most cases capture the structure responsible for the shedding (Åkervik *et al.* 2007), and the flow can accordingly be classified as globally unstable. However, self-sustained oscillations are also frequently appearing in turbulent flows in which the flow state is far from the laminar base flow. In those cases, it is not obvious how to quantify the instabilities. In particular, if a a linear stability analysis is employed, which base flow is to be chosen: the laminar steady-state solution or the time-averaged mean flow? The former of these two was employed by Schlatter *et al.* (2011*a*) for a linear stability analysis of a highly non-linear jet in crossflow. It was concluded that the frequencies obtained from the global eigenvalue spectrum approximately matches the ones directly observed in the non-linear DNS simulation. Barkley (2006) instead used a weakly turbulent mean flow as base flow for the stability analysis of a two-dimensional cylinder wake and was able to match the documented shedding frequency very well. Pujals *et al.* (2009); del Álamo & Jiménez (2006) even used a fully turbulent mean velocity profile in a channel flow to predict the large scale structures with good precision. While the first of these two choices is mathematically well-founded, it can be argued that the laminar base flow is rather far from the turbulent flow under consideration is rather, and hence that the obtained structures ought be more of academic than practical interest. On the other hand, studying linear perturbations in a highly non-linear flow around a turbulent mean flow, which is never realizable, may be questionable.

This thesis considers two modal decompositions: the *proper orthogonal decomposition* (Lumley 1967; Holmes *et al.* 1996) and the *Koopman mode decomposition* (Rowley *et al.* 2009). Both circumvent the issue of which base flow to use and therefore works for linear and non-linear flows. In addition, an eigenvalue decomposition of the full Navier–Stokes system is never performed, which makes the techniques suitable also for experiments, where the full system is not

known. Dominant frequencies in a flow can be detected using these approaches: Schlatter *et al.* (2011*a*) matched approximately the dominant frequencies seen in the DNS by employing POD, and Rowley *et al.* (2009) used Koopman mode decomposition for the same flow to get good agreement between the obtained frequencies and the ones observed in the DNS.

More specifically, given a sequence of flow fields or 'snapshots', saved at m discrete times $\{\boldsymbol{u}(t_1), ..., \boldsymbol{u}(t_m)\}^{\mathrm{T}}$, both approaches find modes spanning this particular space. The POD is concerned with finding eigenfunctions of the two-point spatial correlation tensor, which will give modes corresponding to the most energetic structures in the flow. Koopman modes are eigenfunctions of the approximated linear evolution operator between two successive snapshots, and will provide modes that are clearly separated in spectral space, *i.e.* each mode contains one specific frequency. More detailed discussions regarding the two decompositions follow below.

Among other modal decompositions used in fluid mechanics are the so-called *balanced modes*. They are used when constructing low-dimensional models for control purposes, *e.g.* transition delay (see Rowley 2005; Bagheri *et al.* 2009, and the references therein).

4.1.1. *Proper orthogonal decomposition (POD)*

Lumley (1967) outlined a mathematical technique, in which the flow is decomposed into empirical eigenfunctions (*i.e.* 'modes') with random coefficients, based on the two-point spatial correlation tensor. Hence, no assumption about the nature of the flow state (linear or non-linear) or any *a priori* knowledge of the flow is needed — only observations of the flow itself. Lumley's idea, which went under the name 'proper orthogonal decomposition' (POD), was however not new and had existed for sixty years in data analysis of stochastic processes under different names, such as *principal component analysis (PCA)* (Pearson 1901), *Karhunen-Loève transform (KLT)* Karhunen (1946); Loève (1955), *empirical orthogonal function (EOF) analysis* (Lorenz 1956) and *empirical eigenfunction analysis (EEF)* (Sirovich 1987) to mention a few. The procedure is widely used in data analysis in many fields, and the great achievement by Lumley was to apply it in the field of fluid mechanics. POD has been applied to numerous flows, *e.g.* Moin & Moser (1989); Sirovich (1989); Sirovich *et al.* (1990) to name a few pioneering studies. It has also frequently been used for model reduction, see Rowley *et al.* (2004); Ma & Karniadakis (2002); Noack *et al.* (2010). It is often claimed that the main strength of the technique is that the most energetic flow structures are provided, which are thought to be the most relevant ones. In laminar, transitional and weakly turbulent flows, a few dominant well-converged and smooth structures are typically obtained, given that enough snapshots are used. In high Reynolds number turbulent flows, where the energy spectrum is flatter, the modes are usually degenerate, with no distinguished modes. However, as soon as some large-scale dynamics is present, *e.g.* shedding, it will usually show up as a mode. No clear separation

in spectral space is obtained using POD, *i.e.* the coefficient pertaining to one specific mode contains a broad range of frequencies. Such a separation is instead obtained using the Koopman mode decomposition, discussed in Chapter 4.1.2.

Mathematical background

Generally, the procedure is based on a given data, generated by some known (as in the case of the Navier–Stokes equations) or unknown process. Based on this data, the two-point spatial correlation matrix $\boldsymbol{R}(\boldsymbol{x},\boldsymbol{x'}) = \frac{1}{T}\int_T \boldsymbol{u}(\boldsymbol{x},t)\boldsymbol{u}(\boldsymbol{x'},t)^{\mathrm{T}}\,\mathrm{d}t$, where T denotes the total time over which the flow is observed, can be constructed. The proper orthogonal decomposition will decompose this matrix into eigenvectors and eigenvalues, which correspond to orthogonal directions in the data where most of the variance is found. In other words, the POD procedure finds deterministic, bi-orthogonal functions, $\boldsymbol{\phi}_j(\boldsymbol{x})$, which maximise the energy in the field $\boldsymbol{u}$. A necessary condition for this to hold is that $\boldsymbol{\phi}_j(\boldsymbol{x})$ is an eigenfunction of the two-point spatial correlation matrix (rigorously shown in Holmes *et al.* 1996). Finding the eigenvalues, λ_j, and corresponding eigenfunctions, $\boldsymbol{\phi}_j$, of $\boldsymbol{R}(\boldsymbol{x},\boldsymbol{x'})$ amounts to solving,

$$\iiint_V \boldsymbol{R}(\boldsymbol{x},\boldsymbol{x'})\boldsymbol{\phi}_j(\boldsymbol{x'})\,\mathrm{d}\boldsymbol{x'} = \lambda_j\boldsymbol{\phi}_j(\boldsymbol{x}). \tag{4.2}$$

Equation (4.2) is the continuous and original definition of POD. In practice, however, the discrete formulation is used. Therefore, the rest of this chapter is devoted to the discrete derivation. For the continuous counterpart, the reader is referred to Paper 7 or Manhart & Wengle (1993).

By letting $\mathbf{U}_m = [\boldsymbol{u}_0\ \boldsymbol{u}_1\ \boldsymbol{u}_2\ ...\ \boldsymbol{u}_m]^{\mathrm{T}}$ be the sequence of m snapshots, the discrete equivalent of the two-point spatial correlation matrix is now defined as $\mathbf{R} = \frac{1}{m}\mathbf{U}^{\mathrm{T}}\mathbf{U}\mathbf{G}$, where $\mathbf{G}$ is a matrix containing the spatial integration weights. Now, the analogy of equation (4.2) reads,

$$\mathbf{R}\boldsymbol{\Phi}^{\mathrm{T}} = \boldsymbol{\Phi}^{\mathrm{T}}\boldsymbol{\Lambda}, \tag{4.3}$$

where $\boldsymbol{\Phi} = [\boldsymbol{\phi}_0\ \boldsymbol{\phi}_1\ \boldsymbol{\phi}_2\ ...\ \boldsymbol{\phi}_m]^{\mathrm{T}}$ is the matrix of the spatial modes in equation (4.1), and $\boldsymbol{\Lambda}$ is the diagonal matrix with the corresponding eigenvalues $\lambda_1, \lambda_2, ..., \lambda_m$. The m temporal coefficients at m discrete times in equation (4.1), written in matrix form as $\mathbf{A} = [a_0\ a_1\ a_2\ ...\ a_m]$, can then in a successive step be solved for by projecting the spatial modes onto the snapshots,

$$\mathbf{A} = \mathbf{U}\mathbf{G}\boldsymbol{\Phi}^{\mathrm{T}}. \tag{4.4}$$

where we have used the bi-orthogonality in space, $\boldsymbol{\Phi}\mathbf{G}\boldsymbol{\Phi}^{\mathrm{T}} = \mathbf{I}$. Note that $\mathbf{R}$ will be of size $n \times n$, where $n = 3 \times n_x \times n_y \times n_z$ and n_x, n_y, n_z are the number of grid points in the spatial directions, respectively. Therefore, for high spatial resolutions, $\mathbf{R}$ can be very large and equation (4.3) is usually intractable to solve. However, using the snapshot method (Sirovich 1987), equation (4.3) can be circumvented by solving an eigenvalue problem of the generally smaller

temporal two-point correlation matrix $\mathbf{C} = \frac{1}{m}\mathbf{U}\mathbf{G}\mathbf{U}^{\mathrm{T}}$ of size $n \times m$[1]. Hence, we are now instead solving

$$\mathbf{C}\mathbf{A} = \mathbf{A}\mathbf{\Lambda}. \tag{4.5}$$

Then, as a second step, the spatial eigenfunctions are constructed as

$$\mathbf{\Phi} = \frac{1}{m}\mathbf{\Lambda}^{-1}\mathbf{A}^{\mathrm{T}}\mathbf{U}. \tag{4.6}$$

Here, the division by the respective eigenvalue ensures that the modes are normalised to unit energy. Once this is done, the temporal coefficients can be computed according to equation (4.4), and the ones obtained from equation (4.5) are disregarded.

In the following section, we will apply the procedure described above to a minimal channel flow, briefly mentioned in Chapter 3.1.

Example: POD of a minimal channel flow

Let us for simplicity consider the *minimal channel flow*, also exploited for this purpose by Webber *et al.* (1997). Despite being fully turbulent and thus displaying correct turbulent statistics (see Jiménez & Moin 1991), it contains less degrees of freedom than a high Reynolds number flow. Therefore, as mentioned above, POD is likely to deliver well converged structures pertaining to the most energetic events in the flow. In this case, the mean flow — being the first mode in the decomposition — takes up as much as 98.5 % of the total energy. Even though being a small fraction of the total energy, the modes constituting the fluctuating part of the flow may give important information about the dynamics. In agreement with Webber *et al.* (1997), the most energetic POD modes consist of structures with no streamwise dependence, shown by positive and negative surfaces of constant streamwise velocity in figure 4.1(*a*). As mentioned earlier, this is one of the coherent structures observed in wall-bounded turbulence, namely the near-wall streaks. The next type of structure provided by the POD displays streamwise dependence and is tilted from the wall at an angle, shown in figure 4.1(*b*). These can be identified as the quasi-streamwise vortices, which together with the streaks play a crucial role in the self-sustained turbulent 'near-wall cycle' (see Waleffe 1997).

As the decomposition (4.1) states, each one of these structures possesses a time dependence, reported in figures 4.2(*a*-*b*). It shows the chaotic nature of turbulence: one would never be able to predict the exact path of the signal in figure 4.2(*a*) *a priori*. Even so, there exists a characteristic time scale pertaining to each mode, with the mode in figure 4.1(*a*) having a much longer typical period than the one in figure 4.1(*b*). This is confirmed by the power spectral density (PSD) of the two signals shown in figure 4.2(*c*). Each one of the spectra is normalised with its own maximum. It can be seen that each mode has a dominant peak in its spectrum, found at a Strouhal number $St \equiv fh/u_b$ (h

[1]Obviously, this is only true if $m < n$, which is most probably the case for a numerical simulation. For experiments, however, $m > n$ is the more common situation and hence $\mathbf{C}$ would be larger than $\mathbf{R}$.

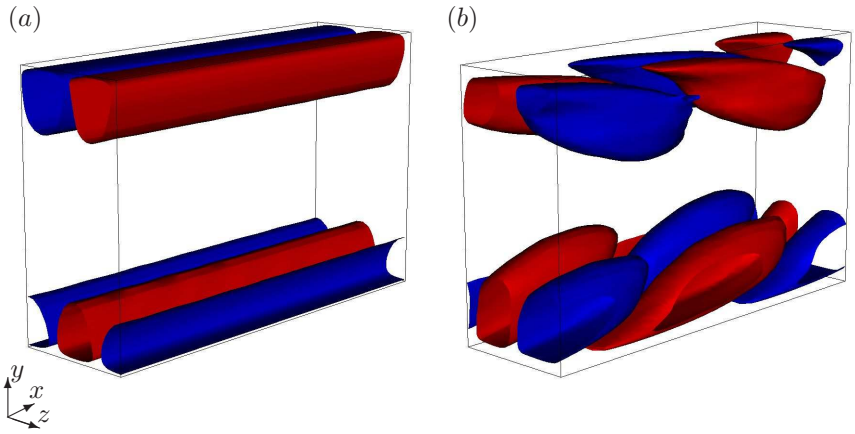

FIGURE 4.1. Isocontours (*red:* $u/u_b = 0.3$, *blue:* $u/u_b = -0.3$) of streamwise velocity of POD mode (*a*) 1 and (*b*) 7.

being the channel half-height and u_b the bulk velocity) of ~ 0.0078 and ~ 0.28, respectively. A comparison with the PSD of a signal obtained from a probe, measuring the streamwise velocity component in the flow, shows that these two frequencies are indeed the two dominant ones in the flow. But whereas this signal contains both frequencies, they could be separated and identified with a corresponding structure by the POD. It should be pointed out that each structure is not assigned a *specific*, but rather a *dominant* frequency, since it indeed contains all frequencies around the peak value.

4.1.2. *Koopman mode decomposition*

As noted in the example above, the most energetic events in the flow, provided by the POD, are in general not fully separated in frequency space, *i.e.* one spatial structure contains a range of different frequencies. A clear separation in frequency space is instead provided by a Koopman mode decomposition. Here, we outline the dynamic mode decomposition (DMD) by Schmid (2010), which is a numerical technique to compute a discrete approximation to the Koopman modes.

Mathematical background

As for the POD, our point of departure is the sequence of m snapshots. We are interested in the properties of the linear operator $\mathbf{A}$, which can propagate one snapshot forward in time, such that

$$\boldsymbol{u}_{i+1} = \mathbf{A}\boldsymbol{u}_i. \tag{4.7}$$

If the underlying equation that generated the snapshots were linear, then equation (4.7) would not involve any assumptions. However, if the snapshots would

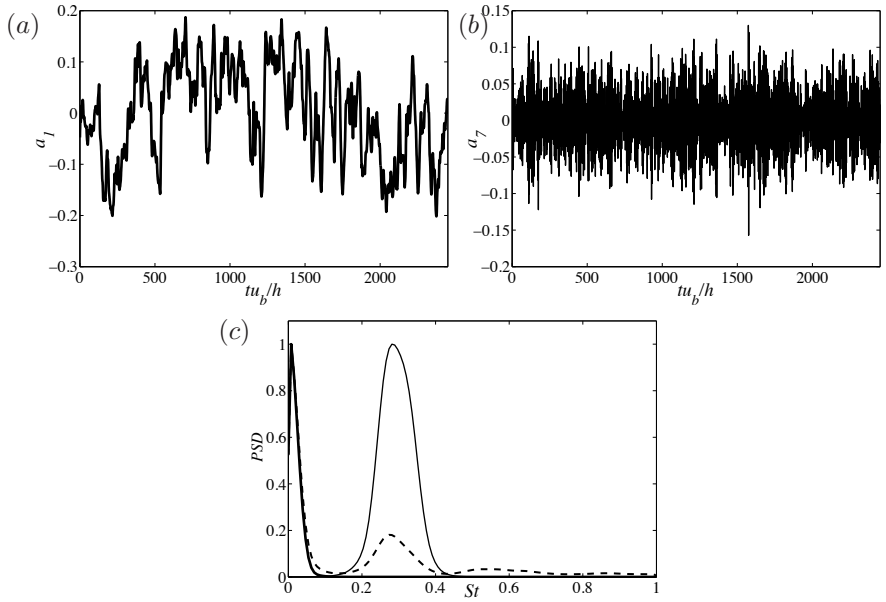

FIGURE 4.2. Temporal evolution of POD mode (a) 1 and (b) 7. (c) Power spectral density (PSD) of the respective signals in (a) (——) and (b) (——) compared to the PSD of the time signal probe (- - - -). Each one of the spectra is normalised with its own maximum.

stem from a non-linear process, then equation (4.7) would be the linear approximation to this process. We will here investigate the assumed linear mapping (4.7) by analysing the the eigenvalues and respective eigenvectors of $\mathbf{A}$.

In fluid mechanics, the system matrix $\mathbf{A}$ is often very large and hence iterative methods, such as the Arnoldi algorithm (see *e.g.* Trefethen & Bau 1997), are the methods of choice in order to find some dominant eigenvalues and eigenvectors of $\mathbf{A}$. The DMD builds on the Arnoldi algorithm, but the great advantage of the DMD is that $\mathbf{A}$ need not to be known explicitly, as would be the case for the Arnoldi method. Instead, the eigenvalues and eigenvectors can be found solely by processing a sequence of snapshots, either velocity fields generated from a numerical simulation (where the system matrix is in general known) or measurement data (1D, 2D or 3D) from a physical experiment. Briefly, the DMD algorithm works as follows, focusing on the procedure based on the companion matrix, $\mathbf{M}$, below (Ruhe 1984). Further details are found in Schmid (2010).

Using the snapshots, we shall define two sequences, given by

$$\mathbf{U}_m = [\boldsymbol{u}_0\ \boldsymbol{u}_1\ \boldsymbol{u}_2\ ...\ \boldsymbol{u}_{m-1}], \tag{4.8}$$

and

$$\mathbf{U}_{m+1} = [\boldsymbol{u}_1\ \boldsymbol{u}_2\ \boldsymbol{u}_3\ ...\ \boldsymbol{u}_m]. \tag{4.9}$$

Our task is now to find the matrix $\mathbf{M}$ such that,

$$\mathbf{U}_{m+1} = \mathbf{U}_m\mathbf{M} + \mathbf{r}, \tag{4.10}$$

where $\mathbf{r}$ is a residual vector. This can be done by solving a least-square problem. Once $\mathbf{M}$ is found, eigenvectors and corresponding eigenvalues to $\mathbf{M}$ are computed, *i.e.* we are solving

$$\mathbf{MT} = \mathbf{T}\boldsymbol{\Lambda}. \tag{4.11}$$

As for the Arnoldi algorithm, where the decomposition (4.10) also appear, the eigenvalues $\boldsymbol{\Lambda}$ (called Ritz values) approximate some of the eigenvalues of $\mathbf{A}$. Now, the so-called *dynamic modes*, $\boldsymbol{\Phi} = [\boldsymbol{\phi}_0\ \boldsymbol{\phi}_1\ \boldsymbol{\phi}_2\ ...\ \boldsymbol{\phi}_{r-1}]$, are computed analogous to expression (4.6) for the POD modes,

$$\boldsymbol{\Phi} = \mathbf{U}_m\mathbf{T}. \tag{4.12}$$

Example: Koopman mode decomposition of a minimal channel flow

Let us use the minimal channel flow also for the Koopman mode decomposition. The same snapshots used for the POD are processed according to the procedure above. A few selected dynamic modes are shown in figure 4.3(*a-c*). As noted above, they correspond to the finite approximation of the Koopman modes, rigorously shown by Rowley *et al.* (2009). In figure 4.3(*d*), the spectrum is shown. Each one of the red bars corresponds to the amplitude $||\boldsymbol{\phi_j}|| = \sqrt{\boldsymbol{\phi_j}^{\mathrm{T}}\boldsymbol{\phi_j}}$ of one particular mode. The eigenvalues come in complex conjugate pairs, but for simplicity we only show $St > 0$. The dashed line again shows the PSD from the time signal probe, which shows close agreement with the Koopman mode spectrum, in which two dominant peaks can be observed. The first peak (not fully visible in figure 4.3(*d*) due to cutting of the y-axis) has a Strouhal number $St_1 \approx 0.0078$, which is exactly the same frequency compared to what is obtained from the time probe and the POD analyses. A closer look at the second peak in figure 4.3(*d*) reveals that it is a double peak, of which the lower frequency is given by $St_{2a} = 0.26$, corresponding to a time period of $T_{2a} \equiv 1/St_{2a} = 3.8$. This frequency matches the second frequency peak from the POD and analysis of the probe. The higher frequency is located at a Strouhal number of $St_{2b} = 0.33$, which gives the slightly shorter time period of $T_{2b} = 3.0$.

We observe that similar structures are found by the POD and Koopman mode decomposition. In particular, the structures corresponding to the first spectral peak, reported in figure 4.3(*a*), are similar to the modes obtained from the POD analysis in figure 4.1(*a*). Secondly, shown in figure 4.3(*c*), is the mode with frequency St_{2a}, *i.e.* the peak frequency of the inclined POD mode in figure 4.1(*b*). They compare well to each other, save that the Koopman mode is somewhat more noisy. It should be pointed out that this is not a sign of unconverged numerics, but rather inherent in the way the modes are separated

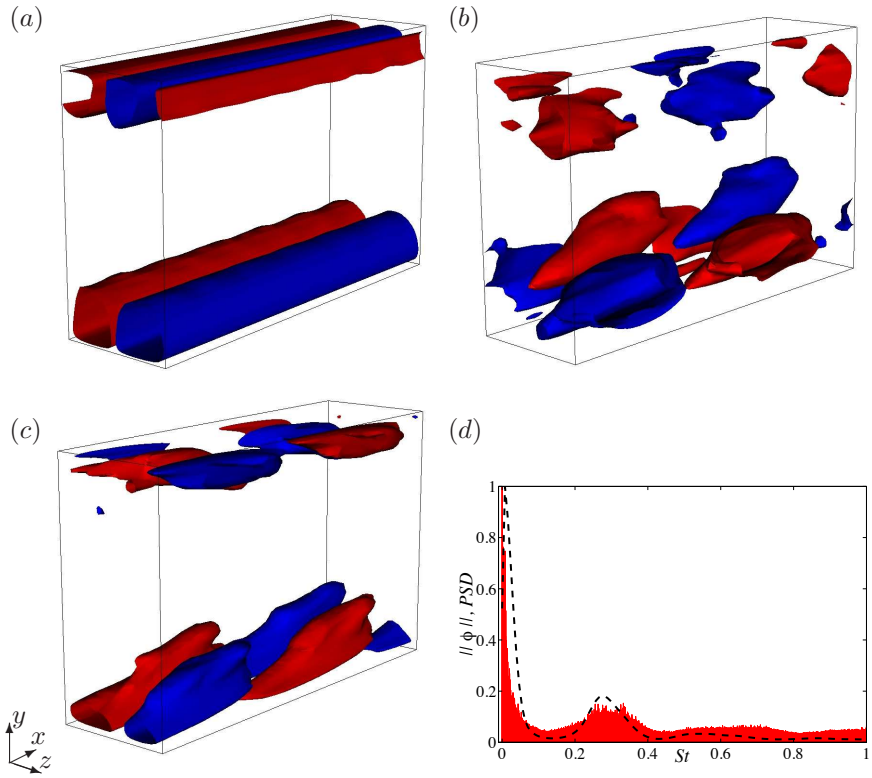

FIGURE 4.3. Isocontours of streamwise velocity of Koopman mode (*a*) 4 (*red:* $u/u_b = 0.4$, *blue:* $u/u_b = -0.4$), (*b*) 129 (*red:* $u/u_b = 0.2$, *blue:* $u/u_b = -0.2$) and (*c*) 140 (*red:* $u/u_b = 0.2$, *blue:* $u/u_b = -0.2$). (*d*) Amplitudes of the modes as a function of frequency (*red*), together with the PSD of the time signal probe (----).

in spectral space. The main feature of the mode pertaining to St_{2a}, is that they are alternating negative and positive and extend all the way from the wall, tilted at an angle. However, the mode corresponding to St_{2b}, shown in 4.3(*b*), can be seen to be located slightly further away from the wall. As the convection velocity is higher in this region, this explains its higher frequency. The intrinsic averaging in frequency space present in the POD makes it impossible to observe this structure, and hence the Koopman mode decomposition adds something to the analysis of this flow.

4.2. An alternative way to define 'coherence'

The coherent structures we have encountered so far have been eigenfunctions of some particular matrix. However, coherent structures can also be defined

using some 'measure' or 'criterion', which can localise the structures in a given instantaneous flow field. The question is, how can one define such a measure?

The term 'coherence' is intuitively clear. Loosely, it denotes a flow structure, where all parts move in a coherent fashion. A strict definition is more difficult to obtain. Hussain (1986) makes the following: *A coherent structure is a connected turbulent fluid mass with instantaneously phase-correlated vorticity over its spatial extent.* Although, in principle, any quantity could be instantaneously phase-correlated over its spatial extent, coherence has traditionally been connected to vortices in some way or another. For instance, much research has been devoted to finding measures defining a 'vortex', among which the most widely used are the Π-criterion and the λ_2-criterion proposed by Hunt *et al.* (1988) and Jeong & Hussain (1995), respectively. For incompressible flow, the Π-criterion is equivalent to the negative of the second tensor invariant, $-Q$, discussed by Chong *et al.* (1990). Also the Δ-criterion introduced by Chong *et al.* (1990) belongs to the same class of vortex identification methods. All these measures are based on the velocity gradient tensor. Localising low pressure areas in the flow can give a rough estimate of the orientation of vortices (see *e.g.* Robinson 1991), but will in general favour larger structures and miss the small vortices in the flow. A review and more thorough definitions of the above measures together with an *a posteriori* analysis in turbulent flows can be found in Dubief & Delcayre (2000) and Chakraborty *et al.* (2005).

The developed structures identified by these criteria are not necessarily the areas in a flow of most dynamical interest, *e.g.* regions where instabilities are growing. Generally, a vortex can be created (by some yet unspecified mechanism) after which it may be convected away from the active region of the flow. Thus, locating the vortex itself does not directly help to position the area of interest. On the other hand, by identifying the production of vorticity the active region of the flow would instead be pinpointed. Among the various production terms in the vorticity transport equation, vorticity stretching is the one that can provide exponential growth, and is therefore the candidate for developing dynamics. In Paper 5, a new diagnostic measure based on the vorticity stretching terms is defined. The procedure is outlined below.

Consider the vorticity transport equation in an incompressible flow,

$$\frac{D\omega_i}{Dt} = \omega_j \frac{\partial u_i}{\partial x_j} + \frac{1}{Re}\frac{\partial^2 \omega_i}{\partial x_j \partial x_j}, \tag{4.13}$$

where the terms (no summation on α)

$$\omega_\alpha \frac{\partial u_\alpha}{\partial x_\alpha}, \qquad \alpha = 1, 2, 3, \tag{4.14}$$

are denoted *vorticity stretching terms*, in each spatial direction respectively. Vorticity stretching alone is a three-dimensional vector field, which in general is difficult to visualise and interpret. A scalar field is more conceivable, since it tells the observer where high 'concentrations' of the quantity in question can be found. Therefore, we propose our measure as the maximum vorticity

stretching component in every point in space, thus yielding a three-dimensional scalar field.

In order to locate the largest occurrence of vorticity stretching in the flow, we will formally define the scalar measure as:

$$\Gamma_p(x,y,z,t) = \max\{\alpha|\omega_\alpha|, \beta|\omega_\beta|, \gamma|\omega_\gamma|\}, \tag{4.15}$$

where α, β and γ are the eigenvalues of the strain tensor $S_{ij} = \frac{1}{2}(\frac{\partial u_i}{\partial u_j} + \frac{\partial u_j}{\partial u_i})$ and ω_α, ω_β and ω_γ are the vorticity components along the principal axes given by the eigenvectors of S_{ij}. The subscript 'p' indicates that we are in a principal axis system, aligned with the direction of strain. Thus, this measure is a true scalar quantity, since it is indeed independent of coordinate system. The procedure of decomposing the strain tensor into its eigenvectors is commonly adopted in studies of homogeneous turbulence where the usual spatial coordinate directions have a subordinated meaning, (see *e.g.* She *et al.* 1991; Nomura & Post 1998). We will compare this measure to the following definition:

$$\Gamma_c(x,y,z,t) = \max\{|\omega_x|\frac{\partial u}{\partial x}, |\omega_y|\frac{\partial v}{\partial y}, |\omega_z|\frac{\partial w}{\partial z}\}, \tag{4.16}$$

where the subscript 'c' denotes 'Cartesian'. Note that this measure, in contrast to definition (4.15), is formally not a scalar quantity, since it is dependent on the fixed Cartesian coordinate directions. However, the actual differences may not be very large for simple wall-bounded flows where the streamwise, spanwise and wall-normal directions are clearly defined and the flow is generally aligned with one coordinate axis. In those cases, for the sake of implementation and computational effort (since (4.15) involves solving an eigenvalue problem in every point in space), definition (4.16) might be preferable, provided that the corresponding results agree well with the more rigorous measure (4.15). To our knowledge, this is generally the case. In some cases when the flow structures are inclined, Γ_c can miss and artificially cut the structures.

A sample result of Γ_c (*red*) together with λ_2 (*green*) in an asymptotic suction boundary layer (ASBL) at $Re = U_\infty\delta^*/\nu = U_\infty/V_\infty = 750$ (U_∞ being the free-stream velocity, δ^* the displacement thickness and V_∞ the imposed vertical velocity) is shown in figure 4.4. The combination of Re, box size and amplitude of (random) initial condition are tuned such that a so-called 'edge state' is obtained, in which the flow neither becomes turbulent nor goes laminar (Schneider *et al.* 2007). The result is a time-periodic orbit with a period of $T = 3347$. Under certain parts of the period, the flow consists of a laminar low-speed streak (gray isosurface in figure 4.4*a*-*b*). This streak soon goes unstable and breaks down (figure 4.4*c*-*d*). In this fashion, the procedure repeats itself. The edge state in the ASBL flow was first computed and studied by Madré (2011) and discussed by B. Eckhardt (ETC-12, 2009, Marburg). The aim of the present case is however not to study its state-space properties, in the style of Schneider *et al.* (2007) and the references therein, but merely to use the case as an alternative to minimal channel flows in an effort to simplify

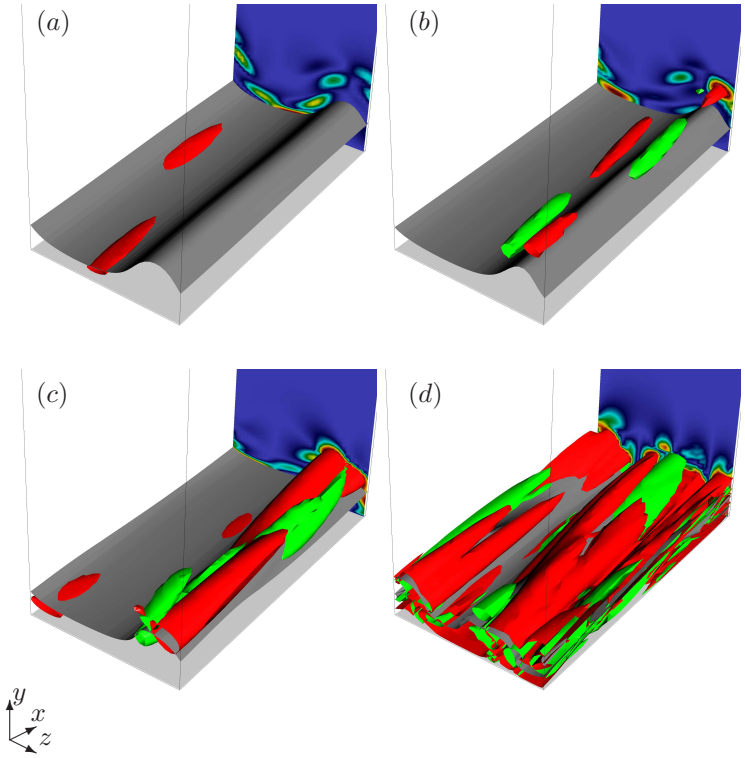

FIGURE 4.4. Evolution of Γ_c (*red*) and λ_2 (*green*) shown at (*a*) $t = t_0$, (*b*) $t = t_0 + 0.16T$, (*c*) $t = t_0 + 0.30T$ and (*d*) $t = t_0 + 0.39T$, where T denotes the period of the periodic orbit. The levels of the corresponding isosurfaces are fixed. The isosurface of streamwise velocity, $u = 0.5$ (*gray*), indicates streaks and the crossflow plane is coloured by Γ_c.

turbulent dynamics as much as possible[2]. We note, in figure 4.4, that during the laminar phase of the cycle, Γ_c is present as flat 'pancake' structures in the high-speed streak, where the highest occurrence is alternating from side to side. Then, as the instability starts to grow on the low-speed streak, the highest concentration of Γ_c can be found on top of the streak, still alternating from side to side, such that the highest values are always found on the convex side of the streak. The vortices identified with λ_2 are instead found on the concave side of the streak (also noted in *e.g.* Jeong *et al.* 1997). An explanation for this behaviour regarding Γ_c is given in figure 4.5. Due to the mean shear, there are always high values of spanwise vorticity, ω_z, present close to the wall (A). In the case of a straight streak (figure 4.5*a*) this vorticity is lifted by the

[2]For the relatively low Reynolds numbers studied, the turbulent structures on the two walls of a minimal channel flow interact and will therefore complicate the dynamics.

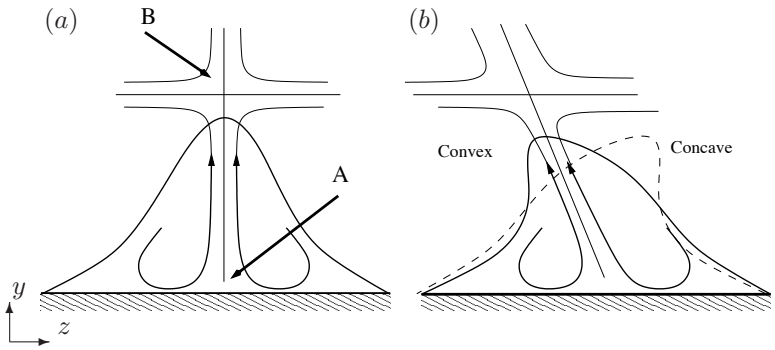

FIGURE 4.5. Explanation for the behaviour seen in figure 4.4(b): (a) straight streak, where high values of ω_z are lifted from A and multiplied by spanwise strain in B. (b) Similar mechanism for a bent streak in one of its outer positions. Thick lines denote a contour of constant streamwise velocity, thin lines show streamlines of in-plane flow and the dashed line shows the opposite outer position of the streak.

streamwise vortices, due to the well-known lift-up effect (Landahl 1980). In the braid region above the streak (B) the highest values of $\partial w/\partial z$ are found, which together with the lifted vorticity creates large spanwise vorticity stretching, $\omega_z \partial w/\partial z$. A similar situation is found to be present when the streak is bent (figure 4.5b). Since the braid region has moved over to the convex side of the streak (left in figure 4.5b), this is where we find high values of Γ_c. Similarly, high values of Γ_c are found to the right as soon as the streak 'wiggles' over to this side (the dashed line). It should be pointed out that the same mechanism is responsible for the high values of spanwise stretching alternating from side to side below the high-speed streak, given that the sketch in figure 4.5 in that case would be upside down.

When approaching the turbulent breakdown in figure 4.4(c), the structures provided by Γ_c and λ_2 are mixed, but still on top of the low-speed streak. Finally, as the flow reaches its most chaotic state, in figure 4.4(d), high values of both quantities are found basically everywhere in the flow.

CHAPTER 5

Physics of a turbulent three-dimensional separated diffuser flow

Now we have reached the point when we are ready to attack a complex flow at a realistic Reynolds number. Our tool is a high-order, accurate code with good scaling properties, which has proved to perform very well in turbulent, transitional and separated flow simulations. In addition, we have implemented and tested an inflow condition free from artificial turbulence and spurious temporal frequencies.

5.1. Towards more realistic flows: A test case for three-dimensional separated diffusers

The flow case we have chosen to consider is a diffuser flow, first investigated by the experimental group at The Center for Turbulence Research (CTR), Stanford University, under supervision of Prof. John Eaton. This diffuser differs in one important respect to the many diffusers studied in the literature before: it is *truly* three-dimensional, which means that not only the instantaneous flow is three-dimensional as in the diffuser we have encountered so far, but also the mean flow. This is achieved by constructing the diffuser such that the flow is surrounded by walls in an asymmetric fashion, as can be seen in figure 5.1, where the experimental set-up is shown. The working fluid is water, which is triggered to turbulence by the use of a grid in the upstream region. Subsequently, it develops to a fully turbulent state in a long duct of rectangular cross section and eventually enters the diffuser. There, the flow undergoes pressure-induced separation due an adverse pressure gradient. The diffuser walls are deflected 11.3° in the y-direction and 2.56° in the z-direction, with the resulting corners being smoothly rounded with a radius of 6.0 cm. The Reynolds number based on inlet-duct height, $h = 1$ cm, and bulk velocity, $u_b \approx 1$ m/s, is $Re = u_b h/\nu \approx 10\,000$. A pioneering experimental technique (Elkins *et al.* 2003) called 'magnetic resonance velocimetry' (MRV) is used to collect three-dimensional velocity data, which means that the entire experimental set-up is placed into an MRI-tunnel. Experimental mean flow results have been published in Cherry *et al.* (2008, 2009).

Originally, Prof. Eaton and his group investigated *two* three-dimensional diffusers with the same developed inflow but slightly different diffuser opening angles. Their motivation for this was threefold: (i) diffuser flows in practical

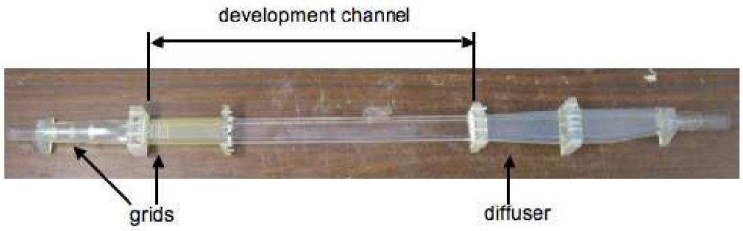

FIGURE 5.1. Experimental set-up of one of the geometries ('diffuser 1') in Cherry *et al.* (2008) showing the development region, diffuser expansion, converging section and outlet. Courtesy of Erica M. Cherry.

applications, such as engines and turbines, are likely to be of three-dimensional character and good benchmarking cases in the literature are rare; (ii) separated flows can be very sensitive to geometrical changes, but this sensitivity is not often studied; (iii) to facilitate comparison with numerical simulations the use of walls instead of an assumed infinite spanwise direction is the preferred choice. For simulations, a periodic spanwise direction often results in an insufficient spanwise width, which is known to influence the flow (see *e.g.* the discussion in Kaltenbach *et al.* 1999). For experiments, 3D effects are very difficult to eliminate. Or, as expressed by Prof. Eaton himself: "Separation wants to be three-dimensional" (14th ERCOFTAC SIG15 Workshop on Turbulence Modelling, Rome, September 2009). In fact, it is often reported that credible 2D data is lacking due to 3D contamination. Therefore, the strategy to go for a fully three-dimensional flow appears to be wise. In their examination, Cherry *et al.* (2008) noted that the two diffusers (here, denoted by 'diffuser 1' and 'diffuser 2'), although sharing identical inflow properties, experienced very different separation behaviour.

It is well-known (see *e.g.* Wang *et al.* 2004, among others), that RANS closures have difficulties to predict separation, particularly of the pressure-induced type, where the point of separation is not given *a priori*. Prior to separation, the mean flow slows down and the flow typically experiences large fluctuations and instationarity. Thus, the amplitude of the turbulent kinetic energy is no longer small compared to the mean flow, and the modelled part becomes not only more important, but also more difficult to predict. This in combination with point (i) above, and the fact that RANS is the most widely used approach for complex engineering flows implies that more research is needed. Therefore, the two diffuser flows are now selected as benchmarking cases in the *'ATAAC'* test suite (Advanced Turbulence Simulation for Aerodynamic Application Challenges). Likewise, 'diffuser 1' was used as test case in the *13th ERCOFTAC SIG15 Workshop on Turbulence Modelling*[1]. In the forthcoming

[1]Held at Graz University of Technology, Austria, September 25–26, 2008.

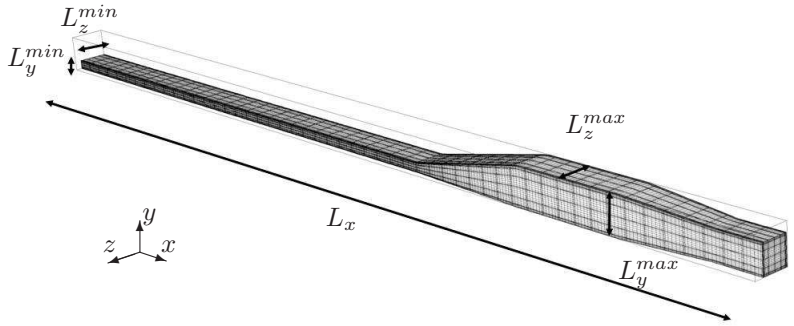

FIGURE 5.2. Computational grid of 'diffuser 1' in Cherry *et al.* (2008) showing the development region, diffuser expansion, converging section and outlet.

14th ERCOFTAC SIG15 Workshop on Turbulence Modelling[2] both 'diffuser 1' and 'diffuser 2' were studied. It was concluded that many models had difficulties in predicting the separated region, in particular models based on isotropic eddy-viscosity assumptions. However, models including the anisotropy of the Reynolds stresses improved the results significantly (Jakirlić *et al.* 2010*b*). A major improvement of the results could be noticed when using eddy-resolving techniques compared to steady RANS, which proves the difficulties involved in modelling such a complex, but yet realistic, flow. More specifically, Jakirlić *et al.* (2010*a*) showed promising results employing a hybrid RANS/LES scheme, whereas Schneider *et al.* (2009) obtained very good results using LES.

Since the present flow case has turned into an established test case for turbulence modelling, there exist a number of published RANS results *e.g.* Jeyapaul & Durbin (2010); Cherry *et al.* (2006), and LES or hybrid RANS/LES *e.g.* Abe & Ohtsuka (2010) in addition to the aforementioned LES and hybrid RANS/LES. However, results from a direct numerical simulation (DNS) have up until now not been presented. Therefore, due to the lack of detailed analyses of this important test case, we have chosen to perform a DNS of this flow. Because of the computational expenses (see Chapter 2.2), the focus is on one of the diffusers ('diffuser 1'), rather than aiming at quantifying the differences between the two of them. Our intention is to understand the complex physics and mechanisms leading to the particular separation behaviour seen in the experiments. To succeed with this objective, the first step is to reproduce the experimental results, which is undertaken by mimicking the experimental set-up as closely as possible. The computational grid employed in the simulations is depicted in figure 5.2. It consists of all the parts which can be seen in figure 5.1, namely: the inflow development duct with a length of almost 63 duct heights, h, (starting at the non-dimensional coordinate $x = -62.9$); the

[2]Held at Università di Roma 'La Sapienza', Rome, September 18, 2009.

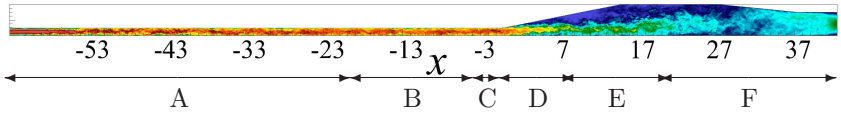

FIGURE 5.3. Instantaneous snapshot showing streamwise velocity in a side view of the entire flow domain, where one observes: the transitional region (A), the fully turbulent duct region (B), turbulent duct flow with some downstream influence (C), initial deceleration and instantaneous separation (D), the mean separated region (E) and finally the reattachment region and outflow (F). Velocity ranges from -0.1 (*blue*) to 1.6 (*red*).

diffuser expansion located at $x = 0$; the straight section and finally the converging section upstream of the outlet. The corners resulting from the diffuser expansion are smoothly rounded with a radius of $6.0h$ in accordance with the experimental set-up. The maximum dimensions are $L_x = 105.4h$, $L_y = [h, 4h]$, $L_z = [3.33h, 4h]$. The fixed mass flux in the simulation enables the Reynolds number based on bulk velocity and inflow-duct height to be kept exactly at $Re = 10\,000$, which matches the value reported in the experiment. The resolution of approximately 220 million grid points is obtained by a total of 127 750 local tensor product domains (elements) with a polynomial order of 11 respectively, resulting in $\Delta z^+_{max} \approx 11.6$, $\Delta y^+_{max} \approx 13.2$ and $\Delta x^+_{max} \approx 19.5$ in the duct centre and the first grid point off the wall being located at $z^+ \approx 0.074$ and $y^+ \approx 0.37$ respectively. This resolution is carefully verified to yield accurate results compared to the experimental findings. Unlike many other studies of this flow, we have chosen to incorporate the entire inflow duct in the simulation. Here, laminar flow undergoes natural transition by the use of the unsteady and random trip force, described in Chapter 3.1. In figure 5.3, the resulting transitional (A) and fully turbulent regions (B), can be seen in a side view showing an instantaneous picture of the flow. Here, (C) denotes a region where the flow starts to sense downstream influence from the separation. One may argue that many grid points are 'wasted' far upstream of the area of interest. However, when performing such a large simulation one would like to be certain that no spurious frequencies (discussed in Chapter 3.1 in conjunction with inflow recycling methods) influences the separation. Secondly, incorporating the laminar-turbulent transition in the same computational box as the separation, further strengthens the similarities between simulation and experiment. The regions where instantaneous (D) and mean (E) separation dominates the flow, and where the flow has reattached (F), are further pointed out in figure 5.3. A 'sponge region' is added at the end of the contraction in order to smoothly damp out turbulent fluctuations by forcing the flow to a turbulent mean profile, thereby eliminating spurious pressure waves back into the domain. It is followed by a homogeneous Neumann condition for the velocities at the outflow

boundary.

The simulation was performed on the Blue Gene/P at ALCF, Argonne National Laboratory (32 768 cores and a total of ~ 10 million core hours), the cluster 'Ekman' (2048 cores and a total of ~ 6.0 million core hours) and on the Cray XE6 at PDC, Stockholm (32 768 cores and a total of ~ 0.33 million core hours). The lack of homogeneous directions together with the fact that the flow involves a wide range of scales, called for long integration time in order to average the statistics.

5.2. Mean flow results

The quality of the flow in the inflow duct is carefully verified by several means, such that it can be ensured that the flow is fully turbulent prior to reaching the diffuser opening. The turbulent mean flow profile in the duct as a function of both wall distances, reported in figure 5.4, has an established viscous sublayer, a buffer region and the beginning of a log layer of approximately one decade. In addition to the time average, the flow in figure 5.4 was averaged in space over the two duct walls as well as over a streamwise distance of $9h$ between $x = -13$ and $x = -4$, where it was considered to be fully developed. Besides the comparison to the standard law of the wall, a comparison to a periodic turbulent duct flow simulation (*i.e.* a temporal flow configuration) conducted at the same Reynolds number is included in figure 5.4 as a cross-validation. This simulation has the same crossflow dimensions as the inflow duct: $L_y = h$ and $L_z = 3.33h$. The length is $L_x = 20h$, based on the findings by Huser & Biringen (1993). The resolution of the temporal duct flow is identical (in all spatial directions) to the last part of the inflow duct. The initial condition consisted of random noise, which eventually triggered transition to turbulence. Collection of statistics started after approximately 55 flow-through times ($tu_b/L_x = 55$) when a fully turbulent state was reached and continued over additionally 36 flow-through times. Spatial averaging was performed in the streamwise direction over the entire domain length and over the four quadrants. We observe very good agreement between the temporal and spatial simulations, which gives a strong indication that the flow in the last part of the inflow duct is in a fully turbulent state.

Another indicator of the fully developed turbulent state is the presence of *secondary flow* in the duct. Among all canonical turbulent wall-bounded flows (pipes, channels, ducts and boundary layers) duct flows is namely the only member where a secondary flow (*i.e.* a flow in the crossflow plane) is part of the mean flow. The appearance of such secondary mean flow motions were first documented in experiments by Nikuradse (1926). Numerous studies of duct flow, *e.g.* numerically by Huser & Biringen (1993), have subsequently confirmed that the role of the secondary flow is to drive high-speed fluid from the centre of the duct towards the corners and thereby enhance mixing of momentum. As opposed to secondary flow of the *first kind*, which is most commonly present whenever there are curvature effects of the main flow, and appears both in laminar and turbulent flows, secondary flow of the *second*

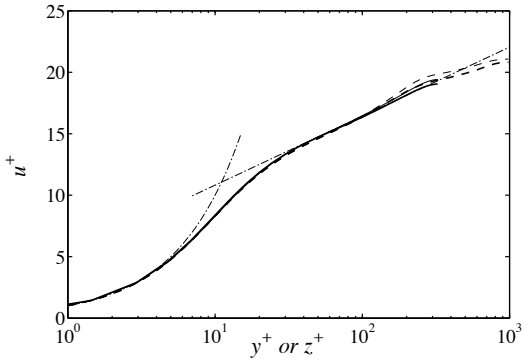

FIGURE 5.4. Mean velocity profiles $u^+(y^+)$ (——) and $u^+(z^+)$ (- - - -) extracted at $L_y/2$ and $L_z/2$ in the inflow duct, respectively. Comparison to the log law (—·—) with $\kappa = 0.41$ and $B = 5.2$, and a periodic turbulent duct flow simulation (—— and - - - -).

kind occurs due to the presence of gradients in the Reynolds stresses (see *e.g.* Piquet 1999). This generates forces in the crossflow plane and thus crossflow velocities. Being dependent on the Reynolds stresses, this flow can only exist in turbulent flows. The present flow case consists of turbulent flow in a rectangular duct which eventually separates in the diffuser. Hence, secondary flow of the second kind is present. In figure 5.5, it is visualised by means of streamwise vorticity computed from the mean flow field, *i.e.* $\langle\omega_x\rangle = \partial\langle v\rangle/\partial z - \partial\langle w\rangle/\partial y$. We compare the secondary flow in the inflow duct (*a*) to the corresponding flow in the periodic duct (*b*). Again, spatial averaging was performed in the streamwise direction over the domain length of $L_x = 20h$ for the latter case, while averaging was done over a streamwise distance of $9h$ between $x = -13$ and $x = -4$ in the former case. In both cases, the flow was averaged over the four quadrants. We observe that the secondary flow in the inflow duct, visible as positive (*red*) and negative (*blue*) streamwise vorticity, is in good agreement with the temporal periodic duct simulation, which again certifies that the inflow length is long enough. Since the duct is not a square, the two corner vortices can be seen to be different in size.

An indication that this secondary flow might have an effect on the separation behaviour were given by the several RANS predictions documented in Steiner *et al.* (2009); Jakirlić *et al.* (2010*b*). There, it was observed that most eddy-viscosity models, which assume isotropic conditions and hence no secondary flow in the duct, fail to predict the separation correctly. By contrast, Reynolds-stress models which were able to compute the secondary flow in the duct, were in general much better in their predictions. Indeed, as we will soon see, although very week in magnitude (typically a few per cent of the bulk velocity), this secondary flow plays an important role in the subsequent flow

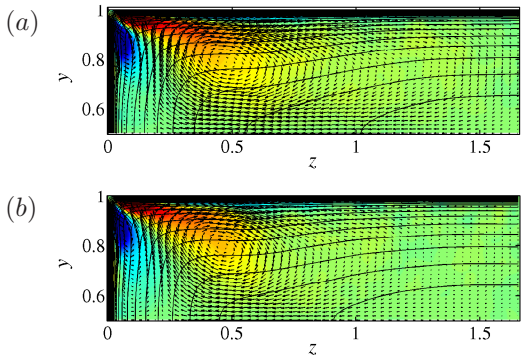

FIGURE 5.5. Crossflow planes of mean streamwise vorticity, $\langle\omega_x\rangle$, in the inflow duct (a) and in a periodic duct (b). In (a) the flow is averaged over a streamwise distance of $9h$ between $x = -13$ and $x = -4$, where the flow is in a fully turbulent state, whereas spatial averaging in (b) is performed over the domain length of $L_x = 20h$. Vorticity ranges from -0.5 (*blue*) to 0.5 (*red*). Contour lines of mean streamwise velocity, spaced 0.05 u_b apart, as well as velocity vectors of mean crossflow velocities are superimposed.

separation. This idea has recently been exploited by Schneider *et al.* (2011) as an efficient method to control (and decrease) the separation in the diffuser.

The increased complexity of a three-dimensional flow, as compared to the statistically two-dimensional flow in Chapter 3.3, has implications on the definition of separation itself. For instance, difficulties arise when we try define a two-dimensional stream function and a corresponding mean dividing streamline in a three-dimensional mean flow. Furthermore, in three-dimensional flows the boundary layer can separate without the surface shear stress necessarily falling to zero (Simpson 1989), which also rules out the definition given by equation (3.10). Williams (1977) and Schetz & Fuhs (1999) have collected a few definitions of three-dimensional separation, which are: (i) a line along which some component of the skin friction vanishes, (ii) a line along which the solution to the boundary layer equations is singular, (iii) an envelope of limiting streamlines, or (iv) a line which divides the flow coming from different regions. Schetz & Fuhs (1999) further state that none of these definitions appear to be universally valid, but some of them may have some element of validity. Here, we will follow Cherry *et al.* (2008) who used definition (i), since they defined the separation bubble as the region where the streamwise component of the mean flow is zero or below. The boundary of this region is the set of all points where $U = 0$. A sample result is given by the thick black line in figure 5.6, where a crossflow plane at $x = 8$ of mean streamwise velocity is shown. In general, good agreement with the experimental data can be inferred (*cf.* figure 5.6*a* and

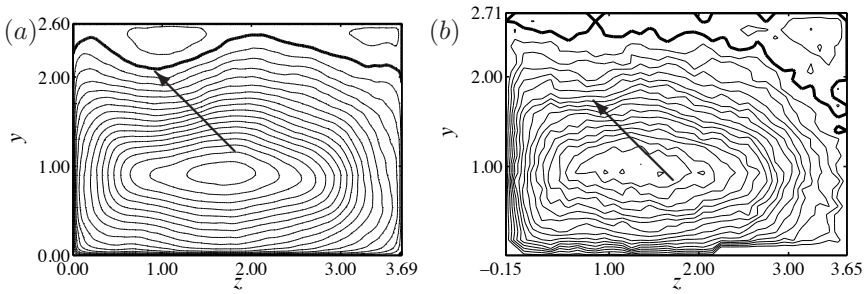

FIGURE 5.6. Mean streamwise velocity in a crossflow plane $8h$ downstream of the diffuser throat given by the present DNS data (a) and the experimental data by Cherry *et al.* (2008) (b). The arrow in (a) indicates the location of the so-called 'bump', whereas the arrow in (b) shows a compression of the velocity contours visible in the experimental data. The contour lines are spaced 0.05 u_b apart. Note that the coordinate system for figure (b) is unchanged with respect to the published data base.

figure 5.6b). In the very upstream region of the diffuser (not shown) the flow first separates in the upper right corner where the adverse pressure gradient is the strongest. At $x \approx 5$ the separated flow suddenly covers the top expanding wall of the diffuser. Instead of highlighting all similarities, we shall focus on one of the slight discrepancies found in the two data sets, reported in figure 5.6. Attention should be pointed towards the position of the arrow in figure 5.6(a), where the separated region extends somewhat from the top diffuser wall. This particular shape of the separated region, a feature which we simply have called the 'bump', is at first sight very different from the experimental counterpart in figure 5.6(b). Here, a similar 'bump' is not observed — at least not in the zero streamwise velocity contour (*thick line*). A closer look at the experimental data, however, reveals that the same feature can be noticed in most velocity contours except the zero velocity contour, pointed out by the arrow in figure 5.6(b) (note the compression of the velocity contours), indicating that the actual discrepancies between the experiments and our DNS are indeed small. An excellent cross-validation and another strong verification of the existence of the 'bump' was established in Jakirlić *et al.* (2010b) and in Schneider *et al.* (2009) where the latter authors show a strikingly similar 'bump' by employing a different simulation technique (LES and wall-functions), numerical scheme (finite volume), inflow conditions (recycling) and slightly different domain configuration (*e.g.* no converging section and sharp corners at the diffuser inlet).

Since the RANS closures, which are able to capture the secondary flow in the inflow duct, tend to see a similar 'bump', we suspect that the secondary flow is the main candidate for this phenomenon. Consequently, we investigate the evolution of the secondary flow into the diffuser, as before, by means of the

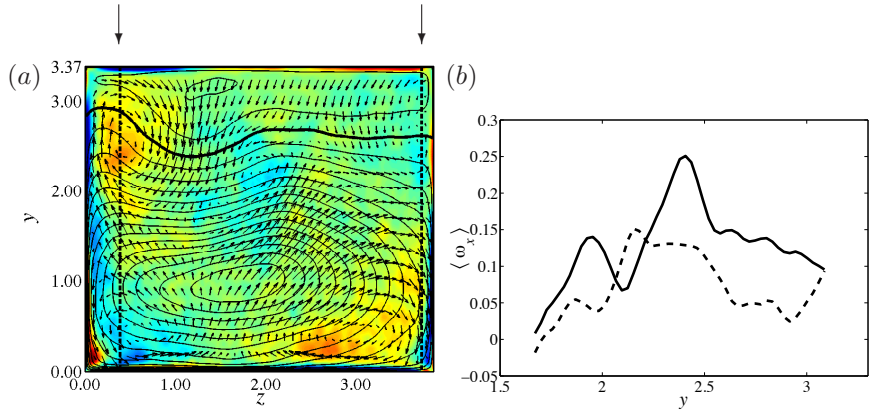

FIGURE 5.7. (a) Crossflow plane of mean streamwise vorticity, $\langle\omega_x\rangle$, $12h$ downstream of the diffuser throat, ranging from -0.5 (*blue*) to 0.5 (*red*). Contour lines of mean streamwise velocity, spaced 0.05 u_b apart, as well as velocity vectors of mean crossflow velocities are superimposed. The thick black line corresponds to the zero velocity contour. (b) Mean streamwise vorticity $\langle\omega_x\rangle$ at $z = 0.368$ (——) and $-\langle\omega_x\rangle$ at $z = 3.73$ (- - - -) along y in the crossflow plane in (a) across the two primary vortex centres (indicated by black arrows and dashed lines) responsible for the maximum vorticity magnitude in the upper left and right corners, respectively.

streamwise vorticity. (Due to slow variation of mean quantities in the streamwise direction, all quantities are averaged over a distance h in x. Moreover, a smoothing in the yz-plane is performed by applying a mean filter over a rectangle of size 2-by-2 points, which basically replaces point i by the mean of the rectangle centred on i.) As discussed above, when entering the diffuser, the flow separates first in the upper right corner. As an effect of the separation, the turbulence intensity increases (values of u_{rms}/u_b reaching 25 % were observed by Cherry *et al.* (2008) and in Paper 6 in the shear layer bounding the separation bubble). The increased turbulent activity enhances the turbulent diffusion in this region, and accordingly, the secondary flow is diffused and weakened — in particular the negative vorticity, visible in a crossflow plane at $x = 12$ in figure 5.7(a), to the upper right. In the upper left corner, on the other hand, the secondary flow has a magnitude similar to that in the duct, as shown by the similar colours in figures 5.5(a) and 5.7(a). Hence, we can conclude that this flow persists. The appearance of the 'bump' can now be clarified by noting the imbalance between the positive vorticity to the left and the negative vorticity to the right in figure 5.7(a). The magnitude of the vorticity to the left is greater than the magnitude of the vorticity to the right, quantified in figure 5.7(b), where the vorticity along y in the crossflow plane at $x = 12$ is shown.

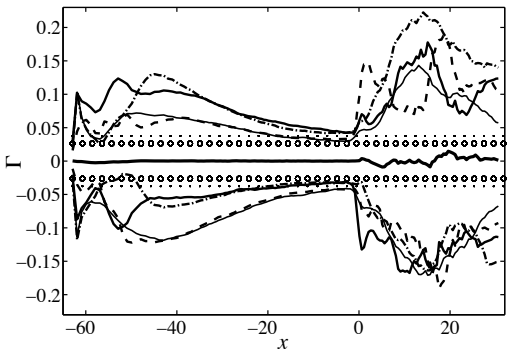

FIGURE 5.8. Positive and negative circulation, Γ_i, as a function of x in the four quadrants q_i with $i = 1, ..., 4$ being numbered clockwise starting from the upper left quadrant. Positive and negative circulation are defined as $\Gamma_i = \iint_{q_i} \langle\omega_x\rangle H(\langle\omega_x\rangle)\,\mathrm{d}q_i$ and $\Gamma_i = \iint_{q_i} \langle\omega_x\rangle H(-\langle\omega_x\rangle)\,\mathrm{d}q_i$, respectively, H being the Heaviside function. (a) Positive and negative Γ_1 (——), Γ_2 (- - - -), Γ_3 (—·—), Γ_4 (——), $\Gamma_1 + \Gamma_2 + \Gamma_3 + \Gamma_4$ (——), 'large vortex' (·····) and 'small vortex' (○) in the periodic duct simulation.

Here, $z = 0.368$ and $z = 3.73$ denote the spanwise coordinates (indicated in figure 5.7(a) by the black arrows and dashed lines) where the maximum magnitudes of positive vorticity in the upper left and negative vorticity in the upper right corners are found, respectively. The primary vortices responsible for the crossflow in the vicinity of the zero streamwise velocity contour are of main focus, and hence the boundaries — where the vorticity locally can be very high — are excluded. From figure 5.7(b), it is evident that the left vortex is stronger (almost a factor two) than the one to the right. This is thought to be the basic mechanism to create the observed asymmetry in the zero streamwise velocity contour.

Finally, we perform a quantitative tracking of the individual corner vortices. The axial dependence of the mean streamwise vorticity is examined by computing the positive and negative circulation, Γ_i, of the mean streamwise vorticity as a function of x. Here, $i = 1, ..., 4$ denote the circulation in the four quadrants of the duct and the diffuser, numbered clockwise and starting from the upper left. More specifically, the following integrals are computed:

$$\Gamma_i^+ = \iint_{q_i} \langle\omega_x\rangle H(\langle\omega_x\rangle)\,\mathrm{d}q_i \;;\;\; \Gamma_i^- = \iint_{q_i} \langle\omega_x\rangle H(-\langle\omega_x\rangle)\,\mathrm{d}q_i,$$

for the positive and negative circulation, respectively. Here, H is the Heaviside function and q_i are the regions of the four quadrants. The results are shown in figure 5.8. We see that the action of the trip force ($x < -60$) provides a strong initial increase of circulation in all four corners. In the following

transitional region there is first a slight decrease and then a large increase of circulation, indicating the late stages of transition. After this point, a fairly extended development region follows, where the secondary flow in the four corners approaches a fully developed equilibrium state, which is reached around $x = -13$. Here, all eight corner vortices have an approximately equal strength. Specifically, the 'large' vortices contain slightly more circulation ($|\Gamma| \approx 0.04$) than the 'small' vortices ($|\Gamma| \approx 0.03$), confirmed by the counterparts computed in the periodic duct. Interestingly, as the flow enters the diffuser ($x = 0$) there is a sudden increase in magnitude of the circulation in all four corners. The peak is reached where the diffuser stops expanding ($x = 15$). In the following straight section, the magnitude of the circulation in the various corners again drops. The sum of the total circulation (thick black line in figure 5.8) reveals that the circulation is approximately conserved along the streamwise length of the duct and the diffuser, *i.e.* the positive and negative circulation in all four quadrants add up to zero. The *approximate* conservation stems from the smoothing and averaging process prior to computing the circulation. As discussed earlier, the weak secondary flow created in the inflow duct needs to be represented by a turbulence model in order to get the correct separation prediction in the diffuser. Having access to the evolution of the eight individual corner vortices, provided in figure 5.8, will undoubtedly facilitate the validation of such a model.

5.3. Large-scale dynamics

The literature is sparse when it comes to large-scale quasi-periodic motions detected in turbulent pressure-induced separated flows. Often a broad spectral content is observed (Kaltenbach *et al.* 1999; Herbst *et al.* 2007; Törnblom *et al.* 2009; Na & Moin 1998). In geometry-induced separated flows, on the other hand, dominant low frequencies have been reported in numerous studies (*e.g.* Le *et al.* 1997; Eaton & Johnston 1980; Friedrich & Arnal 1990; Kiya & Sasaki 1985). Clearly, this phenomenon emerges more easily in the latter type of flow. However, it might not be the pressure-induced separation *per se* that prevents quasi-periodic motions to occur. In fact, most studies on pressure-induced separated flows have been performed in *two-dimensional* configurations. In such a set-up, the flow never becomes 'locked', but can always move freely in the homogeneous direction. If some sort of additional confinement is added to the flow, as in the present set-up, recirculation zones (at least instantaneous) on two or more sides of the flow will form. They will tend to influence the dynamics to a greater extent than for unconfined flows. Moreover, if the Reynolds number is high, then the diffuser shares many similarities with 'confined jets' which is a class of flows extensively studied. The experimental set-ups in these studies differ slightly, but in essence they consist of a turbulent jet entering a rectangular confinement of some variable or fixed size, and exits on the other side. A generic set-up of such an experiment is shown in figure 5.9, where the jet and recirculation zones are indicated. In some studies (*e.g.* Lawson & Davidson 2001; Maurel *et al.* 1996; Villermaux & Hopfinger 1994; Moreno *et al.* 2004), it has been noted that recirculation zones forming on each side of

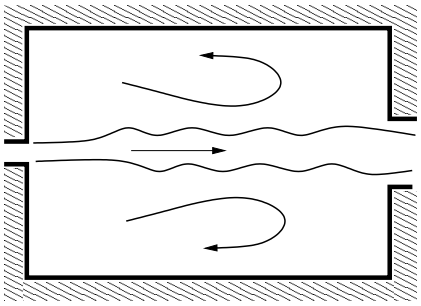

FIGURE 5.9. A typical flow configuration for a confined jet experiment.

the jet can, under particular circumstances, render the flow globally unstable. Consequently, the flow is governed by a dominant frequency, which manifests itself in shedding of some sort.

The first sign of large-scale motions in the present diffuser flow was observed through instantaneous snapshots, indicating that the flow is subjected to a motion that resembles the 'flapping' or meandering of an unstable jet. An example is shown in figure 5.10, where the snapshots are separated in time by $\Delta t u_b/h = 10$. From figure 5.10(a) we can estimate a streamwise wavelength of roughly $10h$. In the subsequent figures 5.10(b) and (c) we can observe this wave propagating downstream. Quantitatively, this is studied by a set of time signal probes placed in the flow domain and by proper orthogonal decomposition (POD) of the flow. Three-dimensional visualisations of the first few fluctuating POD modes (here 1 and 3) are given in figure 5.11. Their time dependence (computed as outlined in Chapter 4.1) is shown in figure 5.12. As is often the case in POD of inhomogeneous turbulent flows (see *e.g.* Manhart & Wengle 1993), a large fraction, here 86 %, of the energy resides in the mean flow (mode 0). The remaining 14 % belong to the fluctuating modes. Among these, mode 1 and 3 contain 4.8 % and 2.5 % of the fluctuating energy, respectively. Thus, they do not contain a very large fraction of the total energy, but as we will see they are important in order to explain the dynamics in the diffuser. From figure 5.11 one can deduce that the modes are large streaky structures with alternating positive and negative streamwise fluctuation velocity. The combined effect of these fluctuations is to bend the confined jet and create a wave. For mode 1, these streaks are indicated by ① (positive) and ② (negative). Mode 3 displays a very clear wave, whose oscillation mainly goes along z, since negative ③ and positive ④ fluctuations are located side by side in the z-direction. Note that the modes here are shown at one specific time and since each mode has a particular time dependence given by the (nearly) sinusoidal variation in figure 5.12(a), the wave has at some later time shifted its positive and negative side. We observe approximately four periods in 5.12(a), whose length can be estimated by $T \sim 100h/u_b$, giving a non-dimensional period of $T^* = Tu_b/h \sim 100$. The corresponding Strouhal number (non-dimensional frequency) is therefore

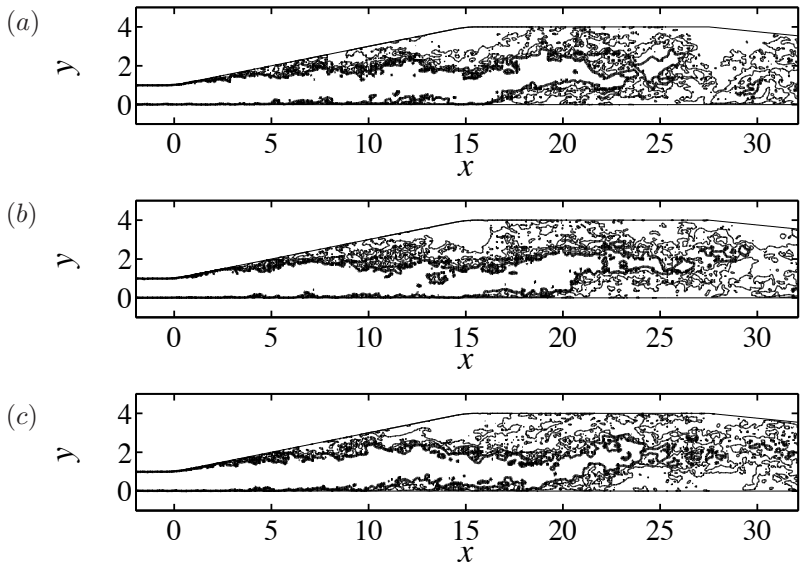

FIGURE 5.10. Three snapshots in an xy-plane at $z = 1.87$ shown at (a) $t = t_0$, (b) $t = t_0 + 10h/u_b$, (c) $t = t_0 + 20h/u_b$. Thin contour lines of streamwise velocity are shown for $u/u_b = 0, 0.2$ and 0.3, whereas the thick contour line is shown for $u/u_b = 0.4$.

$St = 1/T^* \sim 0.01$. This frequency compares well to the spectral peak in the power spectral density (PSD) in figure 5.12(b), deduced from time signal probes placed in the upper part of the flow domain at $x = 5, 8, 12, 15$. The structures shown in figure 5.11 resemble POD modes originating from a jet with inherent low-frequency flapping (see *e.g.* Moreno *et al.* 2004), supporting the fact that there is a sinusoidal motion present in the diffuser. Based on figure 5.11, the streamwise wavelength is estimated to be $\lambda_x \approx 10h$, which is consistent with the meandering visible in the instantaneous snapshots in figure 5.10. In the two cross-stream directions (y and z), the modes span the entire cross section, such that $\lambda_y = \lambda_z \approx 4h$, since $L_y = L_z = 4h$ in the region where the modes are active. These structures are thus the largest possible for the given geometry. This is in agreement with Villermaux & Hopfinger (1994), who concluded that for confined flapping jets in asymmetric configurations, the largest confinement dimension will dominate the flow. It is interesting to note that the modes pass through the mean separated region, which extends from $x \approx 7$ to $x \approx 20$, suggesting a coherent movement of the flow inside and outside the mean separated region. Higher modes ($\sim$ 7–20) have shorter wavelengths, but still with a high degree of coherence. They do not extend into the mean separated region as much as the first few mods (1–6), which indicates that the separated zone shares its frequencies rather with the largest structures in

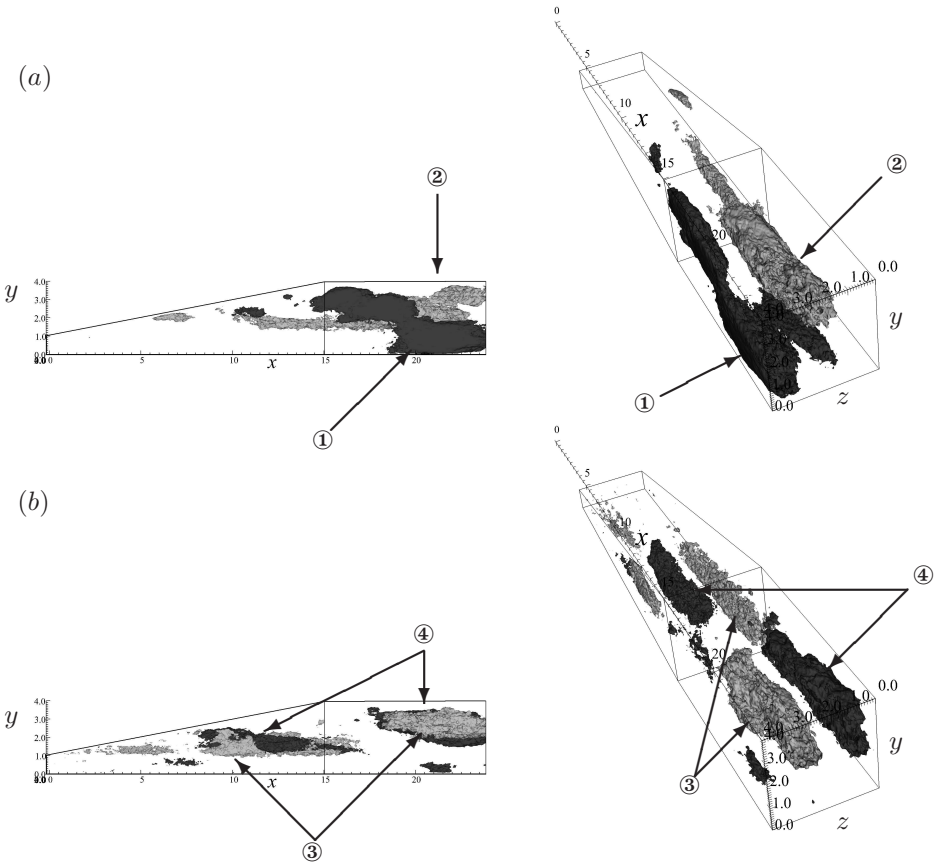

FIGURE 5.11. Isosurfaces (*dark gray:* 0.1, *light gray:* −0.1) of streamwise velocity pertaining to POD mode 1 (*a*) and 3 (*b*), shown at two different angles. The arrows indicate specific structures of the respective modes, further described in the text.

the diffuser. At some point ($\gtrsim$ mode 60) most of the coherence is lost and small-scale turbulence remains.

Two modes shifted approximately 90 degrees in time are needed to define a wave that moves downstream, *i.e.* a *travelling* wave. Testing for the existence of such a wave can be undertaken by projecting the flow onto the two-dimensional phase space spanned by the fluctuating POD modes at hand, *i.e.* the time evolution of modes i and j are drawn simultaneously. In the case of a travelling wave, the two-dimensional phase portraits would correspond to a circle, *i.e.* a periodic orbit: $\boldsymbol{r}(t) = a_i(t)\boldsymbol{\psi_i} + a_j(t)\boldsymbol{\psi_j} = A\cos(t)\boldsymbol{e_x} + A\sin(t)\boldsymbol{e_y}$, where A is the amplitude of the mode and t is the time. If the time axis is included as a third direction, the resulting parameterised curve would be a helix, mathematically

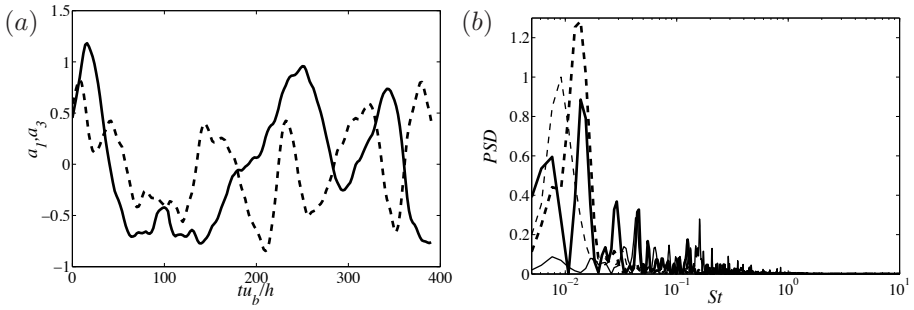

FIGURE 5.12. (a) Temporal evolution of mode 1 (——) and 3 (- - - -), (b) power spectral density of time probes placed in the upper part of the flow domain at $x = 5$ (——), $x = 8$ (——), $x = 12$ (- - - -) and $x = 15$ (- - - -).

described by $\boldsymbol{r}(t) = A\cos(t)\boldsymbol{e_x} + A\sin(t)\boldsymbol{e_y} + t\boldsymbol{e_z}$. On the other hand, no particular coherence would correspond to a joint probability density function (PDF) of two random variables, uniformly distributed between $-A/2$ to $A/2$. If the time signal were not exactly periodic, *i.e.* quasi-periodic, then the circle would not be closed, but rather spiral either inwards or outwards. In figure 5.13(a), the two-dimensional projection for the fluctuating POD modes 1 and 2, *i.e.* the trajectory in the subspace $(\boldsymbol{\psi}_1, \boldsymbol{\psi}_2)$, is shown. Time is included as a third direction and the start and end points of the trajectory are indicated for clarity. It can be seen that the trajectory completes a bit more than three revolutions, approximately taking the form of a helix. Considering the high turbulence levels of the present flow (u_{rms}/u_b up to 25 %), this phase portrait show a remarkable clarity. Finally, we study this low-dimensional motion in terms of flow variables, here streamwise velocity, by following the procedure previously employed in *e.g.* Cazemier *et al.* (1998) and the references therein, where the most energetic modes are superimposed with their corresponding temporal weight. Here, we use modes 0–6. Isosurfaces of constant streamwise velocity are shown in figure 5.13(b) at two specific times ($tu_b/h = 8$ and $tu_b/h = 54$) in figure 5.12(a). The travelling wave is now clearly seen to propagate through the domain. In particular, in figure 5.13(*b, upper*), the sinusoidal shape of the high-speed core of the flow has one of its minima located at $x \approx 20$ ①. As a consequence of the confinement of the flow, high velocity fluid is pushed up on the sides, close to the side walls. One half period later, in figure 5.13(*b, lower*), the minimum has propagated downstream (not visible anymore), and is now replaced by a maximum at $x = 20$ ②. Now, the confinement instead forces flow in the crossflow plane downwards in the vicinity of the side walls. Another half period later (not shown), the flow is back to its approximate original state. It is noteworthy that an effect of this meandering seen in the diffuser is the strong secondary flow (in the crossflow directions), superimposed on the weak secondary flow inherent in the mean flow.

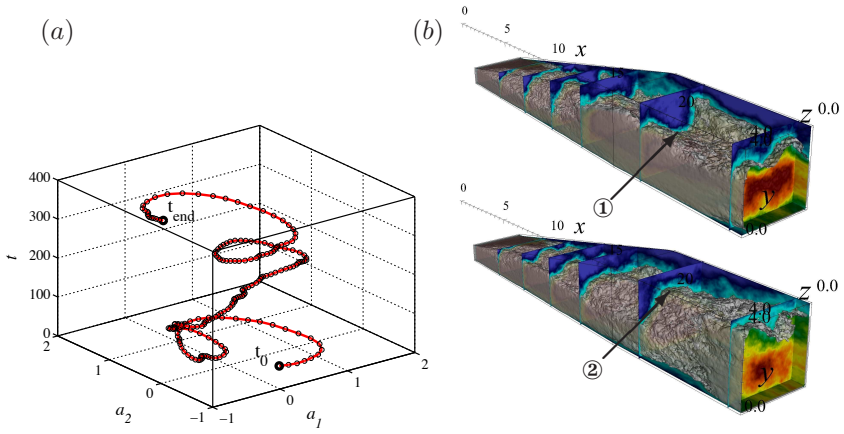

FIGURE 5.13. (*a*) Temporal orbit in the subspace (ψ_1, ψ_2) showing the quasi-periodic motion of the largest structures present in the diffuser. Time is increasing along the vertical axis. (*b*) Superposition of POD modes 0–6 shown at $tu_b/h = 8$ (*upper*) and $tu_b/h = 54$ (*lower*) in figure 5.12(*a*). Gray isosurface show constant streamwise velocity, $u/u_b = 0.1$. Crossflow planes show streamwise velocity ranging from -0.1 (*blue*) to 0.5 (*red*). The arrows highlight the wave propagating through the domain, further described in the text.

CHAPTER 6

Conclusions and outlook

Initially, turbulent flows were mainly simulated relying on fully spectral discretization methods. Also at KTH Mechanics, such a code was developed and continuously extended (see the manual for the code `simson` Chevalier *et al.* 2007). This accurate and efficient code has over the past fifteen years led to an extensive number of published articles in turbulent and transitional boundary-layer research. Although there are many complex phenomena appearing in boundary-layer flows, the time is now mature to proceed to more complex flows. Four and a half years ago this new era started when Prof. Paul F. Fischer kindly offered us to use and further develop his spectral-element code `nek5000`.

This thesis focuses on turbulent wall-bounded flows in moderately complex geometries. The work is of purely numerical nature and the tool for the numerical simulations is the spectral-element method (SEM). A thorough validation of the spectral-element code in canonical flow cases, involving turbulence and transition in channels, has been carried out. In addition, a slightly more complex case including separation, was used for the benchmarking. For these flows, long experience and solid expertise concerning *e.g.* expected results, required resolution and efficiency exist within our group. Through this, we have not only been able to quantify the accuracy and resolution requirements, but also realised that fully turbulent flows at moderate Reynolds numbers are well-suited for the spectral-element method. To support this statement further and disprove the long-standing fear of instability issues of the spectral-element method in turbulent flow simulations, two stabilisation tools for the spectral-element method were investigated on simpler test problems in 1D and 2D, with an *a posteriori* analysis in transitional and turbulent channel flow simulations. It was shown that the spectral-element method needs stabilisation as soon as the flow transitions to turbulence, even in well-resolved simulations. The instability is cured either by filter-based stabilisation or over-integration, where it was found that the full 3/2-rule is not needed for stability.

Strengthened by the excellent outcome of the validation part of the thesis and prepared with reliable turbulent inflow conditions involving an unsteady trip-forcing technique, we were able to tackle the problem of three-dimensional separation and perform the first direct numerical simulation of the experimental diffuser set-up by Cherry *et al.* (2008). The problem involved $\sim$ 220 million grid points and was running on up to 32 768 processors. The agreement to the

experimental data was close, in particular the sensitive separated region could be captured with high accuracy. It also became clear that the presence of the secondary flow, which arises in the inflow duct, has a profound effect upon the separation behaviour. Moreover, the diffuser could be seen to share many similarities with confined jets, where the separated zones under some conditions can render the flow globally unstable. More specifically, a large-scale motion with frequency $St \equiv fh/u_b \sim 0.01$ (h being the inflow-duct height and u_b the bulk velocity) pertaining to the meandering of the incoming flow was detected.

The present thesis also reports some results regarding coherent structures in canonical wall-bounded turbulent flows. To this extent, so-called Koopman modes were used for the spectral analysis of a minimal channel flow. For this particular flow, strongly dominated by two frequencies, it could be concluded that classical proper orthogonal decomposition (POD) could suffice to pick up the dominant frequencies. However, since the Koopman modes (as opposed to the POD modes) are clearly separated in spectral space, a more detailed analysis of the second peak in the spectrum pertaining to the 'bursting' phenomenon could be provided using these modes. Moreover, an alternative measure used to locate coherent structures in turbulent and transitional flows was proposed. Contrary to most other identification criterions suggested earlier, the present one focuses on the production of vorticity, rather than vortices.

A natural continuation of the present work is to perform a more 'classical' analysis of the turbulent three-dimensional diffuser flow, focusing on evaluation of the Reynolds stress budgets. Other than contributing with enhanced understanding of the flow itself, it would benefit RANS modellers in the development of new turbulence closures. For further spectral analysis of the flow, the use of Koopman modes might be advantageous, as the flow in the diffuser could be seen to be clearly separated in spectral space.

For the numerical part of this thesis, work on the skew-symmetric properties of the numerical discretization is ongoing. This is certainly an important topic and is at the present not fully understood.

These years have shown what the spectral-element method is capable of. The numerical code `nek5000` is already involved in many other research projects at KTH Mechanics and at other universities and research institutes world wide. There are countless flows in complex geometries to be discovered, and in fifteen years `nek5000` has probably generated as many articles in fluid mechanics research at this department as the old spectral boundary-layer code.

CHAPTER 7

Summary of papers, author contributions and presented work

Paper 1

Ohlsson, J., Schlatter, P., Mavriplis, C., & Henningson, D. S. 2011 The spectral-element and pseudo-spectral methods: A comparative study. *Spectral and High Order Methods for Partial Differential Equations, LNCSE* **76**, 459–468.

This paper compares the code `nek5000` based on the spectral-element method with the pseudo-spectral code `simson` in terms of computational speed and accuracy in turbulent and transitional wall-bounded flows. It is found that the pseudo-spectral code is approximately 4–6 times faster per time step than the spectral-element code in fully developed turbulent flow simulations, and up to 10–20 times faster when taking into account the more severe CFL restriction in the spectral-element code. Mesh refinement studies show that the two methods need similar amount of spatial resolution to capture the relevant physics.

The simulations were performed by Johan Malm (JM). The paper was written by JM with input from Dr. Philipp Schlatter (PS) and Prof. Catherine Mavriplis (CM).

The work was presented at the **8th International Conference On Spectral and High Order Methods (ICOSAHOM 8)**, June 22–26, 2009, *Trondheim, Norway.*

Paper 2

Ohlsson, J., Schlatter, P., Fischer, P. F. & Henningson, D. S. 2011 Stabilization of the spectral-element method in turbulent flow simulations. *Spectral and High Order Methods for Partial Differential Equations, LNCSE* **76**, 449–458.

This paper deals with the numerical stability of the spectral-element method at moderate to high Reynolds numbers. With the use of appropriate

stabilisation tools (over-integration, *i.e.* dealiasing, or filter-based stabilisation), it is shown *a priori* on simpler model problems and *a posteriori* using the full Navier–Stokes equations, that the method can be stabilised without the need of the full 3/2 dealiasing rule.

A spectral-element solver for Burgers' equation was implemented by JM with feedback from PS. The implementation of a spectral-element solver for the scalar transport equation was provided by Prof. Paul F. Fischer (PF). The paper was written by JM with input from PF and PS.

The work was presented at the **8th International Conference On Spectral and High Order Methods (ICOSAHOM 8)**, June 22–26, 2009, *Trondheim, Norway.*

Paper 3

Ohlsson, J., Schlatter, P., Fischer, P. F. & Henningson, D. S. 2010 Large-eddy simulation of turbulent flow in a plane asymmetric diffuser by the spectral-element method. *Direct and Large-Eddy Simulation VII.* 197–204.

In this paper, the ability of the spectral-element code to handle moderately complex geometries is investigated by means of a large-eddy simulation (LES) of a plane asymmetric diffuser with an opening angle of 8.5°, also numerically investigated by Herbst *et al.* (2007). Two different Reynolds numbers are studied: $Re_b = 4500, 9000$ based on bulk velocity and inflow channel half-height. A dynamic Smagorinsky model is used as SGS model. Good results compared to Herbst *et al.* (2007) are obtained, in particular it is noticed that less grid points can be used to predict the separated flow with similar accuracy, leading to the conclusion that the use of a high-order method is advantageous for flows featuring pressure-induced separation.

The simulations were performed by JM. The SGS model for the LES was implemented by PF. The paper was written by JM with input from PS.

The work was presented at the

- **7th ERCOFTAC Workshop On Direct and Large-Eddy Simulations (DLES 7)**, September 8–10, 2008, *Trieste, Italy*,
- **61st Annual Meeting of the American Physical Society (APS), Division of Fluid Dynamics**, November 23–25, 2008, *San Antonio, Texas.*

Paper 4

Malm, J., Bagheri, S., Schlatter, P. & Henningson, D. S. 2010 Koopman mode decomposition of a minimal channel flow. *Internal report.*

The recent Koopman mode decomposition (Rowley *et al.* 2009) is applied to a turbulent and fully non-linear minimal channel flow. The modes are computed according to the dynamic mode decomposition (DMD) outlined in (Schmid 2010). The acquired modes and frequencies are compared to classical proper orthogonal decomposition (POD) of the same flow. The two decompositions identify similar structures, associated with the dynamics of the single low-speed streak present in the flow. However, since the Koopman mode decomposition provides a clear separation in spectral space, two separate structures relating to the 'bursting' phenomenon could be identified.

The simulations were performed by JM. A snapshot based POD code building on a code written by Dr. Shervin Bagheri (SB) was re-written by JM for the present simulation code and extended by JM to account for the computation of Koopman modes. The paper was written by JM with input from PS and SB.

Paper 5

Malm, J., Schlatter, P. & Sandham, N. D. 2011 A vorticity stretching diagnostic for turbulent and transitional flows. *Theor. Comput. Fluid Dyn.* Accepted.

A new diagnostic measure, based on the maximum vorticity stretching component in every spatial point, is designed. It is shown that the structures associated with intense vorticity stretching in all investigated flow cases have the shape of flat 'pancake' structures in the vicinity of high-speed streaks and on top of unstable low-speed streaks. The largest occurrence of vorticity stretching in a fully turbulent wall-bounded flow is present in the transition between the viscous sublayer and buffer layer, with associated structures having a streamwise length of $\sim$ 200–300 wall units.

The simulations were performed by JM and PS. The theory was formulated by JM, PS and Prof. Neil Sandham (NS). Implementations and post-processing were performed by JM. The paper was written by JM with input from PS and NS.

Parts of the work were presented at the **7th International Symposium On Turbulence and Shear Flow Phenomena (TSFP 7)**, July 28–31, 2011, *Ottawa, Canada.*

Paper 6

Ohlsson, J., Schlatter, P., Fischer, P. F. & Henningson, D. S. 2010 Direct numerical simulation of separated flow in a three-dimensional diffuser. *J. Fluid Mech.* **650**, 307–318.

In this paper we perform the first direct numerical simulation (DNS) of a truly three-dimensional, turbulent and separated diffuser flow at $Re = 10\ 000$ (based on bulk velocity and inflow-duct height), experimentally investigated by Cherry *et al.* (2008). The massively parallel capabilities of the spectral-element method are exploited by running the simulations on up to 32 768 processors. Very good agreement with experimental mean flow data is obtained. In addition, an explanation for the discovered asymmetry of the mean separated flow is provided.

The simulations and necessary implementations into the simulation code were performed by JM with input from PF and PS. The paper was written by JM with input from PS, Prof. Dan Henningson (DH) and PF.

Parts of the work were presented at the

- **13th ERCOFTAC Nordic Pilot Centre (NPC 13)**, June 8–9, 2009, *Bergen, Norway*,
- **12th EUROMECH European Turbulence Conference (ETC 12)**, September 7–10, 2009, *Marburg, Germany*,
- **14th ERCOFTAC SIG 15 Workshop on Refined Turbulence Modelling**, September 18, 2009, *Rome, Italy*.

Paper 7

Malm, J., Schlatter, P., Fischer, P. F. & Henningson, D. S. 2011 Coherent structures and dominant frequencies in a turbulent three-dimensional diffuser. *J. Fluid Mech.* Under revision.

This paper is a continuation of Paper 6, focusing on a time-dependent analysis, where dominant frequencies and coherent structures are investigated and quantified. It is shown that the flow contains multiple phenomena, well separated in frequency space. A dominant frequency $St \equiv fh/u_b \sim 0.01$ (based on bulk velocity and inflow-duct height) is detected by time signal probes in the flow, and associated structures are identified by POD.

The simulations were performed by JM. A snapshot based POD code building on a code written by SB was re-written by JM for the present simulation code. The paper was written by JM with input from PS and DH.

Parts of the work were presented at the **8th EUROMECH Fluid Mechanics Conference (EFMC 8)**, September 13–16, 2010, *Bad Reichenhall, Germany*.

Acknowledgements

The present thesis summarises four and a half years of research in Prof. Dan S. Henningson's group at the KTH Mechanics. I would like to thank my supervisor Dan Henningson for his enthusiasm and skills in defining good research projects. With his experience and confidence I have never feared that I am walking on the wrong path. His generosity has given me opportunities to attend conferences, workshops and going abroad. My co-advisor Philipp Schlatter is especially acknowledged for sharing his vast knowledge and understanding for flow physics, numerical analysis and computer science. Most importantly, you have patiently taught me how to perform research in a disciplinary and accurate[1] manner, which is what has made me develop as a researcher. Paul F. Fischer is greatly acknowledged for providing us with his research code and helping us along to get started in the very beginning, as well as for his support during the large computer simulations. To cooperate with you has always been a pleasure and you have inspired me in the curious and joyful way you approach science. I am grateful to my other external collaborators Catherine Mavriplis and Neil Sandham for their great ideas and tireless correcting of my written English.

Outi Tammisola, Gabriele Bellani and Onofrio Semeraro are acknowledged for sharing ideas and experience. Thanks to Stefan Wallin for suggesting me to go to the SIG15 Workshop in Rome, where my data was used as reference. There, I also had the great pleasure to meet Hayder Schneider and Dominic von Terzi, with whom I had many valuable and interesting discussions. Thank you!

During these years I have had the opportunity to get to know many interesting people and good friends at conferences and meetings, too many to be mentioned here. I have truly enjoyed the friendly atmosphere at the Department of Mechanics, which would not have been possible without my roommates Antonios Monokrousos, Espen Åkervik, Onofrio Semeraro, Qiang Li and Armin Hosseini, and the PhD students/post-docs Andreas Vallgren, Andreas Carlson, David Tempelmann, Enrico Deusebio, Lailai Zhu, Lars-Uve Schrader, Miloš Ilak, Shervin Bagheri, Marit Berger, Stevin van Wyk, Peter Lenaers, Florian von Stillfried, Reza Dadfar, Sasan Sarmast, Robert Pettersson, Zeinab

[1] Two files are not the same until they are *binary the same*, *i.e.* every single bit is identical.

Pouransari, Amin Rasam, Outi Tammisola, Gabriele Bellani, Karl Håkansson, Gaetano Sardina, Krishnagoud Manda, Azad Noorani and Iman Lashgari. The 'seniors' Luca Brandt, Yohann Duguet and Ardeshir Hanifi are acknowledged for interesting and useful discussions as well as their happy appearance. Hanno Essén[2], Erik Lindborg, Nicholas Apazidis, Anders Dahlkild and Gunnar Maxe have never failed to transform my lunches and coffee breaks into scientific journeys. Without Carolina Eneqvist, Heide Hornk, Malin Landin, Nina Bauer, Hans Silverhag, Gunnar Tibert, Karina Bellbrant and Bubba, this department would have been a cold and dry place. Thanks for your enthusiasm and energy!

Thanks to Stefan Kerkemeier at ETH Zürich for interesting and fruitful discussions at our shared office at Argonne National Laboratory as well as his help and expertise with the code `nek5000`. Of the friendly people I met at Argonne National Laboratory, Aleksandr Obabko is especially acknowledged. Philipp Schlatter, Paul F. Fischer, Stefan Kerkemeier and Susanna Malm are further acknowledged for their valuable comments on the manuscript and Geert Brethouwer for internally reviewing the material.

The Linné FLOW Centre, financed by the Swedish Research Council (Vetenskapsrådet), is gratefully acknowledged for funding of the project. The Swedish National Infrastructure for Computing (SNIC), with a generous grant by the Knut and Alice Wallenberg (KAW) Foundation, is acknowledged for computer time at the Centre for Parallel Computers (PDC), Stockholm, Sweden and the National Supercomputer Centre (NSC), Linköping, Sweden. Argonne Leadership Computing Facility (ALCF) at Argonne National Laboratory (ANL), Chicago, USA is acknowledged for computer time on the IBM BG/P *Intrepid*.

Last, but not least, thanks to my good old friends, sister, mother and father in Stockholm for distracting my thoughts away from science from time to time. I am particularly grateful to my father for giving me, and always supporting, my interest in science.

And finally, to those, who have the biggest share in this thesis. Susanna, your desire to understand what I am doing has always impressed me and made me feel that I am never alone. Margit, it will take some time until you can read this, but nevertheless I want you to know that although being so small you have added so much to my life. I love you both.

[2]Probably the most well-read person the department can offer.

Bibliography

Abe, K. & Ohtsuka, T. 2010 An investigation of LES and Hybrid LES/RANS models for predicting 3-D diffuser flow. *Int. J. Heat Fluid Flow* **31** (5), 833–844.

Adams, N. A. 2000 Direct simulation of the turbulent boundary layer along a compression ramp at $M = 3$ and $Re_\theta = 1685$. *J. Fluid Mech.* **420**, 47–83.

Åkervik, E., Hœpffner, J., Ehrenstein, U. & Henningson, D. S. 2007 Optimal growth, model reduction and control in a separated boundary-layer flow using global eigenmodes. *J. Fluid Mech.* **579**, 305–314.

del Álamo, J. C. & Jiménez, J. 2006 Linear energy amplification in turbulent channels. *J. Fluid Mech.* **559**, 205–213.

Arrow, K., Hurwicz, L. & Uzawa, H. 1958 *Studies in Nonlinear Programming*. Stanford University Press, Stanford, USA.

Bagheri, S., Brandt, L. & Henningson, D. S. 2009 Input-output analysis, model reduction and control of the flat-plate boundary layer. *J. Fluid Mech.* **620**, 263–298.

Barkley, D. 2006 Linear analysis of the cylinder wake mean flow. *Europhys. Lett.* **75**, 750–756.

Blackburn, H. M. & Schmidt, S. 2003 Spectral element filtering techniques for large-eddy simulation with dynamic estimation. *J. Comput. Phys.* **186** (2), 610–629.

Blackwelder, R. F. & Eckelmann, H. 1979 Streamwise vortices associated with the bursting phenomenon. *J. Fluid Mech.* **94**, 577–594.

Bouffanais, R., Deville, M., Fischer, P.F., Leriche, E. & Weill, D. 2006 Large-eddy simulation of the lid-driven cubic cavity flow by the spectral element method. *J. Sci. Comput.* **27**, 151–162.

Buice, C. U. & Eaton, J. K. 2000 Experimental investigation of flow through an asymmetric plane diffuser. *J. Fluids Engng.* **122** (2), 433–435.

Canuto, C., Hussaini, M.Y., Quarteroni, A. & Zang, T.A. 1988 *Spectral Methods in Fluid Dynamics*. Springer-Verlag, Berlin, Germany.

Cazemier, W., Verstappen, R. W. C. P. & Veldman, A. E. P. 1998 Proper orthogonal decomposition and low-dimensional models for driven cavity flows. *Phys. Fluids* **10** (7), 1685–1699.

Chakraborty, P., Balachandar, S. & Adrian, R. J. 2005 On the relationships between local vortex identification schemes. *J. Fluid Mech.* **535**, 189–214.

Charney, J. G., Fjørtoft, R. & Von Neumann, J. 1950 Numerical integration of the barotropic vorticity equation. *Tellus* **2** (4), 237–254.

Cherry, E. M., Elkins, C. J. & Eaton, J. K. 2008 Geometric sensitivity of three-dimensional separated flows. *Int. J. Heat Fluid Flow* **29** (3), 803–811.

Cherry, E. M., Elkins, C. J. & Eaton, J. K. 2009 Pressure measurements in a three-dimensional separated diffuser. *Int. J. Heat Fluid Flow* **30** (1), 1–2.

Cherry, E. M., Iaccarino, G., Elkins, C. J. & Eaton, J. K. 2006 Separated flow in a three-dimensional diffuser: preliminary validation. *CTR Annual Research Briefs* pp. 31–40.

Chevalier, M., Schlatter, P., Lundbladh, A. & Henningson, D. S. 2007 A Pseudo-Spectral Solver for Incompressible Boundary Layer Flows. *Tech. Rep.* TRITA-MEK 2007:07. Royal Institute of Technology (KTH), Dept. of Mechanics, Stockholm, Sweden.

Chong, M. S., Perry, A. E. & Cantwell, B. J. 1990 A general classification of three-dimensional flow fields. *Phys. Fluids A* **2** (5), 765–777.

Cousteix, J. & Mauss, J. 2007 *Asymptotic Analysis and Boundary Layers*. Springer-Verlag, Berlin, Germany.

Couzy, W. 1995 Spectral element discretization of the unsteady Navier–Stokes equations and its iterative solution on parallel computers. PhD thesis, École Polytechnique Fédérale de Lausanne, Switzerland.

Deville, M., Fischer, P. F. & Mund, E. 2002 *High-Order Methods for Incompressible Fluid Flow*. Cambridge University Press, Cambridge, UK.

Dubief, Y & Delcayre, F 2000 On coherent-vortex identification in turbulence. *J. Turbulence* **1**, 1–22.

Eaton, J. K. & Johnston, J. P. 1980 Turbulent flow reattachment - an experimental study of the flow and structure behind a backward-facing step. *Tech. Rep.* Rept MD-39. Thermosciences Division, Stanford Univ., USA.

Elkins, C. J., Markl, M., Pelc, N. & Eaton, J. K. 2003 4D magnetic resonance velocimetry for mean velocity measurements in complex turbulent flows. *Exp. Fluids* **34**, 494–503.

Etheridge, D. W. & Kemp, P. H. 1978 Measurements of turbulent flow downstream of a rearward-facing step. *J. Fluid Mech.* **86**, 545–566.

Fischer, P. & Mullen, J. 2001 Filter-based stabilization of spectral element methods. *C.R. Acad. Sci. Paris* **t. 332, Serie I**, p. 265–270.

Fischer, P. F. 1997 An overlapping Schwarz method for spectral element solution of the incompressible Navier–Stokes equations. *J. Comput. Phys.* **133** (1), 84–101.

Fischer, P. F. 1998 Projection techniques for iterative solution of with successive right-hand sides. *Comput. Methods Appl. Mech. Eng.* **163** (1–4), 193–204.

Fischer, P. F., Lottes, J., Pointer, D. & Siegel, A. 2008*a* Petascale algorithms for reactor hydrodynamics. *J. Phys. Conf. Series* **125**.

Fischer, P. F., Lottes, J. W. & Kerkemeier, S. G. 2008*b* nek5000 Web page. http://nek5000.mcs.anl.gov.

Friedrich, R. & Arnal, M. 1990 Analysing turbulent backward-facing step flow with the lowpass-filtered Navier-Stokes equations. *J. Wind Engng. Indust. Aerodyn.* **35**, 101 – 128.

Fromm, J. E. & Harlow, F. H. 1963 Numerical solution of the problem of vortex street development. *Phys. Fluids* **6** (7), 975–982.

Germano, M., Piomelli, U., Moin, P. & Chabot, W.H. 1991 A dynamic subgrid-scale eddy viscosity model. *Phys. Fluids* **3(7)**, 1760–1765.

Gilbert, N. & Kleiser, L. 1990 Near-wall phenomena in transition to turbulence. In *Near-Wall Turbulence* (ed. S.J. Kline & N.H. Afgan), pp. 7–27. 1988 Zoran Zarić Memorial Conference, New York, USA.

Gombosi, T. I. 1994 *Gaskinetic Theory*. Cambridge University Press, Cambridge, UK.

Henningson, D. S. & Åkervik, E. 2008 The use of global modes to understand transition and perform flow control. *Phys. Fluids* **20** (3), 031302.

Herbst, A. H., Schlatter, P. & Henningson, D. S. 2007 Simulations of turbulent flow in a plane asymmetric diffuser. *Flow Turbulence Combust.* **79**, 275–306.

Holmes, P., Lumley, J. & Berkooz, G. 1996 *Turbulence, Coherent Structures, Dynamical Systems and Symmetry*. Cambridge University Press, Cambridge, UK.

Huerre, P & Monkewitz, P. A. 1990 Local and global instabilities in spatially developing flows. *Annu. Rev. Fluid Mech.* **22** (1), 473–537.

Hunt, J. C. R., Wray, A. A. & Moin, P. 1988 Eddies, streams, and convergence zones in turbulent flows. In *Proceedings of the 1988 CTR Summer Program*, pp. 193–208.

Huser, A. & Biringen, S. 1993 Direct numerical simulation of turbulent flow in a square duct. *J. Fluid Mech.* **257**, 65–95.

Hussain, A. K. M. F. 1986 Coherent structures and turbulence. *J. Fluid Mech.* **173**, 303–356.

Iliescu, T. & Fischer, P.F. 2003 Large eddy simulation of turbulent channel flows by the rational large eddy simulation model. *Phys. Fluids* **15** (10), 3036–3047.

Jakirlić, S., Kadavelil, G., Kornhaas, M., Schäfer, M., Sternel, D.C. & Tropea, C. 2010*a* Numerical and physical aspects in LES and hybrid LES/RANS of turbulent flow separation in a 3-D diffuser. *Int. J. Heat Fluid Flow* **31** (5), 820 – 832.

Jakirlić, S., Kadavelil, G., Sirbubalo, E., Breuer, M., v. Terzi, D. & Borello, D. 2010*b* In *14th ERCOFTAC SIG15 Workshop on Refined Turbulence Modelling: Turbulent Flow Separation in a 3-D Diffuser*. *ERCOFTAC Bulletin*. December Issue 85, case 13.2 (1). ERCOFTAC.

Jeong, J. & Hussain, F. 1995 On the identification of a vortex. *J. Fluid Mech.* **285**, 69–94.

Jeong, J., Hussain, F., Schoppa, W. & Kim, J. 1997 Coherent structures near the wall in a turbulent channel flow. *J. Fluid Mech.* **332**, 185–214.

Jeyapaul, E. & Durbin, P. A. 2010 Three-dimensional turbulent flow separation in diffusers. In *48th AIAA Aerospace Sciences Meeting*. Orlando, Florida.

Jiménez, J. & Moin, P. 1991 The minimal flow unit in near-wall turbulence. *J. Fluid Mech.* **225**, 213–240.

Jiménez, J. & Pinelli, A. 1999 The autonomous cycle of near-wall turbulence. *J. Fluid Mech.* **389**, 335–359.

Kachanov, Y. S. 1994 Physical mechanisms of laminar-boundary-layer transition. *Annu. Rev. Fluid Mech.* **26** (1), 411–482.

Kaltenbach, H.-J. 1993 Large eddy simulation of flow in a plane, asymmetric diffuser. *CTR Annual Research Briefs* pp. 101–109.

Kaltenbach, H.-J., Fatica, M., Mittal, R., Lund, T.S. & Moin, P. 1999 Study of flow in a planar asymmetric diffuser using large-eddy simulation. *J. Fluid Mech.* **390**, 151–185.

Kaneda, Y., Ishihara, T., Yokokawa, M., Itakura, K. & Uno, A. 2003 Energy dissipation rate and energy spectrum in high resolution direct numerical simulations of turbulence in a periodic box. *Phys. Fluids* **15** (2), L21–L24.

Karamanos, G-S. & Karniadakis, G. E. 2000 A spectral vanishing viscosity method for large-eddy simulations. *J. Comput. Phys.* **163** (1), 22–50.

Karhunen, K. 1946 Zur Spektraltheorie stochastischer Prozesse. *Ann. Acad. Sci. Finnicae, Ser. A* **1**, 34.

Kasagi, N. 1998 Progress in direct numerical simulation of turbulent transport and its control. *Int. J. Heat Fluid Flow* **19** (2), 125–134.

Keating, A., Piomelli, U., Balaras, E. & Kaltenbach, H.-J. 2004 A priori and a posteriori tests of inflow conditions for large-eddy simulation. *Phys. Fluids* **16** (12), 4696–4712.

Kempf, A., Klein, M. & Janicka, J. 2005 Efficient generation of initial- and inflow-conditions for transient turbulent flows in arbitrary geometries. *Flow Turbulence Combust.* **74** (1), 67–84.

Kim, J., Moin, P. & Moser, R. 1987 Turbulence statistics in fully developed channel flow at low reynolds number. *J. Fluid Mech.* **177**, 133–166.

Kirby, R. M. & Karniadakis, G. E. 2003 De-alising on non-uniform grids: algorithms and applications. *J. Comput. Phys.* **191**, 249–264.

Kiya, M. & Sasaki, K. 1985 Structure of large-scale vortices and unsteady reverse flow in the reattaching zone of a turbulent separation bubble. *J. Fluid Mech.* **154**, 463–491.

Kline, S. J., Reynolds, W. C., Schraub, F. A. & Runstadler, P. W. 1967 The structure of turbulent boundary layers. *J. Fluid Mech.* **30**, 741–773.

Kundu, P.K. & Cohen, I.M. 2008 *Fluid Mechanics*. Academic Press, San Diego, USA.

Landahl, M. T. 1980 A note on an algebraic instability of inviscid parallel shear flow. *J. Fluid Mech.* **98**, 243–251.

Lawson, N. J. & Davidson, M. R. 2001 Self-sustained oscillation of a submerged jet in a thin rectangular cavity. *J. Fluid Struct.* **15** (1), 59 – 81.

Le, H. & Moin, P. 1994 Direct numerical simulation of turbulent flow over a backward-facing step. *Tech. Rep.* TF-58. Dept. Mech. Eng., Stanford University, USA.

Le, H., Moin, P. & Kim, J. 1997 Direct numerical simulation of turbulent flow over a backward-facing step. *J. Fluid Mech.* **330**, 349–374.

Lee, S., Fischer, P. F., Bassiouny, H. & Loth, F. 2008 Direct numerical simulation of transitional flow in a stenosed carotid bifurcation. *J. Biomech.* **41**, 2551–2561.

Lee, S., Lele, S. & Moin, P. 1992 Simulation of spatially evolving turbulence and the applicability of Taylor's hypothesis in compressible flow. *Phys. Fluids* **A4**, 1521–1530.

Leveque, R. J. 2002 *Finite Volume Methods for Hyperbolic Problems*. Cambridge University Press, Cambridge, UK.

Lilly, D. K. 1992 A proposed modification of the Germano subgrid-scale closure method. *Phys. Fluids* **4** (3), 633–635.

Loève, M. 1955 *Probability Theory*. Van Nostrand, Princeton, USA.

Lorenz, E. N. 1956 Empirical orthogonal functions and statistical weather prediction. *Tech. Rep.* Statistical Forecasting Project. Dept. of Meteorology, MIT.

Lottes, J. W. & Fischer, P. F. 2005 Hybrid multigrid/schwarz algorithms for spectral element method. *J. Sci. Comput.* **24**, 45–78.

Lumley, J. L. 1967 The structure of inhomogeneous turbulent flows. In *Atm. Turb. Radio Wave Prop.* (ed. A. M. Yaglom & V. I. Tatarsky), pp. 166–178. Nauka, Moscow, Russia.

Lund, T. S., Wu, X. & Squires, D. 1998 Generation of turbulent inflow data for spatially-developing boundary layer simulations. *J. Comput Phys.* **140**, 233.

Lygren, M. & Andersson, H. 1999 Influence of boundary conditions on the large scale structures in turbulent plane couette flow. In *Turbulence and Shear Flow Phenomena 1* (ed. S. Banerjee & J. Eaton), pp. 15–20. Santa Barbara, California: Begell House, New York, USA.

Lynch, P. 2008 The origins of computer weather prediction and climate modeling. *J. Comput. Phys.* **227** (7), 3431 – 3444.

Lynch, R., Rice, J. & Thomas, D. 1964 Direct solution of partial difference equations by tensor product methods. *Numer. Math.* **6**, 185–199.

Ma, X. & Karniadakis, G. E. 2002 A low-dimensional model for simulating three-dimensional cylinder flow. *J. Fluid Mech.* **458**, 181–190.

Maday, Y. & Patera, A. 1989 Spectral element methods for the Navier–Stokes equations. In *State of the Art Surveys in Computational Mechanics* (ed. A.K. Noor), pp. 71–143. ASME.

Maday, Y., Patera, A. T. & Rønquist, E. M. 1990 An operator-integration-factor splitting method for time-dependent problems: application to incompressible fluid flow. *J. Sci. Comput.* **5** (4), 263–292.

Maday, Y. & Rønquist, E. M. 1990 Optimal error analysis of spectral methods with emphasis on non-constant coefficients and deformed geometries. *Comput. Methods Appl. Mech. Eng.* **80** (1-3), 91–115.

Madré, T. K. 2011 Turbulence transition in the asymptotic suction boundary layer. Diplomarbeit, Philipps-Universität, Marburg, Germany.

Manhart, M. & Wengle, H. 1993 A spatiotemporal decomposition of a fully inhomogeneous turbulent flow field. *Theor. Comput. Fluid Dyn.* **5**, 223–242.

Maurel, A., Ern, P., Zielinska, B. J. A. & Wesfreid, J. E. 1996 Experimental study of self-sustained oscillations in a confined jet. *Phys. Rev. E* **54** (4), 3643–3651.

Moin, P. & Kim, J. 1997 Tackling turbulence with supercomputers. *Scientific American* **276** (1), 62–68.

Moin, P. & Mahesh, K. 1998 Direct numerical simulation: A tool in turbulence research. *Annu. Rev. Fluid Mech.* **30** (1), 539–578.

Moin, P. & Moser, R. 1989 Characteristic-eddy decomposition of turbulence in a channel. *J. Fluid Mech.* **200**, 471–509.

Moore, G. E. 1965 Cramming more components onto integrated circuits. *Electronics* **38** (8), 114–117.

Moreno, D., Krothapalli, A., Alkislar, M. B. & Lourenco, L. M. 2004 Low-dimensional model of a supersonic rectangular jet. *Phys. Rev. E* **69** (2), 026304.

Moser, R. D., Kim, J. & Mansour, N. 1999 Direct numerical simulation of turbulent channel flow up to $\mathrm{Re}_\tau = 590$. *Phys. Fluids* **11** (4), 943–945.

Na, Y. & Moin, P. 1998 Direct numerical simulation of a separated turbulent boundary layer. *J. Fluid Mech.* **374**, 379–405.

Nikuradse, J. 1926 Untersuchungen über die Geschwindigkeitsverteilung in turbulenten Strömungen. PhD thesis, Göttingen, Germany.

Noack, B. R., Schlegel, M., Morzyński, M. & Tadmor, G. 2010 System reduction strategy for galerkin models of fluid flows. *Int. J. Numer. Meth. Fluid* **63** (2), 231–248.

Nomura, K.K. & Post, G.K. 1998 The structure and dynamics of vorticity and rate of strain in incompressible homogeneous turbulence. *J. Fluid Mech.* **377**, 65–97.

Nordström, J., Nordin, N. & Henningson, D. S. 1999 The fringe region technique and the fourier method used in the direct numerical simulation of spatially evolving viscous flows. *SIAM J. Sci. Comput.* **20**, 1365–1393.

Obi, S., Nikaido, H. & Masuda, S. 1993 Experimental and computational study of turbulent separating flow in an asymmetric diffuser. In *Proceedings of the Ninth Symposium on Turbulent Shear Flows*, pp. 305.1–305.4.

Ohlsson, J., Schlatter, P., Fischer, P. F. & Henningson, D. S. 2010 Direct numerical simulation of separated flow in a three-dimensional diffuser. *J. Fluid Mech.* **650**, 307–318.

Örlü, R. & Alfredsson, P. H. 2010 On spatial resolution issues related to time-averaged quantities using hot-wire anemometry. *Exp. Fluids* **49**, 101–110.

Örlü, R., Fransson, J. H. M. & Alfredsson, P. H. 2010 On near wall measurements of wall bounded flows–The necessity of an accurate determination of the wall position. *Prog. in Aeros. Sci.* **46** (8), 353–387.

Orszag, S. A. 1972 Comparison of pseudospectral and spectral approximations. *Stud. Appl. Math.* **51**, 253–259.

Orszag, S. A. & Patterson, G. S. 1972 Numerical simulation of three-dimensional homogeneous isotropic turbulence. *Phys. Rev. Lett.* **28** (2), 76–79.

Pasquetti, R. 2006 Spectral vanishing viscosity method for large-eddy simulation of turbulent flows. *J. Sci. Comput.* **27** (1-3), 365–375.

Patera, A. T. 1984 A spectral element method for fluid dynamics: Laminar flow in a channel expansion. *J. Comput. Phys.* **54**, 468–488.

Pearson, K. 1901 On lines and planes of closest fit to systems of points in space. *Philosophical Magazine* **2** (6), 559–572.

Perot, J. B. 1993 An analysis of the fractional step method. *J. Comput. Phys.* **108**.

Piquet, J. 1999 *Turbulent Flows: Models and Physics*. Springer-Verlag, Berlin, Germany.

Pond, S. & Pickard, G. L. 1983 *Introductory Dynamical Oceanography*, 2nd edn. Pergamon, Oxford, UK.

Pope, S. 2000 *Turbulent Flows*. Cambridge University Press, New York, USA.

Prandtl, L. 1924 The mechanics of viscous fluids. In *Aerodynamic Theory* (ed. W. F. Durand), pp. 34–208. Springer, Berlin, Germany.

Pujals, G., García-Villalba, M., Cossu, C. & Depardon, S. 2009 A note on optimal transient growth in turbulent channel flows. *Phys. Fluids* **21** (1), 015109.

Robinson, S. K 1991 Coherent motions in the turbulent boundary layer. *Annu. Rev. Fluid Mech.* **23**, 601–639.

Rowley, C. W. 2005 Model reduction for fluids, using balanced proper orthogonal decomposition. *Int. J. Bifurc. Chaos* **15** (3), 997–1013.

Rowley, C. W., Colonius, T. & Murray, R. M. 2004 Model reduction for compressible flows using POD and Galerkin projection. *Physica D: Nonlinear Phenomena* **189**, 115–129.

Rowley, C. W., Mezić, I, Bagheri, S, Schlatter, P & Henningson, D. S. 2009 Spectral analysis of nonlinear flows. *J. Fluid Mech.* **641**, 115–127.

Ruhe, A. 1984 Rational Krylov sequence methods for eigenvalue computation. *Linear Algebr. Appl.* **58**, 391–405.

Runge, C. 1901 Über empirische Funktionen und die Interpolation zwischen äquidistanten Ordinaten. *Z. für Math. Phys.* **46**, 224–243.

Sagaut, P. 2006 *Large Eddy Simulation for Incompressible Fluid Flow*. Springer-Verlag Berlin, Germany.

Sandham, N. D. & Kleiser, L. 1992 The late stages of transition to turbulence in channel flow. *J. Fluid Mech.* **245**, 319–348.

Schetz, J. A. & Fuhs, A. E. 1999 *Fundamentals of Fluid Mechanics*. Wiley, Hoboken, USA.

Schlatter, P., Bagheri, S. & Henningson, D. S. 2011*a* Self-sustained global oscillations in a jet in crossflow. *Theor. Comput. Fluid Dyn.* **25**, 129–146.

Schlatter, P., Malm, J., Brethouwer, G., Johansson, A. V. & Henningson, D. S. 2011*b* Large-scale simulations of turbulence: HPC and numerical experiments. In *7th IEEE Conference on e-Science*. To appear.

Schlatter, P. & Örlü, R. 2010 Assessment of direct numerical simulation data of turbulent boundary layers. *J. Fluid Mech.* **659**, 116–126.

Schlatter, P., Örlü, R., Li, Q., Brethouwer, G., Fransson, J. H. M., Johansson, A. V., Alfredsson, P. H. & Henningson, D. S. 2009 Turbulent boundary layers up to $Re_\theta = 2500$ studied through numerical simulation and experiments. *Phys. Fluids* **21** (5), 051702.

Schlatter, P., Stolz, S. & Kleiser, L. 2004 LES of transitional flows using the approximate deconvolution model. *Int. J. Heat Fluid Flow* **25** (3).

Schmid, P. J. 2010 Dynamic mode decomposition of numerical and experimental data. *J. Fluid Mech.* **656**, 5–28.

Schneider, H., Terzi, D. A., Bauer, H-J & Rodi, W. 2011 A mechanism for control of turbulent separated flow in rectangular diffusers. *J. Fluid Mech.* **687**, 584–594.

Schneider, H., Terzi, D. A. & Rodi, W. 2009 Reliable and accurate prediction of three-dimensional separation in asymmetric diffusers using large-eddy simulation. In *Proceedings of ASME Turbo Expo 2009: Power for Land, Sea and Air*. Orlando, USA.

Schneider, T. M., Eckhardt, B. & Yorke, J. A. 2007 Turbulence transition and the edge of chaos in pipe flow. *Phys. Rev. Lett.* **99** (3), 034502.

Schrauf, G. 2005 Status and perspectives of laminar flow. *Aeronaut. J.* **109** (1102), 639–644.

She, Z.-S., Jackson, E. & Orszag, S. A. 1991 Structure and dynamics of homogeneous turbulence: Models and simulations. *Proc. R. Soc. Lond.* **434** (1890), pp. 101–124.

Sherwin, S. & Karniadakis, G. 1995 A triangular spectral element method; applications to the incompressible Navier–Stokes equations. *Comput. Methods Appl. Mech. Engng.* **123**, 189.

Simens, M. P., Jiménez, J., Hoyas, S. & Mizuno, Y. 2009 A high-resolution code for turbulent boundary layers. *J. Comput. Phys.* **228** (11), 4218–4231.

Simpson, R. L. 1981 A review of some phenomena in turbulent flow separation. *J. Fluid Engng.* **102**, 520–533.

Simpson, R. L. 1989 Turbulent boundary-layer separation. *Annu. Rev. Fluid Mech.* **21** (1), 205–232.

Sirovich, L. 1987 Turbulence and the dynamics of coherent structures, i-iii. *Quart. Appl. Math.* **45**, 561–590.

Sirovich, L. 1989 Chaotic dynamics of coherent structures. *Physica D: Nonlinear Phenomena* **37**, 126–145.

Sirovich, L., Kirby, M. & Winter, M. 1990 An eigenfunction approach to large scale transitional structures in jet flow. *Phys. Fluids* **2** (2), 127–136.

Skote, M. & Henningson, D. S. 2002 Direct numerical simulation of a separated turbulent boundary layer. *J. Fluid Mech.* **471**, 107–136.

Smagorinsky, J. 1963 General circulation experiments with the primitive equations: I. The basic experiment. *Mon. Weather Rev.* **91**, 99–164.

Spalart, P. R & Leonard, A. 1985 Direct numerical simulation of equilibrium turbulent boundary layers. In *5th Symp. on Turbulent Shear Flows*. Ithaca, New York, USA.

Spille-Kohoff, A. & Kaltenbach, H.-J. 2001 Generation of turbulent inflow data with a prescribed shear-stress profile. In *DNS/LES Progress and Challenges* (ed. C. Liu, L. Sakell & T. Beutner). Third AFSOR conference on DNS and LES, Arlington, Texas: Greyden Press, Columbus, USA.

Stanley, S., Sarkar, S. & Mellado, J. 2002 A study of the flow field evolution and mixing in a planar turbulent jet using direct numerical simulations. *J. Fluid Mech.* **450**, 377–407.

Steiner, H., Jakirlić, S., Kadavelil, G., Manceau, M., Saric, S. & Brenn, G. 2009 In *13th ERCOFTAC SIG15 Workshop on Refined Turbulence Modelling: Turbulent Flow Separation in a 3-D Diffuser*. *ERCOFTAC Bulletin.* Issue 79, case 13.2 (1). ERCOFTAC.

Succi, S. 2001 *The lattice Boltzmann equation for fluid dynamics and beyond*. Oxford University Press, New York, USA.

Tadmor, E. 1989 Convergence of spectral methods for nonlinear conservation laws. *SIAM J. Numer. Anal.* **26** (1), 30–44.

Theofilis, V. 2011 Global linear instability. *Annu. Rev. Fluid Mech.* **43** (1), 319–352.

Tomboulides, A. & Orszag, S. 2000 Numerical investigation of transitional and weak turbulent flow past a sphere. *J. Fluid Mech.* **416**, 45–73.

Tomboulides, A. G., Lee, J. C. Y. & Orszag, S. A. 1997 Numerical simulation of low mach number reactive flows. *J. Sci. Comput.* **12** (2), 139–167.

Törnblom, O., Lindgren, B. & Johansson, A. V. 2009 The separating flow in

a plane asymmetric diffuser with 8.5° opening angle: mean flow and turbulence statistics, temporal behaviour and flow structures. *J. Fluid Mech.* **636**, 337–370.

Trefethen, L. N. & Bau, D. 1997 *Numerical Linear Algebra*. SIAM, Philadelphia, USA.

Tropea, Y., Yarin, A. & F., Foss. J. 2007 *Handbook of Experimental Fluid Mechanics*. Springer-Verlag, Berlin, Germany.

Tsuji, Y., Fransson, J. H. M., Alfredsson, P. H. & Johansson, A. V. 2007 Pressure statistics and their scaling in high-Reynolds-number turbulent boundary layers. *J. Fluid Mech.* **585**, 1–40.

Tufo, H. & Fischer, P.F. 1999 Terascale spectral element algorithms and implementations. In *Proceedings of the ACM/IEEE SC99 Conference on High Performance Networking and Computing, Portland, USA*.

Tufo, H. M. & Fischer, P. F. 2001 Fast parallel direct solvers for coarse grid problems. *J. Parallel Distrib. Comput.* **61** (2), 151–177.

Villermaux, E. & Hopfinger, E. J. 1994 Self-sustained oscillations of a confined jet: a case study for the non-linear delayed saturation model. *Physica D: Nonlinear Phenomena* **72** (3), 230–243.

Vos, P. E. J., Sherwin, S. J. & Kirby, R. M. 2010 From h to p efficiently: Implementing finite and spectral/hp element methods to achieve optimal performance for low- and high-order discretisations. *J. Comput. Phys.* **229** (13), 5161 – 5181.

Waleffe, F. 1997 On a self-sustaining process in shear flows. *Phys. Fluids* **9** (4), 883–900.

Wang, C., Jang, Y.J. & Leschziner, M.A. 2004 Modelling two- and three-dimensional separation from curved surfaces with anisotropy-resolving turbulence closures. *Int. J. Heat Fluid Flow* **25** (3), 499–512.

Wasberg, C. E., Gjesdal, T., Reif, B. A. P. & Andreassen, Ø. 2009 Variational multiscale turbulence modelling in a high order spectral element method. *J. Comput. Phys.* **228** (19), 7333–7356.

Webber, G. A., Handler, R. A. & Sirovich, L. 1997 The Karhunen–Loève decomposition of minimal channel flow. *Phys. Fluids* **9** (4), 1054–1066.

Wilcox, D. C. 1998 *Turbulence Modeling for CFD*. DCW Industries, La Cañada, USA.

Williams, J. C. 1977 Incompressible boundary-layer separation. *Annu. Rev. Fluid Mech.* **9** (1), 113–144.

Xu, C. 2006 Stabilization methods for spectral element computations of incompressible flows. *J. Sci. Comput.* **27** (1-3), 495–505.

Part II

Papers

1

Paper 1

The spectral-element and pseudo-spectral methods: A comparative study

By Johan Ohlsson*, Philipp Schlatter*, Catherine Mavriplis† and Dan S. Henningson*

*Linné FLOW Centre, Swedish e-Science Research Centre (SeRC)
KTH Mechanics, 100 44 Stockholm, Sweden

†Department of Mechanical Engineering, University of Ottawa, Ottawa, Canada

Spectral and High Order Methods for Partial Differential Equations, LNCSE **76**, 459–468, 2011

Turbulent and transitional channel flow simulations have been performed in order to assess the differences concerning speed and accuracy in the pseudo-spectral code `simson` and the spectral-element code `nek5000`. The results indicate that the pseudo-spectral code is 4–6 times faster than the spectral-element code in fully turbulent channel flow simulations, and up to 10–20 times faster when taking into account the more severe CFL restriction in the spectral-element code. No particular difference concerning accuracy could be noticed neither in the turbulent nor the transitional cases, except for the pressure fluctuations at the wall which converge slower for the spectral-element code.

1. Introduction

The simulation of fluid flows — sensitive and often complicated — puts large requirements on the numerical method. Due to the nonlinear nature of the flow, accuracy may be one of the most important ingredients. In particular for direct simulation of complex multiscale flows, such as transitional and turbulent flows, high order methods are preferred. However, the choice of methods, *e.g.* fully spectral, multidomain spectral such as spectral-element, or compact differences, is not clear as trade-offs exist between computational efficiency, geometrical flexibility and accuracy. Proper comparisons in terms of speed and accuracy are sorely needed. In order to quantify differences and similarities between high-order methods in a more systematic way, we have chosen to compare two well established codes based on the Chebyshev-Fourier pseudo-spectral method (`simson`, Chevalier *et al.* 2007) and the spectral-element method (`nek5000`, Fischer *et al.* 2008*b*). While the grid is essentially prescribed by the order for the pseudo-spectral method, a more flexible point distribution is possible in the spectral-element method. In order to concentrate the comparison on relative efficiency, we have chosen canonical test cases like turbulent and transitional

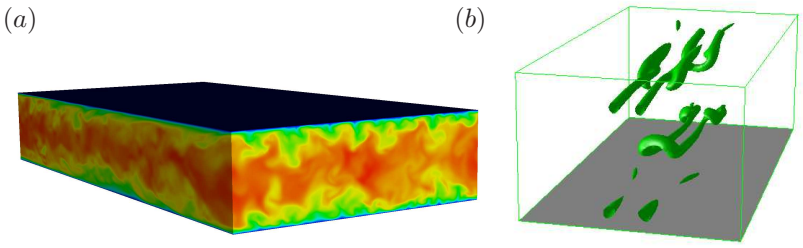

FIGURE 1. The canonical flow cases investigated: (a) snapshot of turbulent channel flow at $Re_\tau = 180$ showing pseudo-color of streamwise velocity and (b) temporal K-type transition showing the hairpin vortex (isosurfaces of λ_2, Jeong & Hussain 1995) emerging at $t = 135$

channel flow, in which the effect of the point distribution might be considerably less crucial for achieving high accuracy.

2. Study setup

The study is divided into two parts: Part A is concerned with the computational efficiency in terms of the wall-clock time per time step and part B deals with accuracy, aiming at establishing a way to compare the number of grid points needed to compute a given turbulent or transitional quantity with comparable accuracy. In the first part of the study, turbulent channel flow simulations at a Reynolds number of $Re_\tau = 180$, based on friction velocity, u_τ, and channel half height, h, were considered in a domain of size comparable to that by Moser *et al.* (1999). Two different resolutions called r1 and r2 were simulated (~ 43 and 95 grid points in each direction respectively). For the spectral-element code this was achieved by fixing the polynomial order (7th) and varying the number of elements (6 and 12 in each direction). It was noted that by using polynomial order 7 instead of 11 for the spectral-element simulations increases the speed by ~ 15 % per time step. In order to make the comparison as fair as possible, the order of the temporal scheme was synchronized so that a third order time discretization was used in both codes. Also, the scalings were adapted so that Re in both codes were based on $Re_b = u_b h/\nu = 2800$, where u_b is the bulk velocity and h is the channel half height. Timings were made in serial mode (one core AMD 3.0 GHz) on the same computer. Dealiasing was used in both codes.

In the second part of the study K-type transition similar to Schlatter *et al.* (2004) and turbulent channel flow similar to Moser *et al.* (1999) at $Re_\tau = 180$, based on friction velocity, u_τ, and channel half height, h, were simulated for a number of different resolutions, given in Table 2. It should be pointed out that the two lowest resolution spectral-element cases had to be stabilized by a filtering procedure described in Fischer & Mullen (2001).

TABLE 1. Overview of the different resolutions in terms of degrees of freedom (dof) used in the present study. Two different polynomial orders were used for the spectral-element simulations. The number of degrees of freedom was matched as closely as possible for all cases.

Fully spectral	24^3	40^3	80^3	128^3	160^3
Spectral-element (7th/11th)	29^3	$43^3/45^3$	$85^3/78^3$	$127^3/122^3$	$155^3/155^3$

Snapshots from each of these two cases are shown in figure 1. Important measures such as the time and amplitude for the skin-friction peak were computed for the transitional cases, whereas mean velocity profile, Reynolds stresses, pressure and pressure fluctuations together with integral quantities such as Re_τ, shape factor and 'point measures', *e.g.* $\max(u_{rms})$, were computed and compared for the turbulent cases.

3. Results

3.1. *Part A: Efficiency*

The wall-clock time per iteration, *i.e.* one full time step using the largest possible time step for the spectral-element code and one full Runge Kutta time step (containing four sub-steps) for the pseudo-spectral code, was measured and is reported in figure 2(a) below. It can be seen that the lines diverge, *i.e.* the spectral code gets relatively faster for larger problem sizes, due to the increasingly efficient fast Fourier transforms (FFT). In particular, the spectral code is 4–6 times faster for these two problem sizes. In addition, we show wall-clock time per unit time in figure 2(b), where it can be seen that the spectral code is 10–20 times faster due to the more severe CFL restriction in the spectral-element code, arising from the clustering of the Gauss-Lobatto-Legendre points close to each element boundary.

3.2. *Part B: Accuracy in transitional flow simulations*

The Reynolds number based on friction velocity, Re_τ, was computed as a function of time, t, for all cases in Table 2 during K-type transition (Schlatter *et al.* 2004) and shown in figure 3. We note that the most underresolved cases lead to a premature transition, also noted by other authors, followed by an overprediction of the skin-friction in the fully turbulent phase. This is more pronounced in the fully spectral results, which is probably due to the fact that the two most underresolved spectral-element cases had to be stabilized by the filter, which in some sense acts like a simple subgrid scale (SGS) model. For higher resolutions, the two codes converge (from below) to the correct Re_τ for essentially the same number of degrees of freedom, as also seen in figure 4. This behavior indicates that the initial stages of transition are essentially a low-order

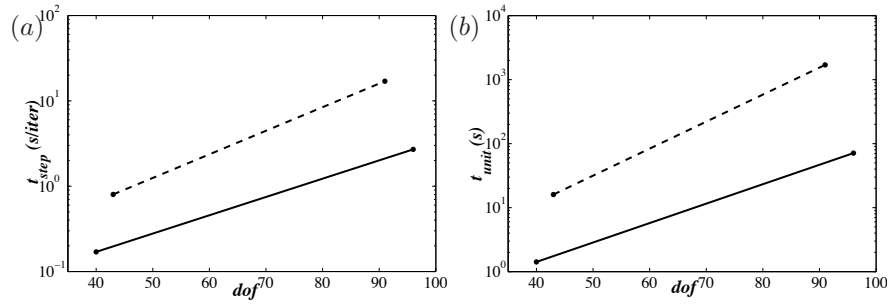

FIGURE 2. Comparison with respect to time advancement in a turbulent channel flow simulation between the spectral-element code (polynomial order 7) (----) and the pseudo-spectral code (———) for the two different resolutions r1 and r2 (degrees of freedom in each direction). (*a*) Wall-clock time per iteration, (*b*) wall-clock time per unit time.

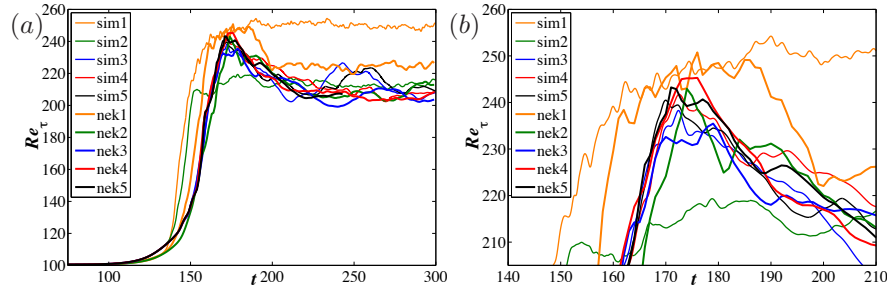

FIGURE 3. (*a*) Skin-friction Reynolds number Re_τ as a function of time, t, computed for all cases shown in Table 2, where sim1-sim5 and nek1-nek5 corresponds to increasing resolutions of the pseudo-spectral and spectral-element codes respectively, (*b*) close-up view of the peak in (*a*).

phenomenon, not requiring full resolution. Thus, the third highest resolution (80^3) yields accurate results.

3.3. *Part B: Accuracy in turbulent flow simulations*

The turbulent mean velocity profile at $Re_\tau = 180$ is shown for all cases in figure 5. The most underresolved cases in both the fully spectral (*a*) and the spectral-element (*b*) code show the same tendency to underpredict the velocity in the log region, which is related mainly to the scaling given by an overpredicted friction velocity, u_τ, since indeed $u^+ = \langle u \rangle / u_\tau$. In a close-up view of the log region (figure 5*c*), where only the three highest resolution cases (80^3, 128^3,

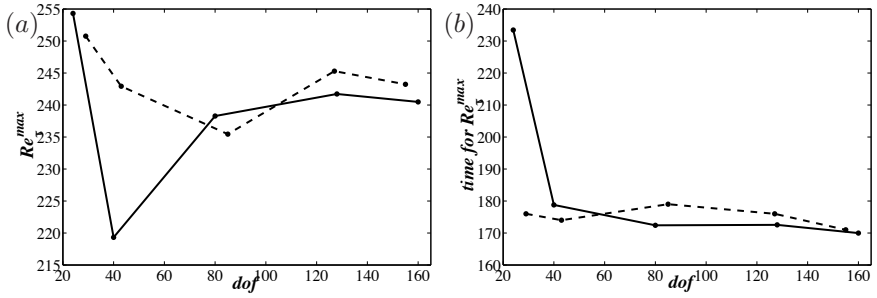

FIGURE 4. (*a*) Skin-friction peak as a function of number of degrees of freedom (in each direction) for the spectral-element code (- - - -) and the pseudo-spectral code (———). (*b*) Time when the peak in (*a*) occurs.

160^3 and 7th order for the spectral-element code) are shown, convergence is seen for the two codes for the same number of degrees of freedom (shown by an arrow). The 128^3 cases are converged and the 160^3 cases do not improve the results further. The spatial distribution of the Reynolds stresses is examined in figure 6. While the fully spectral results capture the peaks correctly when compared to the direct numerical results (DNS) of Moser *et al.* (1999), even for the most underresolved cases, the skin-friction Reynolds number is strongly over-predicted as noted in the transitional simulations. This is in contrast to the spectral-element results, where the peaks are overpredicted for all normal stress components but the skin-friction Reynolds number is only mildly overpredicted. A close-up view of the spectral-element results is shown in figure 6(*c*), where the peak u_{rms} is shown to converge in a zig-zag pattern (indicated by arrows): first, overpredicted for the lowest resolutions, then, underpredicted for intermediate resolutions, and finally, converging to the reference data for the same number of degrees of freedom. A similar but less pronounced zig-zag pattern is seen for the spectral results. The pressure fluctuations (figure 7) from the spectral simulations are fairly good at the wall, whereas those in the channel center are overpredicted. The spectral-element results show the opposite behavior: the fluctuations at the wall are overpredicted, whereas the those in the core of the flow are in fairly good agreement with the reference data. A close-up view reveals that the spectral-element code needs more points (roughly double) than the fully spectral code to converge the pressure fluctuations at the wall (figure 7(*d*)), which would make the spectral code around 40 times faster. The reasons for this may be that in a $\mathbb{P}_N - \mathbb{P}_{N-2}$ spectral-element method (Maday & Patera 1989) the number of degrees of freedom for the pressure is less than the velocities and thus less than for the corresponding pressure resolution in the spectral simulation. Another reason may be the absence of a pressure node at the wall in the spectral-element $\mathbb{P}_N - \mathbb{P}_{N-2}$ formulation, leading to reduced control of the pressure at the wall. Finally, we compare turbulent integral

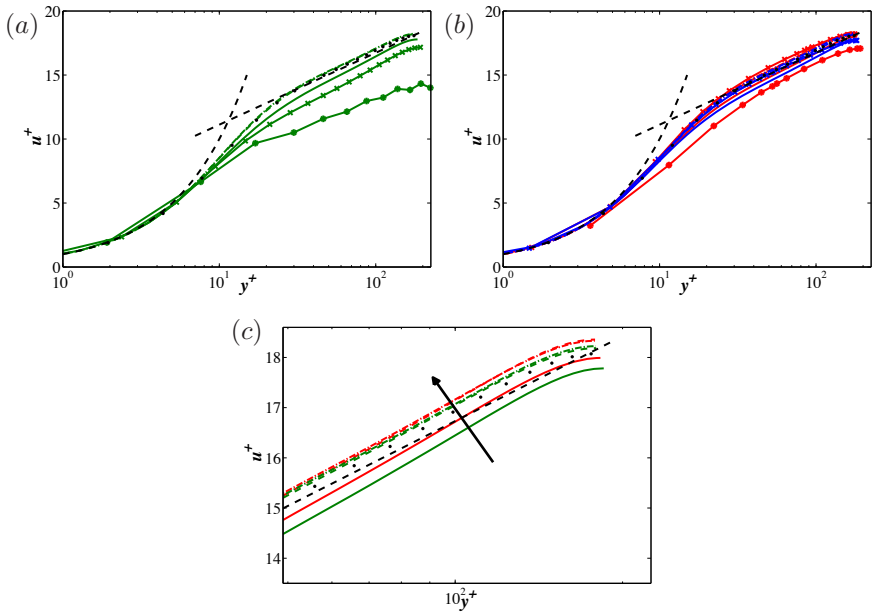

FIGURE 5. Turbulent mean velocity profiles for (a) the spectral code (*green*), (b) the spectral-element code (*blue*: 11th order, *red*: 7th order) and (c) the three highest resolutions of the spectral and spectral-element (7th order) simulations. $-*-(24^3)$, $-\times-(40^3)$, ——— (80^3), - - - - (128^3), $-\cdot-(160^3)$, ····· direct numerical simulation (DNS) of Moser *et al.* (1999).

quantities such as actual Re_τ and 'point measures' such as $\max(u_{rms})$. The actual Re_τ (given as a simulation result when constant mass-flux is prescribed) is shown in figure 8(a), where an overestimation of the Re_τ for the lowest resolution cases in the fully spectral simulations already mentioned can be seen. Similarly, the zig-zag pattern described in section 3.3 for the peak u_{rms} is seen in figure 8(b). For both quantities, convergence seems to follow the same 'slope' for the two codes, as well as for the two different orders in the spectral-element simulations.

4. Conclusions

The present results indicate that the pseudo-spectral code is 4–6 times faster than the spectral-element code in fully turbulent channel flow simulations. Taking into account the more severe CFL restriction in the spectral-element method due to the clustering of the points near the element boundaries, this number rises to 10–20. For higher resolutions, the spectral code is relatively faster, due to the increasing efficiency of the FFTs as the order increases. Of all the turbulent and transitional quantities computed, there seems to be no favor to

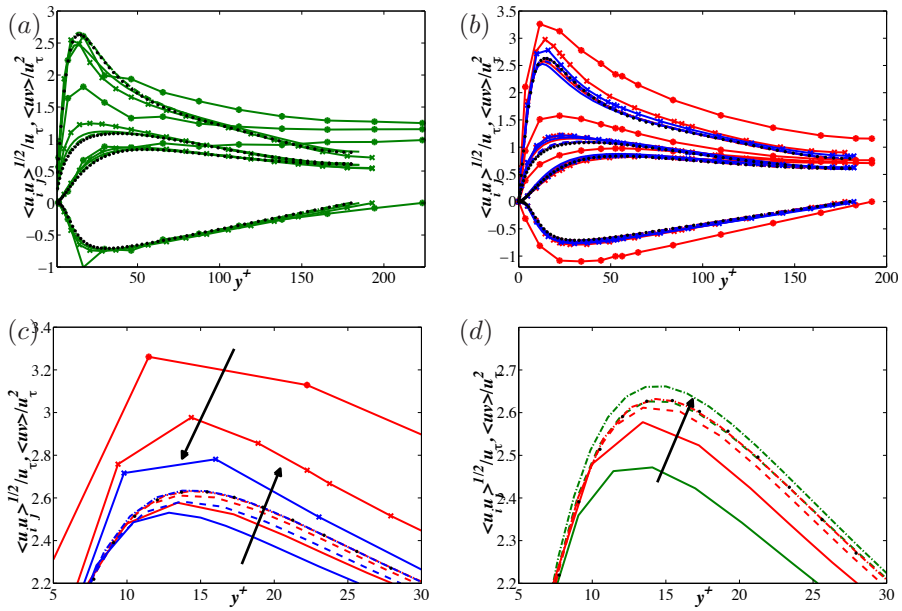

FIGURE 6. Reynolds stresses for (*a*) the spectral code (*green*), (*b*) the spectral-element code (*blue*: 11th order, *red*: 7th order), (*c*) close-up view of the u_{rms} peak in (*b*) and (*d*) the three highest resolutions of the spectral and spectral-element (7th order) simulations. $-*-(24^3)$, $-\times-(40^3)$, ——— (80^3), - - - - (128^3), $-\cdot-(160^3)$, ····· DNS of Moser *et al.* (1999).

any particular method (or order in the spectral-element code) and quantities such as shape factor, Re_τ, $\max(u_{rms})$ and skin-friction peak exhibit the same 'convergence-rate'. The exception seems to be the pressure fluctuations close to the wall which did converge faster in the spectral code. Taking this into account the spectral code may be around 40 times faster. Moreover, by using polynomial order 7 instead of 11 for the spectral-element simulations increases the speed by ~ 15 % per time step which, in addition to the larger time step that can be achieved with a lower order, seems to be a better choice in general.

Naturally, for canonical flows such as channel flows fully spectral methods are superior due to their near optimal point distribution. But it should be noted that being faster on one CPU does not necessarily mean a faster code. For example, taking into account that a spectral-element code performs spectrally in local elements, this method has an enormous parallel scalability and might be faster than spectral codes for very large cases. Moreover, as we progress away from canonical flows towards more complex geometry flows (see *e.g.* Fischer

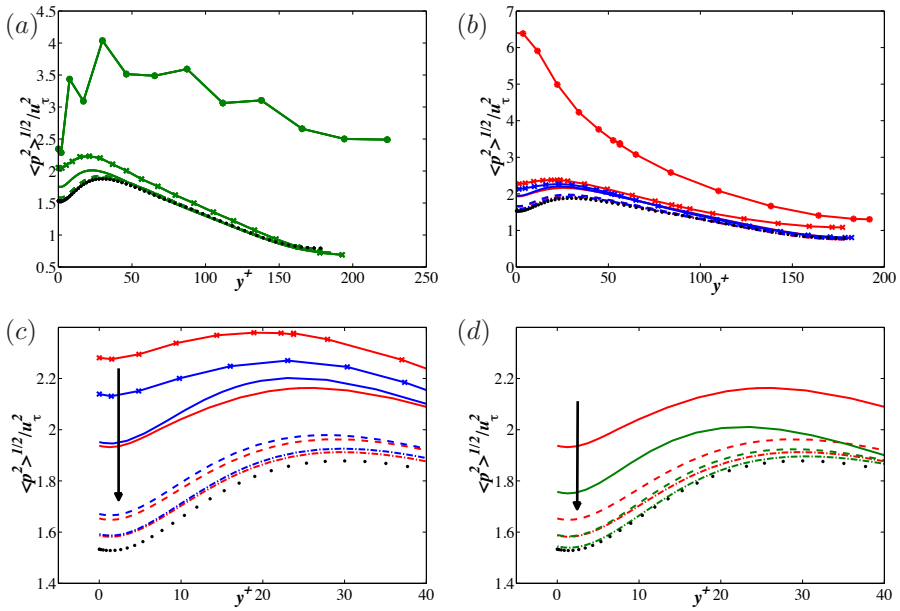

FIGURE 7. Pressure fluctuations for (*a*) the spectral code (*green*), (*b*) the spectral-element code (*blue*: 11th order, *red*: 7th order), (*c*) close-up view of (*b*) close to the wall and (*d*) the three highest resolutions of the spectral and spectral-element (7th order) simulations close to the wall. $-*-(24^3)$, $-\times-(40^3)$, ——— (80^3), - - - - (128^3), $-\cdot-(160^3)$, ····· DNS of Moser *et al.* (1999).

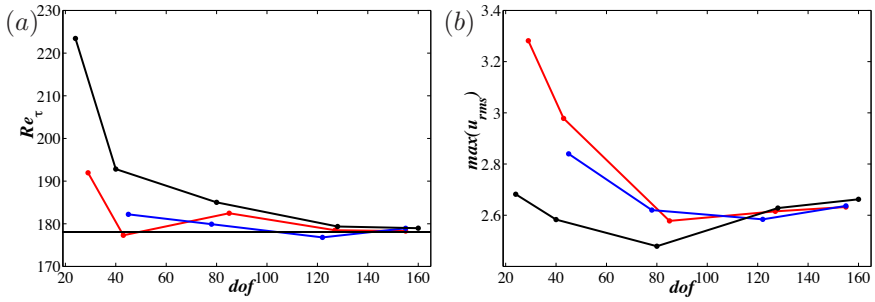

FIGURE 8. (*a*) Computed Re_τ and (*b*) max(u_{rms}) as a function of number of degrees of freedom for the pseudo-spectral code (*black*) and and different polynomial orders for the spectral-element code (*blue*: 11th order, *red*: 7th order). ——— DNS of Moser *et al.* (1999).

et al. 2008*a*) such as real aircraft wing geometries, the geometrical flexibility of the spectral-element approach will be favored over the pseudo-spectral approach.

References

Chevalier, M., Schlatter, P., Lundbladh, A. & Henningson, D. S. 2007 A Pseudo-Spectral Solver for Incompressible Boundary Layer Flows. *Tech. Rep.* TRITA-MEK 2007:07. Royal Institute of Technology (KTH), Dept. of Mechanics, Stockholm, Sweden.

Fischer, P. & Mullen, J. 2001 Filter-based stabilization of spectral element methods. *C.R. Acad. Sci. Paris* **t. 332, Serie I**, p. 265–270.

Fischer, P. F., Lottes, J., Pointer, D. & Siegel, A. 2008*a* Petascale algorithms for reactor hydrodynamics. *J. Phys. Conf. Series* **125**.

Fischer, P. F., Lottes, J. W. & Kerkemeier, S. G. 2008*b* nek5000 Web page. http://nek5000.mcs.anl.gov.

Maday, Y. & Patera, A. 1989 Spectral element methods for the Navier–Stokes equations. In *State of the Art Surveys in Computational Mechanics* (ed. A.K. Noor), pp. 71–143. ASME.

Moser, R. D., Kim, J. & Mansour, N. 1999 Direct numerical simulation of turbulent channel flow up to $\mathrm{Re}_\tau = 590$. *Phys. Fluids* **11** (4), 943–945.

Schlatter, P., Stolz, S. & Kleiser, L. 2004 LES of transitional flows using the approximate deconvolution model. *Int. J. Heat Fluid Flow* **25** (3).

Paper 2

2

Stabilization of the spectral-element method in turbulent flow simulations

By Johan Ohlsson*, Philipp Schlatter*, Paul F. Fischer† and Dan S. Henningson*

*Linné FLOW Centre, Swedish e-Science Research Centre (SeRC)
KTH Mechanics, 100 44 Stockholm, Sweden

†MCS, Argonne National Laboratory, 9700 S. Cass Avenue,
Argonne, IL 60439, USA

Spectral and High Order Methods for Partial Differential Equations, LNCSE **76**, 449–458, 2011

The effect of over-integration and filter-based stabilization in the spectral-element method is investigated. There is a need to stabilize the SEM for flow problems involving non-smooth solutions, *e.g.* turbulent flow simulations. In model problems, such as the Burgers' equation (similar to Kirby & Karniadakis 2003) and the scalar transport equation together with full Navier-Stokes simulations it is noticed that over-integration with the full 3/2-rule is not required for stability. The first additional over-integration nodes are the most efficient to remove aliasing errors. Alternatively, filter-based stabilization can in many cases alone help to stabilize the computation.

1. Introduction

The spectral-element method (SEM) has mainly been applied to relatively low Reynolds numbers, with a focus on laminar and, to some extent, transitional flows (see *e.g.* Sherwin & Karniadakis 1995; Tomboulides & Orszag 2000; Tufo & Fischer 2001). However, for fully turbulent flows at moderate Reynolds numbers ($Re \sim 10^3 - 10^4$), there has been less attention (Blackburn & Schmidt 2003; Chu & Karniadakis 1993; Dong *et al.* 2006; Wasberg *et al.* 2009), which can probably be ascribed to the anxiety about the stability of the SEM at these Reynolds numbers. The cause of this instability is thought to be the accumulation of aliasing errors, which are strongly enhanced in a turbulent flow simulation. Our belief is that as soon as these errors are reduced or eliminated in an appropriate way, the stability of the method can be fully assured for all Re. The reduction or elimination of aliasing errors can be accomplished either by so-called over-integration (see *e.g.* Canuto *et al.* 1988; Kirby & Karniadakis 2003; Maday & Rønquist 1990), spectral vanishing viscosity (SVV) techniques (Karamanos & Karniadakis 2000; Pasquetti 2006; Schlatter *et al.*

2003; Xu & Pasquetti 2004), or filter-based stabilization as proposed in Fischer & Mullen (2001). In the framework of the weak form, the nonlinearity of the governing Navier–Stokes equations gives rise to the integration of three polynomials of order N. Using Gaussian quadrature, this requires approximately $M = 3/2N$ points in each direction in order to get an exact integration, which is similar as the well-known 3/2-rule in pseudo-spectral methods. In this work, we specifically consider the number of Gauss-Lobatto-Legendre (GLL) points, M, needed for stability, which may be considerably less. This is examined first by an eigenvalue analysis of the (linearized) viscous Burgers' equation and the linear scalar transport equation; then these ideas are applied to the full Navier-Stokes equations and evaluated *a posteriori*.

2. Equations and discretization

Our interest lies in understanding the cause of the instability of SEM at high Reynolds numbers. In order to achieve this, simpler model problems in $\mathbb{R}^1$ and $\mathbb{R}^2$ will be analyzed, eventually leading to the full Navier–Stokes in $\mathbb{R}^3$. Following Kirby & Karniadakis (2003) we proceed in $\mathbb{R}^1$ by analyzing the viscous Burgers' equation on the interval $\Omega = [-1, 1]$, written here in non-conservative form,

$$\frac{\partial u}{\partial t} + u\frac{\partial u}{\partial x} = \nu\frac{\partial^2 u}{\partial x^2} \tag{1}$$

with initial condition $u(0, x) = u^0(x) = -\sin(\pi x)$ and periodic boundary conditions. To account for a nontrivial velocity field we need to consider a problem in $\mathbb{R}^2$, here being the scalar transport equation,

$$\frac{\partial q}{\partial t} + \boldsymbol{c} \cdot \nabla q = 0 \tag{2}$$

where q may be a scalar concentration of any kind convected by the velocity field $\boldsymbol{c}$. For simplicity, we assume that $\Omega = [-1, 1]^2$. Finally, the incompressible Navier–Stokes equations in $\mathbb{R}^3$,

$$\frac{\partial \boldsymbol{u}}{\partial t} + \boldsymbol{u} \cdot \nabla \boldsymbol{u} = -\nabla p + \frac{1}{Re}\nabla^2 \boldsymbol{u} \quad \text{in } \Omega, \qquad \nabla \cdot \boldsymbol{u} = 0 \quad \text{in } \Omega \tag{3}$$

are considered, where $\boldsymbol{u}$ is the velocity, p is the pressure and $Re = UL/\nu$ the Reynolds number based on characteristic velocity and length scales, U and L respectively. Discretization in space proceeds by the high-order weighted residual spectral-element technique, extensively described in Fischer (1997), whereas temporal discretization is based on high-order splitting techniques (Maday *et al.* 1990).

3. Stabilization of turbulent flow simulations

The 3/2-rule in pseudo-spectral methods gives the criteria for the evaluation of the nonlinear terms in the Navier-Stokes equations to be free from aliasing errors. The corresponding over-integration in SEM follows the same idea, since the polynomial expansion in Legendre space is indeed truncated at N. But since

the SEM operates in physical space, it might be more straightforward to view the over-integration as the action taken in order for the evaluation (Gaussian quadrature) of the integrals arising from the weak formulation to be exact, as pointed out in Kirby & Karniadakis (2003). Either view yields the same conclusion: 3/2 times more points are needed for the nonlinear terms in order to avoid aliasing errors. If additionally curvature is taken into account, even more points are required depending on the polynomial order of the curvature.

The first sign of aliasing errors is the occurrence of 'spectral blocking', *i.e.* the accumulation of energy in the highest modes. The filter-based stabilization technique proposed in Fischer & Mullen (2001) has the property of suppressing the highest mode, thereby preventing aliasing errors to occur. In a well-resolved calculation, the solution will be smooth, and the amount of energy in the high wavenumber coefficients will be exponentially small. The filter, which operates only on the highest wavenumbers, has the desirable property of not influencing the well-resolved parts of the flow — it only impacts the under-resolved regions, which is precisely what is needed for turbulence. The success of the filter-based stabilization technique was demonstrated in Fischer & Mullen (2001). Considering the one-dimensional case in a domain $\Omega = [-1, 1]$ and $\mathbb{P}_N(\Omega)$ is the space of polynomials of maximum degree N defined on Ω, the filter operator, Π_{N-1}, was originally proposed as the interpolation operator in physical space, $\Pi_{N-1} : \mathbb{P}_N(\Omega) \rightarrow \mathbb{P}_{N-1}(\Omega) \rightarrow \mathbb{P}_N(\Omega)$, but can alternatively and formally equivalent be defined as a filter operator in modal space, (see Boyd 1998). With the use of a relaxation parameter α such that $0 < \alpha < 1$ the filter operator F_α is defined as

$$F_\alpha = \alpha\Pi_{N-1} + (1 - \alpha)I \qquad 0 \leq \alpha \leq 1 \tag{4}$$

with I being the identity matrix. Acting with F_α on the velocity vector at each time step, such that $\underline{u}^{n+1} = F_\alpha \underline{\tilde{u}}^{n+1}$ where $\underline{\tilde{u}}^{n+1}$ is the unfiltered field at the current time step, allows for a smooth damping of the highest mode with effectively no changes to the existing solver. As pointed out in Pasquetti & Xu (2002), due to the opposite parity of the Legendre polynomials L_{N-1} and L_N and the fact that Π_{N-1} preserves parity, the amplitude of the highest mode is not dissipated but rather transferred to the third highest mode.

4. Analysis of model problems

4.1. *1D: Stabilization of the Burgers' equation*

In order to perform a quantitative analysis of the Burgers' equation, the nonlinear problem was transformed into a linear problem by defining the convective operator based on a constant solution (in time) when the gradients are large, mimicking the conditions in a highly fluctuating turbulent velocity field. The distribution of the eigenvalues of the resulting problem, $\mathrm{d}\underline{u}/\mathrm{d}t = \mathrm{A}\underline{u}$, is shown in figure 1($a$) below for the unstabilized, filtered and over-integrated cases. Here, $M = N + 4$ GLL points are used to compute the convective operator (compared to $M = N + 1$ for the other terms), which apparently has a strong

influence on the eigenvalues. In particular, the unstable eigenvalues (compare to the unstabilized case) have been completely moved over to the real negative half-plane. Hence, for a marginally resolved simulation subject to large velocity fluctuations, adding only three extra points for the convective term can help to stabilize the numerical method. The filtered case improves the situation by moving the unstable eigenvalues slightly in the negative real direction. In

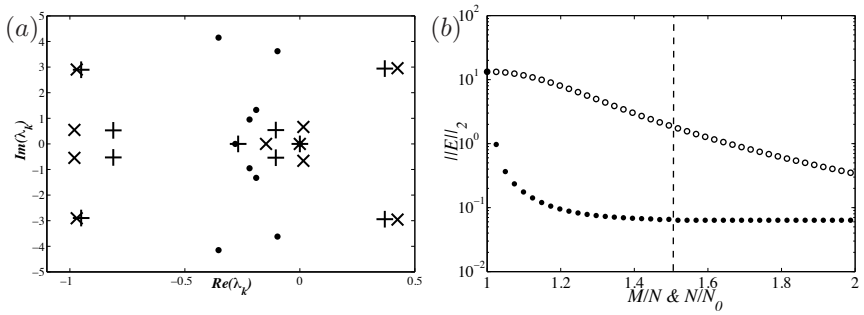

FIGURE 1. (a) Eigenvalues of the right hand side operator of the linear model problem for the ($\times$) unstabilized, ($+$) filtered and ($\bullet$) over-integrated case with $M = N + 4$ points for the convective operator. (b) L_2-error with respect to the 'exact' numerical solution, where the overall resolution is increased ($\circ$) and the nonlinear term is computed with increased number of points ($\bullet$). ----indicates where $M/N = 3/2$.

addition to rendering a simulation stable, one would also like to make sure that the solution is not polluted by aliasing errors. Here, the error is investigated by means of the L_2-error for a various number of extra points, M, for the nonlinear term and reported in figure 1(b). $M/N = 1$ corresponds to equal number of points for the viscous term and for the nonlinear term. As predicted by theory and shown in Kirby & Karniadakis (2003), beyond $M/N = 1.5$ (indicated by the dashed vertical line) the error stays constant. An increased resolution for all terms yields an exponentially decrease of the error as expected. However, the resolution has to be more than doubled in order to get the same error as if 1.5 times more points is added only for the nonlinear term. Notice also that by performing over-integration with only one extra point decreases the error by one order of magnitude.

4.2. *2D: Recovery of skew-symmetry for the SEM convection operator in the scalar transport equation*

In high Reynolds number flows, structures are not readily dissipated but rather convected over long distances and times, thus accurate integration of the convective term is essential to obtain reliable results. Here, we investigate how

this can be achieved in the scalar transport equation in $\mathbb{R}^2$, given by equation (2). In the case $\boldsymbol{c}$ is solenoidal and the domain is closed or periodic, the weak form predicts the convective term in equation (2) to be skew symmetric, *i.e.* $c(v,q) = -c(q,v)$. This is easily seen by casting the convective term in equation (2) in the weak form by multiplying by a test function, v, integrating over the domain, Ω, and using integration by parts, so that

$$\begin{aligned} c(v,q) = \int_\Omega v\boldsymbol{c}\cdot\nabla q \,\mathrm{d}\boldsymbol{x} &= \int_{\partial\Omega} vq\boldsymbol{c}\cdot\hat{\mathbf{n}}\,\mathrm{d}A - \int_\Omega \nabla\cdot(v\boldsymbol{c})q\,\mathrm{d}\boldsymbol{x} \\ &= \int_{\partial\Omega} vq\boldsymbol{c}\cdot\hat{\mathbf{n}}\,\mathrm{d}A - \int_\Omega q\boldsymbol{c}\cdot\nabla v\,\mathrm{d}\boldsymbol{x} - \int_\Omega \nabla\cdot\boldsymbol{c}vq\,\mathrm{d}\boldsymbol{x} \\ &= -c(q,v). \end{aligned} \tag{5}$$

The last equality holds as long as the first and the last term on the left hand side are identically zero. The first term vanishes due to the boundary conditions on v and q (homogeneous Dirichlet, periodicity or symmetry) and the last because of the incompressibility constraint, $\nabla\cdot\boldsymbol{c} \equiv 0$. The remaining equality states the skew-symmetric property of the convective operator. In a discretized form this can only be true if skew-symmetry of the involved matrices is preserved. As we shall see, over-integration may play a crucial role to assure this property. Since the eigenvalues of a skew-symmetric operator are purely imaginary, quadrature errors are easily detected by eigenvalues of the discretized operator with real part $\neq 0$. These errors are reduced by over-integration of the convective term as described earlier. In the case $M = 3(N+1)/2$ the numerical quadrature is exact for all polynomials $\boldsymbol{c} \in \mathbb{P}_N$. If, however, $\boldsymbol{c}$ has a polynomial order less than this, recovery of this skew-symmetry — and hence the elimination of the quadrature errors — can be obtained by performing over-integration with $M \ll 3(N+1)/2$, shown by the following examples. We consider the case $\boldsymbol{c} \in \mathbb{P}_1$, shown in figure 2(*a*) as a vortical convective field given by $\boldsymbol{c_1} = (-y, x)$ and in figure 2(*b*) as a stagnation point given by $\boldsymbol{c_2} = (-x, y)$. Both cases identically fulfil $\nabla\cdot\boldsymbol{c} \equiv 0$. Although the convective field appears as a first order polynomial in both cases, the particular tensor product structure of the spectral-element method distinguishes between the vortical and the stagnation point velocity fields. For both these cases, each component of the velocity field is separable, *i.e.* $\boldsymbol{c_1} = (1\cdot a(y), b(x)\cdot 1)$ and $\boldsymbol{c_2} = (a(x)\cdot 1, 1\cdot b(y))$ and it follows that the double integral in equation (5) can be separated (for both components, x and y) in one symmetric part and one skew-symmetric part. The symmetric part will be symmetric regardless of exact integration, and does not contribute to the skew-symmetric properties of the convective operator. In this respect, it suffices to examine whether the skew-symmetric part is integrated correctly or not. For 'rotational' velocity fields such as the vortex, the skew-symmetric part will indeed be integrated exactly, since the integrand, p, is a polynomial $p = v^N q^{N-1} \in \mathbb{P}_{2N-1}$. The conclusion is thus that skew-symmetry (*i.e.* purely imaginary eigenvalues) is obtained using the original $M = N+1$ grid, which is shown in figure 2(*a*). In the latter case the skew-symmetric part for both

components, x and y, cannot be integrated exactly since the integrand, p, will be a polynomial $p = v^N c^1 q^{N-1} \in \mathbb{P}_{2N}$. However, by adding one extra point for the integration so that $M = N + 2$, skew-symmetry can again be recovered, as can be seen in figure 2(b).

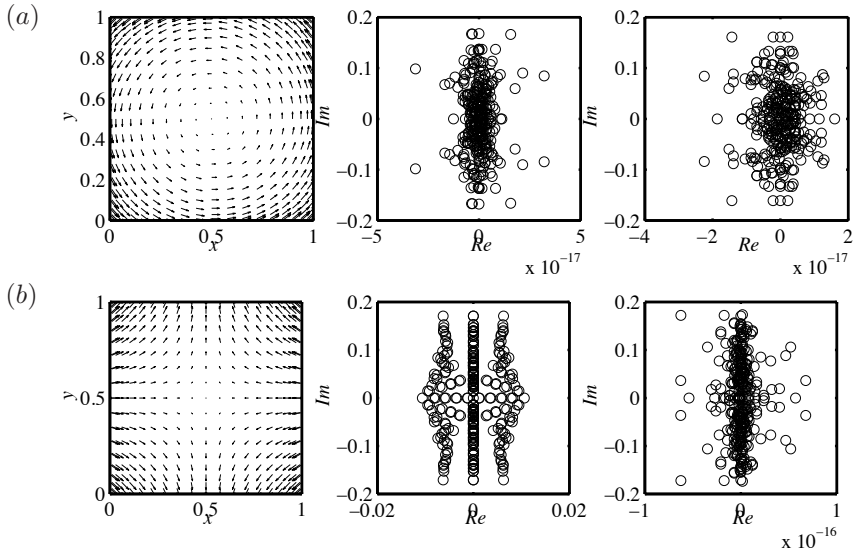

FIGURE 2. (*Row a*) Vortical convective field with associated eigenvalue distribution of the operator when $M = N + 1$ and when $M = N + 2$. (*Row b*) same as (*row a*) for a stagnation convective field.

5. Application to the Navier–Stokes equations

In the following, numerical simulations of the incompressible Navier-Stokes equations (3) are performed and evaluated *a posteriori*. equation (3) are solved using the Legendre polynomial based SEM code `nek5000` (Fischer *et al.* 2008).

5.1. *3D: Subcritical K-type transition simulations*

Direct numerical simulations (DNS) of subcritical K-type transition at $Re_b = 3333$ (similar to Schlatter *et al.* 2004) and a resolution of 91^3 grid points were performed to further highlight the fact that it is indeed the appearance of intermittent turbulence which might render a SEM simulation unstable. The initial disturbances of this classical transition scenario consists of a two-dimensional TS wave (streamwise wave number of $\alpha = 1.12$ and amplitude 3%) together with two three-dimensional oblique waves (wave numbers $\alpha = 1.12$ and $\beta = 2.1$ and amplitude 0.05%) taken from the solution of the Orr-Sommerfeld equation and superimposed on a plane Poiseuille flow profile (see Gilbert & Kleiser

1990; Schlatter *et al.* 2004). The disturbances grow in time, t, and eventually lead to turbulent breakdown. The laminar stage up to $t \approx 160$ is followed by the highly fluctuating transitional stage with an overshoot in the skin friction and finally fully turbulent phase, seen in figure 3 showing the skin friction Reynolds number, Re_τ, as a function of time. Unlike Kirby & Karniadakis (2003), who were able to simulate transition in a triangular duct without any stabilization, we found that performing the simulation without any filtering or over-integration of the nonlinear term would yield a numerical instability exactly at the time just before the skin friction peaks ($t = 165$). Adding one extra point to compute the nonlinear term helped to continue the simulation exactly to the skin-friction peak ($t = 169$). However, adding four more points could stabilize the simulation through transition and continue stably in the following fully turbulent stage. This is exactly half the number of points predicted by the 3/2-rule. It should be pointed out that an increase of the spatial resolution ($91 \rightarrow 127$ points in each direction) could not help to stabilize the simulation, which would experience the instability at approximately the same time, just before the peak of the skin-friction. The filtering alone was also able to stabilize the simulation through the skin-friction peak and during the fully turbulent phase.

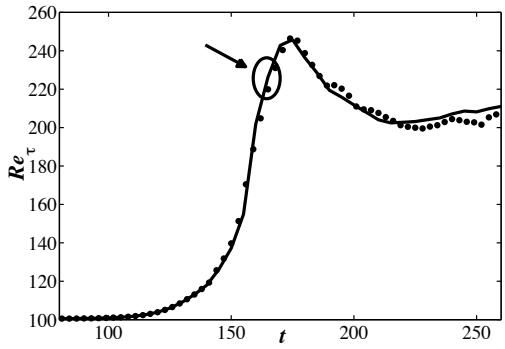

FIGURE 3. Evolution of Re_τ for the (stable) transitional channel flow simulation (——). The arrow shows where the numerical instability occurred. Comparison to DNS by Schlatter *et al.* (2004) (·····).

5.2. *3D: Fully turbulent channel flow simulations at $Re_\tau = 590$*

Finally, fully turbulent flow simulations were performed at a friction Reynolds number of $Re_\tau = 590$ similar to Moser *et al.* (1999) in channel geometry in order to see the effect of the stabilization tools in a moderate Re flow. All statistical quantities were averaged over the homogeneous directions x, z and t (for sufficiently long time) as well as over the two channel halves. An acceptable resolution was chosen of approximately 75 % in each direction of the fine DNS

resolution in Moser *et al.* (1999). Filtering or over-integration were needed to stabilize the calculation. In one of the two cases shown in figure 4, the full 3/2-rule (*dashed*) was used to stabilize the computation, whereas (*solid*) could be rendered stable with only four extra points. No filtering was used for either of these cases. The obtained mean flow results as well as fluctuations show very good agreement with results obtained in Moser *et al.* (1999), and no particular difference can be noticed between the two cases. As an alternative, only filtering could be used to stabilize the computation, shown in figure 4 (*thin solid*). Here, as little as 5 % filtering of the last mode could ensure a stable computation and good results compared to the reference data. The obtained shape factors, defined as,

$$H_{12} = \frac{\delta^*}{\theta} = \int_{-1}^{1} \left(1 - \frac{U(y)}{U_{CL|\mathrm{lam}}}\right) \mathrm{d}y \Big/ \int_{-1}^{1} \frac{U(y)}{U_{CL|\mathrm{lam}}} \left(1 - \frac{U(y)}{U_{CL|\mathrm{lam}}}\right) \mathrm{d}y, \quad (6)$$

where δ^* is the displacement thickness, θ is the momentum thickness, $U_{CL|\mathrm{lam}}$ is the laminar centerline velocity, $U(y)$ is the mean velocity profile and the integration is made between the two walls located at $y = \pm 1$ were $H_{12}^{3(N+1)/2} = 1.583$, $H_{12}^{N+5} = 1.589$ and $H_{12}^{onlyfilt} = 1.589$ compared to the reference data $H_{12} = 1.574$ (Schlatter *et al.* 2004). The obtained skin friction Reynolds number, Re_τ, based on friction velocity, u_τ, and channel half height, h, were $Re_\tau^{3(N+1)/2} = 586.1$, $Re_\tau^{N+5} = 585.7$ and $Re_\tau^{onlyfilt} = 588.6$ compared to the reference data $Re_\tau = 587.2$ (Moser *et al.* 1999; Schlatter *et al.* 2004). Thus, both these turbulent quantities show a difference on the order of a few per mille, compared to the reference data.

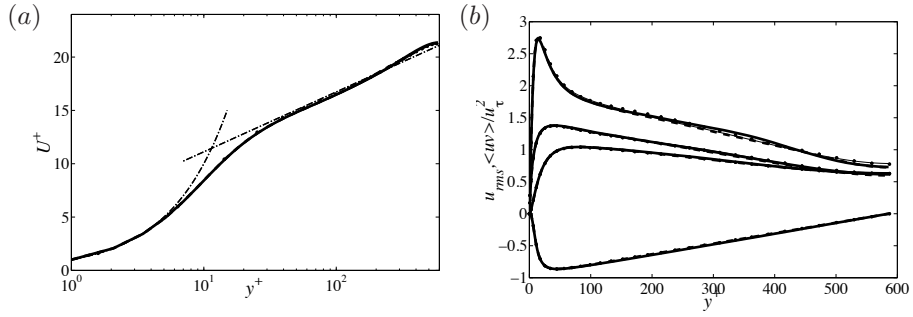

FIGURE 4. Turbulent channel flow simulations at $Re_\tau = 590$ with polynomial order 15 (a resolution of 288 in the homogeneous directions and 192 in the wall-normal direction) showing (*a*) mean velocity profile, (*b*) Reynolds stresses ····· DNS data from Moser *et al.* (1999), −·− log law, —— $M = N + 5$, - - - - $M = 3(N + 1)/2$, and —— only filtering (5 %).

6. Conclusions

Stabilization techniques for the spectral-element method was investigated through two model problems: Burgers' equation in 1D similar to Kirby & Karniadakis (2003) and the scalar transport equation in 2D together with transitional and turbulent Navier–Stokes channel flow simulations in 3D. The general results from the 1D problem show consistently with Kirby & Karniadakis (2003) that applying over-integration with the full 3/2-rule to an equation with a quadratic nonlinearity indeed enhances both the accuracy and stability of the solution. In addition, it could be seen in both model problems and in the full Navier–Stokes simulations that for such equations over-integration with the full 3/2-rule is not needed for stability. Stability was achieved already with $\leq 25\%$ more GLL points, with the first over-integration point being the most efficient to remove aliasing errors. Filter-based stabilization can in most cases alone help to stabilize the computation and is normally not needed together with over-integration, although this combination can be essential for significantly under-resolved cases. The present study suggests that by the use of these techniques stability can be achieved at any Re.

References

Blackburn, H. M. & Schmidt, S. 2003 Spectral element filtering techniques for large-eddy simulation with dynamic estimation. *J. Comput. Phys.* **186** (2), 610–629.

Boyd, J. P. 1998 Two comments on filtering (artificial viscosity) for chebyshev and legendre spectral and spectral element methods: preserving boundary conditions and interpretation of the filter as a diffusion. *J. Comput. Phys.* **143** (1), 283–288.

Canuto, C., Hussaini, M.Y., Quarteroni, A. & Zang, T.A. 1988 *Spectral Methods in Fluid Dynamics*. Springer-Verlag, Berlin, Germany.

Chu, D. C. & Karniadakis, G. E. 1993 A direct numerical simulation of laminar and turbulent flow over riblet-mounted surfaces. *J. Fluid Mech.* **250**, 1–42.

Dong, S., Karniadakis, G. E., Ekmekci, A. & Rockwell, D. 2006 A combined direct numerical simulation-particle image velocimetry study of the turbulent near wake. *J. Fluid Mech.* **569**, 185–207.

Fischer, P. & Mullen, J. 2001 Filter-based stabilization of spectral element methods. *C.R. Acad. Sci. Paris* **t. 332, Serie I**, p. 265–270.

Fischer, P. F. 1997 An overlapping Schwarz method for spectral element solution of the incompressible Navier–Stokes equations. *J. Comput. Phys.* **133** (1), 84–101.

Fischer, P. F., Lottes, J. W. & Kerkemeier, S. G. 2008 nek5000 Web page. http://nek5000.mcs.anl.gov.

Gilbert, N. & Kleiser, L. 1990 Near-wall phenomena in transition to turbulence. In *Near-Wall Turbulence* (ed. S.J. Kline & N.H. Afgan), pp. 7–27. 1988 Zoran Zarić Memorial Conference, New York, USA.

Karamanos, G-S. & Karniadakis, G. E. 2000 A spectral vanishing viscosity method for large-eddy simulations. *J. Comput. Phys.* **163** (1), 22–50.

Kirby, R. M. & Karniadakis, G. E. 2003 De-alising on non-uniform grids: algorithms and applications. *J. Comput. Phys.* **191**, 249–264.

Maday, Y., Patera, A. T. & Rønquist, E. M. 1990 An operator-integration-factor splitting method for time-dependent problems: application to incompressible fluid flow. *J. Sci. Comput.* **5** (4), 263–292.

Maday, Y. & Rønquist, E. M. 1990 Optimal error analysis of spectral methods with emphasis on non-constant coefficients and deformed geometries. *Comput. Methods Appl. Mech. Eng.* **80** (1-3), 91–115.

Moser, R. D., Kim, J. & Mansour, N. 1999 Direct numerical simulation of turbulent channel flow up to $\mathrm{Re}_\tau = 590$. *Phys. Fluids* **11** (4), 943–945.

Pasquetti, R. 2006 Spectral vanishing viscosity method for large-eddy simulation of turbulent flows. *J. Sci. Comput.* **27** (1-3), 365–375.

Pasquetti, R. & Xu, C.J. 2002 Comments on "Filter-based stabilization of spectral element methods". *Note in J. Comput. Phys.* **182**, 646–650.

Schlatter, P., Stolz, S. & Kleiser, L. 2003 Relaxation-term models for LES of turbulent and transitional wall-bounded flows. In *DLES-5*. Accepted.

Schlatter, P., Stolz, S. & Kleiser, L. 2004 LES of transitional flows using the approximate deconvolution model. *Int. J. Heat Fluid Flow* **25** (3).

Sherwin, S. & Karniadakis, G. 1995 A triangular spectral element method; applications to the incompressible Navier–Stokes equations. *Comput. Methods Appl. Mech. Engng.* **123**, 189.

Tomboulides, A. & Orszag, S. 2000 Numerical investigation of transitional and weak turbulent flow past a sphere. *J. Fluid Mech.* **416**, 45–73.

Tufo, H. M. & Fischer, P. F. 2001 Fast parallel direct solvers for coarse grid problems. *J. Parallel Distrib. Comput.* **61** (2), 151–177.

Wasberg, C. E., Gjesdal, T., Reif, B. A. P. & Andreassen, Ø. 2009 Variational multiscale turbulence modelling in a high order spectral element method. *J. Comput. Phys.* **228** (19), 7333–7356.

Xu, C. & Pasquetti, R. 2004 Stabilized spectral element computations of high Reynolds number incompressible flows. *J. Comput. Phys.* **196** (2), 680–704.

Paper 3

3

Large-eddy simulation of turbulent flow in a plane asymmetric diffuser by the spectral-element method

By Johan Ohlsson[*], Philipp Schlatter[*], Paul F. Fischer[†] and Dan S. Henningson[*]

[*]Linné FLOW Centre, Swedish e-Science Research Centre (SeRC)
KTH Mechanics, 100 44 Stockholm, Sweden

[†]MCS, Argonne National Laboratory, 9700 S. Cass Avenue,
Argonne, IL 60439, USA

Direct and Large-Eddy Simulation VII, 197–204, 2010

LES and no-model LES (coarse-grid DNS) have been performed of turbulent flow in a plane asymmetric diffuser by the spectral-element method (SEM). Mean profile and turbulent stresses compare well to LES results from Herbst *et al.* (2007), however the SEM generally predicts a later (*i.e.* further downstream) separation. It can be concluded that the use of a high-order method is advantageous for flows featuring pressure-induced separation.

1. Introduction

The spectral-element method (SEM), introduced by Patera (1984), is a high-order numerical method with the ability to accurately simulate fluid flows in complex geometries. SEM has opened the possibility to study – in great detail – fluid phenomena known to be very sensitive to discretization errors, *e.g.* flows exhibiting separation. Especially pressure-induced separation (as opposed to separation where the separation is induced by sharp edges or obstacles) is known to be particularly challenging, since the separation and reattachment points are hard to predict and are generally very sensitive to disturbances that could stem from an inaccurate numerical discretization. A typical engineering flow where pressure-induced flow separation is dominant is the turbulent diffuser flow. The specific planar asymmetric diffuser considered here has been investigated experimentally by Obi *et al.* (1993) and Buice & Eaton (2000) and numerically by Kaltenbach *et al.* (1999) (opening angle of 10°). A similar geometry with an opening angle of 8.5° was studied by Herbst *et al.* (2007), who performed LES at three different Reynolds numbers (Re_b = 4500, 9000, 20000 based on bulk velocity and channel half-height) with a hybrid second-order finite-difference/spectral code. In the present work, a turbulent diffuser similar to Herbst *et al.* (2007) is simulated by the SEM with large-eddy simulation (LES)

and 'no-model' LES at $Re_b = 4500$ and 9000. For the LES, a version of the dynamic Smagorinsky model, specifically adapted for SEM, is used.

2. Numerical method and simulation set-up

The SEM code `nek5000`, developed by Paul F. Fischer, is used in the present study. It solves the three-dimensional, unsteady, incompressible Navier–Stokes equations by a Legendre-spectral element formulation and uses a rectangular structured grid with the ability to handle curved elements boundaries. It is massively parallelized and has shown a nearly linear speed-up for our computations up to 2048 cores. Two different ways of stabilizing flows at high Reynolds numbers are implemented in the code; over-integration (dealiasing) and polynomial filtering (as proposed by Fischer & Mullen 2001). The combination of LES and SEM has only quite recently been explored, including the Rational LES (RLES) of channel flow by Iliescu & Fischer (2003), the dynamic Smagorinsky LES and the deconvolution based LES of the cubic cavity flow by Bouffanais *et al.* (2006). Here, we use the dynamic Smagorinsky model, where the model coefficient is computed according to the dynamic procedure proposed by Germano *et al.* (1991). In the framework of SEM, the definition of a test filter is implemented in Legendre space and constructed such that approximately half of the modes are affected. To limit the fluctuation of the model coefficient, spatial averaging is used along the homogeneous spanwise (z) direction together with clipping of the model parameter (negative values are discarded).

3. Validation by turbulent channel flow

An extensive validation of the simulation set-up was performed by means of DNS of turbulent channel flow. The aim was to address the open questions about the stability of SEM at moderate to high Reynolds numbers. Fully turbulent periodic channel flow was simulated at two different Reynolds numbers, $\mathrm{Re}_\tau = 180$ and 590. The results, shown in figure 1 for $\mathrm{Re}_\tau = 590$, show that SEM is able to predict the mean velocity profile and the Reynolds stresses with very good agreement to spectral DNS results at moderate Reynolds numbers if one employs either polynomial filtering or over-integration as stabilization technique. If neither over-integration nor polynomial filtering are used, the calculation will experience a numerical instability after a small number of time steps, even for a high resolution (also discussed by Fischer & Mullen 2001). Both filtering and over-integration on their own are able to stabilize the calculation. This was also seen in transition simulations (K-type transition similar to Schlatter *et al.* 2004), where it turned out to be essential to employ a stabilization technique as soon as the turbulent state was reached.

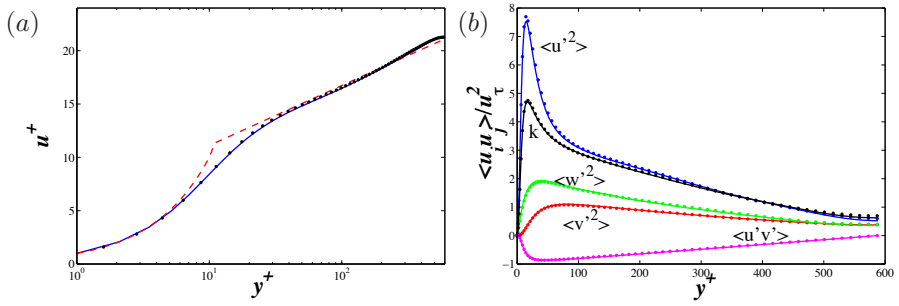

FIGURE 1. Turbulent channel flow at $Re_\tau = 590$ (resolution: $288 \times 192 \times 288$) showing ($a$) mean velocity profile and (b) Reynolds stresses together with turbulent kinetic energy. Comparison to DNS results (resolution: $384 \times 257 \times 384$) from Moser *et al.* (1999) ····· DNS data, ----Log Law, ——— nek5000.

4. Diffuser

4.1. *Geometry and parameter settings*

The geometry of the plane asymmetric diffuser is similar to Herbst *et al.* (2007). The geometry, with visible element boundaries, is sketched in figure 2. The sim-

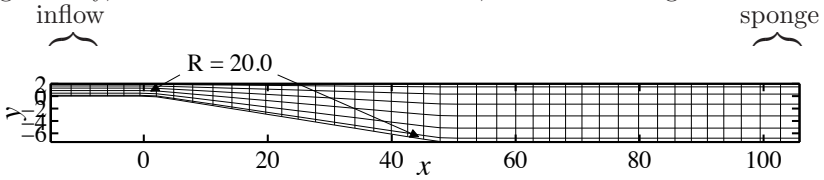

FIGURE 2. Sketch of the diffuser geometry and the grid used for the $Re_b = 4500$ case. Note that only the element boundaries are visible. The edges marked by arrows are rounded with a radius of 20.0.

ulations, including both LES and no-model LES, were performed at a Reynolds number of $\mathrm{Re}_b = 4500$ and 9000, corresponding to the lower and medium Reynolds number of Herbst *et al.* (2007). The cases are summarized in Table 1, with N_i denoting the resolution in each direction respectively. The spanwise width of $L_z = 8$ is chosen in accordance with Kaltenbach *et al.* (1999). The inflow channel has a height of 2, which starts to expand at $x = 0$ with the diffuser wall inclined at a diverging angle of 8.5°. The diffuser reaches its final height of 9.4 at $x = 49.6$. The edges where the inclined wall is attached, are rounded with a radius of 20.0. Spanwise (z) periodicity is used for both cases. The aim was to have a fully developed turbulent flow entering the diffuser expansion. This was achieved by an unsteady Dirichlet boundary condition, where random noise was superimposed on a turbulent mean velocity profile. Having

TABLE 1. Description of the diffuser cases

Re_b	L_x	L_z	N_x	N_y	N_z	Order	# Elements	# Grid points
4500	121	8	260	43	64	7	1998	$0.72 \cdot 10^6$
9000	131	8	346	61	91	15	552	$1.92 \cdot 10^6$

gone through transition to turbulence, the flow was allowed to evolve for sufficiently long distance upstream of the diffuser throat, so that an approximately fully developed turbulent state was reached just before the diffuser expansion. At the outflow, a sponge region is added, where the flow is forced to a turbulent mean flow profile in order to damp out oscillations prior to reaching the zero-pressure outflow boundary.

4.2. *Results*

Selected turbulent statistics, including the evolution of the mean streamwise velocity $\langle\overline{u}\rangle$ and the Reynolds stress $\langle\overline{u}'\overline{v}'\rangle$, are shown in figure 3 at seven streamwise positions at $Re_b = 4500$ and 9000, respectively. The left column (*a* - *g*) shows LES results and the right column (*b* - *h*) shows no-model LES results. The results are compared with LES data from Herbst *et al.* (2007). Good agreement is obtained for LES and no-model LES results at the two different Reynolds numbers. Herbst *et al.* (2007) performed simulations at three different resolutions. The number of degrees of freedom in our simulations correspond (at both Reynolds numbers) to the lowest of the resolutions used in Herbst *et al.* (2007). It should be pointed out, however, that the SEM results, although at the lowest resolution, compares better to the second highest resolution data from Herbst *et al.* (2007), in particular in the separated region. This justifies the idea that a high-order method makes a better use of the grid points than a low-order method. Contours of the stream function for a time and spanwise averaged flow field are shown in figure 4, with (*a* - *c*) and without (*b* - *d*) SGS model for $Re_b = 4500$ and 9000, respectively. The trend of an increased separated region for higher Reynolds number is obvious in our no-model LES simulations (compare *e.g.* figure 4*b* and 4*d*) and further confirmed by numerical results by Herbst *et al.* (2007) and experimental results by Obi *et al.* (1993). More specific, the position of the separated region (indicated by the mean diving streamline) almost coincides with data from Herbst *et al.* (2007) (shown by arrows) for the lower Reynolds number (figure 4*b*). In the LES results, however, the separation bubble is not visible. For the higher Reynolds number, there is a general trend towards a later separation in our results compared to Herbst *et al.* (2007). The no-model LES results show a relatively early reattachment (figure 4*d*), whereas the LES results indicate a reattachment point that coincides with Herbst *et al.* (2007) (figure 4*c*). Clearly, the presence of the LES model affects the size and the location of the separation bubble. In figure 5, the highly unsteady nature of pressure-induced separation is highlighted. The instantaneous separated region, here visualized by an isosurface of -0.01

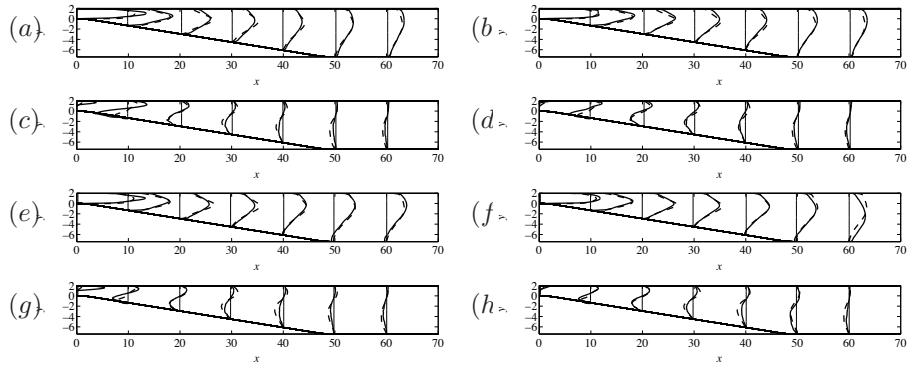

FIGURE 3. Turbulent statistics for the diffuser at $Re_b = 4500$ $(a-d)$ and 9000 $(e-h)$: **a & e** $10 \cdot \langle \overline{u} \rangle + x$ (LES), **b & f** $10 \cdot \langle u \rangle + x$ (no-model LES), **c & g** $500 \cdot \langle \overline{u}'\overline{v}' \rangle + x$ (LES), **d & h** $500 \cdot \langle u'v' \rangle + x$ (no-model LES), ——— nek5000, - - - - Herbst *et al.* (2007).

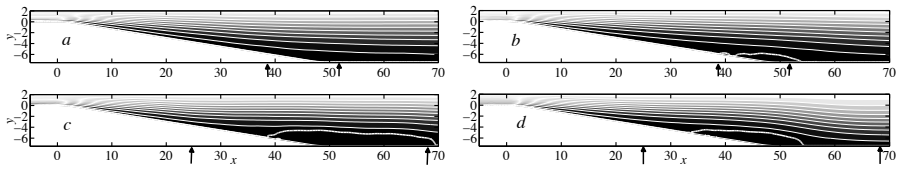

FIGURE 4. Contours of the stream function at $Re_b = 4500$ $(a-b)$ and 9000 $(c-d)$: **a & c** LES, **b & d** no-model LES. Thick white contour levels indicate the value 10^{-5} of the stream function, thin white contours range from -0.1 to 2.0 with spacing 0.2. Black arrows show the streamwise extent of the mean dividing streamline in Herbst *et al.* (2007)

for the streamwise velocity, show different separation and reattachment points compared to the averaged equivalences.

5. Conclusion and outlook

LES and no-model LES have been performed of turbulent flow in a plane asymmetric diffuser by the SEM. Turbulent statistics compare well to LES results by Herbst *et al.* (2007). It can be concluded that the use of a high-order method is advantageous, both in terms of the parallel efficiency of the method, but also the fact that less grid points were needed to predict a result with the same given accuracy compared to a low-order method. The influence of the SGS model is hardly noticeable in the statistics, except close to the diffuser throat where the SGS model might be slightly too dissipative (*e.g.* reduced turbulent activity in that region) and close to the outlet where the model seems to

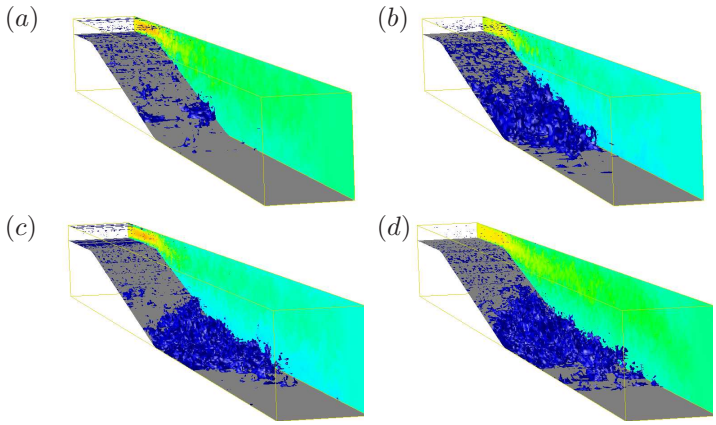

FIGURE 5. Isosurface of -0.01 for the streamwise velocity of an instantaneous velocity field at $Re_b = 4500$ $(a - b)$ and 9000 $(c - d)$, **a & c** LES, **b & d** no-model LES.

improve the results. Investigation of the location of the separation bubble reveals that the separation generally starts more downstream in the SEM results compared to Herbst *et al.* (2007). Improved methods of treating the turbulent inflow condition, *e.g.* the use of trip-forcing, will be considered and compared to the present method. The dynamic Smagorinsky model will be compared to other SGS models, in particular those based on high-pass filtering. Further, as pointed out by Kaltenbach *et al.* (1999), it may be desirable to increase the width of the domain in order decrease the presence of artificial coherent structures, which seems to delay the reattachment.

References

Bouffanais, R., Deville, M., Fischer, P.F., Leriche, E. & Weill, D. 2006 Large-eddy simulation of the lid-driven cubic cavity flow by the spectral element method. *J. Sci. Comput.* **27**, 151–162.

Buice, C. U. & Eaton, J. K. 2000 Experimental investigation of flow through an asymmetric plane diffuser. *J. Fluids Engng.* **122** (2), 433–435.

Fischer, P. & Mullen, J. 2001 Filter-based stabilization of spectral element methods. *C.R. Acad. Sci. Paris* **t. 332, Serie I**, p. 265–270.

Germano, M., Piomelli, U., Moin, P. & Chabot, W.H. 1991 A dynamic subgrid-scale eddy viscosity model. *Phys. Fluids* **3(7)**, 1760–1765.

Herbst, A. H., Schlatter, P. & Henningson, D. S. 2007 Simulations of turbulent flow in a plane asymmetric diffuser. *Flow Turbulence Combust.* **79**, 275–306.

Iliescu, T. & Fischer, P.F. 2003 Large eddy simulation of turbulent channel flows by the rational large eddy simulation model. *Phys. Fluids* **15** (10), 3036–3047.

Kaltenbach, H.-J., Fatica, M., Mittal, R., Lund, T.S. & Moin, P. 1999 Study of flow in a planar asymmetric diffuser using large-eddy simulation. *J. Fluid Mech.* **390**, 151–185.

Moser, R. D., Kim, J. & Mansour, N. 1999 Direct numerical simulation of turbulent channel flow up to $\mathrm{Re}_\tau = 590$. *Phys. Fluids* **11** (4), 943–945.

Obi, S., Nikaido, H. & Masuda, S. 1993 Experimental and computational study of turbulent separating flow in an asymmetric diffuser. In *Proceedings of the Ninth Symposium on Turbulent Shear Flows*, pp. 305.1–305.4.

Patera, A. T. 1984 A spectral element method for fluid dynamics: Laminar flow in a channel expansion. *J. Comput. Phys.* **54**, 468–488.

Schlatter, P., Stolz, S. & Kleiser, L. 2004 LES of transitional flows using the approximate deconvolution model. *Int. J. Heat Fluid Flow* **25** (3).

Paper 4

4

Koopman mode decompisition of a minimal channel flow

By Johan Malm[*], Shervin Bagheri[†*], Philipp Schlatter[*] and Dan S. Henningson[*]

[*]Linné FLOW Centre, Swedish e-Science Research Centre (SeRC)
KTH Mechanics, 100 44 Stockholm, Sweden

[†]DICAT, University of Genoa, Via Montallegro 1, 16145 Genoa, Italy

Internal report

The recent Koopman mode decomposition (Rowley *et al.* 2009) is applied to a turbulent and fully non-linear minimal channel flow. The acquired structures and frequencies are compared to classical proper orthogonal decomposition (POD) of the same flow, also performed by Webber *et al.* (1997). In addition, the frequencies are compared to spectral analysis based on a time signal probe placed in the flow domain. It is found that the POD and Koopman mode decomposition are able to identify similar structures, associated with the dynamics of the single low-speed streak present in the minimal flow unit. These structures can be categorised into two different groups: One consisting of structures with no streamwise dependence; the other with a streamwise dependence of one wavelength (so-called 'roll modes' and 'propagating modes' in Webber *et al.* 1997). Each one of these coherent structures are associated with a specific frequency. For the Koopman mode analysis, these frequencies come out naturally, whereas spectral analysis of the respective time coefficients has to be performed for the POD. Both procedures find that the roll mode has a time period of $T_{roll} \equiv tu_b/h \approx 128$, whereas the propagating mode has a time period of $T_{prop} \approx 3.5$, in agreement with the analysis of the time signal probe. The former is thought to be the structure connected to the long intermittency cycle identified by Jiménez & Moin (1991), whereas the latter can be directly related to the imposed streamwise periodicity via the length of the flow domain and a convection velocity. The structures obtained from the two procedures are in general very similar, in particular the roll modes. However, the Koopman analysis could identify a double peak for the propagating modes, where the structure pertaining to the lower frequency extends all the way to the wall. The propagating mode with the slightly higher frequency (*i.e.* a faster moving structure) is localised further out from the wall.

1. Introduction

Turbulent flows have for centuries puzzled researchers due to their complicated nature and apparent disorder. Many of the turbulent flows we find around us, such as geophysical and engineering flows, are so complex that smaller subsystems have to be chosen in order gain some understanding. Even so, one is often limited to the study of mean properties without a proper knowledge of the time-dependent dynamics. To include the effect of solid walls on the turbulence, the study of turbulent flow in a spanwise and streamwise homogeneous channel is one of the most popular test cases in turbulence research. Despite its geometrical simplicity it involves rich physics far from being fully understood. The *minimal* channel flow was first introduced by Jiménez & Moin (1991) in order to reduce the complexity of an ordinary plane channel flow. Their objective was to identify the minimal set of structures necessary to sustain turbulence with correct statistical properties. They found the width of a minimal flow unit to coincide with the sub-layer streak spacing, $\lambda_z^+ \approx 100$, *i.e.* the minimal flow unit enables the study of one isolated streak and its dynamics. They claimed that this would give the streak a 'dynamical rather than statistical significance'.

Another way to reduce the complexity of a turbulent flow is to decompose it into typical, *coherent*, structures. Ever since the introduction of the proper orthogonal decomposition (POD) into the field of turbulence by Lumley (1967) (see also Holmes *et al.* 1996) this has greatly contributed to the understanding of turbulence by facilitating a classification of the flow into typical events. Given any sequence of flow fields or 'snapshots' (linear or non-linear) generated either from a numerical simulation or an experiment, this procedure decomposes the flow into its most energetic parts — thereby ranking the flow structures according to their kinetic energy. The application of POD to a minimal channel flow was explored by Webber *et al.* (1997). The identified structures were found to have strong similarities to structures seen in experiments. They found the most energetic modes identified by the POD to be two counter rotating vortices, so-called 'roll modes', with no streamwise dependence, and with a spacing spanning the entire channel width ($\lambda_z^+ = 128$). The second most energetic mode were quasi-streamwise vortices tilted away from the wall at an angle, so-called 'propagating modes' with a streamwise dependence. By tracking the energy evolution of these respective modes, Webber *et al.* (1997) could conclude that a turbulent *burst* was preceded by a rapid growth of the propagating modes and corresponding decay of the roll modes. Moreover, they found that the roll mode and propagating modes made independent contributions to the Reynolds stress, with the roll modes being active near the wall and the propagating modes closer to the channel centre.

The flow structures having most of the energy need not be the dynamically most important ones. But since high frequency oscillations in a flow are damped due to viscosity they will generally have a low energy content. These structures are therefore ranked low and could easily be overlooked by POD. The Koopman mode decomposition (Rowley *et al.* 2009) is instead associating each spatial flow

structure with one frequency. Thus, given the same sequence of snapshots the POD and Koopman modes are spanning the same space, but whereas each POD mode contains many frequencies, each one of the Koopman modes are beating with one distinct frequency. This makes it easier to locate high frequency modes, although containing little energy.

To conclude, the concept of a minimal flow unit has introduced a simpler system in which the dynamics of wall-bounded turbulence can be studied. Proper orthogonal decomposition of this flow has been shown to give further insight to the dynamics. However, this particular decomposition does not give the full temporal understanding of the flow. Therefore, we here attempt to apply a Koopman mode analysis to this flow in order to find the physically relevant structures of wall-bounded turbulence having the most dominant frequencies. The following outline of the paper is given. In section 2, the numerical method and simulation set-up is presented. Then, in section 3, time probes from the simulation are analysed. In section 4.1, the flow is decomposed into POD modes and compared to the findings by Webber *et al.* (1997), after which a Koopman mode analysis is presented and evaluated in section 4.2. Finally, in section 5, the conclusions are given.

2. Numerical method and simulation set-up

The minimal channel flow is simulated by means of a direct numerical simulation, where the incompressible Navier–Stokes equations are solved without any modelling. Sufficiently high resolutions in time and space are used in order to resolve all scales of motion. The equations are solved in a streamwise (x) and spanwise (z) periodic domain, with no-slip conditions applied in the wall-normal direction (y). The domain, shown in figure 1(a), is discretized using a high-order spectral element method implemented in the code `nek5000`, developed by Fischer *et al.* (2008). Further details on space discretization and time integration can be found in Fischer (1997). The size of the domain is chosen in accordance with Webber *et al.* (1997), where the box lengths were set to $L_x = \pi h$, $L_y = 2h$, $L_z = 0.3\pi h$, h being the channel half width. The spatial resolution of $(N_x, N_y, N_z) = (48, 129, 24)$, similar to Webber *et al.* (1997), is obtained using $6 \times 16 \times 3$ elements, each having a polynomial order of 7, in the streamwise, wall-normal and spanwise directions, respectively. A Reynolds number of $Re = u_b h/\nu = 2000$, based on bulk velocity and channel half width, was achieved through a constant mass flux. The corresponding friction Reynolds number, $Re_\tau = u_\tau h/\nu$ based on friction velocity and channel half height, was computed to be 133.6, in close agreement with Webber *et al.* (1997) who reported a friction Reynolds number of 135.5.

3. Temporal analysis of the direct numerical simulation

Temporal information of the minimal channel flow was obtained by placing a time signal probe in the flow at the position $\boldsymbol{x} = (0, -0.75, 0)$ and measuring the streamwise velocity component. The recording started when the

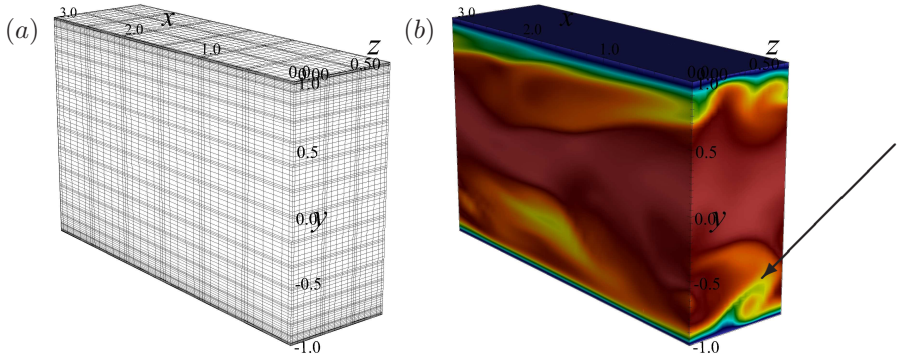

FIGURE 1. (*a*) Computational domain and spectral element mesh employed in the present study. (*b*) Snapshot of the minimal channel at $Re_\tau = 133.6$.

flow had reached a fully turbulent state and continued over a non-dimensional time of $tu_b/h = 2451$, corresponding to approximately 780 flow-through times, *i.e.* $tu_b/L_x = 780$. The obtained time signal is shown in figure 2(*a*), with its power spectral density (PSD) shown to the right in figure 2(*b*). Note that in the following all spectra are normalised with their own maximum. The two first frequency peaks correspond to Strouhal numbers of $St_1 \equiv fh/u_b = 0.0078$ (giving a time period of $T_1 = 128$), $St_2 = 0.27$ ($T_2 = 3.7$). The third peak is just a higher harmonic of St_2. Naturally, the peaks in the power spectrum vary slightly depending on the location of the probe. However, these two frequency-ranges are undoubtedly dominant in the near-wall region. The detected frequencies are thought to origin from the 'wiggling' of the low speed streak, captured by the snapshot in figure 1(*b*) close to the lower wall (indicated by the arrow), also supported by animations of the flow. Due to the imposed streamwise periodicity on the flow, it seems plausible that the dominant frequencies are connected to the length of the domain via a convection velocity. Hence, using a convection velocity of $u^+_{\text{conv}} \approx 10$ (Kim & Hussain 1993) — which together with $u_\tau = \frac{Re_\tau}{Re_b} = \frac{133.6}{2000} \approx 0.07$ gives $u_{\text{conv}} = 0.7$ — this period will be $T_c = L_x/u_{\text{conv}} = \pi/0.7 \approx 4.5$, which agrees roughly with T_2 above. The lowest frequency, whose time period is given by T_1, corresponds to the findings by Jiménez & Moin (1991), who were able to identify a very long intermittency cycle of $T \equiv u_{c,\text{lam}}t/h \approx 100$ in their minimal flow configuration.

4. Modal decomposition

Consider the turbulent flow $\boldsymbol{u}(\boldsymbol{x}, t)$ with velocity vector $\boldsymbol{u} = (u, v, w)$, defined in physical space $\boldsymbol{x} = (x, y, z)$ and time t. A modal decomposition of this flow

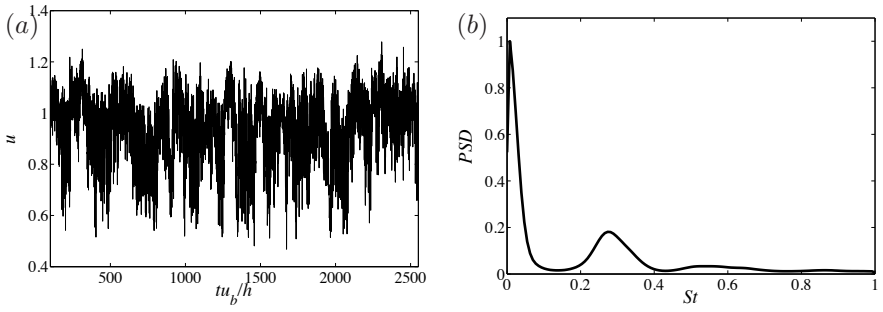

FIGURE 2. (*a*) Time signal from a probe located at $\boldsymbol{x} = (0, -0.75, 0)$, (*b*) power spectral density (PSD) of the time signal in (*a*).

attempts to split the space and time dependence, and is thus of the form,

$$\boldsymbol{u}(\boldsymbol{x}, t) = \sum_{j=0}^{\infty} a_j(t)\boldsymbol{\phi}_j(\boldsymbol{x}). \tag{1}$$

Since our velocity fields are truncated by the numerical simulation, this sum can without loss of generality be taken up to some $m \ll \infty$. The spatial modes $\boldsymbol{\phi}_j(\boldsymbol{x})$ and the temporal coefficients $a_j(t)$ remain to be determined. The decomposition (1) is however not at all unique. For linear problems, where $\dot{\boldsymbol{u}} = \mathbf{A}\boldsymbol{u}$, a natural choice for the modes are the eigenfunctions of the linear operator $\mathbf{A}$. For non-linear problems, however, one has to resort to other techniques. Here, we shall discuss two techniques, which given a sequence of flow fields or 'snapshots', saved at m discrete times $\{\boldsymbol{u}(t_1), ..., \boldsymbol{u}(t_m)\}^{\mathrm{T}}$, will find modes spanning this particular space. The proper orthogonal decomposition is concerned with finding eigenfunctions of the two-point spatial correlation tensor, whereas Koopman modes are eigenfunctions of the approximated linear evolution operator — both to be discussed in more detail in the next section.

4.1. *Proper orthogonal decomposition*

As mentioned above, the proper orthogonal decomposition amounts to finding the eigenvalues and corresponding eigenvectors of the spatial two-point correlation tensor $\boldsymbol{R}(\boldsymbol{x}, \boldsymbol{x'}) = \frac{1}{T}\int_T \boldsymbol{u}(t)\boldsymbol{u}(t)^{\mathrm{T}}\,\mathrm{d}t$. By letting $\mathbf{U}_m = [\boldsymbol{u}_0\ \boldsymbol{u}_1\ \boldsymbol{u}_2\ ...\ \boldsymbol{u}_m]^{\mathrm{T}}$ be the sequence of m snapshots, the above can in a discrete form be written $\mathbf{R} = \frac{1}{m}\mathbf{U}^{\mathrm{T}}\mathbf{U}\mathbf{G}$, where $\mathbf{G}$ contains the spatial integration weights. Thus, one is interested in solving

$$\mathbf{R}\boldsymbol{\Phi}^{\mathrm{T}} = \boldsymbol{\Phi}^{\mathrm{T}}\boldsymbol{\Lambda}, \tag{2}$$

where $\boldsymbol{\Phi} = [\boldsymbol{\phi}_0\ \boldsymbol{\phi}_1\ \boldsymbol{\phi}_2\ ...\ \boldsymbol{\phi}_m]^{\mathrm{T}}$ is the matrix of the spatial modes in equation (1), and $\boldsymbol{\Lambda}$ is the diagonal matrix with the corresponding eigenvalues $\lambda_1, \lambda_2, ..., \lambda_m$. The m temporal coefficients at m discrete times in equation (1), written in matrix form as $\mathbf{A} = [a_0\ a_1\ a_2\ ...\ a_m]$, can then in a successive step be solved

for by projecting the spatial modes over the snapshots,

$$\mathbf{A} = \mathbf{U}\mathbf{G}\mathbf{\Phi}^{\mathrm{T}}. \tag{3}$$

For high spatial resolutions $\mathbf{R}$ can be very large and equation (2) is usually intractable to solve. However, using the snapshot method (Sirovich 1987), equation (2) can be circumvented by solving an eigenvalue problem of the generally smaller temporal two-point correlation tensor $\mathbf{C} = \frac{1}{m}\mathbf{U}\mathbf{G}\mathbf{U}^{\mathrm{T}}$, such that

$$\mathbf{C}\mathbf{A} = \mathbf{A}\mathbf{\Lambda}. \tag{4}$$

Then, as a second step, the spatial eigenfunctions are constructed as

$$\mathbf{\Phi} = \frac{1}{m}\mathbf{\Lambda}^{-1}\mathbf{A}^{\mathrm{T}}\mathbf{U}. \tag{5}$$

Here, the division by the respective eigenvalue ensures that the modes are normalised to unit energy. Once this is done, the temporal coefficients can be computed according to equation (3). For the present POD analysis, a set of $m = 4903$ snapshots, spanning a total time of $tu_b/h = 2451$, is used. The temporal resolution is thus given by $\Delta tu_b/h = 0.5$. This data was generated by the DNS and analysed in terms of time signal probes in section 3. The energy of the respective modes are shown in figure 3(a), with the most energetic mode — containing as much as 98.5 % of the total energy — being the mean flow, from now on called 'mode 0'. The spectrum falls initially rapidly and mode number 100 has already five orders of magnitude less energy than the mean flow. As one would expect for a turbulent flow, beyond this point the slope of the spectrum levels off and the last 98 % of the modes contain a rather similar amount of energy, also in agreement with Webber *et al.* (1997). Similar conclusions can be drawn from the cumulative energy sum, $s_p = \sum_{i=0}^{p} \lambda_i$, shown in figure 3($c$). A closer look at the energy of the 30 first modes in figure 3(b) shows that the first few modes seem to form a group of similar energy, which might be a sign of a travelling structure. Then, however, the energy in the respective modes decrease rather monotonically. The reason may be that only the large anisotropic structures can be said to travel, whereas the small-scale turbulence does not have any preferred direction. In agreement with Webber *et al.* (1997) the most energetic POD modes consist of structures with no streamwise dependence, shown by positive and negative surfaces of constant streamwise velocity in figure 4(a). This structure (referred to as 'roll modes' by Webber *et al.* 1997) corresponds to a high and a low speed streak, with a spanwise width coinciding with the streak spacing of $\lambda^+ \approx 100$ observed in numerous wall-bounded turbulent flows (see *e.g.* Kline *et al.* 1967; Smith & Metzler 1983). The next group of modes are structures with a streamwise dependence of one wavelength ('propagating modes' in Webber *et al.* 1997), exemplified by mode 7 in figure 4(b), which is the most energetic mode in this family. They appear as quasi-streamwise vortices tilted away from the wall at an angle. Note that the energy contained in mode 1 and mode 7 compared to the total energy are tiny fractions only: 0.13 % and 0.021 %, respectively. Note also that mode 7 has only 16 % of the energy compared to mode 1. Higher modes

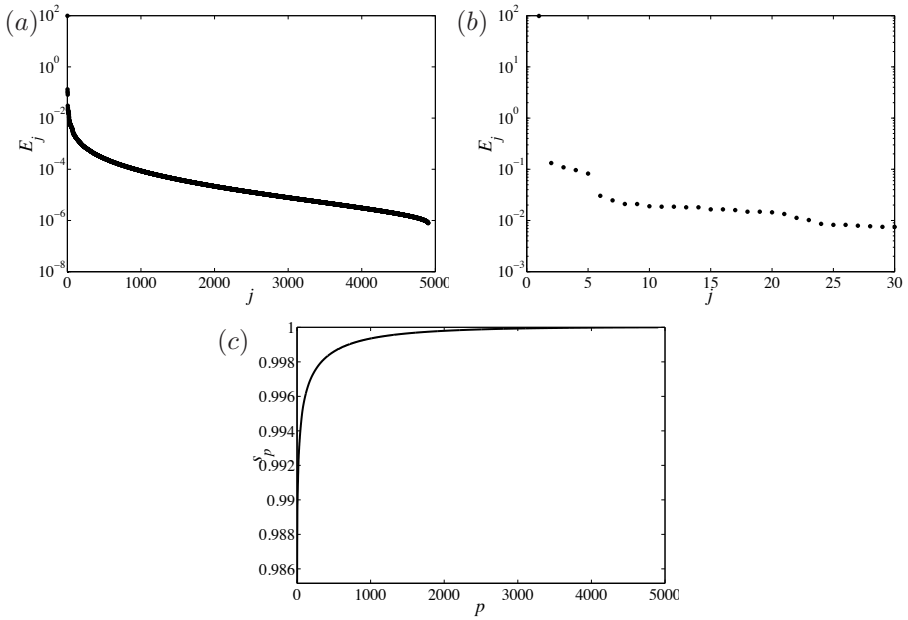

FIGURE 3. (*a*) The energy $E_j = (\lambda_j / \sum_i \lambda_i) \times 100$ of the POD modes with $j = 1, ..., 4903$, (*b*) close-up view showing the energy of the first 30 POD modes, (*c*) cumulative energy sum, $s_p = \sum_{i=0}^{p} \lambda_i$.

are essentially similar structures (*i.e.* roll modes and propagating modes), but shifted in the streamwise and spanwise directions.

These modes provide useful information about the typical structures found in near-wall turbulence. Next, the respective time evolutions of one of the roll modes (mode 1) and one of the propagating modes (mode 7) are shown in figure 5(*a*-*b*), with a close-up view provided in figure 5(*c*). We observe a considerable difference in terms of frequency between the two modes. The peaks in the PSD (figure 5*d*) coincide well with the frequency peaks detected with the time signal probe, indicated by the dashed line. More specifically, the roll mode has a peak Strouhal number of $St_{roll} = 0.0078$ ($T_{roll} = 128$), whereas the propagating mode has a peak Strouhal number of $St_{prop} = 0.28$ ($T_{prop} = 3.6$). These findings provide us with structures associated with the peaks in the PSD from the DNS. In particular, a structure can be connected to the long intermittency cycle identified by Jiménez & Moin (1991). No comparison regarding dominant frequencies could be made with Webber *et al.* (1997), since no spectra were provided therein.

Even though the frequency peaks in figure 5(*d*) are distinct and well-defined, the flow structures given by the POD procedure will inevitable contain

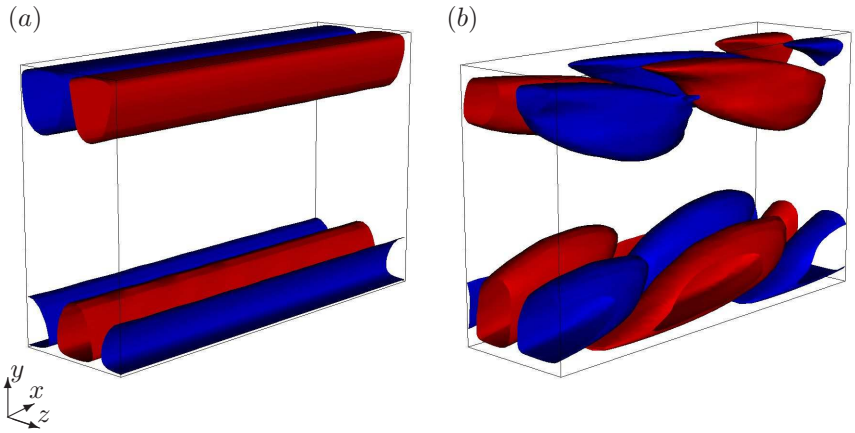

FIGURE 4. Isocontours (*red:* $u/u_b = 0.3$, *blue:* $u/u_b = -0.3$) of streamwise velocity of POD mode (*a*) 1 and (*b*) 7.

a wide range of frequencies. In order to give a rigorous spectral analysis of the flow, we now proceed with the Koopman mode analysis.

4.2. *Koopman mode decomposition*

The most probable events in the flow, provided by the POD, are in general not separated in frequency space, *i.e.* one spatial structure contains a range of different frequencies. A clear separation in frequency space is instead provided by a Koopman mode decomposition. Here, we outline the 'dynamic mode decomposition' (DMD) by Schmid (2010), which is a numerical technique to compute a discrete approximation to the Koopman modes.

As for the POD, our point of departure is the sequence of $m = 4903$ snapshots. We are interested in the properties of the linear operator $\mathbf{A}$, which can propagate one snapshot forward in time, such that

$$\boldsymbol{u}_{i+1} = \mathbf{A}\boldsymbol{u}_i. \tag{6}$$

If the underlying equation that generated the snapshots were linear, then equation (6) would not involve any assumptions. However, if the snapshots would stem from a non-linear process, then equation (6) would be the linear approximation to this process. We will here investigate the assumed linear mapping (6) by analysing the the eigenvalues and respective eigenvectors of $\mathbf{A}$.

In fluid mechanics, the system matrix $\mathbf{A}$ is often very large and hence iterative methods, such as the Arnoldi algorithm (see *e.g.* Trefethen & Bau 1997), are the methods of choice in order to find some dominant eigenvalues and eigenvectors of $\mathbf{A}$. The DMD builds on the Arnoldi algorithm, but the great advantage of the DMD is that $\mathbf{A}$ need not to be known explicitly, as would be the case for the Arnoldi method. Instead, the eigenvalues and eigenvectors can be found solely by processing a sequence of snapshots, either velocity fields

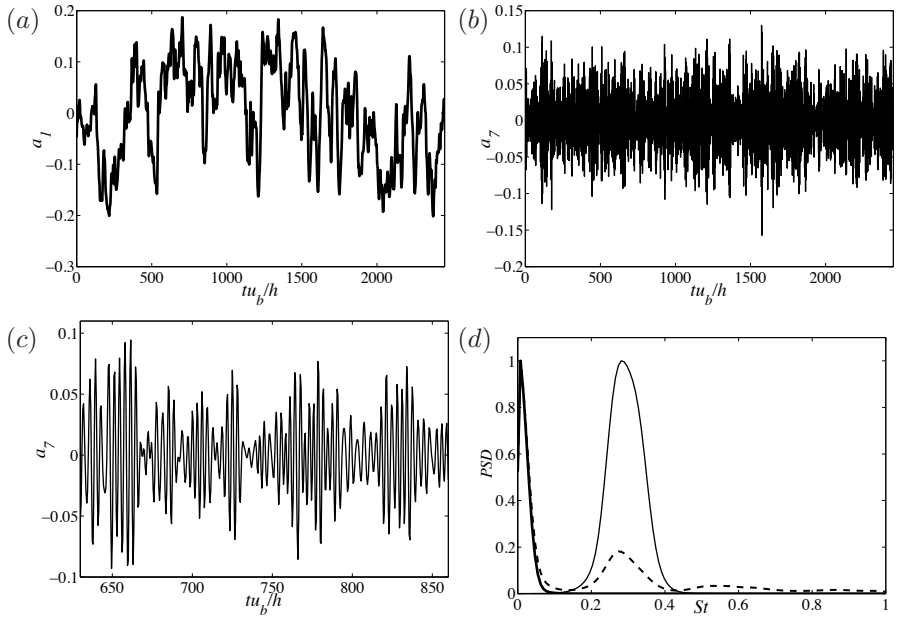

FIGURE 5. Temporal evolution of POD mode (*a*) 1 and (*b*) 7. (*c*) Close-up view of (*b*) showing some of the higher frequencies. (*d*) Power spectral density (PSD) of the respective signals in (*a*) (——) and (*b*) (——) compared to the PSD of the time signal probe (- - - -).

generated from a numerical simulation (where the system matrix is in general known) or measurement data (1D, 2D or 3D) from a physical experiment. Briefly, the DMD algorithm works as follows, focusing on the procedure based on the companion matrix, $\mathbf{M}$, below (Ruhe 1984). Further details are found in Schmid (2010).

Using the snapshots, we shall define two sequences, given by

$$\mathbf{U}_m = [\boldsymbol{u}_0\ \boldsymbol{u}_1\ \boldsymbol{u}_2\ ...\ \boldsymbol{u}_{m-1}] \tag{7}$$

and

$$\mathbf{U}_{m+1} = [\boldsymbol{u}_1\ \boldsymbol{u}_2\ \boldsymbol{u}_3\ ...\ \boldsymbol{u}_m]. \tag{8}$$

Our task is now to find the matrix $\mathbf{M}$ such that,

$$\mathbf{U}_{m+1} = \mathbf{U}_m\mathbf{M} + \mathbf{r}, \tag{9}$$

where $\mathbf{r}$ is a residual vector. This can be done by solving a least-square problem. Once $\mathbf{M}$ is found, eigenvectors and corresponding eigenvalues to $\mathbf{M}$ are computed, *i.e.* we are solving

$$\mathbf{MT} = \mathbf{T}\boldsymbol{\Lambda}. \tag{10}$$

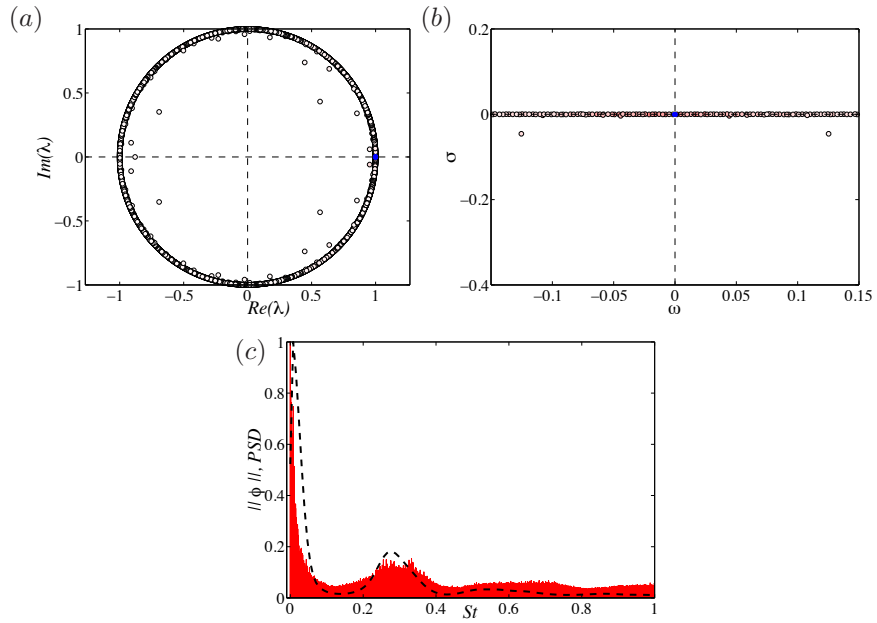

FIGURE 6. (*a*) Koopman (Ritz) eigenvalues and (*b*) spectrum obtained as $\omega_j = \mathrm{Im}\{\log(\lambda_j)\}/\Delta t$ and $\sigma_j = \mathrm{Re}\{\log(\lambda_j)\}$, where the amplitude of the respective modes vary smoothly from red (high) to white (low). The first Koopman eigenvalue (λ_0) corresponding to the mean flow is shown in blue. (*c*) Amplitudes of the modes as a function of frequency (*red*), together with the PSD of the time signal probe (----).

As for the Arnoldi algorithm, where the decomposition (9) also appear, the eigenvalues $\mathbf{\Lambda}$ (called Ritz values) approximate some of the eigenvalues of $\mathbf{A}$. Now, the so-called *dynamic modes*, $\mathbf{\Phi} = [\boldsymbol{\phi}_0\ \boldsymbol{\phi}_1\ \boldsymbol{\phi}_2\ \ldots\ \boldsymbol{\phi}_{r-1}]$, are computed analogous to expression (5) for the POD modes,

$$\mathbf{\Phi} = \mathbf{U}_m \mathbf{T}. \tag{11}$$

The dynamic modes and the Ritz values, of which the latter are shown for the present case in figure 6(*a*), correspond to the finite approximation of the Koopman modes and Koopman eigenvalues, rigorously shown by Rowley *et al.* (2009). We observe that most of the eigenvalues lie on the unit circle ($|\lambda_j| = 1$), which shows that the flow under consideration is in equilibrium, as no growth or decay is present (Mezić 2005; Rowley *et al.* 2009). This is also seen by plotting the growth rate σ_j as a function of angular frequency ω_j (converted into Strouhal numbers as $St = \omega h/2\pi u_b$) in figure 6(*b*). (Note that only part of the spectrum is shown.) Since the Koopman eigenvalues $\lambda_j \in \mathbb{C}$ characterise the temporal behaviour of the Koopman modes in that the phase determines its

frequency and the amplitude determines the growth rate, the angular frequency is obtained by $\omega_j = \mathrm{Im}\{\log(\lambda_j)\}/\Delta t$. Correspondingly, the growth rate is given by $\sigma_j = \mathrm{Re}\{\log(\lambda_j)\}$. As for the POD modes, the zeroth Koopman mode is the steady mean flow and indicated by the blue symbol in figures 6(*a*-*b*), where indeed the phase and the frequency are zero, respectively. The rest of the unsteady Koopman eigenvalues vary in colour from red to white, where red denotes a mode with high amplitude and white a mode being weak in amplitude. The amplitude is here defined as the global energy norm of the eigenvectors, such that $||\boldsymbol{\phi_j}|| = \sqrt{\boldsymbol{\phi_j}^{\mathrm{T}}\boldsymbol{\phi_j}}$.

By plotting the amplitudes of the Koopman modes as a function of the frequency of the corresponding eigenvalue (figure 6*c*), we can directly compare the result from the Koopman analysis to that from the time probe and the POD analyses. The eigenvalues come in complex conjugate pairs, but for simplicity we only show $St > 0$. The dashed line again shows the PSD from the time signal probe. Two dominant peaks and higher harmonics of the second one can be observed, in agreement with the PSD obtained from the time probe. The first peak (not fully visible in figure 6(*c*) due to cutting of the y-axis) has a Strouhal number $St_1 \approx 0.0078$ ($T_1 = 128$), which is exactly the same frequency compared to what is obtained from the time probe and the POD analyses. A closer look at the second peak in figure 6(*c*) reveals that it is a double peak, of which the lower frequency is given by $St_{2a} = 0.26$, corresponding to a time period of $T_{2a} = 3.8$. This frequency matches the previously discussed frequencies. The higher frequency is located at a Strouhal number of $St_{2b} = 0.33$, which gives the slightly shorter time period of $T_{2b} = 3.0$. It is interesting to compare the spatial structures connected to these peaks, depicted in figure 7. First of all, the structures corresponding to the first peak, reported in figure 7(*a*), are similar to the roll modes obtained from the POD analysis in figure 4(*a*). In fact, all modes with a frequency less than the second peak in the spectra in figure 6(*c*) correspond to these structures. Secondly, shown in figure 7(*c*) is the mode with frequency St_{2a}, *i.e.* the peak frequency of the propagating POD mode. They compare well to each other, save that the Koopman mode is somewhat more noisy. Their main feature is that they are alternating negative and positive and extend all the way from the wall, tilted at an angle. However, the mode corresponding to St_{2b}, shown in 7(*b*), can be seen to be located slightly further away from the wall. As the convection velocity is higher in this region, this explains its somewhat higher frequency.

Overall, similar structures are found by the two techniques. However, compared to the structures obtained from the POD in figure 4, it can be observed that the Koopman modes in figure 7 are less smooth. It should be pointed out that this is not a sign of unconverged numerics, but rather inherent in the way the modes are separated in spectral space.

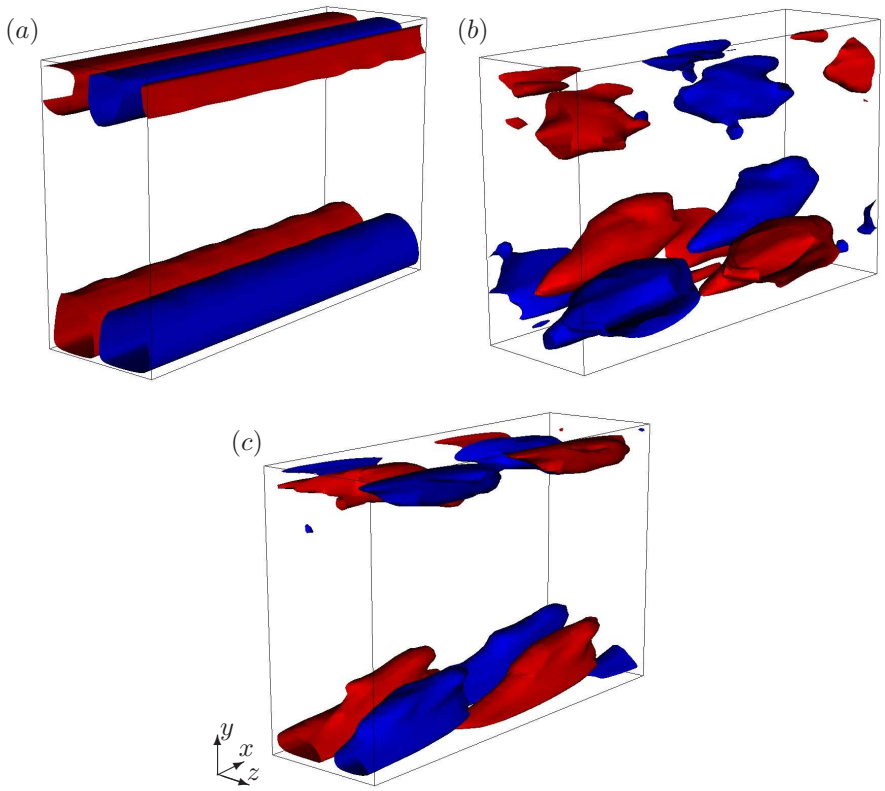

FIGURE 7. Isocontours of streamwise velocity of Koopman mode (*a*) 4 (*red:* $u/u_b = 0.4$, *blue:* $u/u_b = -0.4$), (*b*) 129 (*red:* $u/u_b = 0.2$, *blue:* $u/u_b = -0.2$) and (*c*) 140 (*red:* $u/u_b = 0.2$, *blue:* $u/u_b = -0.2$).

5. Conclusions

A modal analysis has been performed on a fully non-linear minimal channel flow using DNS data from a high-order spectral element code. In particular, the classical proper orthogonal decomposition (POD) (Lumley 1967; Holmes *et al.* 1996) was compared to the more recent Koopman mode decomposition (Rowley *et al.* 2009), where we followed Schmid (2010) for the implementation. In addition, spectral analysis was performed of a time signal probe placed in the flow domain. It can be concluded that both the POD and Koopman mode decomposition are able to identify coherent structures associated with the dynamics of the single low-speed streak present in the minimal flow unit. The structures found by both procedures can be categorised into two different groups: One consisting of structures with no streamwise dependence, so-called

'roll modes' (after Webber *et al.* 1997), which are the streamwise streaks observed in wall-bounded turbulence. The other group contains structures with a streamwise dependence of one wavelength, (termed 'propagating modes' in Webber *et al.* 1997). They are tilted away from the wall at an angle and can be related to quasi-streamwise vortices, commonly seen in physical experiments in conjunction with turbulent bursts. Each one of the coherent structures found can be associated with a specific frequency. More specifically, the roll mode has a time period of $T_{roll} \equiv tu_b/h \approx 128$, whereas the propagating mode has a time period of $T_{prop} \approx 3.5$. The latter can be directly related to the imposed streamwise periodicity via the length of the flow domain and a convection velocity. The former is thought to be the structure connected to the long intermittency cycle identified by Jiménez & Moin (1991). Both the POD and Koopman mode decomposition are able to detect these two dominant frequencies. The structures from the two procedures pertaining to these frequencies are in general very similar, in particular the roll modes. Concerning the propagating modes there are small detectable differences. More specifically, the Koopman analysis could identify a double peak in the spectra connected to the propagating mode. For the lower frequency, a structure extending all the way to the wall was found, whereas for the higher frequency a structure localised further out from the wall could be identified.

Whereas for the POD the frequencies pertaining to the modes are found through a spectral analysis of the time coefficient of the respective modes, these frequencies come out naturally from the Koopman mode analysis. Moreover, each one of the POD modes contain a wide range of frequencies centred around the peak frequency, referred above to as the dominant frequency. The Koopman modes, on the other hand, are clearly separated in spectral space, such that each mode contains only one distinct frequency. In flow configurations which are not as dominated by one frequency as the present one, this could serve to locate parts of the flow where dominant frequencies occur. An excellent example of this was shown by Rowley *et al.* (2009) on the jet in crossflow, where structures connected to the high-frequency Kelvin-Helmholtz instability on the jet could be separated from the low shedding of a von Kármán-type structure closer to the wall. However, when the dynamics are totally governed by one forced frequency, as the present case clearly show, the POD can equally well suffice to pick them up.

Finally, it was noticed that the Koopman modes are less smooth in space, and it was pointed out that this is a cause of the separation in spectral space. The POD modes, on the other hand, can be seen as an average of all the Koopman modes around the peak frequency, and will hence appear smoother in space. In time, however, the opposite is observed: the POD time signals in figure 5 are not smooth at all, whereas the corresponding Koopman mode only has one specific spectral component (*i.e.* a single sine wave) and will therefore be smooth.

Computer time was provided by SNIC (Swedish National Infrastructure for Computing) with a generous grant by the Knut and Alice Wallenberg (KAW) Foundation at the Centre for Parallel Computers (PDC) at the Royal Institute of Technology (KTH). Onofrio Semeraro is acknowledged for fruitful discussions and for proofreading the current manuscript.

References

Fischer, P. F. 1997 An overlapping Schwarz method for spectral element solution of the incompressible Navier–Stokes equations. *J. Comput. Phys.* **133** (1), 84–101.

Fischer, P. F., Lottes, J. W. & Kerkemeier, S. G. 2008 nek5000 Web page. http://nek5000.mcs.anl.gov.

Holmes, P., Lumley, J. & Berkooz, G. 1996 *Turbulence, Coherent Structures, Dynamical Systems and Symmetry*. Cambridge University Press, Cambridge, UK.

Jiménez, J. & Moin, P. 1991 The minimal flow unit in near-wall turbulence. *J. Fluid Mech.* **225**, 213–240.

Kim, J. & Hussain, F. 1993 Propagation velocity of perturbations in turbulent channel flow. *Phys. Fluids* **5** (3), 695–706.

Kline, S. J., Reynolds, W. C., Schraub, F. A. & Runstadler, P. W. 1967 The structure of turbulent boundary layers. *J. Fluid Mech.* **30**, 741–773.

Lumley, J. L. 1967 The structure of inhomogeneous turbulent flows. In *Atm. Turb. Radio Wave Prop.* (ed. A. M. Yaglom & V. I. Tatarsky), pp. 166–178. Nauka, Moscow, Russia.

Mezić, I. 2005 Spectral properties of dynamical systems, model reduction and decompositions. *Nonlinear Dyn.* **41**, 309–325.

Rowley, C. W., Mezić, I, Bagheri, S, Schlatter, P & Henningson, D. S. 2009 Spectral analysis of nonlinear flows. *J. Fluid Mech.* **641**, 115–127.

Ruhe, A. 1984 Rational Krylov sequence methods for eigenvalue computation. *Linear Algebr. Appl.* **58**, 391–405.

Schmid, P. J. 2010 Dynamic mode decomposition of numerical and experimental data. *J. Fluid Mech.* **656**, 5–28.

Sirovich, L. 1987 Turbulence and the dynamics of coherent structures, i-iii. *Quart. Appl. Math.* **45**, 561–590.

Smith, C. R. & Metzler, S. P. 1983 The characteristics of low-speed streaks in the near-wall region of a turbulent boundary layer. *J. Fluid Mech.* **129**, 27–54.

Trefethen, L. N. & Bau, D. 1997 *Numerical Linear Algebra*. SIAM, Philadelphia, USA.

Webber, G. A., Handler, R. A. & Sirovich, L. 1997 The Karhunen–Loève decomposition of minimal channel flow. *Phys. Fluids* **9** (4), 1054–1066.

Paper 5

5

A vorticity stretching diagnostic for turbulent and transitional flows

By Johan Malm*, Philipp Schlatter* and Neil. D. Sandham†

*Linné FLOW Centre, Swedish e-Science Research Centre (SeRC)
KTH Mechanics, 100 44 Stockholm, Sweden

†School of Engineering Sciences, University of Southampton
Southampton, SO17 1BJ, UK

Theor. Comput. Fluid Dyn. Accepted.

Vorticity stretching in wall-bounded turbulent and transitional flows has been investigated by means of a new diagnostic measure, denoted by Γ, designed to pick up regions with large amounts of vorticity stretching. It is based on the maximum vorticity stretching component in every spatial point, thus yielding a three-dimensional scalar field. The measure was applied in four different flows with increasing complexity: (a) the near-wall cycle in an asymptotic suction boundary layer (ASBL), (b) K-type transition in a plane channel flow, (c) fully turbulent channel flow at $Re_\tau = 180$ and (d) a complex turbulent three-dimensional separated flow. Instantaneous data shows that the coherent structures associated with intense vorticity stretching in all four cases have the shape of flat 'pancake' structures in the vicinity of high-speed streaks, here denoted 'h-type' events. The other event found is of 'l-type', present on top of an unstable low-speed streak. These events (l-type) are further thought to be associated with the exponential growth of streamwise vorticity in the turbulent near-wall cycle. It was found that the largest occurrence of vorticity stretching in the fully turbulent wall-bounded flows is present at a wall-normal distance of $y^+ = 6.5$, *i.e.* in the transition between the viscous sublayer and buffer layer. The associated structures have a streamwise length of $\sim 200 - 300$ wall units. In K-type transition, the Γ-measure accurately locates the regions of interest, in particular the formation of high speed streaks near the wall (h-type) and the appearance of the hairpin vortex (l-type). In the turbulent separated flow, the structures containing large amounts of vorticity stretching increase in size and magnitude in the shear layer upstream of the separation bubble, but vanish in the backflow region itself. Overall, the measure proved to be useful in showing growing instabilities before they develop into structures, highlighting the mechanisms creating high shear region on a wall and showing turbulence creation associated with instantaneous separations.

1. Introduction

A significant aspect of turbulence research over the last 40 years has been the search for typical or 'coherent' structures, following for example the work of Lumley (1967) (see also Holmes *et al.* 1996). This has greatly enhanced the fundamental understanding for turbulence, since it has brought some order to the otherwise chaotic picture of turbulence. Thus, in any recent introductory book on turbulence one finds that turbulence is composed of 'eddies' or vortices, and numerous studies have focused their attention on the dynamics of these. Though conceptually clear, a strict definition of a vortex has never been fully achieved. Consequently, there are a number of identification criteria available in the literature, see *e.g.* the comparison by Chakraborty *et al.* (2005). The various measures have their respective strengths and weaknesses, and are not universally applicable. The most obvious way to locate vortices would be to look for high values of vorticity. However, it is well-known (see *e.g.* Dubief & Delcayre 2000) that close to a solid wall the high values of mean shear creates vorticity which is usually significantly higher than the vorticity contained in coherent structures elsewhere. Localising low pressure areas in the flow can give a rough estimate of the orientation of vortices (see *e.g.* Robinson 1991), but will in general favour larger structures and miss the small vortices in the flow. Among the more sophisticated measures and nowadays the most widely used are the Π-criterion and the λ_2-criterion proposed by Hunt *et al.* (1988) and Jeong & Hussain (1995), respectively. For incompressible flow, the Π-criterion is equivalent to the negative of the second tensor invariant, $-Q$, discussed by Chong *et al.* (1990). Also the Δ-criterion introduced by Chong *et al.* (1990) belongs to the same class of vortex identification methods. All these measures are in one way or another based on the velocity gradient tensor. A review and more thorough definitions of the above measures can be found in Dubief & Delcayre (2000), which also includes an *a posteriori* analysis of a series of turbulent flows. The developed structures identified by these criteria are not necessarily the areas in a flow of most dynamical interest, *e.g.* regions where instabilities are growing. Generally, a vortex can be created (by some yet unspecified mechanism) after which it may be convected away from the active region of the flow. Thus, locating the vortex itself does not directly help to position the area of interest. On the other hand, by identifying the production of vorticity[1] the active region of the flow would instead be pinpointed. Among the various production terms in the vorticity transport equation, vorticity stretching is the one that can provide exponential growth, evident when studying the vorticity transport equation in an incompressible flow. Assume there is initially some vorticity, ω_s, and strain, $\partial u_s/\partial s$, in the direction of s, where s is the strain elongation axis. Assume further that the strain is negligible in the other spatial directions so that the vorticity tilting terms vanish, then the vorticity transport equation

[1] Vorticity does not necessarily imply vortices, but conversely, vortices do in general imply vorticity.

reduces to

$$\frac{D\omega_s}{Dt} = \omega_s \frac{\partial u_s}{\partial s}, \tag{1}$$

provided the Reynolds number (Re) is high enough so that the damping term $\nu\nabla^2\omega_s$ is small. Solving for ω_s gives

$$\omega_s \sim \exp\left(\frac{\partial u_s}{\partial s} t\right), \tag{2}$$

i.e. exponential growth of vorticity along s, assuming a constant strain rate following the fluid element.

The fact that vorticity stretching plays a crucial role in turbulent flows is clear, as the following examples will show. In wall-bounded turbulent flows, streamwise velocity streaks (Kline *et al.* 1967) and quasi-streamwise vortices (Smith & Metzler 1983) are known to dominate the near-wall region. It has been shown in several studies (Hamilton *et al.* 1995; Jiménez & Pinelli 1999) that these structures are tied together via a self-sustained cycle, where the streamwise vortices create streaks and the streaks break down to create new streamwise vortices. Minimal flow units (Jiménez & Moin 1991) were used to show that if this cycle was broken at any point the flow is likely to relaminarise. While the mechanism with which streaks are created by streamwise vortices is fully understood and well documented (see *e.g.* Klebanoff *et al.* 1962; Landahl 1980), there has been less consensus on how the streaks break down and the streamwise vortices are recreated. There are however indications (see *e.g.* Waleffe 1997) that the breakdown is preceded by exponential growth of x-dependent disturbances. For the late stages of the streak instability phase, Schoppa & Hussain (2002) elaborated on a mechanism responsible for the formation of streamwise vortex sheets which eventually collapse due to the stretching caused by the streamwise strain, $\partial u/\partial x$. This shows that vorticity stretching may be an important ingredient in the near-wall cycle. There is also some evidence (Jones *et al.* 2009) that vorticity stretching plays an important role in self-sustained transition processes, such as the unsteady vortex shedding in a separated flow. In addition, during the end-stage of K-type transition, it has been noted by Sandham & Kleiser (1992) that the stretching of vorticity involved in the roll-up of detached shear layers leads to turbulence regeneration.

To conclude, the above mentioned examples indicate that vorticity stretching is dynamically important for the growth of instabilities in wall-bounded flows. The importance of vorticity stretching in turbulence is well-documented, but is often presented in a statistical context, exemplified in Tsinober *et al.* (1995); Tsinober (2009). Similarly, extracting dynamically important regions that correspond to active vortical parts of the flow, has been attempted a few times, based on correlating negative λ_2 and *e.g.* TKE production and/or dissipation, see *e.g.* Helgeland *et al.* (2007). In addition, criterions suggested to identify coherent structures in turbulent flows have traditionally been focused on vortices. Therefore, we will propose a measure facilitating the study the local dynamics of the vorticity stretching mechanism. Thereby, one can locate

coherent structures of more dynamical importance than vortices *per se*. By the term 'dynamical importance', we mean a structure that can pinpoint regions where growing instabilities are present, as opposed to the ones just convected (and potentially diffused away) with the flow. The measure, proposed in the next section, will be evaluated in four different flows with successively increasing complexity: The near-wall cycle in an asymptotic suction boundary layer (ASBL); K-type transition in a plane channel flow; fully turbulent channel flow; and finally a fully three-dimensional separated flow. It will further be linked to the birth of vortices by locating high concentration of λ_2 (Jeong & Hussain 1995) in the flow.

2. New diagnostic measure

Consider the vorticity transport equation in an incompressible flow,

$$\frac{D\omega_i}{Dt} = \omega_j \frac{\partial u_i}{\partial x_j} + \frac{1}{Re}\frac{\partial^2 \omega_i}{\partial x_j \partial x_j}, \tag{3}$$

where the terms (no summation on α)

$$\omega_\alpha \frac{\partial u_\alpha}{\partial x_\alpha}, \qquad \alpha = 1, 2, 3, \tag{4}$$

are denoted *vorticity stretching terms*, in each spatial direction respectively. Vorticity stretching alone is a three-dimensional vector field, which in general is difficult to visualise and interpret. A scalar field is more conceivable, since it tells the observer where high 'concentrations' of the quantity in question can be found. Therefore, we propose our measure as the maximum vorticity stretching component in every point in space, thus yielding a three-dimensional scalar field.

In order to locate the largest occurrence of vorticity stretching in the flow, we will formally define the scalar measure as:

$$\Gamma_p(x, y, z, t) = \max\{\alpha|\omega_\alpha|, \beta|\omega_\beta|, \gamma|\omega_\gamma|\}, \tag{5}$$

where α, β and γ are the eigenvalues of the strain tensor $S_{ij} = \frac{1}{2}(\frac{\partial u_i}{\partial u_j} + \frac{\partial u_j}{\partial u_i})$ and ω_α, ω_β and ω_γ are the vorticity components along the principal axes given by the eigenvectors of S_{ij}. The subscript 'p' indicates that we are in a principal axis system, aligned with the direction of strain. Thus, this measure is a true scalar quantity, since it is indeed independent of coordinate system. The procedure of decomposing the strain tensor into its eigenvectors is commonly adopted in studies of homogeneous turbulence where the usual spatial coordinate directions have a subordinated meaning, (see *e.g.* She *et al.* 1991; Nomura & Post 1998). We will compare this measure to the following definition:

$$\Gamma_c(x, y, z, t) = \max\{|\omega_x|\frac{\partial u}{\partial x}, |\omega_y|\frac{\partial v}{\partial y}, |\omega_z|\frac{\partial w}{\partial z}\}, \tag{6}$$

where the subscript 'c' denotes 'Cartesian'. Note that this measure, in contrast to definition (5), is formally not a scalar quantity, since it is dependent on the fixed Cartesian coordinate directions. However, the actual differences may not

be very large for simple wall-bounded flows where the streamwise, spanwise and wall-normal directions are clearly defined and the flow is generally aligned with one coordinate axis. In those cases, for the sake of implementation and computational effort (since (5) involves solving an eigenvalue problem in every point in space), definition (6) might be preferable, provided that the corresponding results agree well with the more rigorous measure (5).

Alternatively, one could locate regions of high enstrophy production, which is already a scalar, frame-invariant quantity. In the equation governing the transport of enstrophy in an incompressible flow,

$$\frac{D\mathcal{E}}{Dt} = \omega_i \omega_j \frac{\partial u_i}{\partial x_j} + \frac{1}{Re}\left[\frac{\partial^2 \mathcal{E}}{\partial x_j \partial x_j} - \left(\frac{\partial \omega_i}{\partial x_j}\right)^2\right], \tag{7}$$

where the enstrophy is defined as $\mathcal{E} = \frac{1}{2}\omega^2$, the production terms are contained in the first expression to the right of the equality sign. This procedure does however not separate out the stretching process, which may be of particular interest, *i.e.* a stretching (not tilting) mechanism that can potentially lead to local exponential growth, as discussed above. The relative importance of the stretching-to-tilting related terms in equation (7) is further discussed in section 4.3.

In the following, we will examine the two variants of the proposed measure in four turbulent and transitional flows, mentioned above. In the next section (section 3), the simulation set-ups together with the numerical methods are introduced. In section 4, the measure is applied to the various flows and its dynamical aspects are investigated. Finally, in section 5, the conclusions from the present study are drawn.

3. Simulation set-up and methods

In this section, the four flow cases are introduced. We focus on three well-known, canonical flow cases in order to analyse the basic vorticity stretching mechanisms. In addition, one engineering flow featuring turbulent separation is included in order to broaden the study. The solutions of the incompressible Navier–Stokes equations were in the first three cases obtained by a Chebyshev-Fourier pseudo-spectral code and in the last case by a Legendre spectral element code described in Chevalier *et al.* (2007) and Fischer *et al.* (2008), respectively. Each one of the four cases are described more in detail below.

3.1. *Near-wall cycle in an asymptotic suction boundary layer (sinuous instability)*

The asymptotic suction boundary layer (ASBL) enables the study of an open boundary layer in the temporal framework, *i.e.* by employing suction at the wall the spatial growth of the boundary layer is removed, which opens the possibility of using a streamwise periodic domain. Hence, for the present simulation, performed at a Reynolds number of $Re = U_\infty \delta^*/\nu = U_\infty/V_\infty = 750$ (U_∞ being

the free-stream velocity, δ^* the displacement thickness and V_∞ the imposed vertical velocity) we used a computational domain with periodic boundary conditions in the spanwise and streamwise directions. A Dirichlet condition in the form of a constant velocity (V_∞) in the negative vertical direction was applied at the bottom of the domain. The dimensions of the domain (non-dimensionalised by δ^*) were chosen as $L_x = 12$, $L_y = 15$ and $L_z = 6$, such that the flow would be a 'minimal flow unit' and the dynamics of a single streak could be studied. A satisfactory spatial resolution was chosen to be $N_x = 32$, $N_z = 32$ Fourier modes in the streamwise and spanwise directions and $N_y = 129$ Chebyshev modes in the wall-normal direction. The critical trajectory ('edge state') was found by bisection where the amplitude of the random initial condition was tuned such that the flow neither becomes turbulent nor goes laminar (Schneider *et al.* 2007). The result is a time-periodic orbit with a period of $T = 3347$. Note that since breakdown to full turbulence never occurs, 32 Fourier modes in the streamwise and spanwise directions are sufficient, as verified by considering energy spectra during various time instants. The edge state in the ASBL flow was first computed and studied by Madré (2011) and discussed by B. Eckhardt (ETC-12, 2009, Marburg). The aim of the present case is however not to study its state-space properties, but merely to use the case as an alternative to minimal channel flows in an effort to simplify turbulent dynamics as much as possible. Some snapshots representative for the streak instability phase, breakdown and streak regeneration are shown in figure 1. The initially straight low-speed streak at $t = t_0$ (figure 1*a*) is indicated by the gray surface of constant streamwise velocity. Soon, around $t = t_0 + 0.16T$, the low-speed streak experiences a sinuous instability (with the plane of oscillation being wall-parallel) and x-dependent disturbances are amplified (figure 1*b*). The sinusoidal shape is more clearly visible in the top view, shown at approximately the same time, provided in figure 5(*a*). As the disturbance growth has reached nonlinear amplitudes ($t = t_0 + 0.39T$, figure 1*c*) the streak breaks down into smaller scales. During this phase, streamwise vortices are regenerated which leads to the growth of a new streak, displaced $L_z/2$ to the left. Thus, the flow at $t = t_0 + 0.5T$ shown in figure 1(*d*), is an exact equivalent to the flow in figure 1(*a*), translated by half the domain in z. [2]

3.2. *Subcritical K-type transition (varicose instability)*

Direct numerical simulation (DNS) of subcritical K-type transition in a periodic channel at $Re_b = 3333$, based on bulk velocity and channel half height, h, were performed in order to examine the role of vorticity stretching in a classical transitional flow (Gilbert & Kleiser 1990). This flow has turned into a canonical test case for transitional flow simulations (see Schlatter *et al.* (2004)). The initial disturbances consist of a two-dimensional Tollmien-Schlichting (TS) wave with a streamwise wave number of $\alpha = 1.12$ and an amplitude of 3% of the laminar centre-line velocity, together with two three-dimensional oblique waves

[2] In a dynamical systems sense, this is defined as a *relative periodic orbit*.

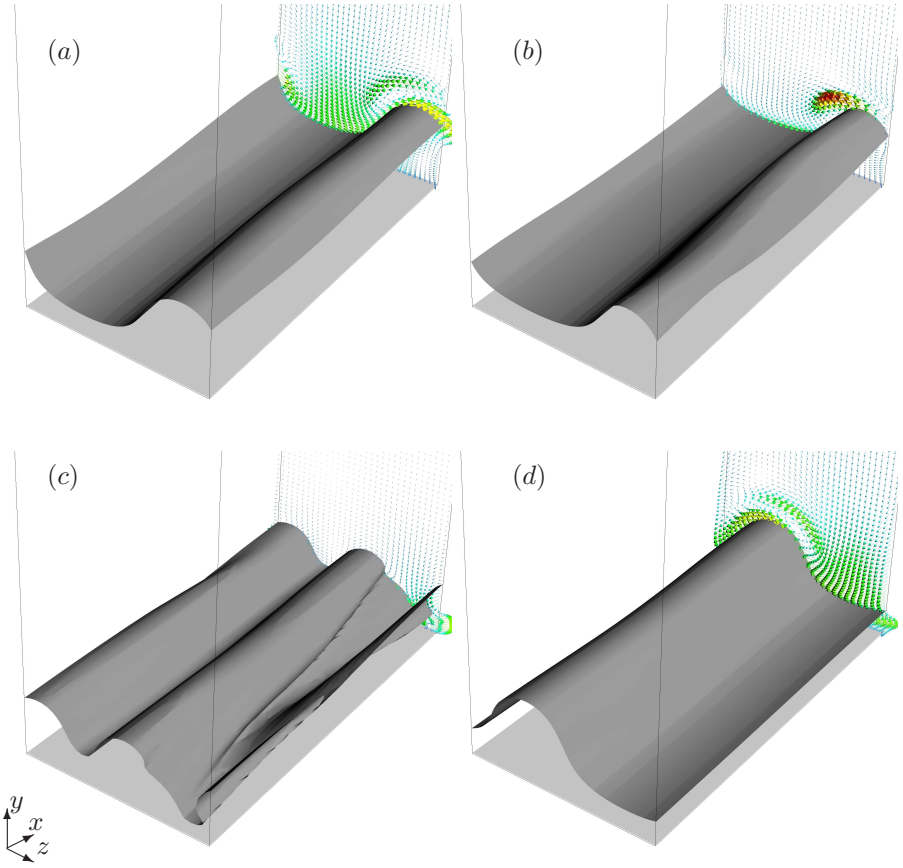

FIGURE 1. Evolution of the low-speed streak indicated by a surface of constant streamwise velocity, $u = 0.6$ (*gray*), at (*a*) $t = t_0$, (*b*) $t = t_0 + 0.16T$, (*c*) $t = t_0 + 0.39T$ and (*d*) $t = t_0 + 0.5T$, where T denotes the period of the periodic orbit. Vectors of crossflow velocities are shown in a crossflow plane.

with wave numbers $\alpha = 1.12$ and $\beta = 2.1$ and amplitudes of 0.05% each. This wave, superimposed on a laminar Poiseuille channel flow, experiences an exponential growth eventually leading to turbulent breakdown. Around $t = 120$ a so-called Λ-vortex appears, which develops into a hairpin vortex at $t \approx 135$ (Sandham & Kleiser 1992). Shortly thereafter ($t \approx 160$), the highly fluctuating transitional phase sets in; and finally, at $t \approx 220$, the flow has reached a fully developed turbulent state. The box lengths were $L_x \times L_y \times L_z = 2\pi h/\alpha \times 2h \times 2\pi h/\beta$ and the resolution used was $N_x \times N_y \times N_z = 128 \times 129 \times 128$, similar to Gilbert & Kleiser (1990).

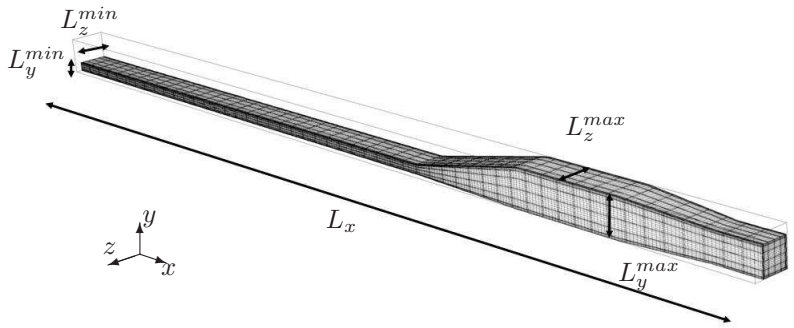

FIGURE 2. Computational domain showing the inflow duct, diffuser and outlet.

3.3. *Turbulent channel flow at $Re_\tau = 180$*

Fully turbulent channel flow simulations were performed at a Reynolds number of $Re_\tau = 180$, based on friction velocity, u_τ, and channel half height, h, in order to study the vorticity stretching diagnostics in a fully turbulent flow. The flow is driven by a fixed bulk given by $Re_b = u_b h/\nu = 2800$. Periodic boundary conditions in both the streamwise and spanwise directions were applied in a domain of size $L_x \times L_y \times L_z = 4\pi h \times 2h \times 2\pi h$ and a resolution of $N_x \times N_y \times N_z = 128 \times 129 \times 128$, similar to Moser *et al.* (1999). (Note that in this reference, the spanwise width was chosen to be $4\pi h/3$, *i.e.* slightly smaller than in the present simulation.)

3.4. *Turbulent 3D separation at Re = 10 000*

As a last example, a separated flow in a three-dimensional diffuser at $Re_b = 10\,000$ (based on bulk velocity and inflow duct height, h) is considered. The proposed measures are computed based on instantaneous velocity fields from the DNS presented in Ohlsson *et al.* (2010). The computational domain of size $L_x = 105.4h$, $L_y = [h, 4h]$, $L_z = [3.33h, 4h]$ is shown in figure 2. Laminar flow transitions to turbulence in the long inflow duct of rectangular cross-section through the action of an unsteady trip force applied in the very upstream region. Thus, fully turbulent flow enters the diffuser where the separation takes place. The diffuser is asymmetric, with two different opening angles in the y and z-directions, respectively. As a consequence, the separation is fully three-dimensional.

4. Application of the diagnostic measures

In the following, the evaluation of Γ_c and Γ_p in the four flow cases described in the previous section is presented.

4.1. *The effect of sinuous instabilities on vorticity stretching*

In order to facilitate understanding, Γ_c (retaining component information more obviously) is as a first step computed in the asymptotic suction boundary layer, with its evolution shown together with λ_2 in figure 3 at similar instants as in figure 1. What we observe (see also section 3.1) is approximately one quarter of the time-periodic orbit with period $T = 3347$, where the amplitude of the initial condition was tuned such that the flow never becomes fully turbulent nor goes completely laminar (a so-called 'edge state' Schneider *et al.* 2007). Thus, figure 3 shows a low-speed streak experiencing a sinuous instability (*a,b*), which reaches nonlinear amplitudes (*c*) and finally breaks down (*d*). Shortly thereafter (not shown), the flow approaches a more laminar-like state again and the exact same process would start again, with a spanwise phase shift. As long as the high- and low-speed streaks are (reasonably) straight, most of the vorticity stretching activity resides in the high-speed streak, close to the wall (figure 3*a*). Here, we observe that isosurfaces of constant Γ_c appear as flat 'pancake' structures close to the wall. A closer investigation reveals that Γ_c is dominated by $|\omega_z|\partial w/\partial z$, *i.e.* vorticity is stretched most intensively in the spanwise direction. As soon as the x-dependent disturbances are amplified and the streak starts to 'wiggle', we instead observe the highest values of Γ_c on the top of the low-speed streak (figure 3*b*). Henceforth, we will refer to the former event as 'h-type' (high-speed) and the latter as 'l-type' (low-speed). It is found that for this case Γ_c is always given by the spanwise vorticity stretching component, save that the sign is different due to the absolute value in the Γ_c-measure. As for the high-speed streak, the appearance of vorticity stretching alternates from side to side also on the low-speed streak, such that the highest values are always found on the convex side of the streak. The reason for this can be understood by studying the sketch in figure 4. Due to the mean shear, there are always high values of spanwise vorticity, ω_z, present close to the wall (A). In the case of a straight streak (figure 4*a*) this vorticity is lifted by the streamwise vortices, due to the well-known lift-up effect (Landahl 1980). In the braid region above the streak (B) the highest values of $\partial w/\partial z$ are found, which together with the lifted vorticity creates large spanwise vorticity stretching, $\omega_z\partial w/\partial z$. A similar situation is found to be present when the streak is bent (figure 4*b*). Since the braid region has moved over to the convex side of the streak (left in figure 4*b*), this is where we find high values of Γ_c. Similarly, high values of Γ_c are found to the right as soon as the streak 'wiggles' over to this side (the dashed line). It should be pointed out that the same mechanism is responsible for the high values of spanwise stretching alternating from side to side below the high-speed streak, given that the sketch in figure 4 in that case would be upside down. The cartoon in figure 4 is confirmed by results from the numerical simulation. In particular, a top view of a velocity field at $t = t_0 + 0.18T$ is provided in figure 5(*a*), where the relation between Γ_c, Γ_p, λ_2 and the low-speed streak can be seen. It shows that high values of $\Gamma_{c,p}$ are indeed located on the convex side of the bent streak. Here, we also note that

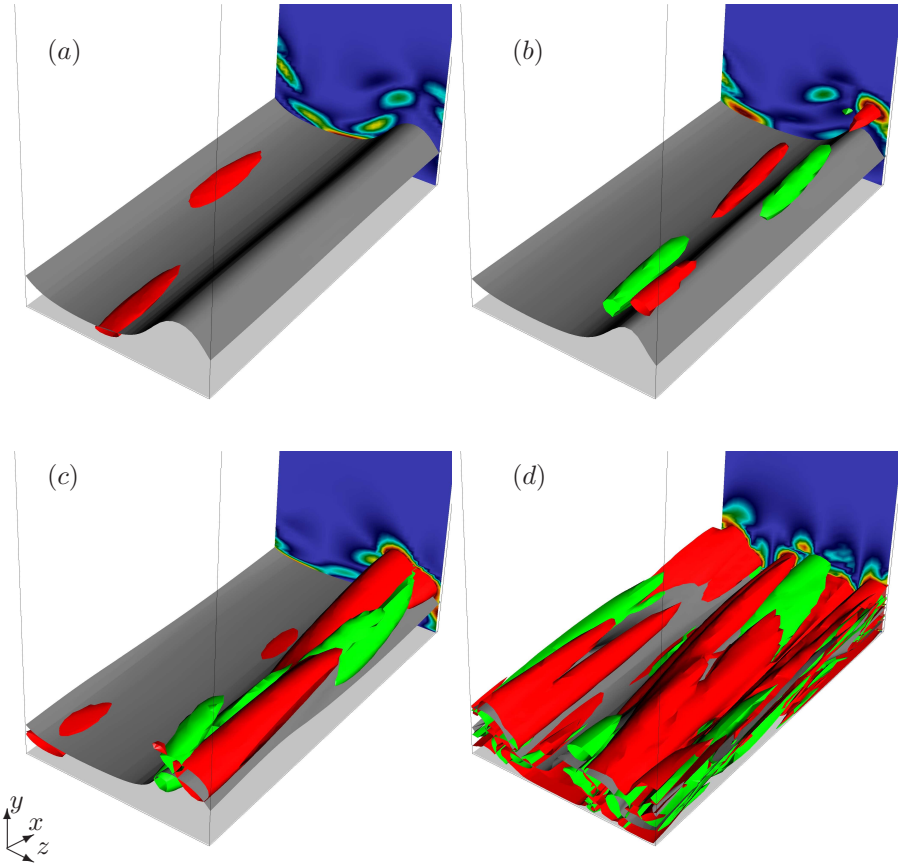

FIGURE 3. Evolution of Γ_c (*red*) and λ_2 (*green*) shown at (*a*) $t = t_0$, (*b*) $t = t_0 + 0.16T$, (*c*) $t = t_0 + 0.30T$ and (*d*) $t = t_0 + 0.39T$, where T denotes the period of the periodic orbit. The levels of the corresponding isosurfaces are fixed. The isosurface of streamwise velocity, $u = 0.5$ (*gray*), indicates streaks and the crossflow plane is coloured by Γ_c.

the differences between Γ_c and Γ_p are small. A more detailed comparison is given in figure 5(*b*,*c*), where the isosurface level is decreased approximately by a factor of two. Still, Γ_c and Γ_p are located in similar regions in the flow. More specifically, they both pick up vorticity stretching on top of the low-speed streak and beneath the high-speed streak near the wall associated with the creation of drag (*i.e.* the 'pancake' structures). It is evident that, although being located in the same regions, tilted at the same angle from the wall and being similarly flat, larger pancake structures are present in the case of Γ_c as compared to Γ_p. The main noteworthy difference is that, whereas Γ_c is decoupled from the

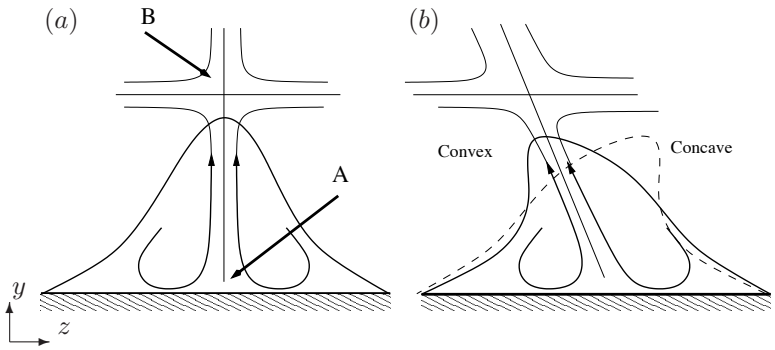

FIGURE 4. Explanation for an l-type event: (*a*) straight streak, where high values of ω_z are lifted from A and multiplied by spanwise strain in B; (*b*) similar mechanism for a bent streak in one of its outer positions. Thick lines denote a contour of constant streamwise velocity, thin lines show streamlines of in-plane flow and the dashed line shows the opposite outer position of the streak.

quasi-streamwise vortices, Γ_p is capable of picking up the associated vorticity stretching, as shown in 5(*b*). The reason for this is thought to be the slight tilting of the vortices in the flow, such that the vorticity stretching in the streamwise direction is small. In a principal axis system, however, this tilting is accounted for. Similar structures as the ones shown in figures 3 and 5 are obtained when visualising the instantaneous enstrophy production. However, as noted earlier in section 2, the enstrophy production does not allow for a separation of the various vorticity production mechanisms (*i.e.* stretching and tilting).

In order to see if $\Gamma_{c,p}$ can be linked to the existence of exponential growth, we show the evolution of the vorticity components $|\omega_i|$ together with $|\lambda_2|$ and $|\Gamma_{c,p}|$ in figure 6. More specifically, at each time the maximum absolute value over the domain, Ω, is found, *i.e.* $\max_\Omega\{|\cdot|\}$. Note that in the case of λ_2, only negative values isolate vortices (Jeong & Hussain 1995), *i.e.* $\max_\Omega\{|\min(\lambda_2, 0)|\}$ would be the correct operation. However, we have noted that the maximum absolute value always equals the absolute value of the largest negative value, *i.e.* $\max_\Omega\{|\lambda_2|\} \equiv \max_\Omega\{|\min(\lambda_2, 0)|\}$. The variables are scaled in outer units and $t/T = 0$ corresponds to t_0 in figure 3. Due to the mean shear, ω_z is the strongest vorticity component. The second strongest component is ω_y due to the existence of high- and low-speed streaks and the corresponding shear layer in between them. The first aspect to notice is that there is a slight decrease of these two vorticity components before the nonlinear breakdown ($t/T < 0.3$). However, at the same time the weakest component, ω_x, is increasing. As indicated by the straight dash-dotted line the growth is weakly exponential. A similar growth rate is observed for λ_2. As $\Gamma_{c,p}$ involves

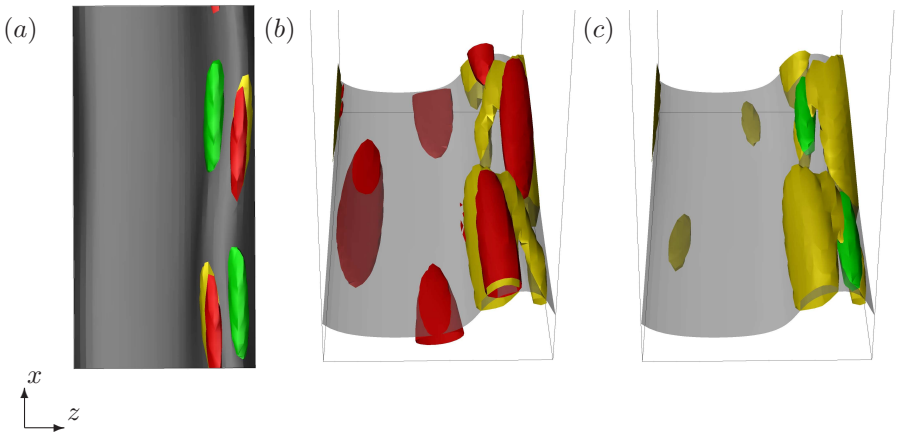

FIGURE 5. Isosurfaces of (a) $\Gamma_c = \Gamma_p = 0.0040$ (*red* and *yellow*, respectively) in a top view (aligned with the coordinate axes) and (b,c) $\Gamma_c = \Gamma_p = 0.0023$ from behind at an angle, at $t = t_0 + 0.18T$, together with $u = 0.6$ (*gray*) and λ_2 (*green*).

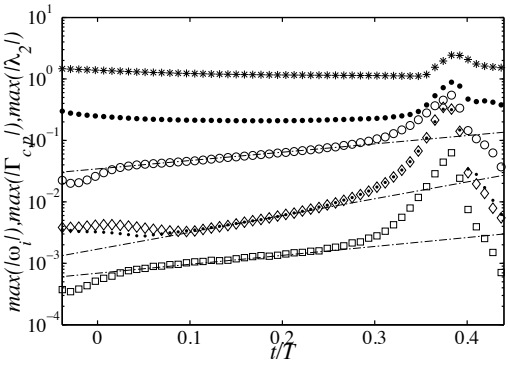

FIGURE 6. Maximum absolute value over Ω of ω_z $(*)$, ω_y $(\bullet)$, ω_x $(\circ)$ together with λ_2 $(\square)$, Γ_c $(\diamond)$, Γ_p $(\cdot)$ during the streak instability phase and the nonlinear breakdown. Straight lines indicating exponential growth are included for reference. Here, $t/T = 0$ corresponds to t_0 in figure 3.

the large spanwise vorticity, its growth rate is higher than the former two, albeit still exponential. Furthermore, the two measures are observed to behave very similarly. None of the ω_x-tilting terms (not shown) show any tendencies to grow exponentially.

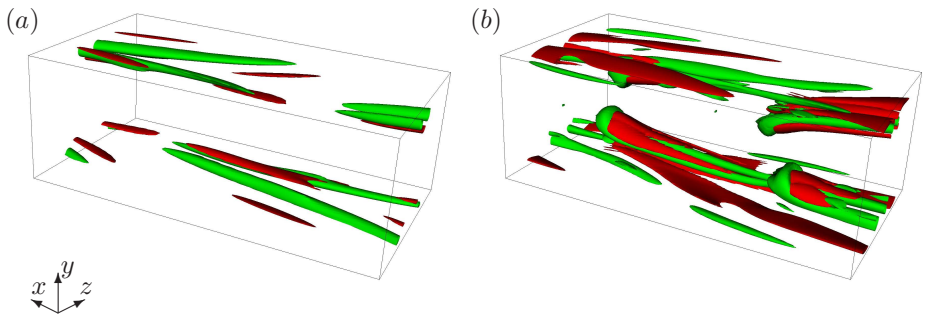

FIGURE 7. Isosurfaces of λ_2 (*green*) and Γ_c (*red*) during K-type transition at (a) an early stage ($t = 125.5$) and (b) at $t = 136.5$ when the hairpin vortex has emerged in the peak plane (Sandham & Kleiser 1992). Flow from right to left.

4.2. *Vorticity stretching during K-type transition*

As a second step, $\Gamma_{c,p}$ is computed in K-type transition. This is a classical modal transition scenario (Gilbert & Kleiser 1990), where a TS wave packet superimposed on a laminar Poiseuille channel flow profile grows exponentially in time before reaching nonlinear amplitudes and breaking down to turbulence. The initial spanwise vortex is tilted in the streamwise direction and stretched as the hairpin vortex emerges in the peak plane (Sandham & Kleiser 1992). The reader is referred to section 3.2 for more details regarding the simulation and flow physics. In figure 7 isosurfaces of Γ_c and λ_2 are plotted shortly before (a) and after (b) the hairpin is created. Very similar results are obtained for Γ_p, and are thus not shown separately. In the early stage (figure 7a) the Γ-measure acts as a precursor to the shear layer and the hairpin vortex formation. As for the ASBL, it also identifies the role of vorticity stretching in generating high speed streaks near the wall (h-type). Similarly, high values of vorticity stretching are found slightly above and in between the legs of the Λ-vortex, where the head of the hairpin vortex is about to appear (l-type). This mechanism is similar to the one sketched in figure 4, due to the positive wall-normal velocity induced by the legs of the Λ-vortex. In figure 7(b) we note that the Γ-measure is properly aligned with the hairpin vortex. As for the previous flow case, we include the evolution of the maximum absolute values in figure 8 for a more quantitative comparison. Again, it can be observed that the amplitude of spanwise vorticity is nearly constant, while the streamwise and wall-normal components grow exponentially. Previously having approximately twice the growth rate compared to ω_x and λ_2, both Γ-measures are now observed to grow at the exactly same rate as ω_x and ω_y. It is interesting to notice that λ_2 is constant for a long time, but starts to increase rapidly at $t = 80$. This shows that Γ is capable of identifying the instabilities that later develop into vortices.

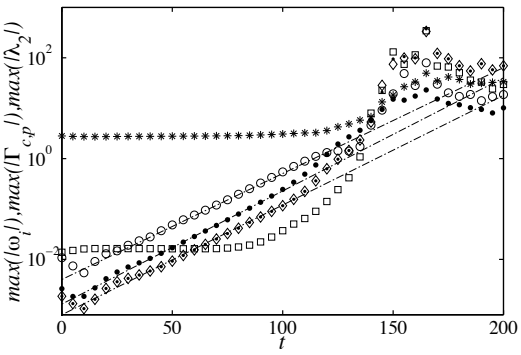

FIGURE 8. Maximum absolute value over Ω of ω_z ($*$), ω_y ($\bullet$), ω_x ($\circ$) together with λ_2 ($\square$), Γ_c ($\diamond$), Γ_p ($\cdot$) during the TS wave growth stage and the subsequent laminar-turbulent transition. Straight lines indicating exponential growth are included for reference.

4.3. *Vorticity stretching in a fully turbulent wall-bounded flow*

Next, we investigate the role of the vorticity stretching diagnostics in a fully turbulent wall-bounded flow. In particular, we are interested to see if similar events ('h' and 'l') can be observed as in the two previous 'model' flows. The diagnostic measures are computed based on fully turbulent velocity fields from a simulation performed with the Chebyshev-Fourier pseudo-spectral code described in Chevalier *et al.* (2007), employed at a Reynolds number $Re_\tau = 180$. In figure 9 a snapshot of the flow in its fully developed state is shown in a top view, depicting the near-wall region ($y^+ \approx 5$). The axes are scaled in viscous units, $l^* = \nu/u_\tau$. As before, streaks are indicated by an isosurface of streamwise velocity ($u = 0.3$, *gray*) and isosurfaces of Γ_c are shown (*red*). Vortices are indicated by λ_2 (*green opacity*). In figure 9(b) the absolute values of the thresholds of Γ_c and λ_2 have been increased by 50 % with respect to their values in (a). It can be seen that Γ_c (also true for Γ_p) remain localised when changing the iso-level, also in comparison to λ_2, indicating that the present measures are robust in locating coherent structures. The relevant structures are indicated by arrows in figure 9(a). It should be pointed out that Γ_p gives quantitatively the same results for the same iso-level, but is different in one particular respect, which will be further discussed in connection with figure 10 below. Remaining with figure 9, we note that the most prominent and most commonly occurring events are the 'pancake' structures (h-type) adjacent to the high-speed streaks. It can be observed that the typical length of these structures are roughly 200 wall units, *i.e.* approximately 1/5 of the well-documented near-wall streak length $l_x^+ \sim 1000$ (see *e.g.* Klebanoff *et al.* 1962) and about the same as the streamwise vortices connected to the streaks Jeong *et al.* (1997). A few l-type events can be found in locations of strong low-speed streak activity. These areas seem to be associated with a higher degree of disorder, compared to the high-speed areas

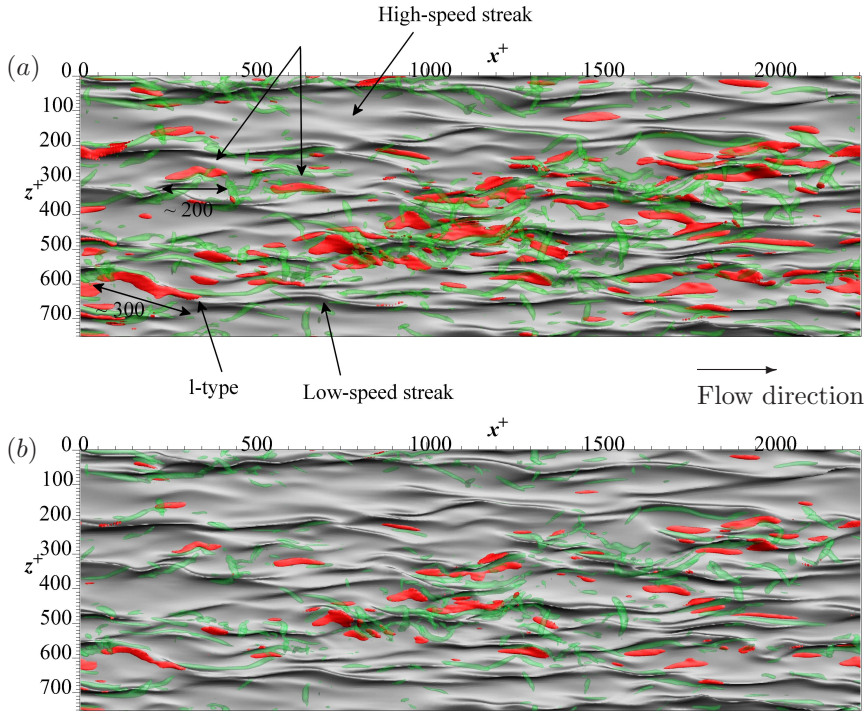

FIGURE 9. Top view showing Γ_c (*red*), $u = 0.3$ (*gray*) and λ_2 (*green opacity*) in a fully turbulent channel flow at $y^+ \approx 5$. The arrows indicate typical l-type and h-type events and their respective sizes in wall units. The absolute values of the thresholds in (b) have been increased by 50 % with respect to the values in (a).

where the h-type structures are found. Furthermore, the l-type structures are slightly longer in the streamwise direction ($l_x^+ \sim 300$) compared to the h-type structures. Figure 10 shows Γ_c (a) and Γ_p (b), together with λ_2, and highlights the only significant difference between the two Γ-measures. We note that the 'pancake' structures are essentially the same in both cases. The main difference is highlighted by ① in figure 10(b), where the structure forms a 'front' in the case of Γ_p that is not present in the case of Γ_c. This difference is thought to be of the same origin as the one in figure 5, namely that the region of intense stretching is inclined and therefore artificially cut by Γ_c but shown to its full extent by Γ_p. In some locations in figure 10(a,b) it can be seen that regions of strong vorticity stretching give rise to quasi-streamwise vortices. As soon as a vortex is created, it is convected away from the 'active' region of the flow. Many of these 'passive' vortices are seen to be located far from the wall, where the turbulent production is low. In that sense, the location of vorticity stretching

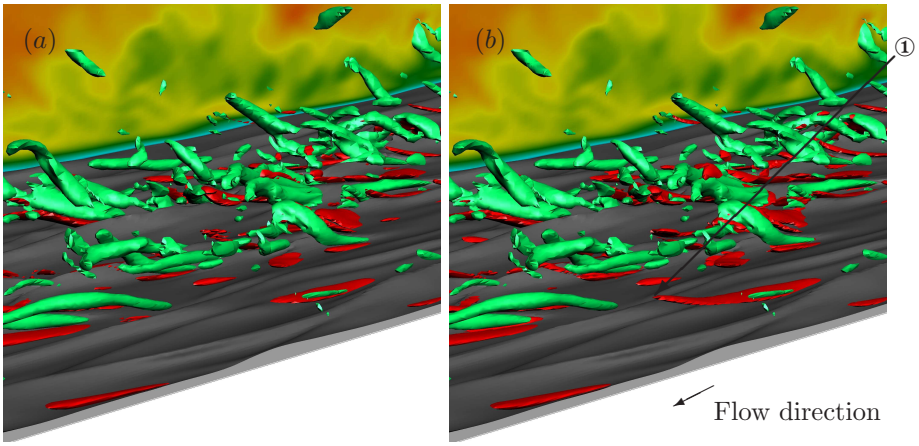

FIGURE 10. Close-up view of the flow field in figure 9, where Γ_c (a) is compared to Γ_p (b) and shown together with λ_2 (*green*) and a plane of streamwise velocity. The arrow shows the 'front' of the l-type structure captured by Γ_p.

(as opposed to vortices) pinpoints the regions in a flow that are dynamically relevant.

Mean and root-mean-square (r.m.s) profiles of $\Gamma_{c,p}$ and λ_2 are shown in figure 11(a) and (b), respectively. The mean, $\langle\cdot\rangle$, is taken over the homogeneous directions x, z, t. We observe the peak of both Γ-measures to be located at $y^+ = 6.5$, *i.e.* in the transition between the viscous sublayer and the buffer region. The peak of $\langle\Gamma_p\rangle$ is around 50 % higher compared to $\langle\Gamma_c\rangle$, whereas the r.m.s levels of Γ_c show a nearly identical behaviour compared to that of Γ_p, with its maximum located slightly closer to the wall, at $y^+ = 4.4$. The fact that the r.m.s levels peak at approximately the same wall-normal distance as the mean suggests that the strongest vorticity stretching events are fluctuating the most, and hence are part of a dynamical process. As also noted by Jeong *et al.* (1997), since $\lambda_2 > 0$ for $y^+ \lesssim 10$, no vortices are present in the viscous sublayer. These authors further point out that the peak of λ_2' (r.m.s) at $y^+ \approx 21$ infers that the prominence of vortical structures is located in the buffer region. This indicates that, similar to the discussion above, vorticity stretching is most active in the viscous sublayer and is part of the creation of vortical structures, which are then convected outwards in the flow.

In order for the vorticity to grow exponentially, there should be a predominance of stretching (*i.e.* small amounts of tilting) among the production terms contained in the first expression to the right of the equality sign in the enstrophy transport equation, given by equation (7). This implies that $\sum_\alpha \omega_\alpha^2 \frac{\partial u_\alpha}{\partial x_\alpha}$ should dominate over $\omega_i\omega_j \frac{\partial u_i}{\partial x_j}$, $i \neq j$. Therefore, we investigate the ratio

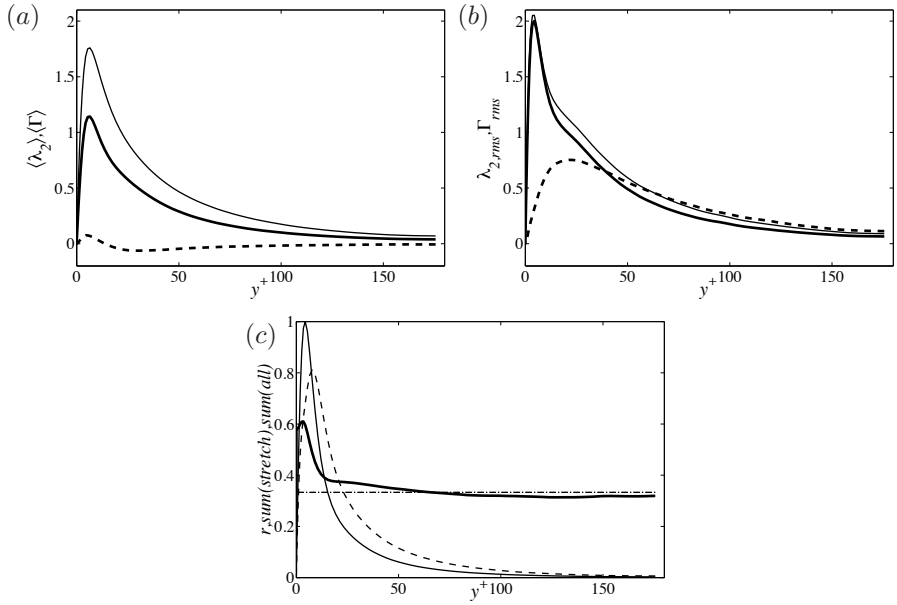

FIGURE 11. Mean (a) and r.m.s (b) profiles of Γ_c (——), Γ_p (——) and λ_2 (- - - -). (c) Enstrophy production ratio, r (——) with —·— indicating $r = 1/3$, together with $\langle|\sum_\alpha \omega_\alpha^2 \frac{\partial u_\alpha}{\partial x_\alpha}|\rangle$ (——) and $\langle|\omega_i\omega_j \frac{\partial u_i}{\partial x_j}|\rangle$ (- - - -).

$r = \langle|\sum_\alpha \omega_\alpha^2 \frac{\partial u_\alpha}{\partial x_\alpha}|\rangle / \langle|\omega_i\omega_j \frac{\partial u_i}{\partial x_j}|\rangle$, where $\langle\cdot\rangle$ is taken over the homogeneous directions. The absolute sign ensures that r is a well-behaved quantity contained in the interval $[0, 1]$. The result after the averaging operation is a function of wall-normal distance, shown in figure 11(c) together with the numerator and denominator separately. The ratio r can be interpreted as the enstrophy produced solely by stretching compared to the total enstrophy production (*i.e.* stretching and tilting). The horizontal line drawn at $r = 1/3$ indicates the degree of equipartition between stretching and tilting. The results suggested by figure 11(c) is that the enstrophy production is dominated by stretching over tilting close to the wall, with the peak of r being attained at $y^+ \approx 3.5$. Further out in the log-region ($y^+ \approx 70$) it approaches the equipartitioned state of 1/3. This demonstrates that the near-wall cycle contains the stretching of vorticity as an important ingredient and confirms that stretching becomes less important further away from the wall.

4.4. *Vorticity stretching in a separated flow*

Finally, a visualisation of Γ_c in a separated flow is given in figure 12. The computation of the diagnostic measure is based on instantaneous data taken from the diffuser simulation presented in Ohlsson *et al.* (2010), where accurate

representation of the solution was provided by the high-order spectral element code described in Fischer *et al.* (2008). Since the set-up is fully asymmetric, the mean flow is truly three-dimensional. Moreover, the separation is turbulent and highly unsteady. A spanwise midplane showing Γ_c (*gray*) and five contours of streamwise velocity ranging from 0 to 1.2 (*blue to red*) are provided in (*a*). We see a part of the turbulent inflow duct and the diffuser opening. The mean separated region starts close to the top expanding wall at $x \approx 6$. We note that high values of vorticity stretching are found close to the walls in the turbulent inflow duct, with structures similar to the turbulent channel flow described in the section above. However, an even greater activity is found shortly after the diffuser opening at around $x = 2$, within the strong shear layer separating the forward and backward flowing streams. In addition to a higher activity, the structures in this region are also larger compared to the structures in the inflow duct. This shear layer is not separated in the mean, but experiences instantaneous separation and the flow is consequently highly intermittent in this region. In the backflow area, considerably less vorticity stretching is observed. A top view is provided in figure 12(*b*), showing a wall-parallel plane selected along the red dashed line in figure 12(*a*) at the approximate distance of 30 wall units (based on $Re_\tau = 500$). Similar conclusions can be drawn, namely that the structures appear more frequently and are increasing in size as we approach the shear layer. In the separated region (*blue*) the activity decreases. In relation to the vortical structures identified by negative λ_2 (not shown) the vorticity stretching-structures are in general larger. However, in the case of attached turbulence in figure 10 the reverse situation occurred, *i.e.* the vortical structures were in general larger than the structures containing vorticity stretching.

5. Conclusions

Vorticity stretching is known to provide a rapid (exponential) growth mechanism, hence the location of vorticity stretching may reveal regions of dynamical importance in a flow. To investigate this in more detail, we have defined a diagnostic measure which can precisely locate such areas. Two variants have been defined, one of which is frame-independent and thus a true scalar quantity (Γ_p), while the other is defined in a Cartesian framework (Γ_c), facilitating implementation and understanding. It can be concluded that the two measures do not differ from each other significantly. Generally, vorticity stretching was found to be present in conjunction with the lift-up effect creating low-speed streaks (and the equivalent effect creating high-speed streaks). In particular, in both the ASBL (acting as a model for wall-bounded turbulence) and in the fully turbulent channel flow at $Re_\tau = 180$, large amounts of vorticity stretching were found on the convex side of high-speed streaks (h-type events), taking the form of large, flat 'pancake' structures. In locations of strong low-speed streak activity a similar but reversed phenomenon was observed on top of the low-speed streaks (l-type events), also occurring on the convex side of the streak. In the case of fully developed wall-bounded turbulence, the streamwise length of these structures was found to be approximately $200 - 300$ wall units. During

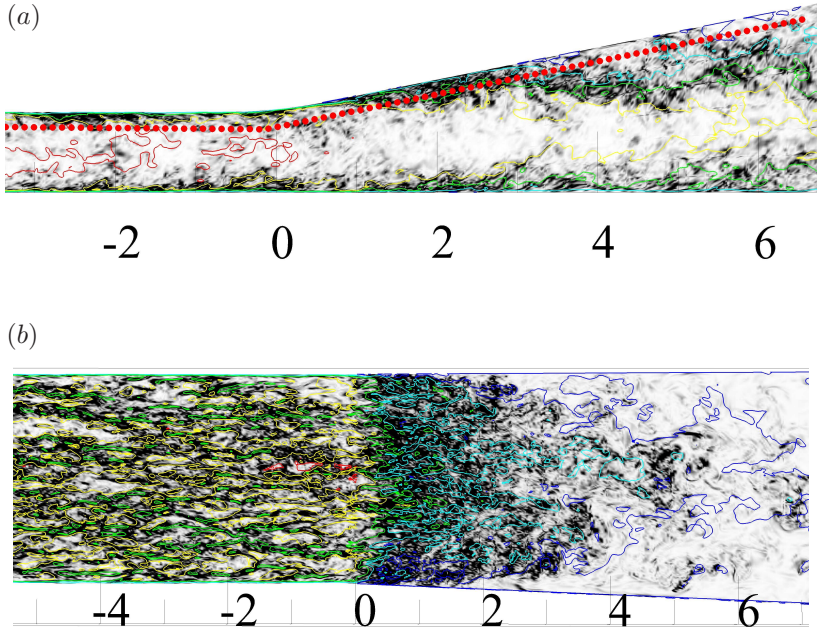

FIGURE 12. (*a*) A spanwise midplane in the diffuser showing Γ_c (*gray*) and five contours of streamwise velocity ranging from 0 (*blue*) to 1.2 (*red*). (*b*) Top view showing a plane parallel to the wall at the approximate distance of 30 wall units.

the streak instability phase, exponential growth of streamwise vorticity was observed in the ASBL, while the other components decayed, in line with the observations of Waleffe (1997). Moreover, the rotationally invariant measure (Γ_p) could detect vorticity stretching located within the core of the streamwise vortices, which gives some support for the mechanism suggested by Schoppa & Hussain (2002), where streamwise vortex sheets break down due to stretching.

In K-type transition, the measures accurately located the regions of interest, in particular the formation of high speed streaks near the wall (h-type) and the appearance of the hairpin vortex (l-type). Here, the vorticity stretching diagnostics were noticed to appear and grow long before the vortices (λ_2) developed. Shortly before the turbulent breakdown the growth of λ_2 rapidly overtook the growth of any other quantity, which shows that Γ is capable of predicting growing instabilities. Statistics from the fully turbulent channel flow showed that vorticity stretching is active in the near-wall region, with a peak in the viscous sublayer ($y^+ \approx 6.5$), and dominates over vorticity tilting. Further out, towards the outer region of the flow where the turbulence is more isotropic,

the enstrophy produced solely by stretching compared to the total enstrophy production attains a constant value of $\sim 1/3$.

In the turbulent separated flow, the diagnostic measures showed the largest occurrence of vorticity stretching within the shear layer preceding the mean separation bubble. This is in agreement with Jones *et al.* (2009), who noted that vorticity stretching plays an important role in self-sustained transition processes, such as the unsteady vortex shedding in a separated flow. The structures in this area not only appeared more frequently compared to the structures in the turbulent inflow duct, but the coherent structures could also be seen to grow in size. In the backflow region, the activity decreased.

In summary, the proposed diagnostic applied to transitional and turbulent flows identifies regions where high-speed streaks create drag or streak instabilities are present (both sinuous and varicose). We have tracked the temporal evolution of our measure in the ASBL and channel cases, and observed a similar degree of spatial and temporal coherence as for the λ_2 measure. As opposed to vortices, which are simply convected away from the 'active' region of the flow as soon as they are created, high concentrations of vorticity stretching are mainly found in regions where growing instabilities are present and hence dynamically important.

The NORDITA Workshop on Turbulent Boundary Layers 2010 is acknowledged for providing a forum for the present collaboration and thus making this project possible.

References

Chakraborty, P., Balachandar, S. & Adrian, R. J. 2005 On the relationships between local vortex identification schemes. *J. Fluid Mech.* **535**, 189–214.

Chevalier, M., Schlatter, P., Lundbladh, A. & Henningson, D. S. 2007 A Pseudo-Spectral Solver for Incompressible Boundary Layer Flows. *Tech. Rep.* TRITA-MEK 2007:07. Royal Institute of Technology (KTH), Dept. of Mechanics, Stockholm, Sweden.

Chong, M. S., Perry, A. E. & Cantwell, B. J. 1990 A general classification of three-dimensional flow fields. *Phys. Fluids A* **2** (5), 765–777.

Dubief, Y & Delcayre, F 2000 On coherent-vortex identification in turbulence. *J. Turbulence* **1**, 1–22.

Fischer, P. F., Lottes, J. W. & Kerkemeier, S. G. 2008 nek5000 Web page. http://nek5000.mcs.anl.gov.

Gilbert, N. & Kleiser, L. 1990 Near-wall phenomena in transition to turbulence. In *Near-Wall Turbulence* (ed. S.J. Kline & N.H. Afgan), pp. 7–27. 1988 Zoran Zarić Memorial Conference, New York, USA.

Hamilton, J. M., Kim, J. & Waleffe, F. 1995 Regeneration mechanisms of near-wall turbulence structures. *J. Fluid Mech.* **287**, 317–348.

Helgeland, A., Reif, B. A. P., Andreassen, Ø. & Wasberg, C. E. 2007 Visualization of vorticity and vortices in wall-bounded turbulent flows. *IEEE Transactions on Visualization and Computer Graphics* **13**, 1055–1067.

Holmes, P., Lumley, J. & Berkooz, G. 1996 *Turbulence, Coherent Structures, Dynamical Systems and Symmetry*. Cambridge University Press, Cambridge, UK.

Hunt, J. C. R., Wray, A. A. & Moin, P. 1988 Eddies, streams, and convergence zones in turbulent flows. In *Proceedings of the 1988 CTR Summer Program*, pp. 193–208.

Jeong, J. & Hussain, F. 1995 On the identification of a vortex. *J. Fluid Mech.* **285**, 69–94.

Jeong, J., Hussain, F., Schoppa, W. & Kim, J. 1997 Coherent structures near the wall in a turbulent channel flow. *J. Fluid Mech.* **332**, 185–214.

Jiménez, J. & Moin, P. 1991 The minimal flow unit in near-wall turbulence. *J. Fluid Mech.* **225**, 213–240.

Jiménez, J. & Pinelli, A. 1999 The autonomous cycle of near-wall turbulence. *J. Fluid Mech.* **389**, 335–359.

Jones, L.E., Sandberg, R.D. & Sandham, N.D. 2009 Local and global stability of airfoil flows at low Reynolds number. In *Seventh IUTAM Symposium on Laminar-Turbulent Transition* (ed. P. Schlatter & D. S. Henningson). Springer-Verlag, Berlin, Germany.

Klebanoff, P. S., Tidstrom, K. D. & Sargent, L. M. 1962 The three-dimensional nature of boundary-layer instability. *J. Fluid Mech.* **12**, 1–34.

Kline, S. J., Reynolds, W. C., Schraub, F. A. & Runstadler, P. W. 1967 The structure of turbulent boundary layers. *J. Fluid Mech.* **30**, 741–773.

Landahl, M. T. 1980 A note on an algebraic instability of inviscid parallel shear flow. *J. Fluid Mech.* **98**, 243–251.

Lumley, J. L. 1967 The structure of inhomogeneous turbulent flows. In *Atm. Turb. Radio Wave Prop.* (ed. A. M. Yaglom & V. I. Tatarsky), pp. 166–178. Nauka, Moscow, Russia.

Madré, T. K. 2011 Turbulence transition in the asymptotic suction boundary layer. Diplomarbeit, Philipps-Universität, Marburg, Germany.

Moser, R. D., Kim, J. & Mansour, N. 1999 Direct numerical simulation of turbulent channel flow up to $\mathrm{Re}_\tau = 590$. *Phys. Fluids* **11** (4), 943–945.

Nomura, K.K. & Post, G.K. 1998 The structure and dynamics of vorticity and rate of strain in incompressible homogeneous turbulence. *J. Fluid Mech.* **377**, 65–97.

Ohlsson, J., Schlatter, P., Fischer, P. F. & Henningson, D. S. 2010 Direct numerical simulation of separated flow in a three-dimensional diffuser. *J. Fluid Mech.* **650**, 307–318, note: change of name from J. Ohlsson to J. Malm.

Robinson, S. K 1991 Coherent motions in the turbulent boundary layer. *Annu. Rev. Fluid Mech.* **23**, 601–639.

Sandham, N. D. & Kleiser, L. 1992 The late stages of transition to turbulence in channel flow. *J. Fluid Mech.* **245**, 319–348.

Schlatter, P., Stolz, S. & Kleiser, L. 2004 LES of transitional flows using the approximate deconvolution model. *Int. J. Heat Fluid Flow* **25** (3).

Schneider, T. M., Eckhardt, B. & Yorke, J. A. 2007 Turbulence transition and the edge of chaos in pipe flow. *Phys. Rev. Lett.* **99** (3), 034502.

Schoppa, W. & Hussain, F. 2002 Coherent structure generation in near-wall turbulence. *J. Fluid Mech.* **453**, 57–108.

She, Z.-S., Jackson, E. & Orszag, S. A. 1991 Structure and dynamics of homogeneous turbulence: Models and simulations. *Proc. R. Soc. Lond.* **434** (1890), pp. 101–124.

Smith, C. R. & Metzler, S. P. 1983 The characteristics of low-speed streaks in the near-wall region of a turbulent boundary layer. *J. Fluid Mech.* **129**, 27–54.

Tsinober, A. 2009 *An Informal Conceptual Introduction to Turbulence (second edition)*. Springer-Verlag, Berlin, Germany.

Tsinober, A., Eggels, J. G. M. & Nieuwstadt, F. T. M. 1995 On alignments and small scale structure in turbulent pipe flow. *Fluid Dyn. Res.* **16** (5), 297.

Waleffe, F. 1997 On a self-sustaining process in shear flows. *Phys. Fluids* **9** (4), 883–900.

Paper 6

6

Direct numerical simulation of separated flow in a three-dimensional diffuser

By Johan Ohlsson[*], Philipp Schlatter[*], Paul F. Fischer[†] and Dan S. Henningson[*]

[*]Linné FLOW Centre, Swedish e-Science Research Centre (SeRC)
KTH Mechanics, 100 44 Stockholm, Sweden

[†]MCS, Argonne National Laboratory, 9700 S. Cass Avenue,
Argonne, IL 60439, USA

J. Fluid Mech. **650**, 307–318

A direct numerical simulation (DNS) of turbulent flow in a three-dimensional diffuser at $Re = 10\ 000$ (based on bulk velocity and inflow-duct height) was performed with a massively parallel high-order spectral element method running on up to 32 768 processors. Accurate inflow condition is ensured through unsteady trip forcing and a long development section. Mean flow results are in good agreement with experimental data by Cherry, Elkins & Eaton (*Intl J. Heat Fluid Flow*, vol. 29, 2008, pp. 803–811), in particular the separated region starting from one corner and gradually spreading to the top expanding diffuser wall. It is found that the corner vortices induced by the secondary flow in the duct persist into the diffuser, where they give rise to a dominant low-speed streak, due to a similar mechanism as the 'lift-up effect' in transitional shear flows, thus governing the separation behaviour. Well-resolved simulations of complex turbulent flows are thus possible even at realistic Reynolds numbers, providing accurate and detailed information about the flow physics. The available Reynolds stress budgets provide valuable references for future development of turbulence models.

1. Introduction

In many engineering flows, such as the flow over airplane wings or in turbomachinery applications, flow separation may lead to degradation of lift, pressure losses, 'hot spots' or even engine failure. On the other hand, maximum performance is often obtained close to separation, hence the design of flow devices such as pumps, fans and compressors inevitably leads to situations where flow separation is necessary to predict, see *e.g.* the review article by Simpson (1989). In practical situations these flows are generally turbulent and fully three-dimensional, hence prediction of highly unsteady, three-dimensional separation is of considerable importance. Often separation is caused by an adverse

pressure gradient and may take place over a smooth surface ('pressure-induced' separation), as opposed to the case where the flow separates from a sharp geometrical obstacle ('geometry-induced' separation). Since, in the latter case the separation point, in principle, is given by the point of highest curvature and is thus easy to predict, the former poses most uncertainties because the point of separation can vary in both time and space.

Rapid developments in computer hardware over the last few years allow predictions of complex flows to be made by numerical simulations. The most widely used approach for complex engineering flows is based on the Reynolds-averaged Navier–Stokes equations (RANS), where an ensemble average of the Navier–Stokes equations is solved for. The averaging process gives rise to an unclosed term, which has to be modelled. Although RANS may be a rather crude way to describe a highly time-dependent flow phenomenon, it may, in many situations, be sufficient to know the mean flow characteristics. However, flows experiencing adverse pressure gradients and separation are very hard to predict, in particular three-dimensional flows, due to rapid changes in mean flow properties (*e.g.* Jakirlić *et al.* 2010). For a more detailed picture of the flow, unsteadiness needs to be taken into account. The concept of large-eddy simulation (LES), where the large scales of the flow are resolved and the small scales are modelled by a subgrid-stress (SGS) model, has in recent years evolved into a promising tool for flow predictions. The drawback, however, is that a SGS model can never be universal, and special care has to be taken as new flow cases are being studied. A numerically more appealing approach and also the most computationally expensive, where the governing equations are solved without averaging or filtering, is referred to as direct numerical simulation (DNS). If proper boundary conditions are imposed and high-enough resolution is used, this approach generally compares very well to experimental data. Numerical schemes of high order, *e.g.* spectral methods, with low amounts of numerical viscosity and dispersion yield particularly satisfactory results. While traditional spectral methods only work efficiently for simple geometries, the spectral-element method (SEM) introduced by Patera (1984), is a high-order numerical method with the ability to accurately simulate fluid flows also in complex geometries. Thus, SEM has opened the possibility to study, in great detail, fluid phenomena known to be very sensitive to discretization errors, *e.g.* flows undergoing pressure-induced separation (Ohlsson *et al.* 2010). SEM has successfully been applied to mainly laminar and transitional flows (*e.g.* Tufo & Fischer 2001; Tomboulides & Orszag 2000; Sherwin & Karniadakis 1995) and also fully turbulent flows (Wasberg *et al.* 2009; Iliescu & Fischer 2003).

Pressure-induced separation has been considered extensively in two-dimensional flow configurations, where the mean flow exhibits one homogeneous direction, *e.g.* Kaltenbach *et al.* (1999) who performed LES of a plane asymmetric diffuser with 10° opening angle, experimentally also investigated by Buice & Eaton (2000). Herbst *et al.* (2007) performed LES of a plane asymmetric diffuser with 8.5° opening angle at higher Reynolds numbers. They

all reported satisfactory agreement with the corresponding experimental data concerning the bulk quantities. Herbst *et al.* (2007), however, found that employing a recycling technique to specify unsteady turbulent inflow conditions may not be optimal for spatially developing flows exhibiting pressure-induced separation, since it might trigger artificial frequencies. Few examples of LES of fully three-dimensional, turbulent, pressure-induced separated flows are found in the literature (Schneider *et al.* 2009) mainly due to the fact that one has to rely solely on one homogeneous direction, time, to average turbulent statistics.

Even though RANS models are getting more sophisticated, many difficulties remain among which some have already been pointed out. In order to continue the development, there is a need for clearly-defined benchmark cases and good quality reference data. Recently, experiments of such a reference case were performed by Cherry *et al.* (2008). The experiments conducted consisted of two three-dimensional diffusers with slightly different expansion angles at, for simulation standards, a fairly high yet realistic Reynolds number of 10 000 based on bulk velocity and height of the inflow duct. It was found that the flow was extremely sensitive to these slight changes in the geometrical set-up. Magnetic resonance velocimetry (MRV) (see Elkins *et al.* 2003) was used to collect three-dimensional velocity data. Emphasis was put on defining a simple truly three-dimensional geometry with well-defined boundary conditions (walls), inlet conditions (fully-developed turbulence) and to avoid any symmetries leading to long-period stall switches, hence facilitating for simulations to mimic the real experiment. The three-dimensionality was reasoned to be a more relevant test case for computational fluid dynamics (CFD), but it would also get rid of the ambiguities a two-dimensional experiment may suffer from, such as dependence on channel width. Here, we present a DNS of one of the diffuser cases ('Diffuser 1') in Cherry *et al.* (2008) at the same Reynolds number as in the experiments. Focus is on accuracy, both in terms of discretization and boundary conditions. The motivation for this is twofold: first, we are aiming at understanding the flow physics involved in three-dimensional separation through a study of mean flow features together with the identification of instantaneous flow structures. Second, our data could be used as an important reference, suitable for further development of turbulence models. A first step towards these goals must be to validate the data against existing experimental data. Here, we focus on careful analysis of mean flow results in order to assess the quality of the simulation data. Mean flow, pressure recovery and turbulent fluctuations are compared to the experimental data of Cherry *et al.* (2008). Further, a brief discussion will be given on some of the new flow physics found in the diffuser.

2. Numerical method and simulation setup

The incompressible Navier–Stokes equations are solved using a Legendre-polynomial-based spectral-element method, implemented in the code `nek5000`, developed by Fischer *et al.* (2008). As in the case of the finite-element method (FEM), the governing equations are cast into weak form and discretized in space by the Galerkin approximation, where the test and trial spaces are restricted to

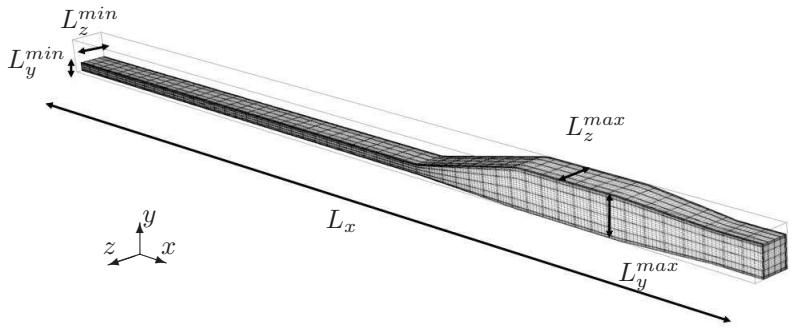

FIGURE 1. Grid of one of the diffuser geometries ('Diffuser 1') in Cherry *et al.* (2008) showing the development region, diffuser expansion, converging section and outlet.

certain (and different) velocity and pressure spaces, respectively, following the $\mathbb{P}_N - \mathbb{P}_{N-2}$ SEM discretization by Maday & Patera (1989). The velocity space is typically a space of Nth-order Lagrange polynomial interpolants, $h_i^N(x)$, based on tensor-product arrays of Gauss-Lobatto-Legendre (GLL) quadrature points in a local element, Ω^e, $e = 1, ..., E$, satisfying $h_i^N(\xi_j^N) = \delta_{ij}$. Here, $\xi_j^N \in [-1, 1]$ denotes one of the $N+1$ GLL quadrature points and δ_{ij} is the Kronecker delta. For a single element in $\mathbb{R}^3$ the representation of the velocity vector, $\boldsymbol{u}$, is

$$\boldsymbol{u}(\boldsymbol{x}^e(r,s,t))|_{\Omega^e} = \sum_{i=0}^{N}\sum_{j=0}^{N}\sum_{k=0}^{N} \boldsymbol{u}_{ijk}^e h_i^N(r) h_j^N(s) h_k^N(t), \tag{1}$$

where $\boldsymbol{x}^e$ is the coordinate mapping from the reference element $\hat{\Omega}$ to the local element Ω^e and $\boldsymbol{u}_{ijk}^e$ is the nodal basis coefficient. The tensor-product structure enables the use of highly optimized matrix–matrix routines (`mxm`) to solve the final system of equations (see *e.g.* Fischer 1997). The non-linear terms are treated explicitly by second-order extrapolation (EXT2), whereas the viscous terms are treated implicitly by a second-order backward differentiation scheme (BDF2) leading to a linear symmetric Stokes system for the basis coefficient vectors $\underline{\boldsymbol{u}}^n$ and $\underline{p}^n$ to be solved at every time step:

$$H\underline{\boldsymbol{u}}^n - D^{\mathrm{T}}\underline{p}^n = B\underline{\boldsymbol{f}}^n, \;\; D\underline{\boldsymbol{u}}^n = 0. \tag{2}$$

Here, $H = (1/Re)K + (3/2\Delta t)B$ is the discrete equivalent of the Helmholtz operator $(-(1/Re)\nabla^2 + 3/2\Delta t)$. In the RHS, $\underline{\boldsymbol{f}}^n$ accounts for the non-linear terms and for the cases we have external forcing in the Navier–Stokes equations. To solve the final problem (see (2)), velocity and pressure are decoupled and solved iteratively using conjugate gradients and GMRES with scalable Jacobi and additive Schwarz preconditioners, respectively (Fischer 1997). For the latter, fast parallel coarse-grid solvers scaling to ten thousands of processors are used (Tufo & Fischer 2001).

The computational domain shown in figure 1 is set up in close agreement with the diffuser geometry in the experiment and consists of the inflow development duct of almost 63 duct heights, h, (starting at the non-dimensional coordinate $x = -62.9$), the diffuser expansion located at $x = 0$ and the converging section upstream of the outlet. The corners resulting from the diffuser expansion are smoothly rounded with a radius of 6.0 in accordance with the experimental set-up. The maximum dimensions are $L_x = 105.4h$, $L_y = [h, 4h]$, $L_z = [3.33h, 4h]$. In the inflow duct, laminar flow undergoes natural transition by the use of an unsteady trip forcing (see *e.g.* Schlatter *et al.* 2009), which avoids the use of artificial turbulence and eliminates artificial temporal frequencies which may arise from inflow recycling methods (Herbst *et al.* 2007). A 'sponge region' is added at the end of the contraction in order to smoothly damp out turbulent fluctuations, thereby eliminating spurious pressure waves. It is followed by a homogeneous Dirichlet condition for the pressure and a homogeneous Neumann condition for the velocities. The resolution of approximately 220 million grid points is obtained by a total of 127 750 local tensor product domains (elements) with a polynomial order of 11, respectively, resulting in $\Delta z^+_{max} \approx 11.6$, $\Delta y^+_{max} \approx 13.2$ and $\Delta x^+_{max} \approx 19.5$ in the duct centre and the first grid point being located at $z^+ \approx 0.074$ and $y^+ \approx 0.37$, respectively. It was verified that the present resolution yields accurate results in turbulent channel flow simulations. In the diffuser, the grid is linearly stretched in both directions, but since the mean resolution requirements decreases with the velocity, which decreases linearly with the area expansion, the resolution in the entire domain will hence be satisfactory. The simulation was performed on the Blue Gene/P at ALCF, Argonne National Laboratory (32 768 cores and a total of 8 million core hours) and on the cluster 'Ekman' at PDC, Stockholm (2048 cores and a total of 4 million core hours). Thirteen flow-through times, $tu_b/L = 13$, based on bulk velocity, u_b, and diffuser length, $L = 15h$, were simulated in order to let the flow settle to an equilibrium state before turbulent statistics were collected over approximately $tu_b/L = 21$ additional flow-through times. The lack of homogeneous directions together with the fact that the flow showed pronounced instationarity with fluctuations on a wide range of scales, called for long integration time in order to average the statistics.

3. Results

3.1. *Inflow section*

The inflow duct was studied in detail to ensure that a fully developed turbulent flow is reached at the end of the development section described in section 2. Mean velocity profiles as a function of y^+ and z^+, respectively, taken from a middle plane a short distance upstream of the diffuser opening are shown in figure 2(a). Here, y^+ and z^+ are the cross-stream directions in the duct normalized with the respective viscous length scale in that direction. It can be seen that the 'law of the wall' is captured with good accuracy. Monitoring the streamwise development of the friction Reynolds number, Re_τ, figure 2(b),

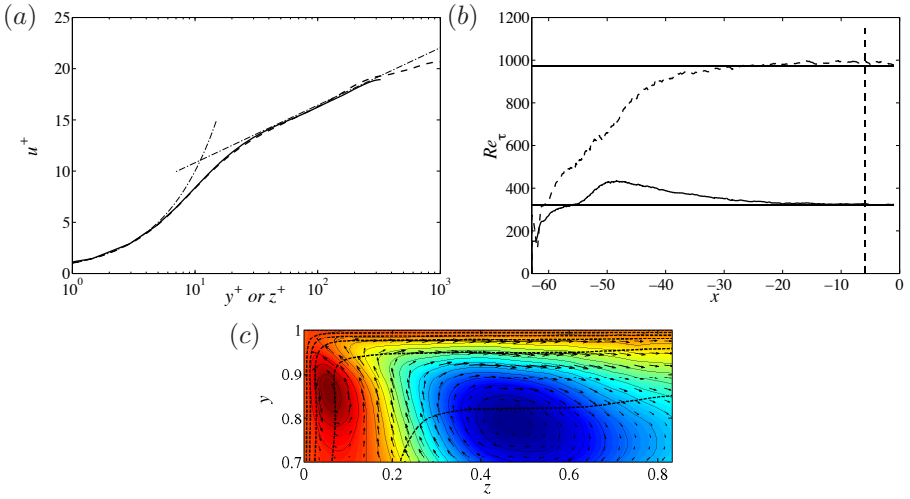

FIGURE 2. (a) Mean centerplane velocity profile $6h$ upstream of the diffuser throat, where ——$u^+(y^+)$, - - - -$u^+(z^+)$, –·–log law with $\kappa = 0.41$ and $B = 5.2$, (b) evolution of $Re_{\tau,y} = u_{\tau,y}h/2\nu$ (——), $Re_{\tau,z} = u_{\tau,z}3.33h/2\nu$ (- - - -) in a midplane of constant z and y respectively in the inflow section; solid horizontal lines showing Re_τ for a periodic duct and vertical dashed line location of the selected velocity profile in (a) and (c) stream function of the time-averaged flow field in a cross-sectional plane $6h$ upstream of the diffuser throat showing the secondary flow in one of the corners. Contour lines of the stream function are spaced $2{\times}10^{-4}$ units apart. Dashed contour lines, 0.2 u_b apart, of streamwise velocity as well as velocity vectors of mean crossflow velocities are superimposed.

provides a measure to detect where a fully turbulent flow is reached. Compared to the value obtained from a periodic duct simulation at the same Re (indicated by solid horizontal lines), this has occurred at $x > -15$ as shown by the dashed vertical line. The secondary flow in the corners of the duct shown in figure 2(c) also gives a good indication on the development of the flow and, although weak (a few percent of u_b), is thought to be important for the correct separation behaviour (Cherry *et al.* 2008). From the measures listed above, we conclude that the flow has converged to a statistically stationary state well upstream of the diffuser throat.

3.2. *Diffuser*

Turning to the flow in the actual diffuser, a qualitative analysis focusing on identifying the size, shape, and location of the separated region is made by selecting a number of crossflow planes, shown in figure 3. At every location

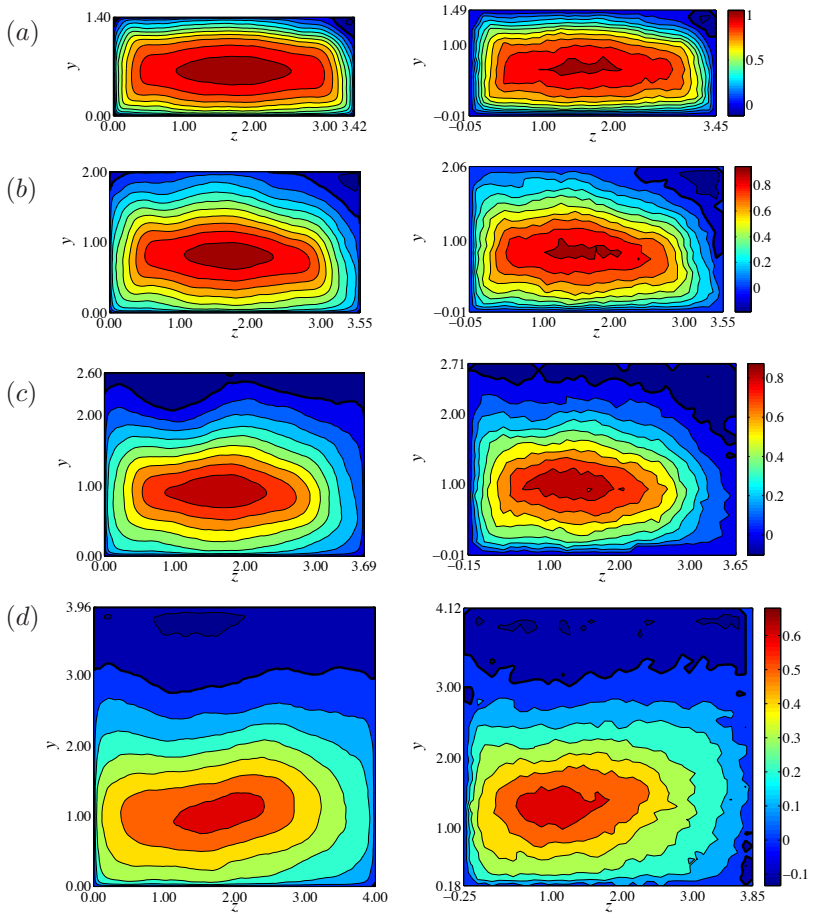

FIGURE 3. Crossflow planes of streamwise velocity 2, 5, 8 and 15h downstream of the diffuser throat. *Left:* Computation by `nek5000`. *Right:* Experiment by Cherry *et al.* (2008) Each streamwise position has its own colour bar on the right. Contour lines are spaced 0.1 u_b apart. Thick black lines correspond to the zero velocity contour.

within the duct until the diffuser throat at $x = 0$, there is no sign of separation, as expected. As soon as the diffuser starts to expand, the separation, as pointed out by Cherry *et al.* (2008), increases rapidly due to the asymmetry of the geometry in the uppermost right corner, where the two inclined walls meet. As can be seen in figure 3(a), at $x = 2$, the agreement between the experimental and simulation data is excellent, both considering the mean flow in general and the separated region in particular. Very good agreement between the simulation data and the experimental data persists for another three units downstream

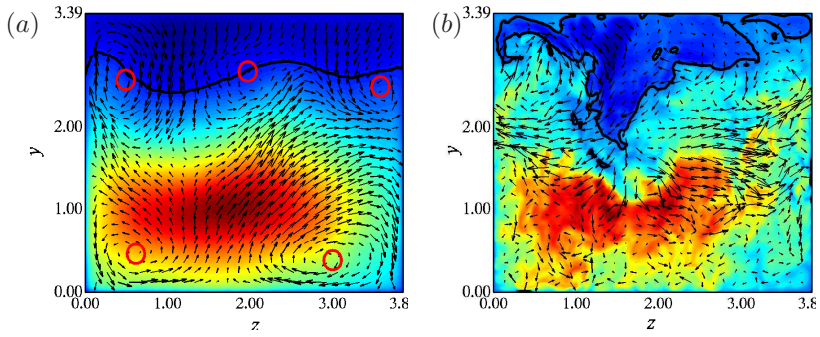

FIGURE 4. Crossflow planes of (a) mean and (b) instantaneous streamwise velocity 12 h downstream of the diffuser throat with superimposed crossflow vectors (scaled so that vectors in (a) are six times larger than vectors in (b)) showing the corner vortices responsible for the bump. Thick black lines correspond to the zero streamwise velocity contour. ∘ refer to (primary) vortex centres.

until $x = 5$, shown in figure 3(b), where the separation in the upper right corner gradually starts to spread and eventually includes the whole top wall of the diffuser. This spreading is present in both data sets, however, in slightly different ways. Studying figure 3(c) it is obvious that the separation in the experimental data advances like a wedge over to the top and uppermost left corner of the diffuser. (Note the slight shift of the coordinate system in the experimental data). The simulation data, on the other hand, indicates that at $x = 6$ (not shown) the smaller separation from the left corner visible in figure 3(b) has grown, although with fixed streamwise magnitude (~ -0.025), into a small, stretched localized region in the top of the diffuser. From here it rapidly continues to grow down into the interior of the diffuser, finally taking the shape of a small 'bump' hanging from the top wall at $x = 8$, figure 3(c). Here, the separation fills the entire top of the diffuser, consistent with the experiments. Even though the bump is not present at $x = 8$ in the experimental data, its presence can be noticed further downstream at $x = 15$ in figure 3(c), where the bulk of the separated flow indeed is located to the left. But even so, the origin of the discrepancy in figure 3(c) is at present unknown. It should be pointed out that the bump is not a transient effect and is thus an artefact of a too short averaging time. Window averaging of the data has shown that it is present at all times. This is also confirmed by Schneider *et al.* (2009), who performed LES of the same diffuser geometry and Reynolds number and could see the same extension of the separation bubble on the top expanding wall. The physical reason for this particular behaviour becomes clear if we superimpose vectors of crossflow velocity onto a crossflow plane, as shown in figure 4. We see that a substantial downwash of slow velocity fluid is present within the

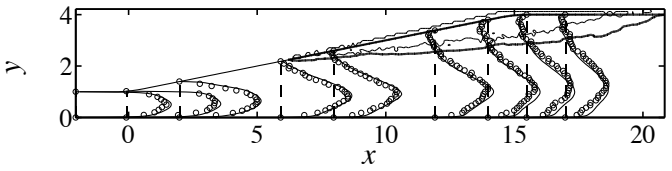

FIGURE 5. Mean centerplane velocity $3\langle u\rangle + x$ in the diffuser. Velocity data: ——— `nek5000`, ∘ experiment by Cherry *et al.* (2008). Separated region: ——— `nek5000`, ——— experiment by Cherry *et al.* (2008).

bump, both in the mean (figure 4*a*) and instantaneously (figure 4*b*), governed by vortical structures in the upper corners. Tracking the secondary flow in the duct, one realizes that although weak in magnitude (a few per cent of the streamwise bulk velocity), the vortices produced by the secondary flow persist into the diffuser, where they give rise to a low-speed streak, because of a similar mechanism as the 'lift-up effect' in transitional shear flows (Landahl 1980). In the remaining part of the diffuser region, the area fraction of separated flow (AFSF) in a cross section is in very good agreement with the experimental data, including the maximum of 23 % AFSF occurring at $x = 15$, figure 3(d), where the straight part of the geometry begins. Between $x = 18$–20 the AFSF is 2 % larger in the simulation data. After $x = 20$ the separation is reduced to zero, a result supported by both data sets. A more quantitative comparison is made in figure 5, where mean velocity profiles are selected in a spanwise midplane. Generally, good agreement is observed. In particular, the upward movement of the velocity peak is well captured. The presence of the large separated region on the upper inclined wall forces the flow upwards, however only slightly, due to the originally high momentum content in the flow. The size and location of the separated region (here defined as a region with negative velocity) in a spanwise midplane, seen in figure 5, is in good agreement with the experimental data, although the previously described extension of the separation in the simulation data is clearly visible. The streamwise root mean square (r.m.s), u_{rms}/u_b, given in figure 6 at the same streamwise locations as the mean flow in figure 3 shows consistency with the mean flow regarding the flow dynamics present in the diffuser. In front of the entrance to the diffuser the fluctuations peak ($u^+_{rms} = 2.6$) close to the walls ($z^+ = 14.9$) very much like in a turbulent channel flow. The strong character of fully developed wall-bounded turbulence is further confirmed by the typical streak spacing of $\Delta z^+_{max} \approx 100$ in the near-wall region. Shortly after the diffuser throat, the fluctuations generally move out from the walls. In particular, the most dominant fluctuations are found in the shear layer bounding the separation bubble in the uppermost right corner (figure 6(a)), reaching a magnitude of 22 % of the bulk inlet velocity, also confirmed by the experimental data. Further downstream, at $x = 5$ (figure 6b), the peak moves downward and increases in magnitude (up to 25 % of the bulk inlet velocity),

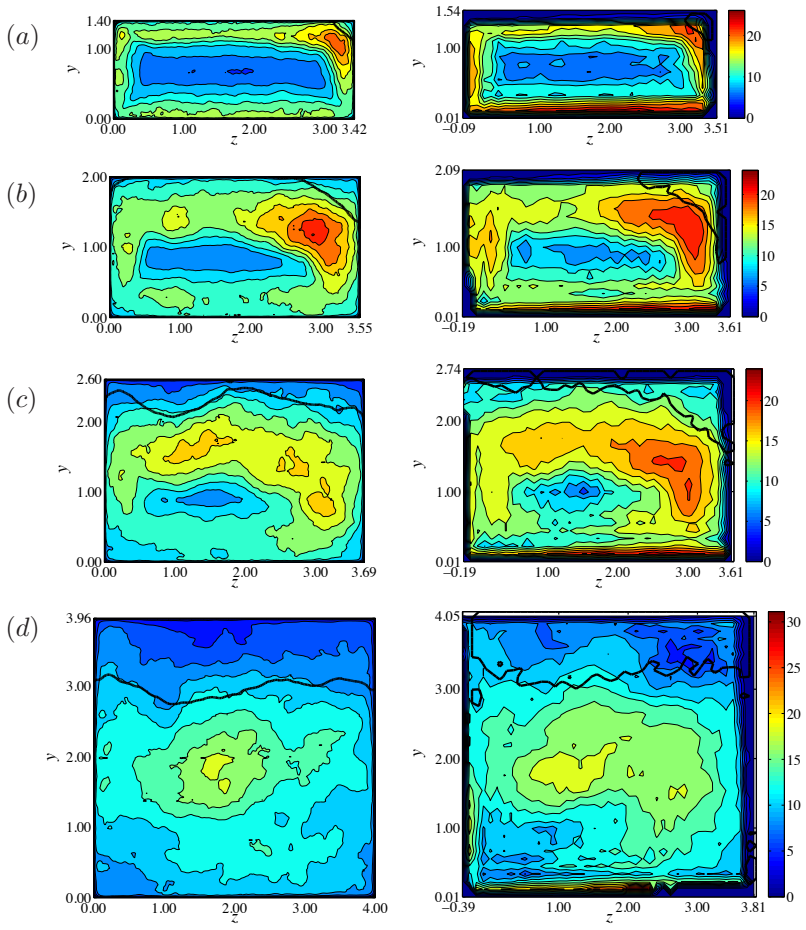

FIGURE 6. Crossflow planes of streamwise velocity fluctuations, $(u_{rms}/u_b) \times 100$, 2, 5, 8 and $15h$ downstream of the diffuser throat. *Left:* Computation by `nek5000`. *Right:* Experiment by Cherry *et al.* (2008). Each streamwise position has its own colour bar on the right. Contour lines are spaced 2 $(u_{rms}/u_b) \times 100$ apart. Thick black lines correspond to the zero streamwise velocity contour.

indicating an intense turbulence activity in this area. At $x = 8$ (figure 6*c*) the turbulent shear layer follows consistently the spreading of the separation to the top wall of the diffuser, clearly seen in both data sets. The localized bump present in the simulation data has a corresponding enhanced turbulent activity around $(z, y) = (1.2, 1.6)$. Here, the agreement with the LES by Schneider *et al.* (2009) is again closer than with the experimental findings. At $x = 15$, shown

in figure 6(*d*), both data sets suggest the turbulence to be more homogeneously spread over the cross-sectional area, with a peak situated in the interior of the diffuser of around 17 % of the bulk inlet velocity. The typical turbulent scales are rapidly increasing in size as soon as the separated flow in the upper right corner has become visible. In the duct, there are approximately ten adjacent streaks in the z-direction close to the wall. This persists until the diffuser throat and approximately $2h$ further downstream ($x = 2$), where this number is suddenly halved to approximately five streaks. Consequently, the typical scales are approximately twice as large in this region compared to the scales in the duct. Another $2h$ further downstream, at $x = 4$, the previously attached boundary layers are dispersed and the flow is to a larger extent mixed over the entire cross section. It should be pointed out that the flow experiences a highly unsteady behaviour, characteristic of separated flow in general and enhanced by the asymmetry in the geometry in particular. Time history data shows that the fast core of the flow oscillates in one direction (*i.e.* y) for some time and then suddenly changes into another direction (*i.e.* z). More specific, the shedding of a low-velocity structure was detected in the bottom of the diffuser around $x = 14$ with a Strouhal number of $St = fh/u_b = 1/50$, *i.e.* at a comparably low frequency. The separated flow was found to be laminar most of the time, as opposed to the highly fluctuating flow further away from the walls, which will contribute to a highly intermittent flow in this region, both in time and space. Finally, we also compare to the pressure data (Cherry *et al.* 2009) conducted for 'Diffuser 1' along the flat wall of the diffuser opposite of the top expanding wall by means of static pressure taps. The dimensionless pressure recovery coefficient, $C_p = (p - p_{ref})/\rho u_b^2$ is plotted against the streamwise coordinate xh/L in figure 7, where p_{ref} is the reference pressure at $x = 0.045$, $L = 15h$ is the length of the diffuser, ρ is the fluid density and u_b is the bulk velocity at the inlet of the diffuser. A constant of -0.02 is added to the experimental C_p in order to facilitate the comparison. The agreement is excellent, including the rapid rise, the gradual reduction in the pressure gradient and the linear part after $x = 0.7$. This result gives important information about the quality of the computed pressure field, which plays an important role in the Reynolds stress budgets. The effective pressure rise over the diffuser computed as $\Delta C_p = C_p(xh/L = 1.48) - C_p(xh/L = 0.045)$ is $\Delta C_p^{sim} = 0.569$ for the simulation and $\Delta C_p^{exp} = 0.587$ for the experiment.

4. Conclusions

Diffuser flows are numerically hard to treat in general, not only due to their sensitivity to discretization errors, but also as a consequence of the slow, separated flow the need for long (and expensive) time integration to obtain converged turbulent statistics. Nevertheless, their importance in technical applications cannot be underestimated. Three-dimensional diffusers, in particular, are even more challenging due to the lack of statistically homogeneous directions, and hence the possibility to average over these. In this paper, we study one of the diffuser geometries ('Diffuser 1') experimentally investigated by Cherry *et al.*

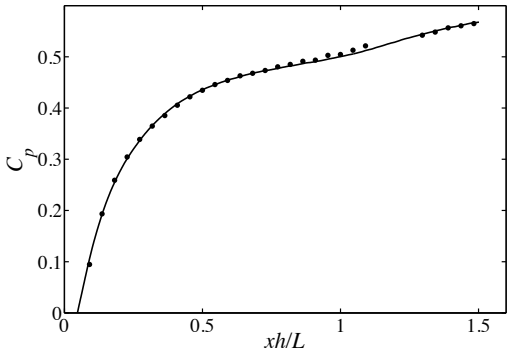

FIGURE 7. Pressure recovery coefficient relative to the pressure on the bottom wall of the diffuser inlet, where $L = 15h$ denotes the length of the diffuser. ——— `nek5000`, • experiment by Cherry *et al.* (2009).

(2008). In the present set-up, special care was taken to make the present computation free from artificial inflow condition through an unsteady trip forcing and a long development section. Taking the above difficulties into account and adding the general resolution requirements of a flow at $Re = 10\ 000$, the mean flow results presented here show very good agreement with experimental studies. The complex flow and the realistic Reynolds number proves that numerical simulations might qualify as a cheaper alternative to experiments. A slight discrepancy in the separated region was found, supported by findings of Schneider *et al.* (2009) and a physical explanation involving the secondary flow was given. As the quality of the data is now assessed, the complex flow physics in the three-dimensional separation will be further investigated. In addition, as turbulence modelling in separated flows continues to be an active area of research, this data will be available as a valuable reference database, where the Reynolds stress budgets might be of particular interest.

Computer time was provided by ALCF, Argonne National Laboratory (ANL) on the IBM BG/P (ANL) and by SNIC (Swedish National Infrastructure for Computing) with a generous grant by the Knut and Alice Wallenberg (KAW) Foundation at the Centre for Parallel Computers (PDC) at the Royal Institute of Technology (KTH). The third author was supported by the US Department of Energy under contract DE-AC02-06CH11357.

References

Buice, C. U. & Eaton, J. K. 2000 Experimental investigation of flow through an asymmetric plane diffuser. *J. Fluids Engng.* **122** (2), 433–435.

Cherry, E. M., Elkins, C. J. & Eaton, J. K. 2008 Geometric sensitivity of three-dimensional separated flows. *Int. J. Heat Fluid Flow* **29** (3), 803–811.

Cherry, E. M., Elkins, C. J. & Eaton, J. K. 2009 Pressure measurements in a three-dimensional separated diffuser. *Int. J. Heat Fluid Flow* **30** (1), 1–2.

Elkins, C. J., Markl, M., Pelc, N. & Eaton, J. K. 2003 4D magnetic resonance velocimetry for mean velocity measurements in complex turbulent flows. *Exp. Fluids* **34**, 494–503.

Fischer, P. F. 1997 An overlapping Schwarz method for spectral element solution of the incompressible Navier–Stokes equations. *J. Comput. Phys.* **133** (1), 84–101.

Fischer, P. F., Lottes, J. W. & Kerkemeier, S. G. 2008 nek5000 Web page. http://nek5000.mcs.anl.gov.

Herbst, A. H., Schlatter, P. & Henningson, D. S. 2007 Simulations of turbulent flow in a plane asymmetric diffuser. *Flow Turbulence Combust.* **79**, 275–306.

Iliescu, T. & Fischer, P.F. 2003 Large eddy simulation of turbulent channel flows by the rational large eddy simulation model. *Phys. Fluids* **15** (10), 3036–3047.

Jakirlić, S., Kadavelil, G., Sirbubalo, E., Breuer, M., v. Terzi, D. & Borello, D. 2010 In *14th ERCOFTAC SIG15 Workshop on Refined Turbulence Modelling: Turbulent Flow Separation in a 3-D Diffuser*. *ERCOFTAC Bulletin.* December Issue 85, case 13.2 (1). ERCOFTAC.

Kaltenbach, H.-J., Fatica, M., Mittal, R., Lund, T.S. & Moin, P. 1999 Study of flow in a planar asymmetric diffuser using large-eddy simulation. *J. Fluid Mech.* **390**, 151–185.

Landahl, M. T. 1980 A note on an algebraic instability of inviscid parallel shear flow. *J. Fluid Mech.* **98**, 243–251.

Maday, Y. & Patera, A. 1989 Spectral element methods for the Navier–Stokes equations. In *State of the Art Surveys in Computational Mechanics* (ed. A.K. Noor), pp. 71–143. ASME.

Ohlsson, J., Schlatter, P., Fischer, P. F. & Henningson, D. S. 2010 Large-eddy simulation of turbulent flow in a plane asymmetric diffuser by the spectral-element method. In *Direct and Large-Eddy Simulation VII* (ed. J. Fröhlich V. Armenio, B. Geurts), pp. 197–204. Springer.

Patera, A. T. 1984 A spectral element method for fluid dynamics: Laminar flow in a channel expansion. *J. Comput. Phys.* **54**, 468–488.

Schlatter, P., Örlü, R., Li, Q., Brethouwer, G., Fransson, J. H. M., Johansson, A. V., Alfredsson, P. H. & Henningson, D. S. 2009 Turbulent boundary layers up to $Re_\theta = 2500$ studied through numerical simulation and experiments. *Phys. Fluids* **21** (5), 051702.

Schneider, H., Terzi, D. A. & Rodi, W. 2009 Reliable and accurate prediction of three-dimensional separation in asymmetric diffusers using large-eddy simulation. In *Proceedings of ASME Turbo Expo 2009: Power for Land, Sea and Air*. Orlando, USA.

Sherwin, S. & Karniadakis, G. 1995 A triangular spectral element method; applications to the incompressible Navier–Stokes equations. *Comput. Methods Appl. Mech. Engng.* **123**, 189.

Simpson, R L 1989 Turbulent boundary-layer separation. *Annu. Rev. Fluid Mech.* **21** (1), 205–232.

Tomboulides, A. & Orszag, S. 2000 Numerical investigation of transitional and weak turbulent flow past a sphere. *J. Fluid Mech.* **416**, 45–73.

Tufo, H. M. & Fischer, P. F. 2001 Fast parallel direct solvers for coarse grid problems. *J. Parallel Distrib. Comput.* **61** (2), 151–177.

Wasberg, C. E., Gjesdal, T., Reif, B. A. P. & Andreassen, Ø. 2009 Variational multiscale turbulence modelling in a high order spectral element method. *J. Comput. Phys.* **228** (19), 7333–7356.

Paper 7

7

Coherent structures and dominant frequencies in a turbulent three-dimensional diffuser

By Johan Malm, Philipp Schlatter and Dan S. Henningson

Linné FLOW Centre, Swedish e-Science Research Centre (SeRC)
KTH Mechanics, 100 44 Stockholm, Sweden

J. Fluid Mech. Under revision.

Dominant frequencies and coherent structures are investigated in a turbulent, three-dimensional and separated diffuser flow at $Re = 10\,000$ (based on bulk velocity and inflow-duct height), where mean flow characteristics were first studied experimentally by Cherry *et al.* (2008) and later numerically by Ohlsson *et al.* (2010)[1]. Coherent structures are educed by proper orthogonal decomposition (POD) of the flow, which together with time probes located in the flow domain are used to extract frequency information. The present study shows that the flow contains multiple phenomena, well separated in frequency space. Dominant large-scale frequencies in a narrow band $St \equiv fh/u_b \in [0.0092, 0.014]$ (where h is the inflow-duct height and u_b is the bulk velocity), yielding time periods $T^* = Tu_b/h \in [70, 110]$ are deduced from the time signal probes in the upper separated part of the diffuser. The associated structures identified by the POD, are large streaks arising from a sinusoidal oscillating motion in the diffuser. Their individual contribution to the total kinetic energy, dominated by the mean flow, is however small. The reason for the oscillating movement in this low frequency range is concluded to be the confinement of the flow in this particular geometric set-up in combination with the high Reynolds number and the large separated zone on the top diffuser wall. Based on this analysis, it is shown that the bulk of the streamwise root mean square (r.m.s) arise due to large-scale motion, which in turn can explain the appearance of two or more peaks in the streamwise r.m.s. The weak secondary flow present in the inflow duct is shown to survive into the diffuser, where it experiences an imbalance with respect to the upper expanding corners, thereby giving rise to the asymmetry of the mean separated region in the diffuser.

1. Introduction

The topic of three-dimensional separation is difficult to attack, and despite its importance in technical applications, relatively few studies have so far been conducted. Rather than predicting three-dimensional separation, some investigations focus merely on interpreting the nature of it from an already given

[1]Due to a name change, 'J. Ohlsson' and 'J. Malm' refer to the same person.

flow field, further discussed in the review by Délery (2001). Other authors have tried to predict the separation by means of turbulence closure models, among them the periodic hill configuration investigated by Wang *et al.* (2004). These authors concluded that even though using an anisotropy-resolving closure on the simplest possible case involving separation in three dimensions, the model misses important mechanisms responsible for *e.g.* multiple-vortex structures in the wake. Even though engineering flows are *practically always fully three-dimensional*, most common turbulence closures fail in predicting three-dimensional separation correctly. In order to accelerate the development of such models, the physical mechanisms involved in this type of separation need to be well understood. A first step in this direction was taken by Cherry *et al.* (2008), who experimentally investigated the turbulent flow in a three-dimensional diffuser. Their idea was to create a truly three-dimensional flow case with well-defined boundary conditions in order to simplify the set-up for numerical simulations. The case has turned out to be an important test case for RANS models, hybrid RANS-LES as well as, to some extent, validation of SGS models (Jakirlić *et al.* 2010*b*). More specifically, Jakirlić *et al.* (2010*a*) showed promising results employing a hybrid RANS/LES scheme, whereas Schneider *et al.* (2009) obtained very good results using LES. The major improvement of the results using an eddy-resolving technique compared to steady RANS proves the difficulties involved in modelling such a complex, but yet realistic, flow.

Although being a valuable reference for some of the mean flow quantities, the experimental compilation by Cherry *et al.* (2008) gives little insight into the presumably complex flow dynamics present in the diffuser, as time-resolved information is lacking. In an attempt to enhance the understanding of this flow, a first direct numerical simulation (DNS) was performed by Ohlsson *et al.* (2010). The good agreement between the experimental data and the numerical simulation was established, thereby founding the validity of the numerical model as a whole. As a next step, the rich data base — including not only turbulence statistics but also temporal information — can now be accessed with high fidelity. In order to obtain converged statistics, long time integration was required. This is not only due to the lack of statistically homogeneous directions and the possibility to average over these, but also the long periods associated with the unsteadiness of the flow. A re-examination of the data showed that this unsteadiness contains regularities: quasi-periodic and coherent motions, which motivated a further analysis.

One question of particular interest in flow analysis is whether there are periodic or quasi-periodic motions with specific frequencies present in the flow. Practical reasons in engineering applications may be that these motions lead to unwanted vibrations, fatigue and possibly premature breakage. If heat transfer is an issue, oscillations in the flow may lead to an uneven heat distribution with decreased heat transfer as an effect. Separated flows, both laminar and turbulent, are characterised by large velocity fluctuations and chaotic and irregular unsteadiness. However, flows in which the separation is induced by an abrupt

change in the geometry (*i.e.* geometry-induced separation) often show the tendency of quasi-periodic motion. A well-studied example of this kind is the turbulent flow over a backward-facing step, where dominant frequencies have been reported in numerous studies. For instance, in a DNS, Le *et al.* (1997) reported a periodic behaviour of the free shear layer with Strouhal number of $St = fh/U_0 \approx 0.06$, U_0 being the free-stream velocity and h the step height. A low frequency 'flapping' motion was also observed by Eaton & Johnston (1980) in an experimental set-up of the backward-facing step. In a large-eddy simulation (LES), Friedrich & Arnal (1990) noticed an oscillation of the free shear layer, which in turn caused the location of the reattachment point to oscillate back and forth. Low-frequency periodic shedding have also been observed in other configurations involving geometry-induced separation. Kiya & Sasaki (1985) found periodic large-scale unsteadiness with some particular frequencies in the turbulent separation bubble formed at the leading edge of a blunt flat plate with right-angled corners.

Considering the experimental and numerical work performed on pressure-induced separated flows, where the separation is induced not by the geometry but rather by the action of the adverse pressure gradient, no such dominant frequencies are to our knowledge reported in the literature. Often the contrary is observed: the point of separation and reattachment varies in time and space with no particular periodicity. Accordingly, in the DNS of a pressure-induced separated turbulent boundary layer, Na & Moin (1998) noted that the shedding of large structures in the separated region is not a periodic process, but that there exists a characteristic Strouhal number $St = f\delta^*/U_0$ of the most energetic structures which ranges between 0.0025 and 0.01, with δ^* being the displacement thickness of the incoming flow and U_0 is the free-stream velocity. Similar conclusions have been deduced in turbulent diffuser flows with smooth rounded corners at the diffuser throat, thus belonging to the same class of pressure-induced separated flows. This was reported to be the case in the LES of the asymmetric diffuser with 10° opening angle by Kaltenbach *et al.* (1999), with a two-dimensional geometry. They found that the separation in the rear part of the expansion is a low-frequency unsteady process involving large scales of motion, but that the unsteadiness is broadband and cannot be characterised through a single frequency. Similar findings are reported by Herbst *et al.* (2007), who for a similar Reynolds number decreased the opening angle to 8.5°. However, the incoming channel flow was observed to penetrate in a 'jet-like' manner into the expanding diffuser section in this reference. Likewise, in the experimental set-up of the latter case, Törnblom *et al.* (2009) did see a 'jet-like' high-velocity region emanating from the inlet channel, but no temporal information on the properties of this jet in particular, or the separation bubble in general were provided, since no dominant frequencies could be detected (Johansson, private communication).

From the above discussion it appears that pressure-induced separated flows contain to a lesser degree quasi-periodic motions. However, up until now we

have considered flows without any type of confinement in the spanwise direction. If some sort of additional confinement is added to the flow, *e.g.* solid walls in the spanwise direction, the dynamics will inevitably change. This has previously been shown by several authors including Lawson & Davidson (2001); Maurel *et al.* (1996); Villermaux & Hopfinger (1994), here briefly summarised. Lawson & Davidson (2001) investigated the oscillatory behaviour of a confined jet in a rectangular cavity and reported that low Strouhal number oscillatory jets ($St \ll 1$, where St is based on the nozzle diameter) may occur when the confinement is such that the jet is bounded by one or two recirculation zones, created due to the close presence of the walls. These zones can under certain circumstances create a feedback mechanism which couples back to the jet nozzle, thereby resulting in self-sustained oscillations. They note that, by removing the recirculation zones, the feedback loop is broken and the regular jet oscillation will not occur. On the contrary, oscillations with $St \sim 1$, relate to the inherent instability of the jet shear layer and can thus be present also without the confinement. They found the low frequency oscillation of the jet to be independent of Re, and that the relevant parameter was the width-to-length ratio of the cavity. A reduction of this ratio would lead to an increase in St until the width coincided with the nozzle diameter and the jet would cease to oscillate. However, a too large increase of this ratio would not allow the recirculation zones to form and thus no oscillations of the jet were observed. The implication is that there exist a peak of the amplitude of the oscillation for some width-to-length ratio, *e.g.* a given shape of the confinement. Lawson & Davidson (2001) found that this ratio corresponded to the same ratio giving the highest crossflow disturbance velocities at the nozzle of the jet, caused by the recirculation. The fact that the width of the cavity is one of the most important parameters governing the presence of self-sustained oscillations was earlier confirmed by Maurel *et al.* (1996), who also argued that the nozzle width imposes the selected wavelengths within the values allowed by the boundary conditions imposed by the length of the domain. Another study on confined jets in a rectangular cavity at different Re by Villermaux & Hopfinger (1994), resulted in similar conclusions. In particular, they concluded that a free jet does not display low-frequency oscillations and that these oscillations are due to the confinement. They further state that the role of the confinement is to establish recirculation zones adjacent to the jet, which then convect high-amplitude perturbations upstream. These perturbations will interact with the shear instability of the jet after a certain time lag, given by the upstream convection velocity in the recirculation zone. They report that, for sufficiently high Re, the mean reattachment length and likewise St becomes independent of Re, and is found to be $St \sim 0.01$ (based on the nozzle diameter). For asymmetric configurations, it was found that the largest confinement dimension will dominate the flow.

The present flow case is both relevant and realistic from an engineering point of view, since it combines many complex phenomena, which are not even

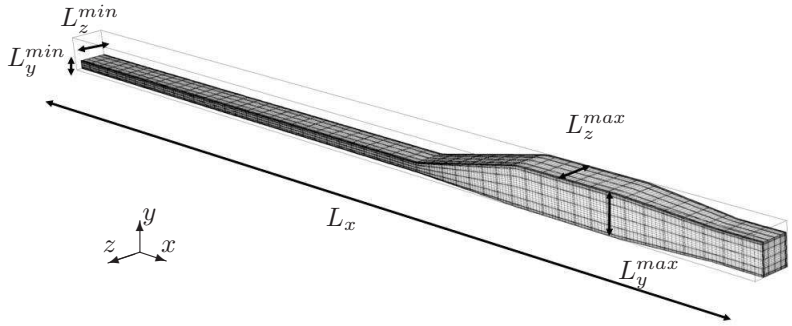

FIGURE 1. Computational grid of one of the diffuser geometries ('diffuser 1') in Cherry *et al.* (2008) showing the development region, diffuser expansion, converging section and outlet.

on their own fully understood but nevertheless exclusively present in most engineering flows: turbulent separation and three-dimensionality of the mean flow in conjunction with confinement. The aim of this paper is to provide an improved physical understanding of this flow by describing the observed dynamics, which up until now has not been described in detail. An extensive investigation of the oscillatory behaviour is made. The search for dominant frequencies is undertaken both by performing spectral analysis on a set of time signal probes and by proper orthogonal decomposition (POD) of the flow. The latter is also used to identify coherent structures associated with the dominant frequencies. The significance of the large-scale structures on the mean fluctuations of the flow is demonstrated by constructing a low-dimensional model of the flow based on the first few energetic POD modes. In Ohlsson *et al.* (2010), a slight discrepancy was found between the present DNS data and the experimental data of Cherry *et al.* (2008) regarding a pronounced vortex (referred to as 'bump') in the mean separated region. This finding gave a first indication that the reasons for and the characteristics of the separation might be more complex than expected. Here, this finding is more rigorously confirmed.

The paper is organised as follows. Section 2 briefly discusses the numerical method and the simulation set-up. In section 3.1 the evolution of the secondary flow in the diffuser together with instantaneous separations are analysed, whereas section 3.2 is devoted to the observed large-scale dynamics seen in the present DNS, investigated by means of time signal probes. Section 4 addresses the decomposition of the flow into POD modes as well as the low-dimensional reconstruction of the flow using only a few energetic modes. In particular, aspects of the global r.m.s distribution are addressed via POD. Finally, in section 5 the main conclusions of the present study are given.

2. Numerical method and simulation set-up

The three-dimensional, unsteady and incompressible Navier–Stokes equations are solved using a Legendre polynomial based spectral-element method, implemented in the code `nek5000`, developed and maintained by Fischer *et al.* (2008). For a detailed description of the spatial discretization and time integration, the reader is referred to Fischer (1997) and Tufo & Fischer (2001), whereas the main steps are outlined in Ohlsson *et al.* (2010). The computational domain, shown in figure 1, is set up in close agreement with the diffuser geometry employed in the experiment and consists of the inflow development duct with a length of almost 63 duct heights, h, (starting at the non-dimensional coordinate $x = -62.9$); the diffuser expansion located at $x = 0$; the straight section and finally the converging section upstream of the outlet. In the following, we mean by 'diffuser' the region between $x = 0$ and $x = 15$. The three-dimensionality arises from the asymmetry in the geometrical configuration: Whereas two of the walls are straight, the other two walls are deflected 11.3° in the y-direction and 2.56° in the z-direction (compare with the Cartesian box in figure 1). The corners resulting from the diffuser expansion are smoothly rounded with a radius of 6.0 in accordance with the experimental set-up. The maximum dimensions are $L_x = 105.4h$, $L_y = [h,\ 4h]$, $L_z = [3.33h,\ 4h]$. The fixed mass flux in the simulation enables the Reynolds number based on bulk velocity and inflow-duct height to be kept exactly at $Re = 10\ 000$, which matches the value reported in the experiment by Cherry *et al.* (2008). The resolution of approximately 220 million grid points is obtained by a total of 127 750 local tensor product domains (elements) with a polynomial order of 11 respectively, resulting in $\Delta z^+_{max} \approx 11.6$, $\Delta y^+_{max} \approx 13.2$ and $\Delta x^+_{max} \approx 19.5$ in the duct centre and the first grid point off the wall being located at $z^+ \approx 0.074$ and $y^+ \approx 0.37$ respectively. This resolution was carefully verified in Ohlsson *et al.* (2010) to yield accurate results compared to the experimental findings of Cherry *et al.* (2008). In the inflow duct, laminar flow undergoes natural transition by the use of an unsteady and random trip force with a prescribed length and time scale, successfully employed *e.g.* in the boundary layer simulation by Schlatter *et al.* (2009). First of all, this avoids the use of artificial turbulence where *ad hoc* parameters specifying the synthetic turbulence have to be set at the inflow plane and tuned in order to provide correct turbulent statistics further downstream. It also eliminates the spurious frequencies which have been observed in pressure-induced separated flow in conjunction with inflow recycling methods, discussed by Herbst *et al.* (2007) for the asymmetric diffuser flow. These are typically low frequencies correlated to the frequency whereby the inflow planes are fed at the inlet, also pointed out by *e.g.* Spille-Kohoff & Kaltenbach (2001) and Lygren & Andersson (1999) and may not be noticeable in flows with favourable or zero pressure gradient. In flows subject to an adverse pressure gradient exhibiting pressure-induced separation, however, a certain periodicity of the inflow signal can potentially trigger unsteady behaviour of the detachment point of a separation bubble, also observed by Adams (2000). In Ohlsson

TABLE 1. Overview of the time range pertaining to the present simulation

Time range (tu_b/h)	Purpose	Discussion
0–202	start-up	—
202–636	statistics	Ohlsson *et al.* (2010)
384–842	time probe data	current
448–840	snapshots	current
636–840	additional statistics	current

et al. (2010), it was demonstrated that the trip forcing mentioned above yields a fully developed flow well before the diffuser opening. Secondly, incorporating the laminar-turbulent transition in the same box further strengthens the similarities between simulation and experiments, since the flow in the experimental set-up indeed undergoes transition. Finally, a 'sponge region' is added at the end of the contraction in order to smoothly damp out turbulent fluctuations, thereby eliminating spurious pressure waves back into the domain. It is followed by a homogeneous Neumann condition for the velocities at the outflow boundary.

The simulation was performed on the Blue Gene/P at ALCF, Argonne National Laboratory (32 768 cores and a total of ~ 10 million core hours), the cluster 'Ekman' (2048 cores and a total of ~ 6.0 million core hours) and on the Cray XE6 at PDC, Stockholm (32 768 cores and a total of ~ 0.33 million core hours). Approximately thirteen flow-through times, $tu_b/L = 13$, based on bulk velocity, u_b, and diffuser length, $L = 15h$ were spent on the start-up phase in order to let the flow settle to an equilibrium state. Then, turbulent statistics for the mean flow results in Ohlsson *et al.* (2010) were collected over approximately $tu_b/L = 29$ additional flow-through times. During part of this time instantaneous snapshots were saved and time probe data was recorded. For the present work, the simulation has been extended with additionally $tu_b/L \approx 13$ flow-through times to ensure convergence of the mean flow results and capture the relevant dynamics in the instantaneous flow. This additional averaging time was observed to have a minute influence on the quantities already shown in Ohlsson *et al.* (2010). An overview of the various parts of the simulation is given in table 1. Already in Ohlsson *et al.* (2010), the flow was observed to be challenging: The three-dimensional configuration in combination with the large separated zones made the flow under investigation very instationary, which together with the lack of spatial homogeneous directions called for long time integration in order to obtain converged statistics and to collect all possible time scales in the flow.

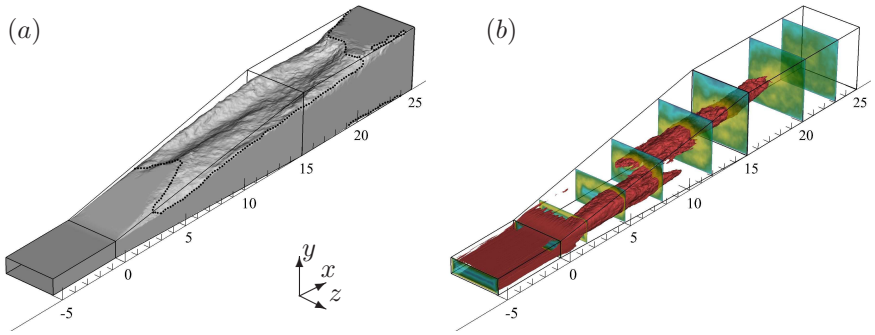

FIGURE 2. (*a*) Isosurface of (nearly) zero mean streamwise velocity ($U/u_b = 10^{-5}$). The dashed black line indicates zero streamwise shear stress, $\nabla U \cdot \boldsymbol{e_x}|_{\text{wall}} = \mathbf{0}$. (*b*) Isosurfaces (*red*) of the streamwise velocity fluctuation level $u_{rms}/u_b = 0.155$, with crossflow planes ($x = -5, 0, 2, 5, 8, 12, 15.5, 20, 23$) showing u_{rms}/u_b with colours ranging from 0 (*blue*) to 0.25 (*red*).

3. Analysis of averaged and instantaneous flow features

3.1. *Mean flow features*

In order to give a comprehensive picture of the flow, three-dimensional visualisations of the time-averaged streamwise velocity component $\langle u \rangle = U$ and the streamwise root mean square (r.m.s), u_{rms}/u_b, are shown in figure 2(*a*) and (*b*), respectively. Here, $\langle \cdot \rangle$ denotes an average over the (only) homogeneous direction time. Two-dimensional visualisations (*i.e.* crossflow plots) were already given in Ohlsson *et al.* (2010), where the emphasis was on the mean flow data and the comparison to the experiment by Cherry *et al.* (2008, 2009). An isosurface of nearly zero streamwise velocity ($U/u_b = 10^{-5}$) is shown in order to demonstrate the extent of the separated flow while excluding the no-slip boundaries. The dashed black line drawn at the wall indicates zero streamwise shear stress, *i.e.* $\nabla U \cdot \boldsymbol{e_x}|_{\text{wall}} = \mathbf{0}$, which here, as well as in Cherry *et al.* (2008), defines the extent of the separation bubble. We can note that the mean separated region is large: it covers approximately half the streamwise length, the entire spanwise length (in z) and the upper quarter of the diffuser. In addition, it continues well into the straight section. As a consequence, the dynamics of the flow is expected to be largely affected by the separation, with shear layers interacting with the incoming turbulence, thereby causing a complex flow with a high degree of unsteadiness. Further, we can observe that shortly after entering the diffuser, the flow separates in the upper right corner due to the asymmetric geometrical configuration, as was also observed in Ohlsson *et al.* (2010) and in agreement with the findings of Cherry *et al.* (2008). As we proceed downstream, the separated zone can be seen to broaden and move more

towards the top expanding wall, which has the largest opening angle. Simultaneously, the flow separates to the left around $x = 6$, and this is where the so-called 'bump' initially appears, first discussed in Ohlsson *et al.* (2010). The name originated from the particular shape of the zero streamwise velocity contour in a crossflow plane. In three dimensions, this structure (*i.e.* the 'bump') takes the form of a long and relatively deep 'valley', visible to the left in figure 2(a). Together with the separated region to the right, this results in two valleys on either side of a 'ridge', a feature which is most prominent between $x = 8$ and $x = 12$, but is nevertheless dominating the shape of the separation bubble for the rest of its streamwise extent. The shape of the zero velocity surface, including the just mentioned feature, and the dashed line are in good agreement with LES of the same flow by Schneider *et al.* (2009), where a similar three-dimensional visualisation is given. The major difference is that therein the first sign of separation appears on the top expanding wall just after the diffuser opening, across the entire spanwise extent of the diffuser and localised to approximately $2h$ in the streamwise direction. However, this finding is supported neither by our DNS nor the experimental data set, but, as we shall see later in this section, instantaneous backflow is present in this region. As also evident from the streamwise fluctuations in figure 2(b), the flow changes drastically from an attached turbulent flow in the duct where the bulk of the fluctuations are present close to the wall, to the separated flow in the diffuser where the highest fluctuations are found around the centre of the domain. As noted in Ohlsson *et al.* (2010) and Cherry *et al.* (2008), when the flow has entered the diffuser, the peak u_{rms} is found in the shear layer bounding the separated zone in the upper right corner. This is also where the highest overall fluctuations occur in the flow. For the particular isosurface visualised in figure 2(b), there is a 'double peak' appearing around $x = 8$. For lower levels of u_{rms} this double peak emerges further downstream. The reasons for this behaviour has up until now not been addressed in any study of this flow. Here, however, this peculiar phenomenon will be further investigated and we will see that it is connected to the large-scale motions found in the diffuser.

The present flow case consists of turbulent flow in a rectangular duct which eventually separates in the diffuser. Hence, secondary flow of the *second kind* is present due to crossflow gradients in the Reynolds stresses (see *e.g.* Piquet 1999). An indication that this flow has an effect on the separation behaviour is given by the several RANS predictions documented in Jakirlić *et al.* (2010*b*). There, it was observed that most eddy-viscosity models, which assume isotropic conditions and hence no secondary flow in the duct, would fail to predict the separation correctly. On the other hand, Reynolds-stress models which were able to compute the secondary flow in the duct, were in general much closer in getting a correct separation behaviour. The finding of the 'bump' discussed earlier initiated a further study on the reasons for this particular phenomenon. It was conjectured that, although very weak in magnitude, the corner vortices induced by the secondary flow in the inflow duct persist into the diffuser (Ohlsson *et al.* 2010). There, they give rise to a dominant low-speed streak,

due to a similar mechanism as the so-called 'lift-up effect' in transitional shear flows (Landahl 1980), which in turn has a large influence on the separation behaviour. To further confirm these conjectures, we track here the secondary flow from the inflow duct into the diffuser by means of streamwise vorticity computed from the mean flow field, *i.e.* $\langle\omega_x\rangle = \partial\langle v\rangle/\partial z - \partial\langle w\rangle/\partial y$. Due to slow variation of mean quantities in the streamwise direction, the vorticity (and all other quantities, to be consistent) are averaged over a distance h in x. Moreover, a smoothing in the yz-plane is performed by applying a mean filter over a rectangle of size 2-by-2 points, which basically replaces point i by the mean of the rectangle centred on i. A three-dimensional visualisation of the mean streamwise vorticity is given in figure 3. Here, isosurfaces of positive vorticity are shown to indicate the corner vortex to the upper left, whereas isosurfaces of negative vorticity (of the same magnitude) show the evolution of the right vortex. Crossflow planes with mean streamwise velocity are included with thin black lines indicating the zero velocity contour. First of all, it is evident that the mean secondary flow continues from the duct into the diffuser. Secondly, one can observe that the right vortex is diffused rather quickly and is therefore less coherent than its left counterpart. (The definition of left and right according to figure 3.) As discussed above, when entering the diffuser, the flow separates first in the upper right corner. As an effect of the separated flow, the turbulence intensity increases (values of u_{rms}/u_b reaching 25 % were observed by Cherry *et al.* (2008) in the shear layer bounding the separation bubble). The increased turbulent activity enhances the turbulent diffusion in this region and, accordingly, the secondary flow is weakened — in particular the negative vorticity. This is further quantified in figure 4, where a crossflow plane at $x = 12$ is selected. The appearance of the 'bump' can now be clarified by noting the imbalance between the positive vorticity to the left and the negative vorticity to the right in figure 4(a). Thus, the magnitude of the vorticity to the left is greater than the magnitude of the vorticity to the right, quantified in figure 4(b), where the vorticity along y in the crossflow plane at $x = 12$ is shown. Here, $z = 0.368$ and $z = 3.73$ denote the spanwise coordinates where the maximum magnitudes of positive vorticity in the upper left and negative vorticity in the upper right corners are found, respectively. The primary vortices responsible for the crossflow in the vicinity of the zero streamwise velocity contour are of main focus, and hence the boundaries, where the vorticity locally can be very high, are excluded. From figure 4(b), it is evident that the left vortex is stronger (almost by a factor two) than the one to the right. This is thought to be the basic mechanism to create and maintain the observed asymmetry in the zero streamwise velocity contour.

To conclude these considerations, due to the choice of delivering the inflow through a duct, there is a secondary flow inherent to the mean flow. This flow has been observed to persist into the diffuser. Evaluation of the magnitude of the local vorticity shows that the left vortex is twice as strong as its right counterpart, which creates an asymmetry in the zero velocity contour. Here it

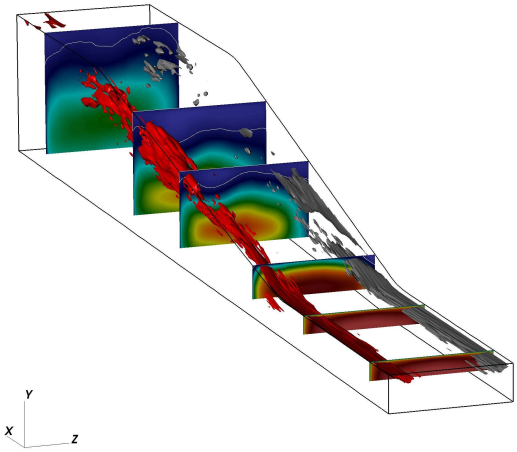

FIGURE 3. Isosurfaces of mean streamwise vorticity $\langle\omega_x\rangle = 0.15$ (*red*) and $\langle\omega_x\rangle = -0.15$ (*dark gray*) showing the evolution of the upper left and right corner vortices, respectively. Crossflow planes of mean streamwise velocity are shown at $x = -7, -2, 2, 8, 12, 20$ ranging from -0.1 (*blue*) to 1.2 (*red*). Thin black lines indicate zero streamwise velocity contour.

can be in place to point out that due to the asymmetry of the geometrical set-up, there is no reason to expect that the separated zone on the top expanding wall should be symmetric with respect to the z-axis. Finally, it should be noted that this weak secondary flow (a few percent of the bulk flow) which originates from the inflow duct appears in the mean. Superimposed on this flow there is momentary a stronger crossflow[2] caused by the large-scale oscillation in the diffuser, to be discussed in the next section.

The mean flow shown in figure 2 does only provide information about the mean separation. Sometimes, however, it can be useful to know to what extent instantaneous separation occurs in the flow. Aiming at providing a fuller picture of this flow, we end this section by investigating the fraction of time that the flow moves in positive streamwise direction. Traditionally, this fraction is denoted by γ (after Simpson 1981), and amounts to the following special cases; $\gamma = 1$: never backflow and $\gamma = 0$: always backflow. In the classical review on separated flows by Simpson (1989), a few intermediate cases are discussed in order to broaden the view on turbulent separated flows. More specific, $\gamma = 0.99$ is the so-called *incipient detachment* (ID) where backflow occurs 1 % of the time; $\gamma = 0.80$ is the *intermittent transitory detachment* (ITD) and $\gamma = 0.50$ is the *transitory detachment* (TD). In the present case,

[2]There is also an in-plane flow caused by the expansion, but it does however not contain vortices.

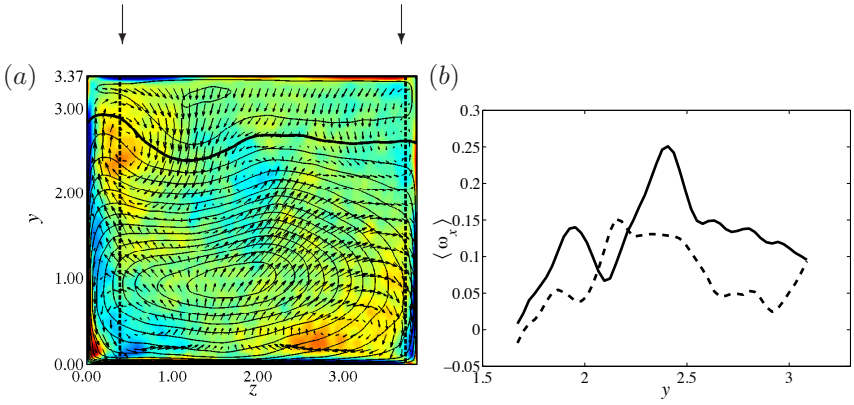

FIGURE 4. (a) Crossflow plane of mean streamwise vorticity, $\langle\omega_x\rangle$, 12 h downstream of the diffuser throat, ranging from -0.5 (*blue*) to 0.5 (*red*). Contour lines of mean streamwise velocity, spaced 0.05 u_b apart, as well as velocity vectors of mean crossflow velocities are superimposed. Thick black lines correspond to the zero mean streamwise velocity contour. (b) $\langle\omega_x\rangle$ at $z_1 = 0.368$ (——) and $-\langle\omega_x\rangle$ at $z_2 = 3.73$ (- - - -) along y in the crossflow plane in (a) across the two primary vortex centres responsible for the maximum magnitude in the upper left and right corners, respectively. Black arrows in (a) indicate z_1 and z_2.

a number of snapshots spanning a total time of $\Delta t u_b/h = 392$ were used. In figure 5(a) γ is computed at all x-locations between $x = -5.15$ and $x = 35.6$. The y and z-positions for the thick black line corresponds to the upper history points in figure 8 (*i.e.* at the same grid point from the wall and at a spanwise midposition). We observe that backflow is never present ($\gamma = 1$) until $x \approx 4$. Then, there is a rapid increase of backflow until $x \approx 15$ when the flow is in the positive x-direction only 10 % of the time, *i.e.* directed backwards 90 % of the time. After this point, there is an almost symmetric recovery until $x \approx 28$, after which the flow is seen to be attached again. The thin black line is computed in a spanwise midposition and in the first y-point off the top expanding wall. This is equivalent to the linear extrapolation of the corresponding fraction of positive and negative streamwise shear stress at the wall. Incipient detachment occurs already at a few places $x \in [-5, 0]$ in the turbulent duct. Then, at the location of the diffuser opening ($x = 0$), γ rapidly drops down to 0.8 ($x = 0.4$) and then increases to 0.5 ($x = 0.58$), after which it quickly recovers to 0.9. This behaviour approximately follows the development of the skin friction coefficient in pressure-induced separated flows, discussed by *e.g.* Kaltenbach *et al.* (1999); Herbst *et al.* (2007). Since three-dimensional velocity fields were used to compute $\gamma(x)$, we are by no means restricted to the particular subset

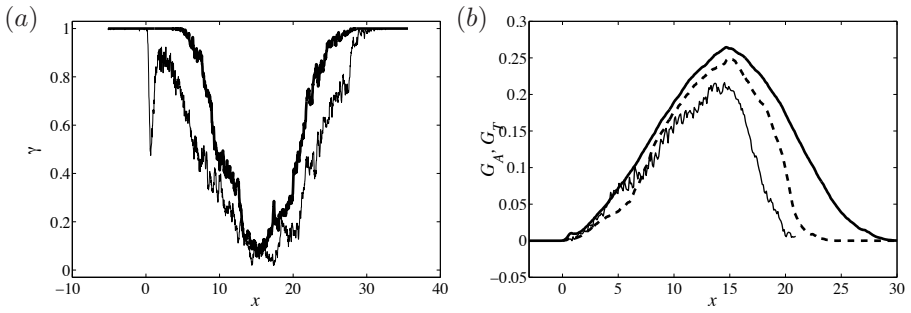

FIGURE 5. (*a*) Backflow ratio $\gamma(x)$ in y-coordinates corresponding to the upper history points in figure 8 (———) and in the first y-point off the top expanding wall (———), both being taken in a spanwise midplane. (*b*) Fraction of cross-sectional area separated, $G_A(x)$: experimental data by Cherry *et al.* (2008) (———), the present DNS data (- - - -) together with the 'temporal backflow ratio', $G_T(x)$ (———).

shown in figure 5(*a*). Thus, instead of choosing one specific trajectory through the data set, we could at each streamwise location integrate γ over a crossflow plane, in order to get a more robust measure of the development of the backflow through the diffuser. More specifically, we compute the following integral in each plane,

$$G(x) = \frac{1}{A(x)} \iint_{A(x)} \gamma(x, y, z) \, \mathrm{d}x\mathrm{d}y. \tag{1}$$

The function $G(x)$ has a shape similar to $\gamma(x)$ (*thick black*) shown in figure 5(*a*). To be able to compare this measure to the fraction of cross-sectional area separated, provided in Cherry *et al.* (2008), here called $G_A(x)$, we will define a new quantity based on $G(x)$ called 'temporal backflow ratio': $G_T(x) = 1-G(x)$. In figure 5(*b*) these two integral quantities are compared, with $G_A(x)$ based on the experimental data included as a reference. First of all, the comparison between $G_A(x)$ in the DNS and the experiment agree reasonably well, especially in most of the diffuser region ($x = 0-10$). Note also that the point of separation is identical. At the end of the diffuser and in the following straight section, the experiment show somewhat less separated flow compared to the DNS with the peak separated flow ($x = 15$) being ~ 10 % less in the experiments. However, at the very end ($x = 20$) the reattachment points coincide. Now, comparing $G_T(x)$ and $G_A(x)$ based on the DNS, we notice that the correspondence is close early on in the diffuser. Both peaks occur at the same streamwise location ($x = 15$), but with G_T being approximately 10 % larger. In the straight section G_T generally attains higher values. In particular, when G_A is zero ($x = 20$), G_T is nonzero for approximately $10h$ more. While this is not surprising, since indeed the contribution to the former quantity is present even for small backflow ratios, it gives important information about the dynamics. Thus, we can conclude

that, in particular in the straight section, instantaneous backflow is to a large extent present, while the mean flow is attached.

In figure 6 we show three-dimensional views of $\gamma(\boldsymbol{x})$, where $\boldsymbol{x} = (x, y, z)$. Here, *red* means $\gamma = 1$, *yellow* is $\gamma = 0.75$, *green* is $\gamma = 0.5$ and *blue* denotes $\gamma = 0$. In figure 6(a), $\gamma(\boldsymbol{x})$ is shown in the first point off the two expanding walls, which again qualitatively behaves as the shear stress at the wall. The arrows indicate where ID, ITD and TD occur for the first time in a spanwise midplane, *i.e.* following the thin black line in figure 5(b). As pointed out in Simpson (1989), $\gamma = 0.5$ approximately correspond to the time-averaged streamwise skin friction being zero (given that the streamwise velocity probability distribution is symmetric about zero velocity), *i.e.* $\langle \boldsymbol{\tau_w} \cdot \boldsymbol{e_x} \rangle = \boldsymbol{0}$. Here, we can confirm this finding by observing a quantitatively similar shape in the green contour in figure 6(a) as in the dashed black line in figure 2(a). It is interesting to note that on the upper wall the flow is attached at all times all the way to the diffuser opening (*red*). Then, there is a short distance where instantaneous backflow occurs (*green*), noted by Schneider *et al.* (2009) as a region with $U/u_b = 0$. Such a region was not observed in our mean flow data. Shortly thereafter, the flow is in a triangular region $75 - 90$ % of the time (*yellow-light red*) aligned with the forward direction. To the right of this region, we see an intensively blue area filling the entire upper right edge. Thus, the flow is always oriented in the negative streamwise direction along this edge. Series of instantaneous visualisations of the flow confirm that separated flow further downstream tend to end up in this edge of the diffuser. The triangular region on the upper wall is around $x = 7$ approaching transitory detachment, where $\gamma = 0.5$. This value of $\gamma = 0.5$ is kept in the middle of the upper wall, accompanied by $\gamma \approx 0$ on both sides, until around $x = 15$ where most of the top wall is covered with backflow. This particular behaviour is due to the presence of the 'bump' underneath, clearly visible in figure 6(b) (the fifth plane shown), where the same crossflow planes as in figure 2(b) are shown, with the colour scheme being the same as in figure 6(a). Here, we also observe the small separated 'triangle' in the upper right corner early in the diffuser (the third plane shown), previously seen in the streamwise mean flow. From both figure 6(a) and (b) we can confirm that most backflow occurs around $x = 15$, as already concluded from figure 5(a) and (b). Further downstream, the flow once again approaches the transitory detachment, *i.e.* the end of the mean separated region. As soon as the converging section starts, the flow can be seen to be attached 100 % of the time. From an engineering point of view, this shows the efficiency of such a region to counteract separation. Secondly, it points out the importance to include this section for the simulation to mimic the experiment as close as possible. Without this region, the flow would probably have required a much longer development section in order to become fully attached duct flow again.

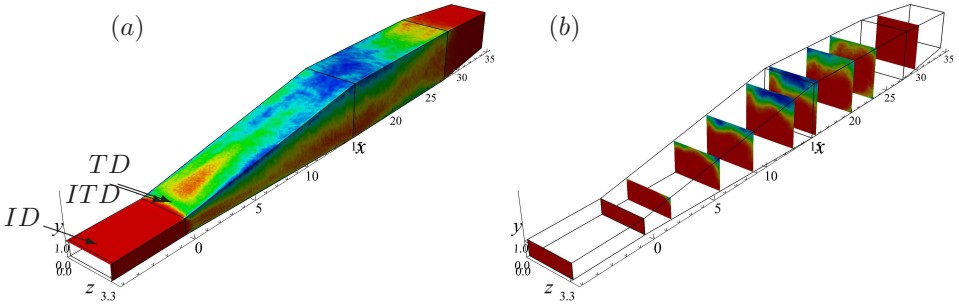

FIGURE 6. (*a*) Pseudocolours of $\gamma(\boldsymbol{x})$ ranging from *blue*: $\gamma = 0$ to *red*: $\gamma = 1$ shown in the first point off the two expanding walls and (*b*) in the same crossflow planes as in figure 2(*b*). Arrows indicate where ID, ITD and TD occur for the first time in a spanwise midplane.

3.2. *Observed large-scale oscillations*

As the turbulent flow enters the diffuser, it will rapidly undergo pressure-induced separation. Instantaneous snapshots, as the ones depicted in figure 7, indicate that the flow is subjected to a motion that resembles the 'flapping' or meandering of a jet. This feature is strong and has been observed at all times during the simulation. A more quantitative analysis of this phenomenon is made from a set of time signal probes placed in the flow domain. We have chosen to study the time signal by placing one probe in the upper part and one in the lower part of the diffuser at $x = 5, 8, 12, 15$, where the latter three are indicated in figure 8. These four placings correspond to locations studied for the mean quantities in Cherry *et al.* (2008).

The recording of the time signal started well after the flow had reached an equilibrium state and spans a total time of $tu_b/h = 458$, which is enough to capture a few periods of the large-scale oscillations observed in the flow. The time signals are shown in figures 9 and 10, with their respective power spectral density (PSD) shown in figure 11. Except for the close-up view in figure 9(*c*), the interval on the ordinate is fixed to $\Delta u = 0.9u_b$ in all figures to facilitate comparisons. All spectra in the following were computed using Welch's method, where the signal is split into two overlapping segments, each of which are windowed by a Hamming window, whose length is the same as the segment. The spectral resolution in terms of non-dimensional frequency $St \equiv fh/u_b$ is therefore $St = 2/T_{\mathrm{win}} = 2/343.5 = 0.0058$, where T_{win} is the length of the windowed signal. The PSD from each signal in figure 11 is normalised by the spectral peak in the time signal given by the upper probe at $x = 15$.

In the symmetric duct (not shown), the flow is governed by rapid velocity fluctuations and small-scale turbulence with a broad spectral content. As we

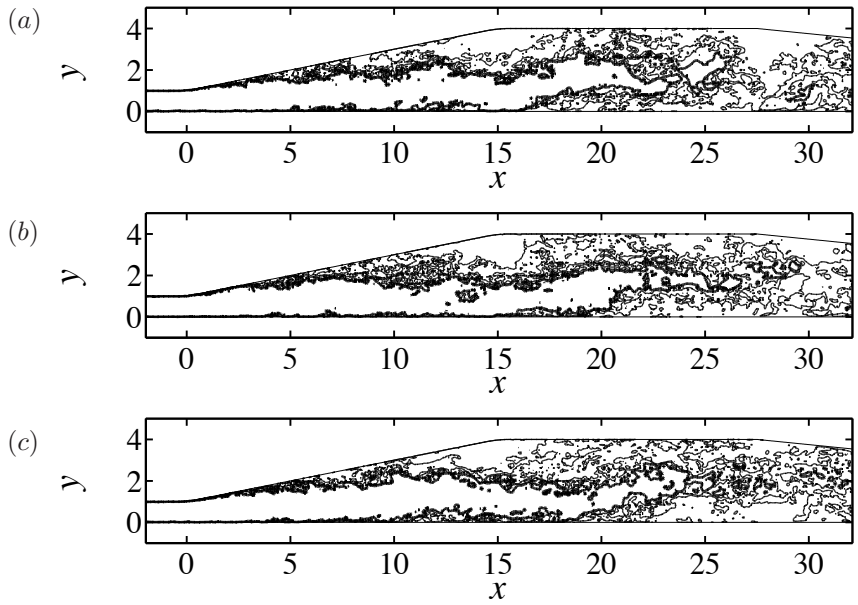

FIGURE 7. Three snapshots in a xy-plane at $z = 1.87$ shown at (a) $t = t_0$, (b) $t = t_0 + 10h/u_b$, (c) $t = t_0 + 20h/u_b$. Thin contour lines of streamwise velocity are shown for $u/u_b = 0, 0.2$ and 0.3, whereas the thick contour line is shown for $u/u_b = 0.4$.

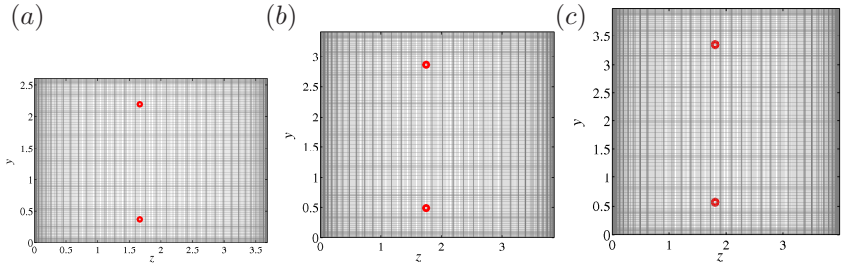

FIGURE 8. Location of history points (*red*) and computational grid at the streamwise positions (a) $x = 8$, (b) $x = 12$ and (c) $x = 15$.

enter the diffuser, the flow quickly becomes different in the upper and the lower parts, respectively. Whereas the flow in upper part rapidly looses its highest frequencies, they continue to be present in the fully attached flow close to the lower wall. This is exemplified in figure 9, where the streamwise velocity signal at $x = 8$ in (a) can be seen to have less high spectral content than the signal in (d), which is taken from $x = 12$, *i.e.* further downstream. At $x = 5$ (only shown

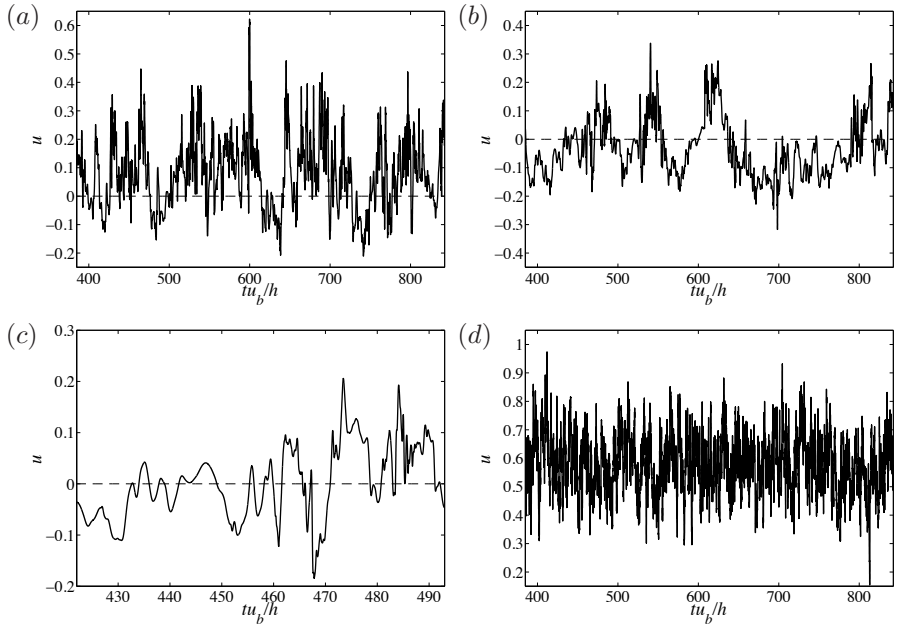

FIGURE 9. Time signals of streamwise velocity from probes located at (*a*) $x = 8$ and (*b*) $x = 12$ in the upper part of the diffuser. (*c*) Close-up view of (*b*) showing the intermittent flow in this region due to the presence of the separation. (*d*) Time signal of streamwise velocity from a probe located at $x = 12$ in the lower part of the diffuser.

in terms of its spectrum in figure 11), a large-scale peak in the upper time signal probe starts to emerge, and we note a peak at $St = 0.044$ besides the one at $St = 0.16$. Still, the small-scale turbulence is significant, evident in figure 11(*c*), where the PSD from the upper probes at $x = 5$ and $x = 12$ are compared in a plot with frequencies and energies on a logarithmic scale. As we approach the mean separated region ($x = 8$, figure 9*a*), the strength of the large-scale peak has become significant. Here, the peak at $St = 0.014$ in figure 11(*a*) is three times stronger than the peaks at $x = 5$. This trend continues further downstream, and at $x = 12$, where the time signal is shown in figure 9(*b*), the same peak at $St = 0.014$ is 50 % stronger than it was at $x = 8$. The location of the upper probe at $x = 12$ coincides roughly with the edge of the mean separation bubble as given in Cherry *et al.* (2008) and Ohlsson *et al.* (2010), explaining why in figure 9(*b*) the fluctuations are evenly distributed around zero. Note that the presence of the edge of the separated zone gives rise to a highly intermittent flow, visible in the close-up view of figure 9(*b*) in figure 9(*c*). At $x = 15$ the two walls are separated even further apart and the upper probe is now located within the mean separated region. This manifests itself in long

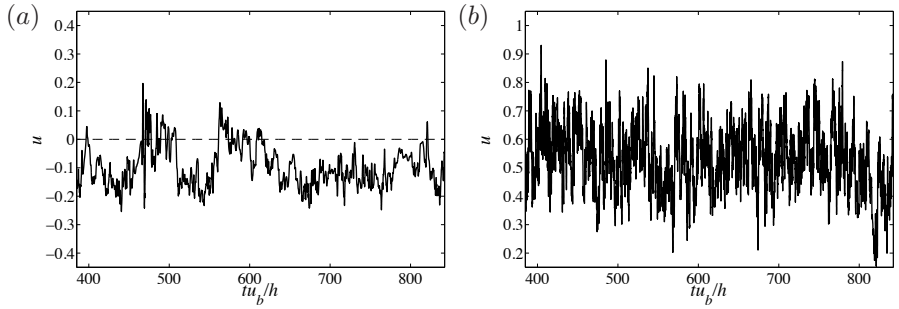

FIGURE 10. (*a-b*) Time signals of streamwise velocity from probes located in the upper and lower regions of the diffuser at $x = 15$, respectively.

periods with negative flow, but also relatively long periods of essentially zero flow, as shown in figure 10(*a*). Still, the spectral peak in figure 11(*a*) is centred around $St \approx 0.01$ ($St = 0.0092$), thus giving an estimate for the frequency of the separated region. The time signal measured by the lower probe is similar to the corresponding signal at $x = 12$, save that the magnitude of the mean flow is slightly lower and the spectra in figure 11(*b*) contains somewhat fewer high frequencies. The peak frequency is found at $St \approx 0.1$, *i.e.* a roughly ten times higher frequency than the dominant frequency in the separated part of the flow at this streamwise location, but only with approximately a fifth of its magnitude.

To conclude, the analysis from the time probes shows that the flow in the upper part of the diffuser contains large-scale dynamics with dominant frequencies in a comparably narrow band $St \in [0.0092, 0.014]$, yielding time periods $T^* = 1/St \in [70, 110]$, where T^* is a non-dimensional time. The fact that there is a narrow band of dominant frequencies seen in the separated part of the diffuser suggests that there may be self-sustained oscillations present, since there is a possibility for disturbances to create a feedback mechanism via the recirculated flow. This is supported by the findings of Lawson & Davidson (2001) and Villermaux & Hopfinger (1994) who found self-sustained oscillations to be present in confined jets in conjunction with adjacent separated zones. At this point it is important to note that in studies of two-dimensional diffuser geometries (Kaltenbach *et al.* 1999; Herbst *et al.* 2007) flat spectra without any distinct peaks were observed.

4. Analysis of modal decomposition

4.1. *Flow decomposition*

The large-scale oscillations observed in the time probes indicate that there might be large-scale energetic and coherent structures present in the flow. To investigate this further, proper orthogonal decomposition (POD) is used to

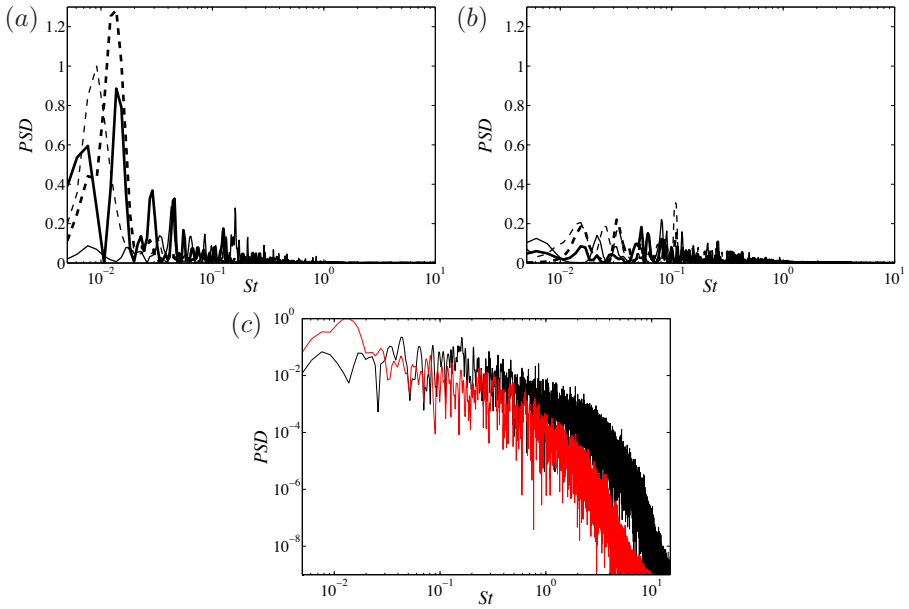

FIGURE 11. Power spectral density (PSD) of the time signals at $x = 5$ (———), $x = 8$ (———), $x = 12$ (- - - -) and $x = 15$ (- - - -) for the (a) upper probe and (b) lower probe, normalised with the maximum intensity of the upper probe at $x = 15$. (c) PSD computed from the upper time signal probe at $x = 5$ (*black*) and $x = 12$ (*red*).

decompose the flow in its most energetic three-dimensional parts (Lumley 1967; Holmes *et al.* 1996). Considering the turbulent flow field $\boldsymbol{u}(\boldsymbol{x}, t)$ with velocity vector $\boldsymbol{u} = (u, v, w)$, defined in physical space $\boldsymbol{x} = (x, y, z)$ and time t, a modal decomposition of this kind attempts to split the space and time dependence, and is thus of the form,

$$\boldsymbol{u}(\boldsymbol{x}, t) = \sum_{j=0}^{\infty} a_j(t)\boldsymbol{\psi}_j(\boldsymbol{x}). \tag{2}$$

Note that $\boldsymbol{u}(\boldsymbol{x}, t)$ indeed is the full velocity field, *i.e.* the mean flow not being subtracted. As we shall soon see, the implication for the POD is that the mean flow will be part of the decomposition. Since our velocity fields are naturally truncated by the numerical simulation, this sum can without loss of generality be taken up to some $m \ll \infty$. The POD procedure finds deterministic, bi-orthogonal functions, $\boldsymbol{\psi}_j(\boldsymbol{x})$, which maximise the energy in the field $\boldsymbol{u}$. A necessary condition for this to hold is that $\boldsymbol{\psi}_j(\boldsymbol{x})$ is an eigenfunction of the two-point spatial correlation tensor $\boldsymbol{R}(\boldsymbol{x}, \boldsymbol{x'}) = \frac{1}{T}\int_T \boldsymbol{u}(\boldsymbol{x}, t)\boldsymbol{u}(\boldsymbol{x'}, t)\,\mathrm{d}t$, where T denotes the total time over which the flow is observed (rigorously shown in

Holmes *et al.* 1996). Finding the eigenvalues, λ_j, and corresponding eigenfunctions, $\boldsymbol{\psi}_j$, of $\boldsymbol{R}(\boldsymbol{x},\boldsymbol{x'})$ amounts to solving,

$$\iiint_V \boldsymbol{R}(\boldsymbol{x},\boldsymbol{x'})\boldsymbol{\psi}_j(\boldsymbol{x'})\ \mathrm{d}\boldsymbol{x'} = \lambda_j \boldsymbol{\psi}_j(\boldsymbol{x}). \tag{3}$$

The m temporal coefficients at m discrete times in equation (2) can then in a successive step be solved for by projecting the spatial modes onto the velocity field,

$$a_j(t) = \iiint_V \boldsymbol{u}(\boldsymbol{x},t)\boldsymbol{\psi}_j(\boldsymbol{x})\ \mathrm{d}\boldsymbol{x}, \tag{4}$$

where we have used the bi-orthogonality in space. Note that the discrete equivalent of $\boldsymbol{R}$ will be a matrix of size $n \times n$, where $n = 3 \times n_x \times n_y \times n_z$ and n_x, n_y, n_z are the resolutions in the spatial directions, respectively. Therefore, for high spatial resolutions, equation (3) is usually impossible to solve directly. However, using the snapshot method (Sirovich 1987), equation (3) can be circumvented by solving an eigenvalue problem of the generally smaller temporal two-point correlation tensor $\boldsymbol{C}(t,t') = \frac{1}{T}\iiint_V \boldsymbol{u}(\boldsymbol{x},t)\boldsymbol{u}(\boldsymbol{x},t')\ \mathrm{d}\boldsymbol{x}$, which is computed using a sequence of flow fields or 'snapshots' saved at m discrete times $\{\boldsymbol{u}(t_1),...,\boldsymbol{u}(t_m)\}$. This yields a matrix of size $n \times m$, which for numerical simulations is typically smaller than $n \times n$. We are now instead solving

$$\int_T \boldsymbol{C}(t,t')a_j(t')\ \mathrm{d}t' = \lambda_j a_j(t). \tag{5}$$

Then, as a second step, the spatial eigenfunctions are constructed as

$$\boldsymbol{\psi}_j(\boldsymbol{x}) = \frac{1}{T\lambda_j}\int_T a_j(t)\boldsymbol{u}(\boldsymbol{x},t)\ \mathrm{d}t. \tag{6}$$

Here, the division by the respective eigenvalue ensures that the modes are normalised to unit energy. Once this is done, the temporal coefficients can be computed according to equation (4), and the ones obtained from equation (5) are disregarded.

For the present POD analysis, a set of $m = 196$ snapshots spanning a time of $\Delta t u_b/h = 392$ is used. The temporal resolution is set to $\Delta t u_b/h = 2$. It has been verified that the mean flow and the mean fluctuations of these snapshots are in close agreement with the results in Ohlsson *et al.* (2010), and thus the experimental data by Cherry *et al.* (2008). A discussion regarding convergence of the POD modes is given at the end of the present section. To avoid equation (5) to be prohibitively expensive to solve, the streamwise extent of the velocity fields was reduced, such that only data between $x = -0.15$ and $x = 23.85$ was used for the POD analysis. After this operation, the resulting matrix containing all snapshots has size $n \times m \sim 10^9$, where $n = 3 \times n_x \times n_y \times n_z = 3 \times 1152 \times 120 \times 420 \approx 1.74 \cdot 10^8$ and $m = 196$. Assuming each entry in the matrix being of double precision accuracy, yields a matrix of size ~ 273 Gb.

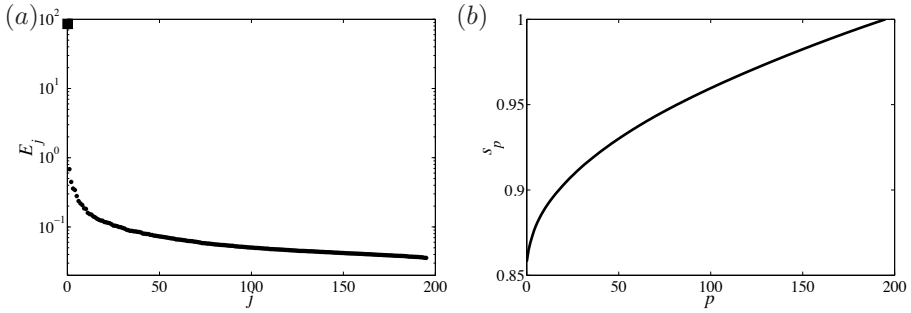

FIGURE 12. (*a*) The total kinetic energy $E_j = (\lambda_j / \sum_{i=0}^{195} \lambda_i) \times 100$ of the POD modes with $j = 0, ..., 195$. The mean flow ($j = 0$) is indicated by the solid rectangle. (*b*) Cumulative energy sum, $s_p = \sum_{i=0}^{p} \lambda_i$, for modes $p = 0, 1, ..., 195$ in the expansion.

The fraction of energy in the respective modes is given by $E_j = (\lambda_j / \sum_{i=0}^{195} \lambda_i) \times 100$ with $j = 0, ..., 195$ and λ_j being the eigenvalues. The entire energy spectrum is shown in figure 12(*a*). Since the mean was not subtracted from the flow fields prior to the decomposition, the first mode in the expansion containing most of the kinetic energy (indicated by the solid square), is the mean flow, denoted by 'mode 0'. The cumulative energy sum, $s_p = \sum_{i=0}^{p} \lambda_i$, is shown in figure 12(*b*), from which we can conclude that the mean flow carries the bulk, approximately 86 %, of the kinetic energy. This is close to what was found for a POD of a fully inhomogeneous turbulent flow over a surface-mounted obstacle by Manhart & Wengle (1993), who noted that 91.4 % of the total kinetic energy was contained in the mean flow. In figure 12(*b*) we also note that the last 90 % of the modes contribute as little as 10 % to the total energy. Since the mean flow is not the main topic of the present section, the discussion will from now on focus on the fluctuating modes. The fluctuating energy, defined as $E_j^{\text{fluct}} = (\lambda_j / \sum_{i=1}^{195} \lambda_i) \times 100$ with $j = 1, ..., 195$ is shown in figure 13(*a*). The corresponding cumulative energy sum, $s_p^{\text{fluct}} = \sum_{i=1}^{p} \lambda_i$, is shown in figure 13(*b*). From figure 13(*a*), we see that the first, second and third mode contribute with 4.8 %, 3.1 % and 2.5 %, respectively, to the fluctuating kinetic energy. Moreover, $E_1^{\text{fluct}} / E_2^{\text{fluct}} = 1.5$ and $E_2^{\text{fluct}} / E_3^{\text{fluct}} = 1.2$, which is similar to Moin & Moser (1989) for their POD analysis of a turbulent channel flow. However, there, the first mode contained approximately 50 % of the fluctuating energy. For the present case, the results are more in line with Manhart & Wengle (1993), where no dominant modes (in terms of energy) could be found by the POD. Based on their typical frequencies and wavelengths (to be discussed in a moment), the fluctuating modes are divided into three groups. They are labelled A, B and C and listed in table 2. Further, they are indicated in figure 13(*a*) by different symbols. We observe that this division roughly coincides with the change of slope of the spectrum, which happens approximately

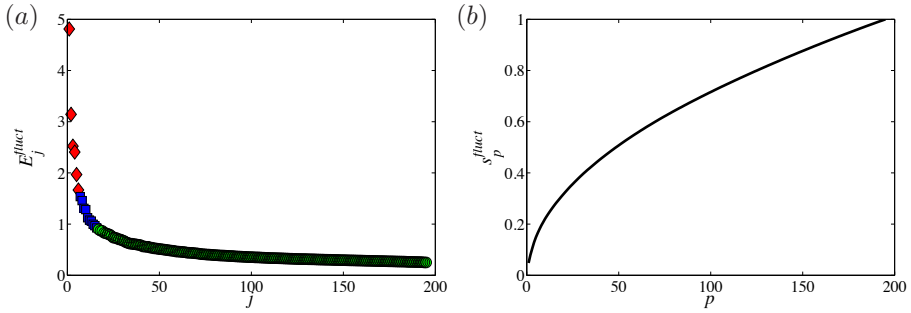

FIGURE 13. (a) The fluctuating kinetic energy $E_j^{\text{fluct}} = (\lambda_j / \sum_{i=1}^{195} \lambda_i) \times 100$ with $j = 1, ..., 195$, where the groups A, B and C in table 2 are indicated by ($\diamond$), ($\square$) and ($\circ$), respectively. (b) Cumulative energy sum of the fluctuating kinetic energy, $s_p^{\text{fluct}} = \sum_{i=1}^{p} \lambda_i$.

TABLE 2. Characteristics of the various groups of POD modes.

Group	Mode(s)	E_j^{fluct} (%)	$St \equiv fh/u_b$	λ_x	λ_y	λ_z
A	$1-6$	16.5	0.005–0.015	$10h$	$4h$	$4h$
B	$7-16$	11.7	0.01–0.04	$2.5h$	$2h$	$2h$
C	$17-195$	71.7	0.04–0.3	$\leq 2.5h$	$\leq 2h$	$\leq 2h$

in the junction between group B and C. In group C, the energy distribution is flatter and the modes are consequently less distinct and more related to smaller-scale turbulence. Figure 13(b) suggests further that approximately 25 % (49 out of 195) of the fluctuating modes are needed to represent 50 % of the fluctuating energy, which is typically observed to be the case for turbulent flows (*e.g.* Manhart & Wengle 1993). From figure 13(a), it is evident that the modes do not pairwise occupy exactly the same energy as would be the case for a POD decomposition of a linear flow where pure travelling structures are commonly present. As we shall see, however, this does not rule out the fact that a travelling coherent structure exist in the present flow.

Three-dimensional visualisations of POD modes $1, 2$ and $3, 8$ are given in figures 14 and 15, respectively. Modes $1, 2, 3$ are representative for group A, whereas mode 8 is characteristic for group B. In terms of energy, mode 1 and 8 are related as $E_1^{\text{fluct}}/E_8^{\text{fluct}} = 3.3$. A number of important observations can be made: First of all, the structures corresponding to the first three fluctuating modes are essentially two large streamwise streaks, with alternating positive and negative streamwise fluctuation velocity. The magnitude of their streamwise velocity component is roughly 500 times the crossflow velocities. The combined effect of these fluctuations is to bend the confined jet and create a streamwise wave. The corresponding wavelength is estimated to be $\lambda_x \approx 10h$.

In the two cross-stream directions (y and z), the modes span the entire cross section, such that $\lambda_y = \lambda_z \approx 4h$. These structures are thus the largest possible for the given geometry, since $L_y = L_z = 4h$ in the region where the modes are active. This is in agreement with Villermaux & Hopfinger (1994) who concluded that for confined flapping jets in asymmetric configurations, the largest confinement dimension will dominate the flow. The streaks in figure 14 resemble the POD modes originating from a jet with inherent low frequency flapping (see Moreno *et al.* 2004), supporting the fact that there is indeed a sinusoidal motion present in the diffuser. Note that the modes here are shown at one specific time and since each mode has a particular time dependence given by the (approximately) sinusoidal variation (to be discussed shortly), the wave has at some later time shifted its positive and negative side. Indeed, the streamwise wavelength noted above is consistent with the meandering visible in the instantaneous snapshots in figure 7. One of the streaks pertaining to mode 1 (figure 14a) is filling the right lower corner ① (when facing in the positive x-direction). The second streak in this mode is located above the first one and centred in the domain with respect to z ②, implying a diagonal wave motion in this region. Mode 2, on the other hand, appears to be located half a wavelength upstream of mode 1. In particular, one of its streaks continues upstream of the recently mentioned streak of mode 1 ③. Likewise, its second streak is somewhat upstream of the first described streak of mode 1 and situated very close to the right wall in the diffuser ④. Both modes extend into the mean separated region (*cf.* the mean flow in figure 2a), implying a coherent movement of the flow inside and outside the mean separated region. Mode 3 (figure 15a) displays a very clear wave, whose oscillation mainly goes along z, since negative ⑤ and positive ⑥ fluctuations are located side by side in the z-direction.

Higher modes, *e.g.* mode 8 (see figure 15b) have wavelengths approximately half that of the first four modes, both in terms of the streamwise and spanwise (*i.e.* y and z) wavelengths, respectively. They are in general more spread throughout the diffuser, but are mainly located upstream of the previous modes. Correspondingly, mode 8 is observed to extend very little beyond $x \approx 15$ in figure 15(b). Due to the location of the positive ⑦ and negative ⑧ fluctuations, it suggests a spanwise flapping mainly located within the diffuser region. In the side-view in figure 15(b), we note that mode 8 does not extend into the mean separated region as much as the previous modes, which indicates that the separated zone shares its dominant frequency rather with the largest structures in the diffuser.

The time dependence of the POD modes is computed by Galerkin projection (equation 4) and shown in figure 16(a-c). Note that the time axes have been redefined such that $t'u_b/h = 0$ in these figures denote the actual time $tu_b/h = 448$, when saving of instantaneous snapshots was initiated (see table 1). At least for the largest structures (figure 16a-b), the behaviour is nearly sinusoidal. We observe approximately four periods in 16(a), whose length can be estimated by $T \sim 100h/u_b$, giving a non-dimensional period of $T^* = Tu_b/h \sim 100$. The corresponding Strouhal number is therefore

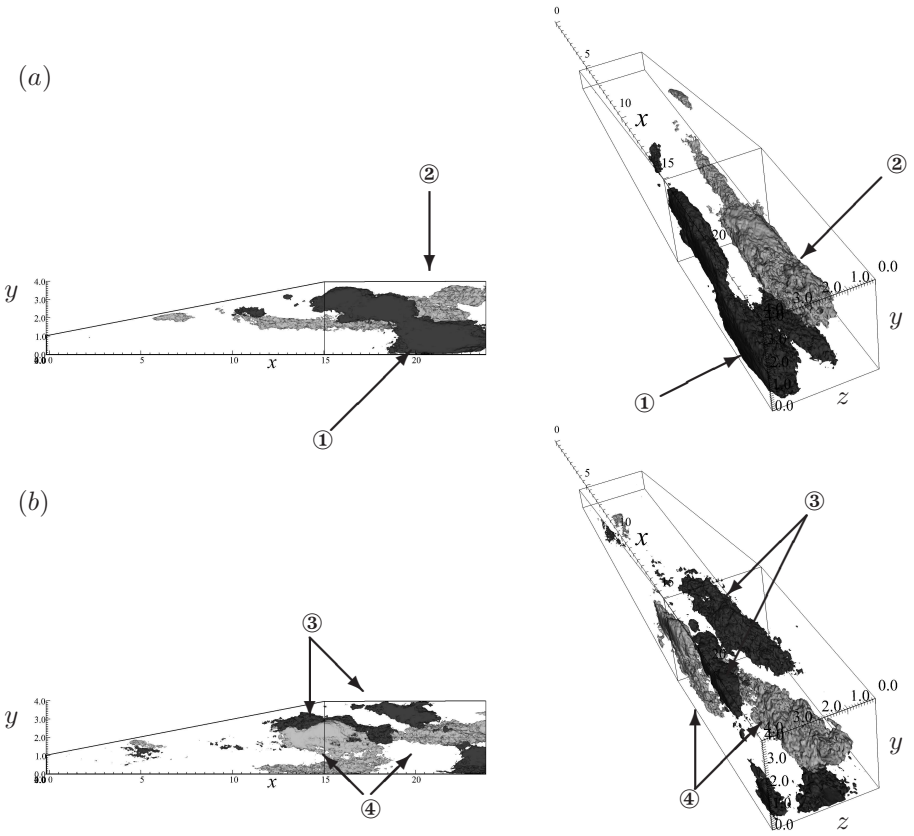

FIGURE 14. Isosurfaces (*dark gray:* 0.1, *light gray:* −0.1) of streamwise velocity pertaining to POD mode 1 (*a*) and 2 (*b*), shown at two different angles. The numbers indicate specific structures of the respective modes; further described in the text.

$St = 1/T^* \sim 0.01$. This frequency compares well to the spectral peak of the PSD in figure 11(*a*). Approximately the same period can be deduced from the evolution pertaining to modes 3 and 4 in figure 16(*b*). Considerably more revolutions (~ 12, *i.e.* 3 times more) are visible for modes 8 and 9 in figure 16(*c*), which roughly corresponds to the spectral peaks with higher frequency around $St = 0.04$ in figure 11(*a*).

A graphical representation of how the energy is distributed among the various fluctuating modes is given in figure 17. The colours show the logarithm of the modal energy, with the maximum of the first fluctuating mode normalised to unity. We see an accumulation of energy in the low frequency range, mainly in a band around $St = 0.01$. Clearly, these first modes are lacking energy in the high-frequency range. Higher modes, on the other hand, have little energy

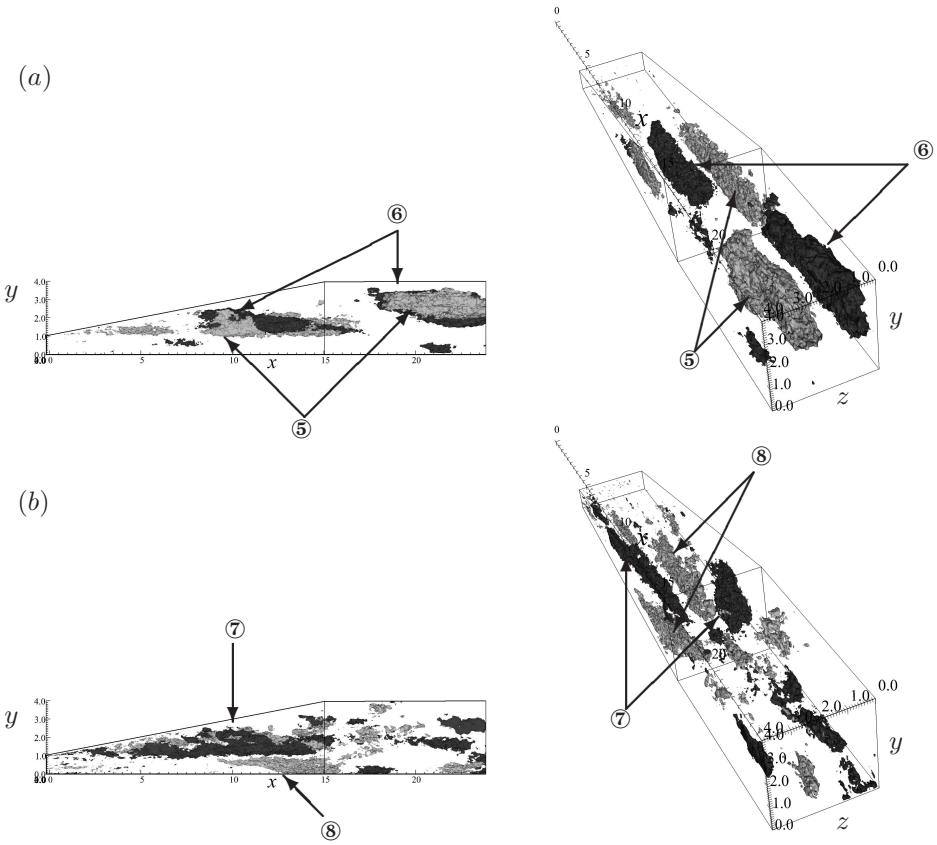

FIGURE 15. Isosurfaces (*dark gray:* 0.1, *light gray:* −0.1) of streamwise velocity pertaining to POD mode 3 (*a*) and 8 (*b*), shown at two different angles. The numbers indicate specific structures of the respective modes; further described in the text.

in the low-frequency range, which indicates that each of the different modes is relatively localised in frequency space. This localisation typically benefits the use of Koopman modes (see Rowley *et al.* 2009) for the flow analysis. This approach enables one specific structure to be associated with one specific frequency. However, we have chosen the more well-established POD route, since it usually provide smoother structures in turbulent flows. Finally, as noted before, in conjunction with figure 13, we see that the energy in figure 17 is quite well-distributed among the various scales, with roughly one order of magnitude in energy from the largest to the smallest scales.

In order to reveal the existence of travelling waves in the diffuser we will next project the flow onto the two-dimensional phase space spanned by the

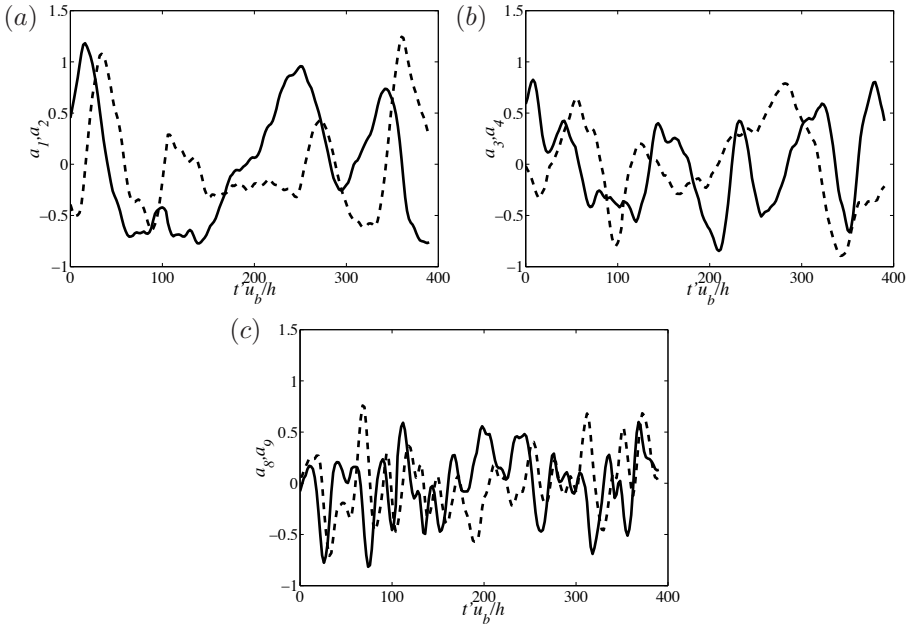

FIGURE 16. Temporal evolution of mode (a) 1 (———) and 2 (- - - -), (b) 3 (———) and 4 (- - - -), (c) 8 (———) and 9 (- - - -).

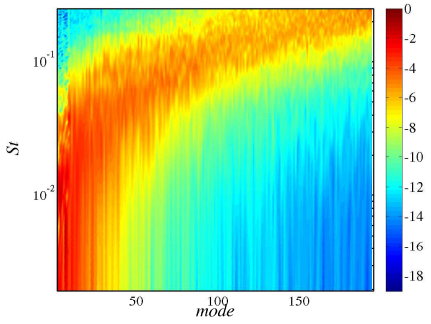

FIGURE 17. Energy distribution among the various fluctuating modes normalised by the peak value of the first fluctuating mode. The colours show the logarithm of the power spectral density of the respective modes.

fluctuating POD modes at hand, *i.e.* the time evolution of modes i and j (computed by equation 4) are drawn simultaneously. A wave in its most simple form may be completely characterised by two modes shifted 90 degrees in time. The two-dimensional phase portraits would in this case correspond to a circle, *i.e.* a

periodic orbit: $\boldsymbol{r}(t) = a_i(t)\boldsymbol{\psi_i} + a_j(t)\boldsymbol{\psi_j} = A\cos(t)\boldsymbol{e_x} + A\sin(t)\boldsymbol{e_y}$, where A is the amplitude of the mode and t is the time. If the time axis is included as a third direction, the resulting parameterised curve would be a helix, mathematically described by $\boldsymbol{r}(t) = A\cos(t)\boldsymbol{e_x} + A\sin(t)\boldsymbol{e_y} + t\boldsymbol{e_z}$. On the other hand, no particular coherence would correspond to a joint probability density function (PDF) of two random variables, uniformly distributed between $-A/2$ to $A/2$. If the time signal was not exactly periodic, *i.e.* quasi-periodic, the circle would not be closed, but rather spiral either inwards or outwards. In figure 18, the two-dimensional projection is shown for the fluctuating POD modes discussed above. In particular, figures 18(a) and 18(b) show the trajectories in the subspaces $(\boldsymbol{\psi}_1, \boldsymbol{\psi}_2)$ and $(\boldsymbol{\psi}_8, \boldsymbol{\psi}_9)$, respectively. Time is increasing counterclockwise in all figures, starting at t_0 and ending at t_{end}. In the right column the time axis is included as a third direction. Considering the high turbulence levels of the present flow (u_{rms}/u_b up to 25 %), these phase portraits show a remarkable coherence. The trajectory in figure 18(*a,left*) completes slightly more than three revolutions. The fact that the revolutions are not on top of each other merely indicates that each oscillation is not exactly the same, but nevertheless at least three cycles are present, more easily seen in figure 18(*a,right*). In figure 18(*b,left*), corresponding to modes 8 and 9, approximately 10 revolutions are present, which are closely on top of each other. Including time as a third direction in figure 18(*b,right*), we see that the motion approximately takes the form of a helix, hence the revolutions are linear in t. The radius of the helix can be seen to change somewhat, which is an effect of the modes not being fully separated in frequency space and consequently containing some lower frequencies. This finding gives a strong indication of the quasi-periodic motion in the diffuser that gives rise to a travelling wave. Two typical frequencies of approximately $St = 0.01$ and $St = 0.04$ have been shown to be active. The convection velocities, v_p, of these waves can be computed approximately using the wavelengths and frequencies given in table 1. Using the expression for phase velocity we find $v_p = f\lambda_x \sim 0.01 \cdot 10 \sim 0.04 \cdot 2.5 \approx 0.1$, which is of the same order of magnitude as can be deduced from the snapshots in figure 7. Note that the number of complete revolutions seen in figure 18(a) and the periods derived from figure 16 are limited but nonetheless ensured to be correct, as the same frequencies have been observed in the entire data set, including earlier simulation times not shown here.

In summary, the POD analysis of the present data has not identified any dominant structure, except for the mean flow, in terms of energy. In spite of this, the first eigenfunctions are large structures with a high degree of spatial coherence, which moreover display a quasi-periodic temporal behaviour. They are consequently important in order to explain the dynamics in the diffuser. Similar structures with similar time dependence were identified by Moreno *et al.* (2004) in an experimental study of a turbulent jet. There, however, a larger fraction of the total energy was contained in the first two modes.

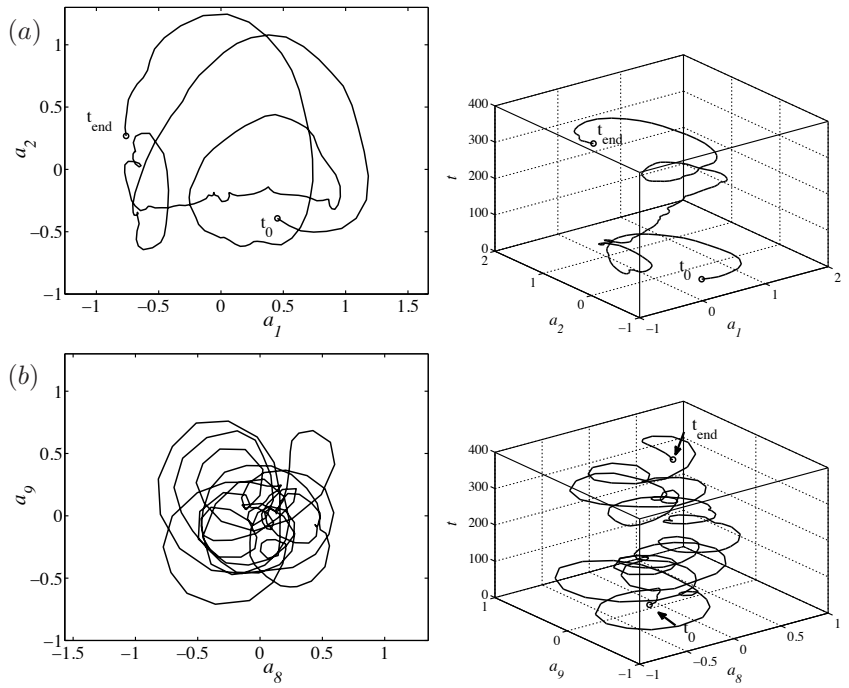

FIGURE 18. Temporal orbits in the subspaces $(\boldsymbol{\psi}_1, \boldsymbol{\psi}_2)$ (a) and $(\boldsymbol{\psi}_8, \boldsymbol{\psi}_9)$ (b) showing the quasi-periodic motions of the largest and second largest structures present in the diffuser, respectively. Time is in the left column increasing counterclockwise. In the right column, the motion is shown along the vertical time axis.

A final remark on the convergence of the POD modes is in place. Ideally, as more and more snapshots are included, the eigenvalues λ_j from problem (5) and the eigenfunctions $\boldsymbol{\psi}_j(\boldsymbol{x})$ from equation (6) should converge. For a flat spectrum, as the one reported in figure 12, many thousands snapshots are needed to converge the eigenvalues (see Manhart & Wengle 1993). The first eigenfunctions of the POD, on the other hand, generally converge much quicker. Since this study aims at quantifying the observed large-scale motion, we limit ourselves to establishing convergence of the first few modes. This can be undertaken by an orthogonality check between the modes. Since POD modes are orthogonal to each other by construction, thus

$$\iiint_V \boldsymbol{\psi}_j(\boldsymbol{x})\boldsymbol{\psi}_i(\boldsymbol{x})\ \mathrm{d}\boldsymbol{x} = \delta_{ij}, \tag{7}$$

where δ_{ij} is the Kronecker delta, holds exactly. If we in equation (7) used modes computed using 98 and 147 or 147 and 196 snapshots, we would get a

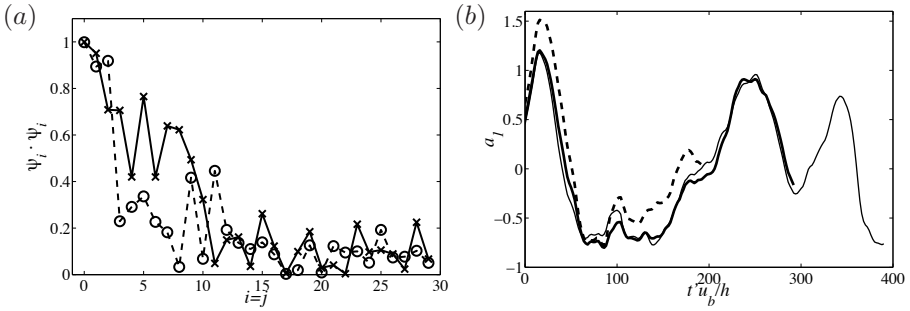

FIGURE 19. Convergence of the POD modes. (*a*) The inner product between the 30 first modes computed with 98 & 147 snapshots (- - - -) and 147 & 196 snapshots (——), respectively. Only $i = j$ is shown, with 1 indicating parallel and 0 orthogonal vectors. (*b*) Time evolution of POD mode 1 computed with 98 (——), 147 (- - - -) and 196 (——) snapshots.

measure for the convergence, *i.e.*

$$\iiint_V \boldsymbol{\psi}_j^{98\ \mathrm{snaps}}(\boldsymbol{x})\boldsymbol{\psi}_i^{147\ \mathrm{snaps}}(\boldsymbol{x})\ \mathrm{d}\boldsymbol{x} = \widetilde{\delta_{ij}^1}, \tag{8}$$

and

$$\iiint_V \boldsymbol{\psi}_j^{147\ \mathrm{snaps}}(\boldsymbol{x})\boldsymbol{\psi}_i^{196\ \mathrm{snaps}}(\boldsymbol{x})\ \mathrm{d}\boldsymbol{x} = \widetilde{\delta_{ij}^2}, \tag{9}$$

respectively. Here, $\widetilde{\delta_{ij}}$ denotes the approximate Kronecker delta. In figure 19(*a*), we compare $\widetilde{\delta_{ij}^1}$ and $\widetilde{\delta_{ij}^2}$ for $i = j$. Clearly, $\widetilde{\delta_{ii}^2}$ (no summation on repeated indices) are closer to unity than $\widetilde{\delta_{ii}^1}$, indicating that the structures change less by adding 49 more snapshots to 147 than to 98. Moreover, the inner product between $\boldsymbol{\psi}_j^{147\ \mathrm{snaps}}$ and $\boldsymbol{\psi}_j^{196\ \mathrm{snaps}}$, shows a value of 0.7 for the first four modes, suggesting that the modes do not change much, even if the data sets are spaced 49 snapshots apart, *i.e.* approximately one of the long periods discussed earlier. A similar check is performed using the time series of mode 1, computed using 98, 147 and 196 snapshots, shown in figure 19(*b*). If the mode is unchanged, then the time series is expected to be identical. We observe that the evolution changes by employing 147 instead of 98 snapshots. However, the change is minor as 49 additional snapshots (*i.e.* a total of 196) are used. For inflow-outflow problems, such as the present flow, the modes are not generally phase-shifted, and consequently orthogonality in space is a valid measure of the convergence of the structures. We therefore conclude that 196 snapshots are enough for the proper orthogonal decomposition in order to get a correct representation of the large-scale spatial structures.

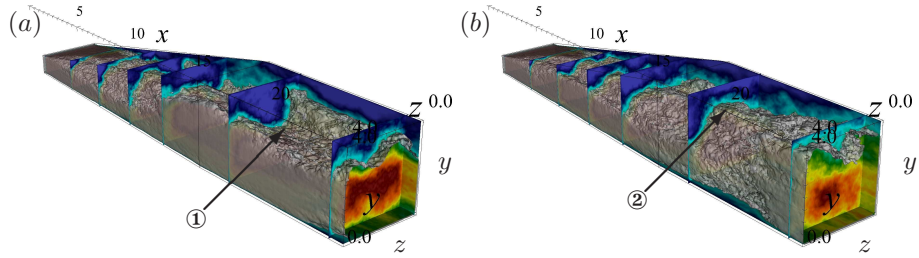

FIGURE 20. Superposition of POD modes 0–6 shown for one period in figure 16(a) at times tu_b/h = (a) 8 and (b) 54. Gray isosurface show constant streamwise velocity, $u/u_b = 0.1$. Crossflow planes show streamwise velocity ranging from -0.1 (*blue*) to 0.5 (*red*).

4.2. *Low-dimensional reconstruction*

The scale separation provided by the POD suggests to study the large-scale anisotropic dynamics without the influence of the small-scale turbulence in a 'low-pass filtered' manner. Hence it facilitates the focus on the relevant dynamics and helps us in our physical understanding of the dominant dynamical processes in the flow. To build the low-pass filtered (*i.e.* low-dimensional) model, we follow the procedure previously employed in *e.g.* Cazemier *et al.* (1998) and the references therein, by superimposing some of the first modes in the expansion — here modes 0–6 — with their corresponding temporal weight and studying the time evolution. Mode 0 is the mean flow, and contains most of the energy in the diffuser, as discussed previously. Modes 1–6 belong to 'group A' where the largest wavelengths and lowest frequencies are found. Therefore, these modes are representative for the large-scale motion in the diffuser, and thus the focus of the present study. Isosurfaces of constant streamwise velocity are shown in figure 20 at two specific times ($t'u_b/h = 8$ and $t'u_b/h = 54$). The travelling wave shown in the phase portraits is now clearly seen to propagate through the domain. Starting from figure 20(a), the sinusoidal shape of the high-speed core of the flow has one of its minima located at $x \approx 20$ ①. As a consequence of the confinement of the flow, high velocity fluid is pushed up on the sides, close to the side walls. One half period later, in figure 20(b), the minimum has propagated forward in the domain (not visible anymore), and is now replaced by a maximum at $x = 20$ ②. Again, the confinement forces the flow in a crossflow plane downwards in the vicinity of the side walls. Another half period later (not shown) the flow is back to its approximate original state. To conclude, the low-dimensional model translates the quasi-periodic motion exemplified in the phase portrait in figure 18(a) into flow variables, and the travelling wave is clearly visible. An effect of this meandering is a strong secondary flow created in the crossflow directions. Thus, relating back to the mean vorticity in figure 4, the unsteady jet motion will generate negative streamwise

vorticity in the upper left corner during an up-sweep, and positive streamwise vorticity during a corresponding down-sweep. In the mean, however, this vorticity is averaged to zero and one is left with the mean streamwise vorticity originating from the inflow duct.

Having access to the POD modes and thus knowledge about the most energetic and largest structures, the r.m.s originating from the low-dimensional model of the flow can be computed. This allows us to investigate the origin (*e.g.* the large or the small scales, respectively) of the contributions to the observed, *i.e.* total, r.m.s. The mean streamwise fluctuations ($\{u_{rms}/u_b\} \cdot 100$) given by the first six fluctuating modes are shown in figure 21 (*middle row*) and compared to the fluctuations from the entire DNS flow field (*upper row*) and the experimental results from Cherry *et al.* (2008) (*lower row*), at two different downstream locations. It can be observed that the first six modes (*i.e.* structures spanning half the length and the entire width of the diffuser) contribute almost entirely to the peaks of the total r.m.s. Elsewhere their fluctuations are close to zero. More specifically, by comparing the respective peak values, one can conclude that the r.m.s of these large-scale structures contribute with $60 - 80$ % to the total r.m.s peaks. Their contribution increases towards the rear of the diffuser due to their spatial distribution and will in the last part of the straight section (not shown) constitute more than 90 % of the peaks of the total r.m.s. This gives an indication that the bulk of the u_{rms} in this region originates from the large-scale oscillation present in the diffuser, rather than fine-scale turbulence. Note that there is no contradiction herein regarding their contribution to the *total* fluctuating energy, since we here only discuss their *local* contribution in a crossflow plane.

In the DNS and the experimental u_{rms} data in figure 21 one can see the tendency of double peaks. Neither in Cherry *et al.* (2008) nor in Ohlsson *et al.* (2010) a satisfactory explanation concerning this particular feature was provided. However, by considering the fluctuations from the low-dimensional reconstruction, the reason for this can be clarified. First, we note that the u_{rms} from the low-dimensional reconstructed model has even more pronounced double peaks, suggesting that this feature most likely derives from the large-scale motion. To get a better understanding of how this is connected to the movement of the high-speed core of the flow, we will next turn to figure 22. Here, a contour defining 95 % of the maximum streamwise velocity in the low-dimensional reconstructed flow (modes 0–6) is shown (*black*) for the entire evolution of the flow. Furthermore, the centre of gravity of the area enclosed by the black contour is computed (*white*). Over the full snapshot time range this gives rise to a trajectory solely based on the large-scale motion. Consequently, the fluctuations of the peak velocity are greatly reduced as opposed to using the original snapshots, which would be far too chaotic to draw any valuable conclusions. The main directions, as given by this trajectory, are sketched by the white arrows in figure 21 (*middle row*). By comparing figure 22 with figure 21 we note that the movement of the high-speed core of the flow is located within the area where the minimum of the u_{rms} is found. Around this area,

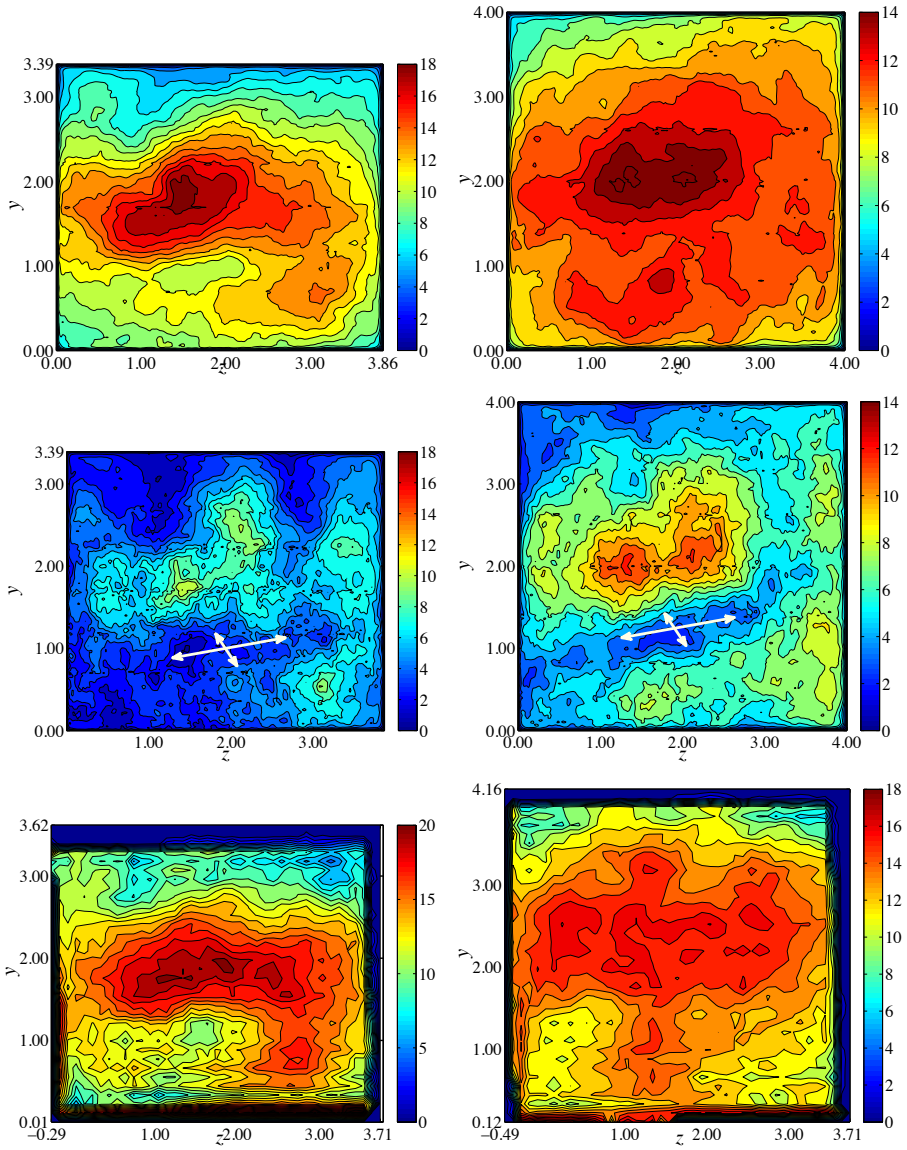

FIGURE 21. Crossflow planes of streamwise velocity fluctuations, $u_{rms}/u_b \cdot 100$, 12 h (*left column*) and 20 h (*right column*) downstream of the diffuser throat. *Upper row:* Fluctuations from entire flow field. *Middle row:* Fluctuations from low-dimensional reconstruction employing the six first fluctuating modes. *Lower row:* Experiment by Cherry *et al.* (2008). Contour lines are spaced $2 \cdot u_{rms}/u_b \cdot 100$ apart. White arrows indicate the large-scale movement.

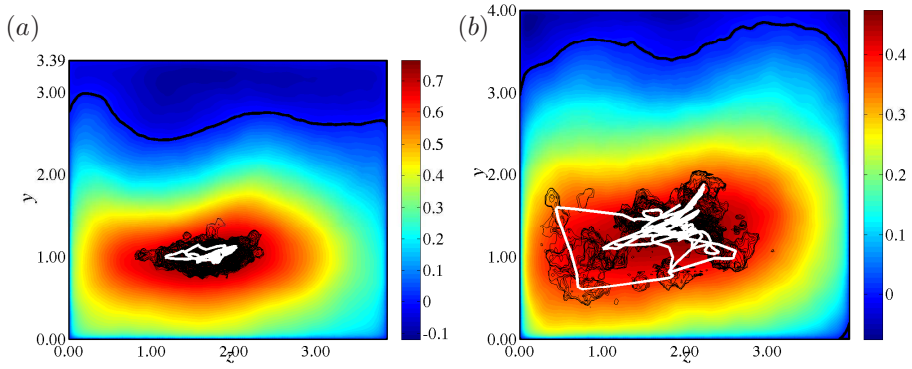

FIGURE 22. Crossflow planes, (*a*) 12 and (*b*) 20 h downstream of the diffuser throat, coloured by streamwise mean velocity, U/u_b. Thin black contours define 95 % of the max streamwise velocity of the low-dimensional reconstruction using the six first fluctuation modes. For each contour, its centre of gravity is shown in white. Thick black line indicates zero velocity contour.

the peaks of u_{rms} are found. At $x = 12$, we observe in figure 22(*a*) that the core moves mainly along the z-direction, but with a slight angle to the y-axis, in agreement with the r.m.s minima in figure 21 (*left column*). Further downstream at $x = 20$, in figure 22(*b*), the bulk of the motion goes along the same diagonal as in figure 22(*a*), but with a significant number of excursions in the y-direction. The corresponding minimum in the total r.m.s is as an effect not as distinct as compared to the one at $x = 12$, but is clearly observed in the r.m.s pertaining to the low-dimensional model. A plausible explanation for the phenomenon that gives rise to the minimum in the u_{rms} and the resulting peaks (two or more) around this minimum is given in figure 23. If we assume the flapping being entirely in z, a simple model for the flapping jet can be written as

$$u(z,t) = e^{-(\{z-\sin(t)\}^2)};\ t \in [0, 4\pi],\ x \in [-\pi, \pi]. \tag{10}$$

The time average and r.m.s of this function are shown in figure 23. We note that the time average has a peak at $z = 0$, *i.e.* in the interior of the domain, in agreement with the colour map in figure 22. Secondly, we note that the r.m.s reaches its minimum where the maximum of the mean is located, *i.e.* at $z = 0$ in this case. Around this minimum, at the turning points of the jet, the r.m.s attains its highest values. This is also what is observed both in the long average u_{rms} in the upper row of figure 21, as well as in the experimental data in the lower row. In the low-dimensional reconstruction shown in the middle row, this effect is strong with the motion indicated by the white arrows. This is of course a simplified model, where we have not taken into account *e.g.* the deformation of the jet. However, it seems probable that the double

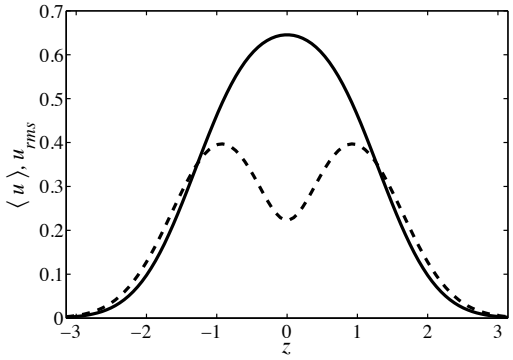

FIGURE 23. Time average (——) and r.m.s (----) of the function $u(z,t) = e^{-(\{z-\sin(t)\}^2)}$.

peaks found in the u_{rms} are a sign of a large-scale motion. It should be pointed out that these conclusions are valid even if only modes 0, 1 and 2 are used for the reconstruction.

5. Conclusions

The flow in a three-dimensional, turbulent and separated diffuser at $Re = 10\ 000$ is studied using numerical data from the direct numerical simulation (DNS) described in Ohlsson *et al.* (2010), which closely mimics the experiment of 'diffuser 1' by Cherry *et al.* (2008). To this extent, the existing DNS database was extended to account for all possible time scales in the flow. The aim is to elucidate some aspects of the complex physics involved in three-dimensional separation in its own interest, as well as to provide a detailed description of this flow, which has recently been established as a test case for turbulence closure models.

We have more rigorously confirmed the findings in Ohlsson *et al.* (2010) that the secondary flow in the inflow duct persist into the diffuser. Due to the asymmetry of the geometrical set-up, the corner vortices close to the top expanding wall are unequally distributed and diffused, which gives rise to an imbalance of vorticity and causes the separated zone to experience the particular asymmetric behaviour. Using time-resolved information, we could deduce that instantaneous backflow is to a large extent present in the straight section after the diffuser, while the mean flow itself is attached.

Analysis from a set of time signal probes in the flow shows that there is a quasi-periodic motion present in the low frequency range in a narrow band $St \equiv fh/u_b \in [0.0092, 0.014]$, yielding time periods $T^* = Tu_b/h \in [70, 110]$. The origin of this low frequency is the meandering of the incoming flow, as it interacts with the separated flow in the diffuser. This finding is supported by proper orthogonal decomposition (POD) of the flow, where large streamwise

streaks spanning half the length and the entire width of the diffuser are identified. In agreement with Moreno *et al.* (2004) this manifests that large-scale shedding is present in the flow. Unlike this study, no particular mode could be identified as being dominant in terms of energy. Projections of the flow onto the two-dimensional phase space spanned by the most energetic fluctuating POD modes show evidence that the large scales of the flow behave quasi-periodically, which results in a travelling wave with convection velocity $v_p \approx 0.1$. Due to the confinement of the flow, this wave creates a strong secondary flow in the crossflow directions.

The root mean square (r.m.s) of the streamwise component, computed from a low-dimensional POD model of the flow, shows that the first few modes contribute with $60 - 80$ % to the total u_{rms} peaks in the diffuser, but are close to zero elsewhere. This finding indicates that the bulk u_{rms} in the later part of the diffuser derives from the large-scale oscillation present and provides an explanation for the scattered r.m.s peaks with a minimum in the centre, seen in both the DNS and the experiments. A trajectory of the high-speed core of the flow solely based on a low-dimensional POD model shows that the core of the flow, moves in preferred directions over a relatively long time scale.

Considering the literature on pressure-induced separated flows, most configurations involve at least one homogeneous direction. Diffusers have commonly been studied in two-dimensional configurations, *i.e.* with a spanwise homogeneous direction. In these flows, no such large-scale spatial coherence, as detected in the present flow case, has to our knowledge been reported. On the other hand, taking into account studies performed on confined jets, low-frequency periodic shedding is frequently appearing, provided that the walls are close enough to form recirculation zones adjacent to the jet. Due to the comparably high Reynolds number ($Re = 10\ 000$, based on bulk velocity and inflow-duct height) in the present diffuser flow, the momentum of the incoming fluid is high and will, in combination with the large opening angle of the diffuser, consequently share many properties with a turbulent jet bounded by separated flow. We therefore conclude that the reason for the observed large-scale quasi-periodic motion is the confinement in combination with the high Reynolds number and the large separated zone on the top diffuser wall. The dominant frequencies found in the present case coincide remarkably well with the finding by Villermaux & Hopfinger (1994), who identified a low frequency flapping of $St \sim 0.01$ in the jet. This is also confirmed by Lawson & Davidson (2001), who in a similar set-up reported a very low Strouhal number ($St \ll 1$) when the confinement is such that the jet is bounded by one or two recirculation zones. The observed frequencies in the present flow are likely to be the result of a self-sustained oscillation created by a feedback mechanism via the recirculated flow, similar to what was reported by Lawson & Davidson (2001) for the confined jet. To be able to fully confirm this statement, more analysis is however needed.

Computer time was provided by ALCF, Argonne National Laboratory (ANL) on the IBM BG/P (ANL), and by SNIC (Swedish National Infrastructure for Computing) with a generous grant by the Knut and Alice Wallenberg (KAW) Foundation at the Centre for Parallel Computers (PDC) at the Royal Institute of Technology (KTH). Dr. Shervin Bagheri is acknowledged for providing a POD code skeleton. We are further grateful to Prof. Neil Sandham, Dr. Miloš Ilak, Onofrio Semeraro, Dr. Gabriele Bellani and Dr. Outi Tammisola for fruitful discussions.

References

Adams, N. A. 2000 Direct simulation of the turbulent boundary layer along a compression ramp at $M = 3$ and $Re_\theta = 1685$. *J. Fluid Mech.* **420**, 47–83.

Cazemier, W., Verstappen, R. W. C. P. & Veldman, A. E. P. 1998 Proper orthogonal decomposition and low-dimensional models for driven cavity flows. *Phys. Fluids* **10** (7), 1685–1699.

Cherry, E. M., Elkins, C. J. & Eaton, J. K. 2008 Geometric sensitivity of three-dimensional separated flows. *Int. J. Heat Fluid Flow* **29** (3), 803–811.

Cherry, E. M., Elkins, C. J. & Eaton, J. K. 2009 Pressure measurements in a three-dimensional separated diffuser. *Int. J. Heat Fluid Flow* **30** (1), 1–2.

Délery, J. M. 2001 Robert Legendre and Henri Werlé: Toward the Elucidation of Three-Dimensional Separation. *Annu. Rev. Fluid Mech.* **33** (1), 129–154.

Eaton, J. K. & Johnston, J. P. 1980 Turbulent flow reattachment - an experimental study of the flow and structure behind a backward-facing step. *Tech. Rep.* Rept MD-39. Thermosciences Division, Stanford Univ., USA.

Fischer, P. F. 1997 An overlapping Schwarz method for spectral element solution of the incompressible Navier–Stokes equations. *J. Comput. Phys.* **133** (1), 84–101.

Fischer, P. F., Lottes, J. W. & Kerkemeier, S. G. 2008 nek5000 Web page. http://nek5000.mcs.anl.gov.

Friedrich, R. & Arnal, M. 1990 Analysing turbulent backward-facing step flow with the lowpass-filtered Navier-Stokes equations. *J. Wind Engng. Indust. Aerodyn.* **35**, 101 – 128.

Herbst, A. H., Schlatter, P. & Henningson, D. S. 2007 Simulations of turbulent flow in a plane asymmetric diffuser. *Flow Turbulence Combust.* **79**, 275–306.

Holmes, P., Lumley, J. & Berkooz, G. 1996 *Turbulence, Coherent Structures, Dynamical Systems and Symmetry*. Cambridge University Press, Cambridge, UK.

Jakirlić, S., Kadavelil, G., Kornhaas, M., Schäfer, M., Sternel, D.C. & Tropea, C. 2010*a* Numerical and physical aspects in LES and hybrid LES/RANS of turbulent flow separation in a 3-D diffuser. *Int. J. Heat Fluid Flow* **31** (5), 820 – 832.

Jakirlić, S., Kadavelil, G., Sirbubalo, E., Breuer, M., v. Terzi, D. & Borello, D. 2010*b* In *14th ERCOFTAC SIG15 Workshop on Refined Turbulence Modelling: Turbulent Flow Separation in a 3-D Diffuser*. *ERCOFTAC Bulletin.* December Issue 85, case 13.2 (1). ERCOFTAC.

Kaltenbach, H.-J., Fatica, M., Mittal, R., Lund, T.S. & Moin, P. 1999 Study of flow in a planar asymmetric diffuser using large-eddy simulation. *J. Fluid Mech.* **390**, 151–185.

Kiya, M. & Sasaki, K. 1985 Structure of large-scale vortices and unsteady reverse flow in the reattaching zone of a turbulent separation bubble. *J. Fluid Mech.* **154**, 463–491.

Landahl, M. T. 1980 A note on an algebraic instability of inviscid parallel shear flow. *J. Fluid Mech.* **98**, 243–251.

Lawson, N. J. & Davidson, M. R. 2001 Self-sustained oscillation of a submerged jet in a thin rectangular cavity. *J. Fluid Struct.* **15** (1), 59 – 81.

Le, H., Moin, P. & Kim, J. 1997 Direct numerical simulation of turbulent flow over a backward-facing step. *J. Fluid Mech.* **330**, 349–374.

Lumley, J. L. 1967 The structure of inhomogeneous turbulent flows. In *Atm. Turb. Radio Wave Prop.* (ed. A. M. Yaglom & V. I. Tatarsky), pp. 166–178. Nauka, Moscow, Russia.

Lygren, M. & Andersson, H. 1999 Influence of boundary conditions on the large scale structures in turbulent plane couette flow. In *Turbulence and Shear Flow Phenomena 1* (ed. S. Banerjee & J. Eaton), pp. 15–20. Santa Barbara, California: Begell House, New York, USA.

Manhart, M. & Wengle, H. 1993 A spatiotemporal decomposition of a fully inhomogeneous turbulent flow field. *Theor. Comput. Fluid Dyn.* **5**, 223–242.

Maurel, A., Ern, P., Zielinska, B. J. A. & Wesfreid, J. E. 1996 Experimental study of self-sustained oscillations in a confined jet. *Phys. Rev. E* **54** (4), 3643–3651.

Moin, P. & Moser, R. 1989 Characteristic-eddy decomposition of turbulence in a channel. *J. Fluid Mech.* **200**, 471–509.

Moreno, D., Krothapalli, A., Alkislar, M. B. & Lourenco, L. M. 2004 Low-dimensional model of a supersonic rectangular jet. *Phys. Rev. E* **69** (2), 026304.

Na, Y. & Moin, P. 1998 Direct numerical simulation of a separated turbulent boundary layer. *J. Fluid Mech.* **374**, 379–405.

Ohlsson, J., Schlatter, P., Fischer, P. F. & Henningson, D. S. 2010 Direct numerical simulation of separated flow in a three-dimensional diffuser. *J. Fluid Mech.* **650**, 307–318, note: change of name from J. Ohlsson to J. Malm.

Piquet, J. 1999 *Turbulent Flows: Models and Physics*. Springer-Verlag, Berlin, Germany.

Rowley, C. W., Mezić, I, Bagheri, S, Schlatter, P & Henningson, D. S. 2009 Spectral analysis of nonlinear flows. *J. Fluid Mech.* **641**, 115–127.

Schlatter, P., Örlü, R., Li, Q., Brethouwer, G., Fransson, J. H. M., Johansson, A. V., Alfredsson, P. H. & Henningson, D. S. 2009 Turbulent boundary layers up to $Re_\theta = 2500$ studied through numerical simulation and experiments. *Phys. Fluids* **21** (5), 051702.

Schneider, H., Terzi, D. A. & Rodi, W. 2009 Reliable and accurate prediction of three-dimensional separation in asymmetric diffusers using large-eddy simulation. In *Proceedings of ASME Turbo Expo 2009: Power for Land, Sea and Air*. Orlando, USA.

Simpson, R. L. 1981 A review of some phenomena in turbulent flow separation. *J. Fluid Engng.* **102**, 520–533.

Simpson, R. L. 1989 Turbulent boundary-layer separation. *Annu. Rev. Fluid Mech.* **21** (1), 205–232.

Sirovich, L. 1987 Turbulence and the dynamics of coherent structures, i-iii. *Quart. Appl. Math.* **45**, 561–590.

Spille-Kohoff, A. & Kaltenbach, H.-J. 2001 Generation of turbulent inflow data with a prescribed shear-stress profile. In *DNS/LES Progress and Challenges* (ed. C. Liu, L. Sakell & T. Beutner). Third AFSOR conference on DNS and LES, Arlington, Texas: Greyden Press, Columbus, USA.

Törnblom, O., Lindgren, B. & Johansson, A. V. 2009 The separating flow in

a plane asymmetric diffuser with 8.5° opening angle: mean flow and turbulence statistics, temporal behaviour and flow structures. *J. Fluid Mech.* **636**, 337–370.

Tufo, H. M. & Fischer, P. F. 2001 Fast parallel direct solvers for coarse grid problems. *J. Parallel Distrib. Comput.* **61** (2), 151–177.

Villermaux, E. & Hopfinger, E. J. 1994 Self-sustained oscillations of a confined jet: a case study for the non-linear delayed saturation model. *Physica D: Nonlinear Phenomena* **72** (3), 230–243.

Wang, C., Jang, Y.J. & Leschziner, M.A. 2004 Modelling two- and three-dimensional separation from curved surfaces with anisotropy-resolving turbulence closures. *Int. J. Heat Fluid Flow* **25** (3), 499–512.